

Title	Grid integration of wave energy & generic modelling of ocean devices for power system studies
Authors	Blavette, Anne
Publication date	2013
Original Citation	Blavette, A. 2013. Grid integration of wave energy & generic modelling of ocean devices for power system studies. PhD Thesis, University College Cork.
Type of publication	Doctoral thesis
Rights	© 2013, Anne Blavette - http://creativecommons.org/licenses/by-nc-nd/3.0/
Download date	2024-05-03 09:34:55
Item downloaded from	https://hdl.handle.net/10468/1129



UCC

Coláiste na hOllscoile Corcaigh, Éire
University College Cork, Ireland



Grid Integration of Wave Energy & Generic Modelling of Ocean Devices for Power System Studies

Anne Blavette

A thesis submitted for the degree of Doctor of Philosophy

National University of Ireland, University College Cork

Supervisors:

Dr. Dara L. O'Sullivan¹, Dr. Michael G. Egan², Prof. Tony W. Lewis¹, Dr. Ray Alcorn¹

¹*Hydraulics & Maritime Research Centre, University College Cork*

²*Electrical & Electronic Engineering Department, University College Cork*

Jury:

Dr. John G. Hayes

Electrical & Electronic Engineering Department, University College Cork, Ireland

Dr. Eduardo Cotilla-Sanchez

Oregon State University, Corvallis, Oregon, USA

Declaration of own work

I hereby declare that this thesis is my own work and effort and that is not been submitted anywhere for any award. Where other sources of information have been used, they have been acknowledged.

Ar c'hlask a zo frank,
Ar c'havout n'eo ket stank.
("Searching is common, finding is not abundant.")
Breton proverb

守破離

Shu, Ha, Ri
("Obey, Digress, Separate")
Japanese martial art concept

Acknowledgments

This thesis has been realised at the Hydraulics & Maritime Research Centre (HMRC) thanks to Science Foundation Ireland whose financial support is gratefully acknowledged.

I wish to thank deeply my supervisors, Dr. Dara O’Sullivan, Dr. Michael Egan and Prof. Tony Lewis for the commitment and the enthusiasm with which they have fulfilled their role. Their high level of requirements in terms of work quality has been an invaluable learning experience for my doctoral education. I also wish to thank Dr. Ray Alcorn who accepted my application for a six-month internship at HMRC in 2009. Despite not being officially nominated as a supervisor, he has always made himself available to discuss technical issues when I needed, and I learnt a lot from him as well. I know how fortunate I was to benefit from their knowledge and expertise over these four past years.

I am also very grateful to all the staff of HMRC as, if it takes a whole village to raise a child according to a Nigerian proverb, it certainly takes a whole research centre to complete a PhD. My thanks also go to the staff of University College Cork in general for their helpfulness and affability.

I would also like to address a special thank to all the people involved in the European FP7 project entitled “CORES” (grant agreement n° 213633) in the framework of which experimental data, which has been a key element in this thesis, has been generated.

My sincere thanks also go to Dr. John Hayes and Dr. Eduardo Cotilla-Sanchez for accepting to participate in the jury of my viva voce.

I wish also to thank my friends for their support and their humour, especially when they asked me if I saw “the light at the end of the thesis”. I am also very grateful to my family for its unwavering support despite the distance.

Last but not least, I wish to thank Fred for agreeing to expatriate with me to Ireland despite the weather to which he never got used. He made our time in this country a wonderful experience. Without him, this thesis would have not been possible.

Abstract

The work presented in this thesis covers four major topics of research related to the grid integration of wave energy. More specifically, the grid impact of a wave farm on the power quality of its local network is investigated. Two estimation methods were developed regarding the flicker level Pst generated by a wave farm in relation to its rated power as well as in relation to the impedance angle Ψ_k of the node in the grid to which it is connected. The electrical design of a typical wave farm design is also studied in terms of minimum rating for three types of costly pieces of equipment, namely the VAr compensator, the submarine cables and the overhead line. The power losses dissipated within the farm's electrical network are also evaluated. The feasibility of transforming a test site into a commercial site of greater rated power is investigated from the perspective of power quality and of cables and overhead line thermal loading. Finally, the generic modelling of ocean devices, referring here to both wave and tidal current devices, is investigated.

List of publications

The work presented in this thesis has produced the following publications:

Book chapters

2013

A. Blavette, J. MacEnri. *Electrical Design for Ocean Wave and Tidal Energy Systems*, chapter Grid integration: Power quality. The Institution of Engineering and Technology (IET), edited by R. Alcorn and D. O'Sullivan, to be published in 2013.

A. Blavette, M. Santos, J. MacEnri, D. Kavanagh. *Electrical Design for Ocean Wave and Tidal Energy Systems*, chapter Grid integration: Case studies. The Institution of Engineering and Technology (IET), edited by R. Alcorn and D. O'Sullivan, to be published in 2013.

Peer-reviewed international conference articles

2013

A. Blavette, M. Egan, D. O'Sullivan, T. Lewis, Dimensioning the equipment of a wave farm: energy storage and cables. In *Proceedings of the EVER13 Conference, Monaco*, 2013.

2012

A. Blavette, D. O'Sullivan, M. Egan, T. Lewis. Grid impact assessment of a medium size wave farm connected to different test sites. In *Proceedings of the 4th International Conference on Ocean Energy, Dublin, Ireland*, 2012.

A. Blavette, D. O'Sullivan, T. Lewis, M. Egan. Impact of a wave farm on its local grid: voltage limits, flicker level and power fluctuations. In *Proceedings of the IEEE/MTS OCEANS12 Conference, Yeosu, South Korea*, 2012.

A. Blavette, D. O'Sullivan, R. Alcorn, T. Lewis, M. Egan. Grid impact of a wave farm on its local network: analysis of voltage and flicker levels, In *Proceedings of the 31th International Conference on Ocean, Offshore and Arctic Engineering, OMAE2012, ISBN 978-0-7918-4494-6, n° 83616, Rio de Janeiro, Brazil*, 2012.

D. O'Sullivan, F. Salcedo, A. Blavette, M. Santos, T. Lewis. Case studies on the benefits of energy storage for power quality enhancement: oscillating water column arrays. In *Proceedings of the 4th International Conference on Ocean Energy, Dublin, Ireland*, 2012.

D. Mollaghan, S. Armstrong, D. O’Sullivan, A. Blavette, R. Alcorn. SEAGRID: A new dynamic modelling tool for power system analysis of ocean energy devices. In *Proceedings of the 4th International Conference on Ocean Energy, Dublin, Ireland*, 2012.

S. Armstrong, D. Mollaghan, A. Blavette, D. O’Sullivan. An initialisation methodology for ocean energy converter dynamic models in power system simulation tools. In *Proceedings of the 4th International Universities’ Power Engineering Conference, London, UK*, 2011.

M. Santos, A. Blavette, E. Tedeschi, D. O’Sullivan, F. Salcedo. Case study on the benefits of energy storage for power quality enhancement: point absorber arrays. In *Proceedings of the 4th International Conference on Ocean Energy, Dublin, Ireland*, 2012.

2011

A. Blavette, D. O’Sullivan, T. Lewis, M. Egan. Grid integration of wave and tidal energy. In *Proceedings of the 30th International Conference on Ocean, Offshore and Arctic Engineering OMAE2011, Rotterdam, the Netherlands*, 2011.

A. Blavette, D. O’Sullivan, M. Egan, T. Lewis. Grid Compliance of Ocean Energy Converters: Control Strategies and Recommendations. In *Proceedings of the 9th European Wave and Tidal Energy Conference series, Southampton, UK*, 2011.

2010

A. Blavette, D. O’Sullivan, M. Egan, R. Alcorn, T. Lewis. Wave energy grid integration in Ireland, a case study. In *Proceedings of the 3rd International Conference on Ocean Energy, Bilbao, Spain*, 2010.

Technical reports

2011

M. Santos, F. Salcedo, D. Ben Haim, J. Mendia, P. Ricci, J.L Villate, J. Khan, D. Leon, S. Arabi, A. Moshref, G. Bhuyan, A. Blavette, D. O’Sullivan, R. Alcorn. *Integrating wave and tidal current power: case studies through modelling and simulation*. A report prepared jointly by Tecnalía (Spain), Powertech Labs (Canada) and HMRC (Ireland) for the OES-IA. Available: www.iea-oceans.org, 2011.

2010

D. O’Sullivan, D. Mollaghan, A. Blavette, R. Alcorn. *Dynamic characteristics of wave and tidal energy converters & A recommended structure for the development of a generic model for grid connection*. A report prepared by HMRC-UCC for the OES-IA Annex III. [Online], Available: www.iea-oceans.org. 2010.

Contents

1	Background: integration of wave energy into power systems	22
1.1	Harnessing wave energy	22
1.1.1	Resources	22
1.1.2	Physics of sea waves	23
1.1.3	Wave energy devices	27
1.1.4	Wave farms	31
1.2	Introduction to the grid integration of wave energy	31
1.2.1	Generator and grid interface types	31
1.2.2	Generator and grid interface type selected in this thesis	33
1.3	Power system simulations	33
1.3.1	Power system simulators	33
1.3.2	RMS and EMT simulations	33
1.4	Grid operators' requirements	35
1.4.1	Introduction	35
1.4.2	Short-duration root-mean-square (RMS) voltage variations	36
1.4.3	Flicker	36
1.4.4	Voltage step	37
1.4.5	Voltage control	37
1.4.6	Influence of the grid strength on power quality	38
1.5	Conclusions	40
2	State-of-the-art	42
2.1	Introduction	42
2.2	Impact of a wave farm on the power quality of its local network	42
2.2.1	Modelling of the individual power profile	42
2.2.2	Computation of the total wave farm power output	43
2.2.3	Wave device technology	43
2.2.4	Generator control strategy and storage means	43
2.2.5	Wave climate and sea-state	44
2.2.6	Layout of the farm	44
2.2.7	Short-circuit ratio and impedance angle Ψ_k	45
2.2.8	Power quality criteria addressed and grid codes	46
2.3	Electrical design of a wave farm	46
2.4	Estimation of flicker results	47
2.5	Generic modelling of ocean devices for power system studies	48
2.5.1	Introduction	48
2.5.2	Experience of the wind energy industry	48
2.5.3	Application of generic modelling to ocean devices	49
2.6	Summary of the contributions of the thesis	50
2.6.1	Chapters 4 and 6	50
2.6.2	Chapter 5	51

2.6.3	Chapter 7	51
2.6.4	Chapter 8	51
3	Simplified analytical case study	52
3.1	The AMETS test site	52
3.2	Numerical modelling	53
3.2.1	Modelling of the electrical network	53
3.2.2	Modelling of the wave energy devices	58
3.2.3	Aggregation of devices	60
3.3	Grid code requirements	61
3.3.1	Maximum amplitude of the voltage variations	61
3.3.2	Voltage limits	62
3.3.3	Flicker	62
3.4	Results	62
3.4.1	Load flow results	62
3.4.2	Quasi-steady simulations	65
3.5	Conclusions	69
4	Grid impact of a medium size wave farm	71
4.1	Introduction	71
4.2	Modelling	71
4.2.1	Modelling of the electrical network	71
4.2.2	Discussion on the modelling method	75
4.2.3	Summary	75
4.2.4	Modelling of the wave farm power output	75
4.3	Theoretical analysis	82
4.3.1	Introduction	82
4.3.2	The Newton-Raphson algorithm applied to load flow problems	85
4.3.3	Application to the different load flow problems considered in this thesis	90
4.4	Studied variables	93
4.4.1	Voltage step	93
4.4.2	Voltage limits	95
4.4.3	Flicker level	96
4.5	Flickermeter design	97
4.5.1	Standards	97
4.5.2	Development and compliance with the IEC standard 61000-4-15	100
4.6	Detail on the simulations and methodology	101
4.6.1	Voltage step	102
4.6.2	Voltage limits	104
4.6.3	Flicker level	104
4.7	Compliance with power quality requirements	104
4.7.1	Voltage step	104
4.7.2	Voltage limits	109
4.7.3	Flicker level	117
4.7.4	Summary	121
4.8	Effect of wave farm direction and device layout within the farm	123
4.8.1	Introduction	123
4.8.2	Voltage limits	123
4.8.3	Flicker level	124
4.9	Conclusions	132

5	Design of a wave farm's electrical network	134
5.1	Introduction	134
5.2	VAr compensator	134
5.2.1	Methodology	134
5.2.2	Theoretical analysis	135
5.2.3	Results	136
5.2.4	Summary	145
5.3	Current rating of the submarine cables	146
5.3.1	Introduction	146
5.3.2	Simplified method	149
5.3.3	Detailed method	153
5.3.4	Summary	159
5.4	Power and energy losses	159
5.4.1	Introduction	159
5.4.2	Methodology	159
5.4.3	Power losses	160
5.4.4	Energy losses	160
5.4.5	Summary	163
5.5	Conclusions	164
5.5.1	VAr compensator	164
5.5.2	Submarine cables	164
5.5.3	Losses	165
5.5.4	Discussion	165
6	Analysis of the obstacles to the transformation of a test site into a commercial site	166
6.1	Introduction	166
6.2	Methodology and models	166
6.2.1	Numerical grid model	166
6.2.2	Device aggregation	169
6.2.3	Power factor control	171
6.2.4	Storage	171
6.2.5	Generator control strategies	172
6.3	Grid compliance	173
6.3.1	Voltage limits	174
6.3.2	Flicker	176
6.3.3	Summary	178
6.4	Current ratings of the cables and of the overhead line	180
6.4.1	Submarine cables	180
6.4.2	Overhead line	182
6.4.3	Summary	182
6.5	Conclusions	184
7	Estimation of the flicker level P_{st} in relation to the farm rated power P_{rated} and to the impedance angle Ψ_k at the connection point	185
7.1	Introduction	185
7.1.1	Estimation of the flicker level P_{st} in relation to the impedance angle Ψ_k	185
7.1.2	Estimation of the flicker level P_{st} in relation to the farm rated power P_{rated}	185
7.2	Input data	186
7.3	Functional blocks composing a flickermeter	187

7.4	Theoretical analysis	188
7.4.1	Introduction	188
7.4.2	Estimation of flicker level Pst with respect to different impedance angles Ψ_k	188
7.4.3	Estimation of the flicker level Pst in relation to the farm rated power P_{rated}	189
7.4.4	Flicker generated by a sinusoidal voltage profile	190
7.4.5	Generalisation to a real voltage profile	194
7.4.6	Determination of an equivalent sinusoidal voltage profile	198
7.4.7	Determination of the scale factors k and k'	199
7.4.8	Summary	201
7.5	Results	202
7.5.1	Relationship between the flicker level Pst and the maximum voltage fluctuation $\Delta V(P, \Psi_k)$	202
7.5.2	Estimation of the flicker level Pst in relation to the farm rated power P_{rated}	207
7.5.3	Estimation of flicker level Pst in relation to different impedance angles Ψ_k	213
7.6	Application of the proposed methods for grid connection studies	215
7.7	Conclusions	216
8	Numerical dynamic modelling of ocean energy devices for power system studies	218
8.1	Introduction	218
8.2	Generic structure of ocean energy devices	219
8.3	Survey results	221
8.3.1	Power optimisation/limitation	221
8.3.2	Actively-controlled parameters	223
8.3.3	Tuning	226
8.4	Conclusions	230
9	Conclusions	233
9.1	Impact of a wave farm on the power quality of its local network	233
9.1.1	Short-circuit ratio and impedance angle Ψ_k	234
9.1.2	Power quality criteria addressed	234
9.1.3	Farm orientation and device layout	234
9.1.4	Sea-state characteristics	234
9.1.5	Additional parameters	234
9.1.6	Results	235
9.2	Flicker estimation methods	235
9.3	Design of the farm's electrical network	236
9.4	Generic modelling of ocean devices	236
9.5	Future work	238
	Appendix A Estimation of the level of error on the short-circuit level and on the impedance angle	239

Nomenclature

Symbol	Definition	Unit
a_{arr}	Percentage of distance D_{row} applied to devices belonging to the same array	%
a_{pos}	Percentage of distance D_{row} applied to devices belonging to the same row	%
a_{row}	Percentage of distance D_{row} applied to devices belonging to two different arrays	%
A_1, A_2, A_3	Amplitude of different analytical voltage sinusoidal fluctuations	V
C_1	Positive sequence shunt capacitance per kilometer	$\mu F.km^{-1}$
C	Positive sequence shunt capacitance	μF
D_{row}	Distance between each row of wave devices	m
D_{total}	Total distance between the WEC i and the reference WEC	m
E	Energy per unit area of a sinusoidal wave	$J.m^{-2}$
E_{ss}	Average energy per unit area of a sea-state	$J.m^{-2}$
E'_L	Energy consumed by the onshore substation	J
E_{losses}	Energy losses dissipated within the farm's electrical network	J
E_G	Energy generated by the wave farm	J
f	Frequency of a sinusoidal wave	Hz
\mathbf{f}	Mismatch array	
f_e	Power system supply frequency	Hz
f_p	Peak frequency of a sea-state	Hz
f_{test}	Reference frequency for the flickermeter performance tests	Hz
g	Acceleration constant (9.81 m.s^{-2})	m.s^{-2}
H	Height of a sinusoidal wave	m
H_{RMS}	RMS wave height of a sea-state	m
H_s	Significant wave height of a sea-state	m
I	Current	A
i_a	Current of phase a	A
I_{avg}	Average current	A
i_b	Current of phase b	A
i_c	Current of phase c	A
i_d	Direct axis current	A
i_i	Imaginary component of the instantaneous current $i(t)$	A
I_{eq}	Equivalent current profile at 10 kV	A
I_{max}	Maximum current	A
i_q	Quadrature axis current	A
i_r	Real component of the instantaneous current $i(t)$	A
I_{rated}	Rated current	A
I_{SC}	Short-circuit current	A
$i(t)$	Instantaneous current	A

J	Jacobian matrix	
k	Scale factor relative to the average voltage	
θ_f	Final conductor temperature	$^{\circ}C$
k'	Scale factor relative to the maximum voltage fluctuation	
k_m	Wave number of a sinusoidal wave	$rad.m^{-1}$
L	Inductance	H
l_c	Submarine cable length	m
l_L	Overhead line length	m
N	Number of wave devices (wind turbines) in a wave (wind) farm	
n_{row}	Row number in a wave farm	
P	Active power	W
P_{avg}	Average active power	W
pf	Power factor	
P_G	Active power generated by the farm	W
P_L	Active power consumption of the 38 kV load	W
P'_L	Active power consumption of the onshore substation	W
P_T	Transformer copper loss	W
P_{loss}	Power losses dissipated within the farm's electrical network	W
P_{min}	Minimum active power	W
P_{max}	Maximum active power	W
P_{PCC}	Active power flowing from the farm to the PCC	W
P_{rated}	Active rated power of a wave farm	W
P_{ref}	Reference active power	W
P_{ss}	Average power per unit length of a sea-state	$W.m^{-1}$
P_{st}	Short-term flicker level	
P_{sti}	Individual short-term flicker level of a grid-connected installation	
P_{stpwr}	Flicker level estimated from the experimental power profile	
P_{stvolt}	Flicker level estimated from the equivalent sinusoidal voltage profile	
pu	Per unit	pu
Q	Reactive power	VAr
Q_{comp}	Reactive power generated by the VAr compensator	VAr
Q_L	Reactive power consumption of the 38 kV load	VAr
Q'_L	Reactive power consumption of the onshore substation	VAr
Q_{PCC}	Reactive power flowing from the farm to the PCC	VAr
Q'_{PCC}	Reactive power flowing from the PCC to the Thevenin impedance	VAr
Q_{ref}	Reactive power reference of the VAr compensator	VAr
R	Resistance	Ω
R_{line}	Resistance of the overhead line	Ω
R_G	Equivalent resistance of the farm's electrical network	Ω
R_S	Thevenin resistance	Ω
R_1	Positive sequence series resistance per kilometer	$\Omega.m^{-1}$
S	Apparent power	VA
$S(f)$	One dimensional energy spectrum	$m^2.s$
S_n	Rated apparent power of an installation	VA
S_{farm}	Rated apparent power of a wave farm	VA
S_{SC}, S'_{SC}	Short-circuit level	VA
T	Period of the equivalent sinusoidal voltage profile	s
T_e	Energy period of a sea-state	s
T_1, T_2, T_3, T_4	Thermal resistance of different types of material	$K.m/W$
T_p	Peak period of a sea-state	s

T_z	Mean zero-crossing period of a sea-state	s
V	Voltage	V
V_{avg}	Average voltage	V
v_i	Imaginary component of the instantaneous voltage $v(t)$	V
V_G	Voltage at the generators' terminals	V
V_{PCC}	Voltage at the PCC	V
v_r	Real component of the instantaneous voltage $v(t)$	V
V_S	Voltage of the voltage source	V
$v(t)$	Instantaneous voltage	V
v_g	Wave group velocity	$m.s^{-1}$
X	Reactance	Ω
\mathbf{x}	Array of unknowns	
X_G	Equivalent reactance of the farm's electrical network	Ω
X_S	Thevenin reactance	Ω
X_{line}	Reactance of the overhead line	Ω
X_{T_1}	Reactance of the 0.4/10 kV (0.4/20 kV) transformers	Ω
X_{T_2}	Reactance of the 10/20 kV transformer	Ω
X_{T_3}	Reactance of the 20/38 kV transformer	Ω
X_1	Positive sequence series reactance per kilometer	$\Omega.km^{-1}$
\mathbf{Y}	Admittance matrix	Ω^{-1}
y_p	Proximity factor	
y_s	Skin effect factor	
Z	Impedance between the 38 kV (33 kV) node and the 110 kV (400 kV) connection point	Ω
Z_S	Thevenin impedance	Ω
Z_1	Positive sequence of the series impedance per kilometer	$\Omega.km^{-1}$
α	Exponent of the flicker summation law	
α_ω	Random phase shift between the power profile of different generators	\circ
β_n	Angle between the axis of propagation of a sinusoidal wave and the x-axis	\circ
δ_G	Voltage angle at the offshore generators' terminals	\circ
ΔP	Maximum active power difference	W
δ_{PCC}	Voltage angle at the PCC	\circ
ΔP_{st}	Maximum flicker level difference	
ΔT_{total}	Total time delay	s
ΔV	Maximum voltage fluctuation of a voltage profile	V
ΔV_{test}	Reference voltage amplitude for the flickermeter performance tests	V
ΔV_{2bus}	Voltage rise in two-bus system	V
ΔV_j	Amplitude of a sinusoidal voltage fluctuation	V
δ_S	Voltage angle at the voltage source	\circ
$\delta_{\Delta V}$	Error on the amplitude ΔV for the flickermeter tests	$\%$
$\Delta \theta$	Temperature rise	$^{\circ}C$
$\Delta \theta_{cst}$	Temperature rise corresponding to a constant current	$^{\circ}C$
ζ	Efficiency of the farm's electrical network	
η_i	Amplitude of a sinusoidal wave	m
$\eta(x, y, t)$	Elevation of the sea surface	m
θ	Conductor temperature	$^{\circ}C$
θ_{amb}	Ambient temperature	$^{\circ}C$

θ_f	Final conductor temperature	$^{\circ}C$
θ_i	Current phase angle	$^{\circ}$
θ_u	Voltage phase angle	$^{\circ}$
ρ	Density of water	$kg.m^{-3}$
ρ_T	Thermal resistivity	$K.m/W$
τ	Thermal time constant of a submarine cable	s
τ_f	Inertia time constant of a wave device	s
τ_s	Time constant of a storage means	s
Φ	Phase angle between the axis of phase a and the direct axis	$^{\circ}$
Φ_j	Phase angle of a sinusoidal voltage fluctuation	$^{\circ}$
Ψ_k	Angle of the Thevenin impedance	$^{\circ}$
ω_e	Radian frequency of the power system supply	$rad.s^{-1}$
$\omega, \omega_i, \omega_j$	Radian frequency of a sinusoidal voltage fluctuation	$rad.s^{-1}$
ω_m	Radian frequency of a sinusoidal wave	$rad.s^{-1}$

Acronyms

AMETS	Atlantic Marine Energy Test Site
BIMEP	Biscay Marine Energy Platform
CORES	Components for Ocean Renewable Energy Systems
CPF	Cumulative probability function
DFIG	Doubly-fed induction generator
EMEC	European Marine Energy Centre
EMT	Electromagnetic transient
ENTSO-E	European Network of Transmission System Operators
ESB	Electricity Supply Board
ESBI	Electricity Supply Board International
FFR	Primary fluid flow rate
FP	Primary fluid pressure
FP7	7 th Framework Programme
IEA	International Energy Agency
IEC	International Electrotechnical Commission
IEEE	Institute of Electrical and Electronics Engineers
IPS	Minimum input power threshold for energy storage
LED	Light-emitting diode
MPPT	Maximum power point tracking
OES-IA	Ocean Energy System-Implementing Agreement
OWC	Oscillating water column
PCC	Point of common coupling
PLL	Phase locked-loop
PM	Pierson-Moskowitz
PMSG	Permanent magnet synchronous generator
RfG	Network Code on Requirements for Grid Connection applicable to all Generators
RMS	Root-mean-square
SCIG	Squirrel-cage induction generator
SCR	Storage charge rate
SDR	Storage discharge rate
SEAI	Sustainable Energy Authority of Ireland
SEM-REV	Site d'Experimentation en Mer pour la Récupération de l'Energie des Vagues
SP	Prime mover speed
TAB	Technical Connection Requirements for the Connection at Distribution Level (Technische Anschlussbedingungen für den Anschluss an das Mittelspannungsnetz)
TQ	Prime mover/generator torque
WEC	Wave energy converter
WECC	Western Electricity Coordinating Council
WRIG	Wound-rotor induction generator

XLPE Cross-linked polyethylene

Introduction

In less than a century, electricity has become the cornerstone of modern society. Thanks to it, living conditions have changed more in fifty years than in two centuries. However, issues such as climate change, fossil fuel depletion, security of energy supply and risk of major-accident hazard prove the limitations of this current energy model. It is in this context that a large number of countries have started a transition process to a more sustainable energy model in which renewables will be exploited at a large scale. Wave energy is one of these sources of renewable electricity for which there has been a growing interest over the past decades. The theoretical potential of wave energy, yet widely untapped, may exceed the annual world electricity consumption.

The idea of converting it into useful power is not new. However, it was only in the 1970s, due to the oil crises, that wave energy began to be considered at political level as an alternative for the generation of electricity. Although this enthusiasm diminished significantly due to the 1980s oil glut, strong momentum has however been regained in this area of research since the end of the 1990s.

The electricity generated from wave energy converters is not intermittent. This constitutes a major advantage compared to other renewables such as wind for instance. However, its high level of variability may deteriorate significantly the power quality of the local network to which a wave farm is connected. This issue must be considered very carefully, as the most important resources in Europe are located off the west of Ireland and off the north of Scotland which have relatively “weak” grids. This implies that the impact of a wave farm of significant rated power in these regions is demultiplied compared to the impact it would have on stronger coastal networks such as those of continental Europe.

However, the current level of knowledge regarding the grid impact of a wave farm is relatively fragmented, as will be detailed in the state-of-the-art. This stems mainly from the fact that the limited number of existing case studies are conducted under different perspectives and/or using different parameters. It is in the context that three case studies were conducted as part of this thesis. The first case study is presented in Chapter 3 and consists of a simplified analytical case study which was conducted in the early stages of this thesis. Its purpose is mainly to illustrate the different notions regarding the grid integration of wave energy which are introduced in Chapter 1. The two other case studies, which are presented in Chapters 4 and 6, are based on experimental power profiles of a quarter-scale oscillating water column prototype. This prototype was deployed at sea during three months between March and May 2011 in the framework of the European FP7 project entitled “CORES”. This project has enabled the generation of a considerable amount of time series data on a number of parameters, including electrical parameters at a high temporal resolution of 0.1 s. Contrary to most available data which is averaged over a sea-state, a season or even a year, the CORES electrical power time series data can be scaled and used directly for grid impact studies. The case study presented in Chapter 4 focuses on the impact of a 20 MW-rated wave farm designed for testing purposes, while

the case study presented in Chapter 6 addresses the impact of a commercial wave farm whose rated power ranges between 20 MW and 50 MW.

Another obstacle to the grid impact assessment of a wave farm stems from the lack of experimental data on the power profile of a wave farm, which may prevent certain power quality studies, such as flicker analyses, from being performed. It is in this context that two flicker estimation laws were developed in this thesis, one in relation to the farm rated power and the other in relation to the impedance angle of the node in the grid to which the wave farm is connected. These estimation laws are complementary to an existing estimation law in relation to the short-circuit ratio. Hence, the combination of these three laws is expected to greatly facilitate the estimation of flicker for any value of the short-circuit level and of the impedance angle, and for any value of the farm rated power. This may enhance the dissemination of experimental results. In addition, this may enable the comparison of the impact of different wave farms, regardless of their rated power or of point of connection to which they are connected. These estimation laws are detailed in Chapter 7.

The last major obstacle to the more in-depth understanding of the grid impact of wave farms is the absence of dynamic models of ocean devices, referring here to both wave and tidal current devices. These models are intended to be used in power system simulators whose principle is described in the next chapter. However, considering the difficulties encountered by the wind energy industry in this field, the ocean energy community decided to tackle this issue much in advance in the process of grid integration. This is the reason why the Ocean Energy Systems-Implementing Agreement (OES-IA), a branch of the International Energy Agency (IEA), launched a collaborative research project on this topic in 2009. It focused on the development of a generic model common to most ocean devices. Several issues were identified during this project, and among them, those related to the implementation of control strategies in this type of model. The contribution of the author of this thesis to this last field of research is described in Chapter 8.

It is also interesting to investigate the design of a medium size wave farm, as it may differ significantly from that of a large offshore wind farm. This difference may have strong implications on the dimensioning of the constituent elements of the farm's electrical network. Firstly, the high level of variability of wave energy transforms dramatically the problem of estimating the ratings required for the submarine cables and for the overhead lines included in the farm's electrical network. Conventional methods are based on constant current profiles which are not representative of, nor relevant to wave energy applications, given the very slow thermal dynamic response of each of these element compared to the rapid current fluctuations generated by a wave farm. In addition, it is particularly important to study the design of a medium size wave farm as it includes relatively long submarine cables which are operated at a medium voltage level contrary to large offshore wind farms where a higher voltage level are used. This means that the level of reactive power compensation which may be required to operate the wave farm according to typical grid operators' requirements is expected to be significantly more important in proportion than in the case of large offshore wind farms. This means also that the percentage loss in the transmission subsystem is expected to be more significant in this case, which may decrease significantly the theoretical revenue generated from the farm. The results of the studies on these topics, which are based on the test site farm described in Chapter 4, are addressed in Chapter 5.

In summary, this thesis is intended to contribute in filling the gap regarding the grid

impact assessment of a wave farm. More specifically, it presents the results of comprehensive case studies based on experimental power profiles. However, as experimental data is very scarce, it describes also methods and models to facilitate the analysis of this impact with a limited amount of information. In addition, it investigates also the optimal design of a wave farm from an electrical perspective. The next chapter introduces several notions regarding wave energy, the devices used to harness it, as well as the issues which may arise from the grid connection of a wave farm.

Chapter 1

Background: integration of wave energy into power systems

1.1 Harnessing wave energy

1.1.1 Resources

The theoretical potential of wave energy, yet widely untapped, may exceed the annual world electricity consumption. It was originally estimated at between 1 TW to 10 TW [1], while recent studies gave more refined figures ranging between 2.1 TW [2] and 3.7 TW [3]. This is considerable as it represents the equivalent of 103% to 181% of the world electricity consumption [4].

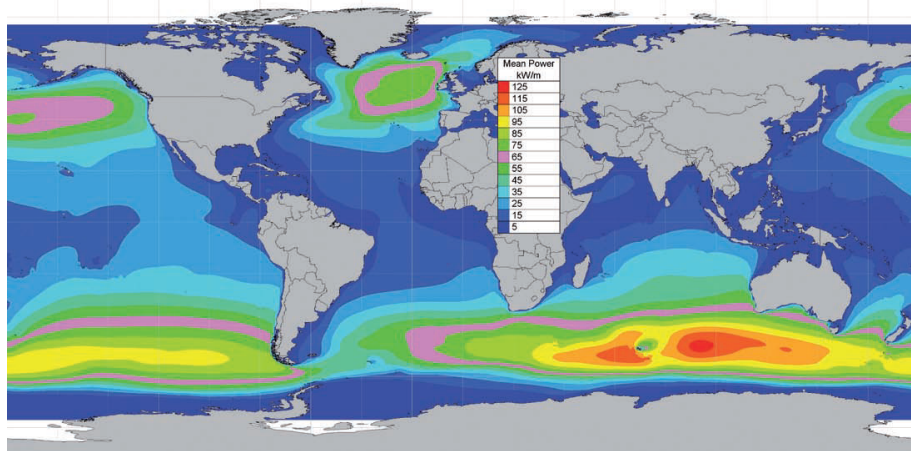


Figure 1.1: Global mean wave power density [5]

The resources are unevenly spread over the globe, resources-rich areas being located at a latitude ranging from 30° to 60° , as shown in Figure 1.1. However, due to both technical and economical constraints, only a fraction of this potential is harnessable. Taking the devices efficiency into account, it was estimated more than a decade ago that the global amount of extractable energy may be around 2,000 TWh/yr (corresponding approximately to 6%-11% of the total energy) provided that potential improvements to devices existing at that time were realised [6]. Other estimations based on the Pelamis power matrix [7] (which has not been validated by any independent authority as yet) were more pessimistic, with only 96.6 GW harnessable, corresponding to 846 TWh/yr, thus representing 2% to 4% of the available energy) [2]. Although it is yet difficult to estimate precisely the amount of energy that can be extracted from waves in the absence of reliable ocean device efficiency

data, the exploitation limit was estimated to range approximately between 10% and 25% at most [8].

1.1.2 Physics of sea waves

Wave formation

Waves are indirectly generated by the action of solar radiation on Earth which, being non-uniformly distributed over the surface of the globe, creates massive air convection cells, as shown in Figure 1.2. Permanent wind direction patterns can thus be observed throughout the globe, as shown in Figure 1.3.

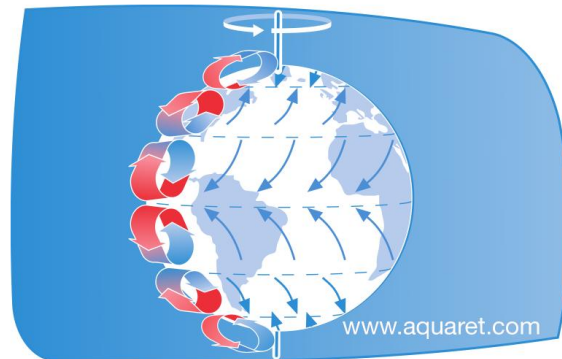


Figure 1.2: Illustration of air masses convection cells created by the non-uniform distribution of solar radiation on Earth

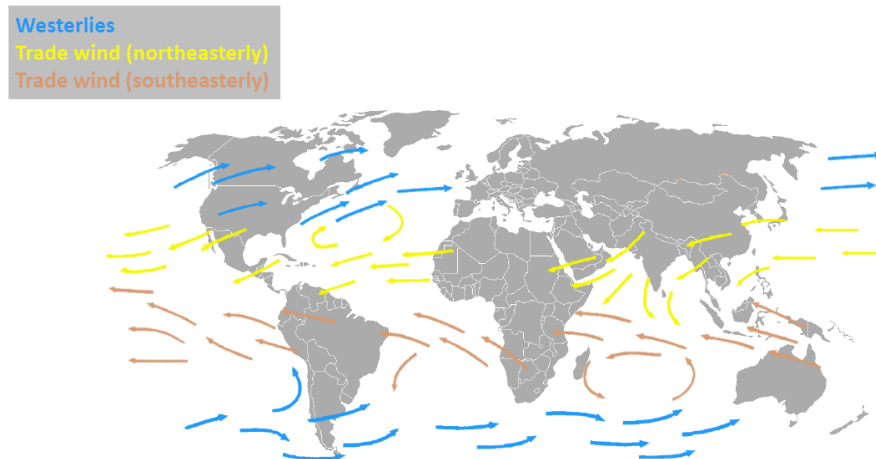


Figure 1.3: Permanent wind patterns [9]

The continual interaction of these winds with the sea surface creates water undulations (as illustrated in Figure 1.4a) which can travel far from their origin point, as illustrated in Figure 1.4b. The swell observed on the west coast of Ireland may for instance be created by a storm located off the east coast of the United States. The influence of local winds (see Figure 1.4c) is also to be considered. The characteristics of a regional wave climate are largely due to these two elements.

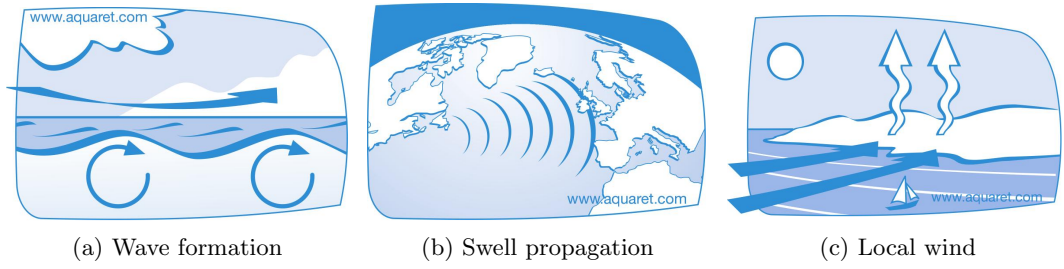


Figure 1.4: Waves are generated by the interaction between the wind and the sea surface. They may propagate over long distances [10].

Wave propagation

Sea waves propagate as gravity waves, thus transporting energy and not matter, as illustrated in Figure 1.5a, where a boat is shown to oscillate around a fixed point. In similar fashion, the trajectory of a fictive “water particule” is circular. The diameter of this circular trajectory decreases exponentially with water depth as illustrated by Figure 1.5b.

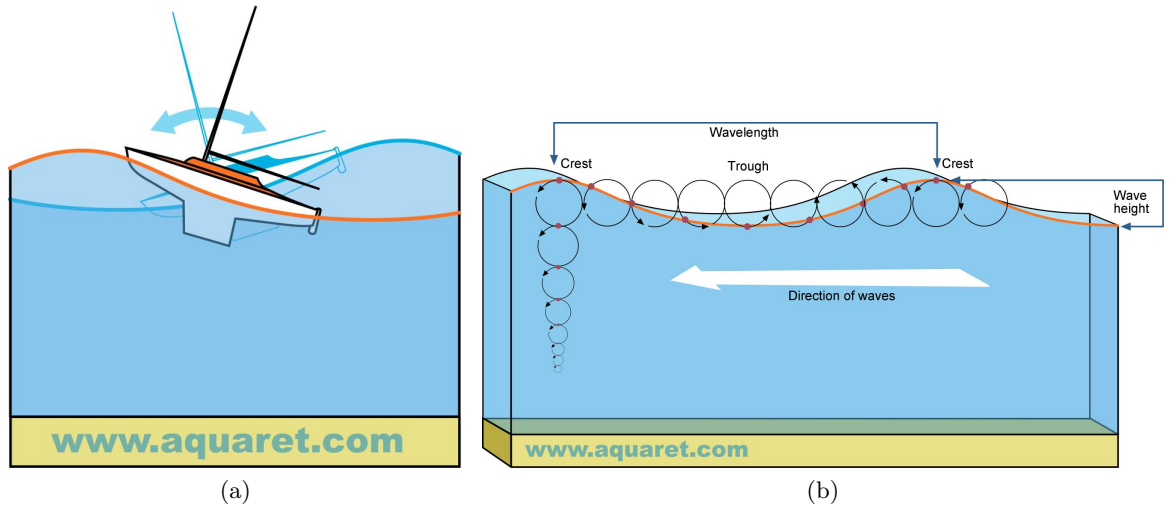


Figure 1.5: Wave propagation is a transport of energy.

Characterisation of a sea-state

A real sea surface is usually more irregular than the examples shown in the previous section. However, the linear wave theory says that it can be physically represented as the superposition of a multitude of sinusoidal waves having different amplitudes η_i , radian frequencies ω_m , wave numbers k_m and direction angles β_n compared to the x-axis [11]. The elevation of the sea surface $\eta(x, y, t)$ induced by the propagation of one of these sinusoidal waves can be expressed mathematically as:

$$\begin{aligned} \eta(x, y, t) &= \eta_i(\omega_m, \beta_n) \cos(\omega_m t - k_m x \cos \beta_n - k_m y \sin \beta_n) \\ &= \Re[\eta_i(\omega_m, \beta_n) \exp[j(\omega t - k_m x \cos \beta_n - k_m y \sin \beta_n)]] \end{aligned} \quad (1.1)$$

Hence, as a general sea-state can be decomposed into sinusoidal components, the sea-surface $\eta(x, y, t)$ in this case can be expressed as:

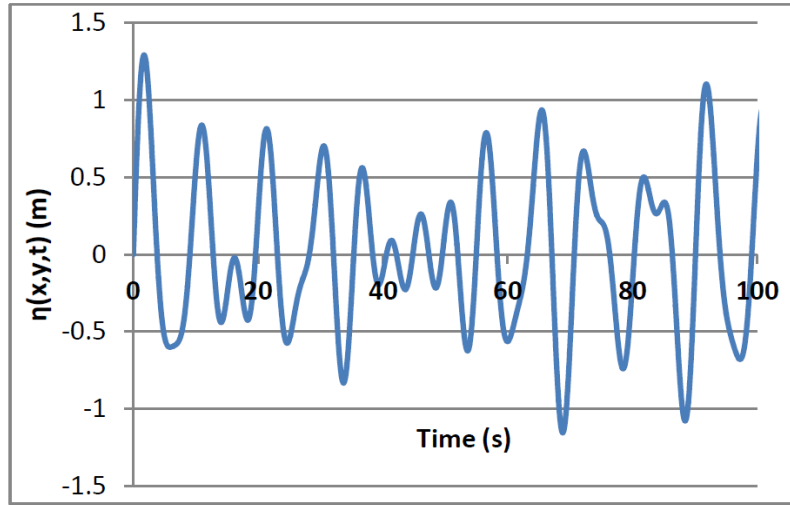


Figure 1.6: Sea surface elevation $\eta(x, y, t)$ in the case of a real sea-state composed of sinusoidal waves of different frequencies

$$\eta(x, y, t) = \Re \left[\sum_{\omega_m > 0} \sum_{\beta_n} \eta_i(\omega_m, \beta_n) \exp[j(\omega_m t - k_m x \cos \beta_n - k_m y \sin \beta_n)] \right] \quad (1.2)$$

This is illustrated by Figure 1.6 which shows the sea surface elevation time series $\eta(x, y, t)$ corresponding to sinusoidal waves of frequencies equal to 5 Hz, 7 Hz, 8 Hz, 9 Hz and 10 Hz. In the case of deep water, the dispersion relationship can be written as:

$$\omega_m^2 = gk_m \quad (1.3)$$

where g is the gravity acceleration constant. Hence, sea-states are usually described by means of a one dimensional energy density spectrum $S(f)$ as:

$$S(f) = \int_{-\pi}^{\pi} s(f, \beta) d\beta \quad (1.4)$$

where f is the frequency of the sinusoidal waves composing the sea-state, β the angle between their direction and the x-axis, and $s(f, \beta)$ the energy spectrum as a function of both these variables. This spectrum can be expressed as:

$$s(f, \beta) = D(\beta)S(f) \quad (1.5)$$

where $D(\beta)$ the spreading function representing the directional distribution of the waves. It can be expressed as:

$$\int_{-\pi}^{\pi} D(\beta) d\beta = 1 \quad (1.6)$$

Wave measurements over the past century have shown that the mono-directional spectrum $S(f)$ corresponding to a sea-state has general characteristics. Hence, it can be expressed in the form of empirical equations. The Pierson-Moskowitz (PM) spectrum for instance is one of the typical spectrum observed for some sea-states, more specifically fully developed sea-states. This type of sea-states is generated by winds blowing steadily during several days at a sufficiently long fetch from the area considered, usually of the order of hundreds of kilometres [12]. This spectrum can be expressed as:

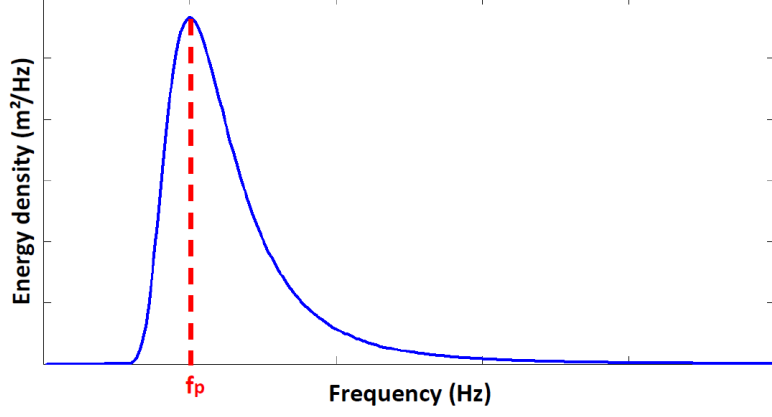


Figure 1.7: Shape of a Pierson-Moskowitz energy spectrum

$$S(f) = \alpha_{ES} g^2 (2\pi)^{-4} f^{-5} \exp \left[-\frac{5}{4} \left(\frac{f}{f_p} \right)^{-4} \right] \quad (1.7)$$

where α_{ES} and f_p are the energy scale and the peak frequency. The energy scale α_{ES} depends on both the significant wave height H_s and on the peak frequency f_p . The significant wave height H_s corresponds to the mean height of the highest one-third of waves observed in a given period of time while the peak frequency f_p corresponds to the apex of the energy density spectrum $S(f)$. Figure 1.7 shows the shape of this spectrum.

The Pierson-Moskowitz spectrum can also be described by means of a formula with two other periods as parameters. These periods are proportional to the peak period T_p (i.e. the inverse of the peak frequency f_p) by a constant which may vary slightly with the location considered. These periods are called the mean zero-crossing period T_z and the energy period T_e . The mean zero-crossing period T_z is the mean value of the periods of the sinusoidal waves composing the sea-state. The energy period T_e corresponds to the period of a fictive sinusoidal wave whose power is equal to this of the sea-state. It can be expressed as:

$$T_e = \frac{\int_0^\infty f^{-1} S(f) df}{\int_0^\infty S(f) df} \quad (1.8)$$

Both these periods are used in this thesis. As will be detailed in Chapter 4, the studies conducted for this thesis are based on experimental data obtained from a wave device prototype deployed at sea during three months. The Pierson-Moskowitz spectrum was used to characterise the sea-states corresponding to each electricity production period by means of the significant wave height H_s and of the mean zero-crossing period T_z . However, as the energy period T_e is more representative of the power fluctuations injected into the network, it was also used in this work.

Since T_e and T_z are proportional to the peak period T_p , their relationship is also proportional. The proportionality coefficient, which varies but slightly depending on the location considered, was found to be approximately equal to 1.3 for the Belmullet test site [13]. Hence, the relation between the periods T_e and T_z can be written empirically as:

$$T_e = 1.3 T_z \quad (1.9)$$

Wave power

The energy per unit area E of a sinusoidal wave of height H can be expressed as [12]:

$$E = \frac{1}{8}\rho g H^2 \quad (J/m^2) \quad (1.10)$$

where ρ is the density of sea water and g is the acceleration constant. Hence, the energy per unit area E_{ss} corresponding to a sea-state composed of sinusoidal waves can be calculated from the RMS wave height H_{RMS} as:

$$E_{ss} = \frac{1}{8}\rho g H_{RMS}^2 \quad (1.11)$$

Consequently, the average power per unit length P_{ss} corresponding to this sea-state is obtained by multiplying its energy E_{ss} by the wave group velocity in deep water [11] which is expressed as:

$$v_g = \frac{gT_e}{4\pi} \quad (1.12)$$

where T_e is the period corresponding to the propagation of an equivalent sinusoidal wave whose power is equal to P_{ss} . Hence, the power P_{ss} of the sea-state can be written as:

$$P_{ss} = \frac{\rho g}{8} H_{RMS}^2 v_g = \frac{\rho g^2}{32\pi} H_{RMS}^2 T_e \quad (kW/m) \quad (1.13)$$

The RMS wave height H_{RMS} is proportional to the significant wave height H_s as [12]:

$$H_{RMS} = \frac{1}{2}\sqrt{2}H_s \quad (1.14)$$

Hence, (1.13) gives

$$P_{ss} = \frac{\rho g^2}{64\pi} H_s^2 T_e = 0.49 H_s^2 T_e \quad (1.15)$$

Considering that the energy period is proportional to the peak period T_p and to the mean zero-crossing period T_z , the power of a sea-state is thus proportional to these periods as well.

1.1.3 Wave energy devices

The idea of converting wave energy into useful power is not new, as a patent regarding a wave energy converter (WEC) was filed by Frenchmen Girard & Son as early as in 1799 [14]. However, it was only in the 1970s, due to the oil crises, that wave energy was re-considered seriously. Although this enthusiasm diminished significantly due to the 1980s oil glut, given the current concerns regarding climate change, energy dependency and the price volatility of fossil fuel, strong momentum has been regained in this area of research since the end of the 1990s.

Since the first prototypes (Edinburgh's duck, Sea Clam [15]) were developed, many designs have emerged. However, they generally all function based on the same principle: wave energy extraction is based on the relative motion between two parts or more of a device in the case of an oscillating device. In the case of overtopping devices, sea water is captured in a large reservoir and work similarly to hydraulic dams. In order to obtain a sufficient power output, wave energy devices are grouped in wave farms as illustrated in Figure 4.10. Most of the current designs fall into the categories described in the following subsections.

Point absorber

The operating principle of the point absorber is based on the relative motion between the upper floating part and its lower part, which can be either floating or fixed to the sea bottom. Due to its symmetrical design, the performance of the point absorber is independent of the wave direction.

Attenuator

The attenuator is a floating structure whose symmetry axis should ideally be parallel to the direction of the incoming waves. The hinges by which the two or more cylindrical sections are linked enable high pressure oil to be either compressed or dilated alternatively to make a hydro-turbine spin.

Wave surge converter

The wave surge converter is also an oscillating device, posed on the sea bottom in shallow waters and which is either mostly or totally submerged. In similar fashion to algae, its back and forth motion is induced by the rotary movement of water particles.

Oscillating water column

The air enclosed in the hollow chamber of an oscillating water column (OWC), being compressed and dilated under the actions of waves, flows alternatively outwards and inwards through an orifice in which an air turbine is placed.

Submerged point absorber

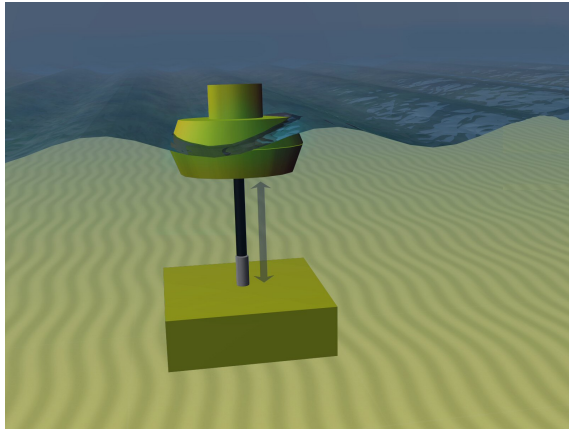
The operating principle of a submerged point absorber is similar to that of a floating point absorber. However, the submerged point absorber harnesses the pressure differential generated at a given point under the surface at the passage of waves, rather than the sea surface elevation as the point absorber does.

Overtopping device

The overtopping device, also called overtopper, functions in similar fashion to a hydraulic dam and is composed of one or more hydro-turbines. The water of incoming waves slips on an inclined ramp and is captured by a large reservoir which is above the sea level. The ramp is sometimes bordered by two reflecting walls for enhancing the device efficiency.

Wave device type selected for the thesis

The work presented in this thesis is based mostly on experimental data in the form of power output time series of a quarter-scale OWC prototype deployed at sea. This data was generated as part of the FP7 European project CORES which is detailed later in Chapter 4. Given the similarities in terms of fluctuating power output between all the wave devices, with the exception of overtoppers, it is expected that the results obtained in this thesis represent a benchmark for the grid impact analysis of oscillating wave devices in general.

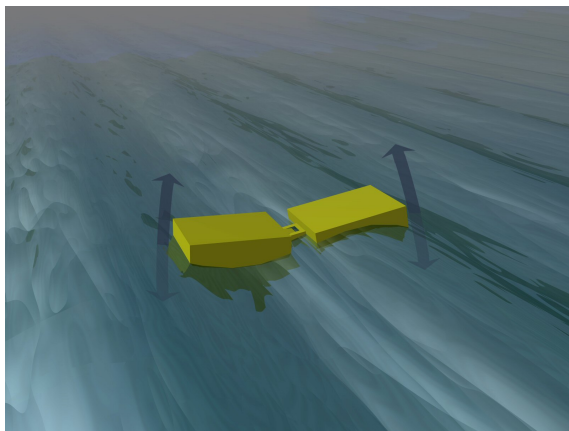


(a) Concept [10]



(b) WaveBob [16]

Figure 1.8: Point absorber

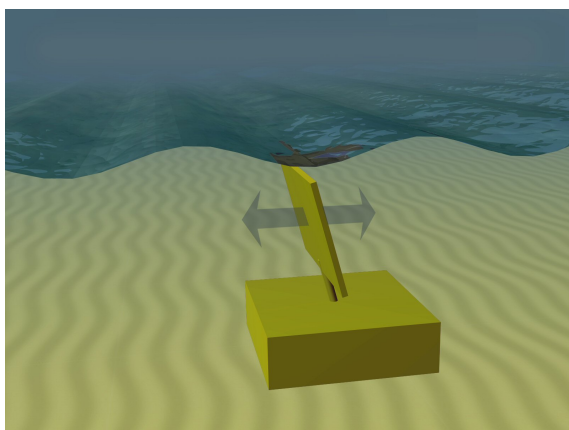


(a) Concept [10]



(b) Pelamis [17]

Figure 1.9: Attenuator

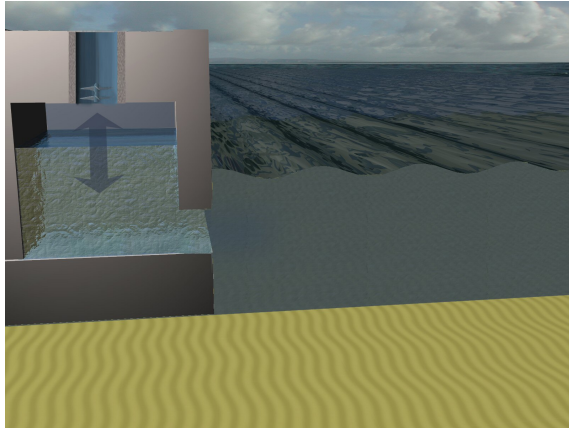


(a) Concept [10]



(b) Oyster [18]

Figure 1.10: Wave surge converter

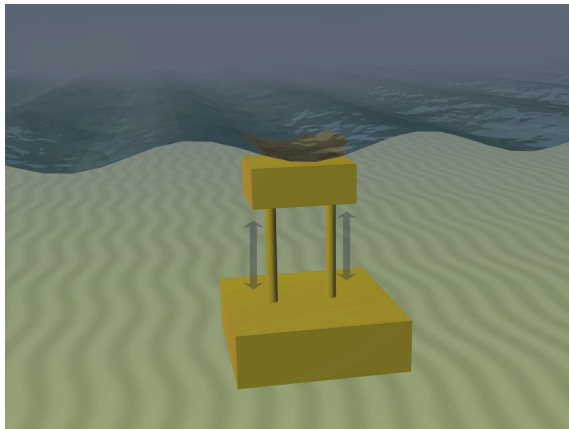


(a) Concept [10]



(b) OE Buoy [19]

Figure 1.11: Oscillating water column (OWC)

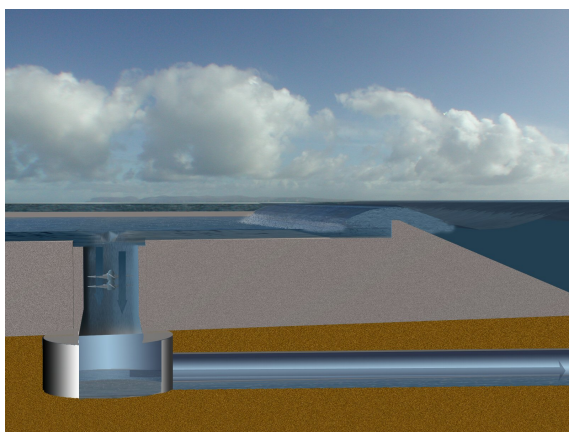


(a) Concept [10]



(b) CETO [20]

Figure 1.12: Submerged point absorber



(a) Concept [10]



(b) WaveDragon [21]

Figure 1.13: Overtopping device

1.1.4 Wave farms

Wave farms are composed of multiple wave devices. The influence of their characteristics (e.g. device layout, orientation) on the power quality of a wave farm are described in Section 4.2.4.

1.2 Introduction to the grid integration of wave energy

1.2.1 Generator and grid interface types

Grid operators tend to classify power plants more and more according to their grid interface type (i.e. partially or fully decoupled from the network, or directly connected) rather than according to the nature of their prime mover (dispatchable, predictable but non-fully controllable, etc.). The imminent “Network Code for Requirements for Grid Connection applicable to all Generators” (RfG) developed by the European Network of Transmission System Operators (ENTSO-E) goes in this direction [22]. It will come into force in 2014 in 34 European countries and defines requirements of an increasing level of constraint depending on the plant rated power, on the voltage of its point of connection and on its type of grid interface only.

Hence, this introduction chapter will detail the electromechanical conversion stage in terms of generator and grid interface. Given the similarities between wind and wave power, the generators and grid interfaces already developed by the wind energy industry are expected to be suitable for the wave energy converters, with the exception of devices using a linear generator. The classification of these generator/grid interface combinations as adopted by the Western Electricity Coordinating Council (WECC) [23] is summarised as follows:

- *Type 1: conventional induction generator* (Figure 1.14a)
This is the typical grid interface of traditional approximately fixed-speed wind turbines using squirrel-cage induction generator (SCIG), which was progressively abandoned due to its poor fault ride-through capability, poor power factor and overall lack of control.
- *Type 2: variable rotor-resistance induction generator* (Figure 1.14b)
This configuration enables variable slip operation but does not provide such a high level of flexibility in terms of speed control as DFIG or fully-rated power electronics interfaces.
- *Type 3: doubly-fed induction generator or DFIG* (Figure 1.14c)
The rotor currents are controlled by means of power electronic converters typically rated to a third of the generator power capacity, which enables flexible variable speed operation. The DFIG interface can however be sensitive to grid disturbances and requires power converter protection systems [24].
- *Type 4: fully-rated unit* (Figure 1.14d)
The generator, either synchronous or asynchronous, is entirely decoupled from the network by means of power electronic converters controlling the stator currents. This interface not only enables variable speed operation, but presents also a controllable fault ride-through capability. However, the cost of the power electronic converters, rated to 100% of the generator power capacity, renders the interface more expensive.

Wave energy designs without inherent energy storage capabilities are not expected to be based on a fixed-speed design (Type 1) as significant inertial storage by means of speed

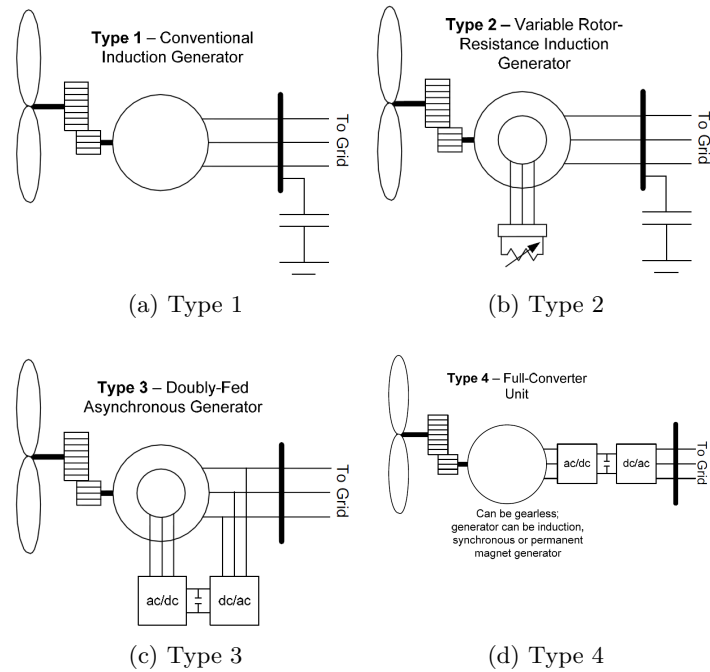


Figure 1.14: Typical wind turbine generator/grid interface combinations utilisable in wave energy applications [23]

control is not available in this type of operation. Hence, incoming wave power fluctuations are directly transmitted to the grid, which may deteriorate significantly the power quality of the local network. In addition, the poor fault ride-through capability demonstrated by the squirrel-cage generator constitutes a technical obstacle to its utilisation as part of wave farms of significant rated power. This has unsurprisingly led to its progressive abandonment by the wind energy industry and it is no longer considered for wave energy applications.

Fully variable speed operation, whose benefits are proven in terms of increasing wind farms efficiency and in terms of power output quality enhancement, is achievable only by means of partially (Type 3) or fully-rated (Type 4) power electronics interfaces. Although the variable slip operation possible with the Type 2 interface provides also some sort of speed control, it is far more limited and decreases the overall efficiency of a wave device.

Hence, grid interfaces including power electronics, despite their higher cost and potential reliability issues, are generally considered as more suitable for wave energy applications, although they present technical drawbacks as well. For instance, power electronics generate harmonics which can however be easily mitigated by means of well tried and tested filters [25]. In addition, the DFIG interface is somewhat sensitive to grid disturbances and requires a special converter protection system as mentioned previously. On the other hand, the fully-rated power electronic interface tend to generate quite a low current under fault conditions, which may render more complex the fault detection by circuit breakers.

In summary, two types of grid interfaces, namely Type 3 and Type 4, are usually envisaged for an oscillating wave device design. This corresponds to four generator/grid interface combinations which are described in Table 1.1.

Generator	Grid interface
Wound-rotor induction generator (WRIG)	Type 3
Permanent magnet synchronous generator (PMSG) Synchronous generator with brushes Asynchronous generator	Type 4

Table 1.1: Generator/grid interface combinations envisaged for oscillating wave devices

1.2.2 Generator and grid interface type selected in this thesis

As will be detailed in Chapter 4, the power system studies presented in this thesis, with the exception of those performed in the context of a simplified analytical case study presented in Chapter 3, are based on experimental data generated by a wave energy design including a fully-rated grid interface (Type 4). It is important to bear in mind that, from a power system’s perspective, the grid impact of this type of grid interface is independent of the type of generator used as the injection of both active and reactive power into the network is controllable by means of the power electronic converters. Hence, the results obtained in this thesis are applicable to three of the four generator/grid interface combinations envisaged for oscillating wave devices which were described in the previous section.

1.3 Power system simulations

1.3.1 Power system simulators

Power system simulators are the tool of choice for assessing the grid impact due to any system changes. They reduce the requirement of performing tests on the actual network, which may cause disturbances detrimental to customers as well as representing a potential threat to the grid stability. Besides being generally much easier to put in place than field tests, these numerical tests allow simulation of the power system behaviour for a full range of conditions, either external (e.g. outdoor temperature, wind speed) or internal (e.g. addition of electrical components such as generation units). The decision to upgrade a part of the grid or to install new generation units are usually taken on the basis of these simulations. A grid impact evaluated as significant by means of power system simulations is for instance a sufficient reason for any grid operator to deny a grid connection application. Given the high economical, technical and human issues at stakes, it is thus imperative that the dynamic models of any electrical equipment implemented in power system simulators are highly reliable, validated and fully trusted.

The power system simulations presented in this thesis were performed with the power system simulator “PowerFactory” developed by DlgSILENT [26]. This company has been one of the leaders in power system modelling, analysis and simulation for more than 25 years. The major advantages of PowerFactory are its overall functional and user-friendly interface, as well as its ease of use for modelling fluctuating power sources. The simulator automation capabilities were also extremely useful in reducing considerably the amount of time required for performing a large number of simulations.

1.3.2 RMS and EMT simulations

Introduction

Power system simulations may be performed using either the so-called “root-mean-square” (RMS) method or the “electromagnetic transient” (EMT) method. In EMT simulations,

the instantaneous values of both the voltage $v(t)$ and of the current $i(t)$ are calculated at any node of the network for each of three phases a , b , and c . Assuming that the level of harmonics in the network is sufficiently low, these variables can be expressed as:

$$\begin{aligned} v(t) &= V(t) \sin(\omega_e t + \theta_u) \\ &= \Im[V(t)e^{j(\omega_e t + \theta_u)}] \\ &= \Im[V(t)e^{j\theta_u} e^{j\omega_e t}] \end{aligned} \quad (1.16)$$

and

$$i(t) = \Im[I(t)e^{j\theta_i} e^{j\omega_e t}] \quad (1.17)$$

where $V(t)$ and $I(t)$ are the amplitudes of the voltage and of the current respectively, ω_e is the power system supply radian frequency, and θ_u and θ_i are the phases of the voltage and of the current respectively. However, EMT simulations require using full electromagnetic transient models with a relatively small time step. Hence, the simulation speed as well as the amount of data generated during these simulations limit usually the duration of the simulations performed with this method, which is generally used for very short simulations only (e.g. fault analyses).

Consequently, power quality analyses are usually based, and it is also the case in this thesis, on simulations performed with the RMS method with which a number of simplifications are made. First, instead of simulating the instantaneous values of the voltage $v(t)$ and of the current $i(t)$, only the terms $V(t)e^{j\theta_u}$ and $I(t)e^{j\theta_i}$, alternatively written as $V(t)\angle\theta_u$ and $I(t)\angle\theta_i$, are simulated. Hence, these terms, which are called “phasors”, are expressed in a frame of reference rotating at the power system supply radian frequency ω_e . This concept is illustrated in Figure 1.15. The second simplification consists of simulating the positive sequence only in the case of balanced conditions.

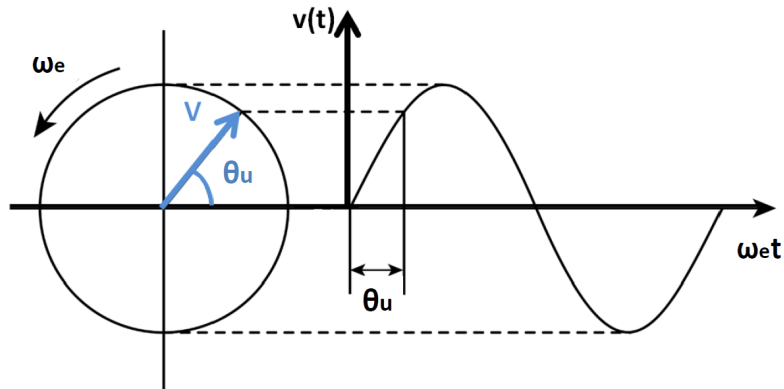


Figure 1.15: Instantaneous voltage value $v(t)$ and its associated phasor $V^{j\theta_u}$ at the power system supply radian frequency ω_e

Discussion

The power fluctuations generated by a wave farm induce voltage fluctuations on the network. However, as a sea-state is composed of sinusoidal waves, as described in Section 1.1.2, the power fluctuations can also be expressed as a sum of sinusoidal terms. In similar fashion, the voltage profile $v(t)$ at any node of the network can be expressed as a sum of

sinusoidal terms of amplitude $\frac{\Delta V}{2}$, of radian frequency ω_j , and of phase Φ_j oscillating around an average value V_{avg} as:

$$v(t) = \left(V_{avg} + \sum_{j=1}^n \frac{\Delta V_j}{2} \sin(\omega_j t + \Phi_j) \right) \sin(\omega_e t) \quad (1.18)$$

Hence, the power fluctuations generate oscillating terms of radian frequency $\omega_e - \omega_j$ and $\omega_e + \omega_j$ as demonstrated below:

$$\begin{aligned} v(t) &= V_{avg} \sin(\omega_e t) + \sum_{j=1}^n \frac{\Delta V_j}{2} \sin(\omega_j t + \Phi_j) \sin(\omega_e t) \\ &= V_{avg} \sin(\omega_e t) + \sum_{j=1}^n \frac{\Delta V_j}{4} [\cos((\omega_e - \omega_j)t + \Phi_j) - \cos((\omega_e + \omega_j)t + \Phi_j)] \end{aligned} \quad (1.19)$$

However, the use of RMS simulations implies that the impedances of the network are simulated based on their value at the power system supply radian frequency ω_e , which may differ from the impedance corresponding to a radian frequency equal to $\omega_e - \omega_j$ or $\omega_e + \omega_j$.

Given that the network considered in this thesis is more inductive than capacitive, the imaginary part of the impedance corresponding to a radian frequency ω can be reasonably assumed to be proportional to this frequency as [27]:

$$\Im(Z) = L\omega \quad (1.20)$$

where L is the inductance of the network. However, the frequencies ω_j are expected to be relatively small compared to the power system supply radian frequency ω_e . Wave devices are indeed designed to harness the energy of waves whose period ranges between 3 s and 20 s [7]. Considering that electrical power is generated at twice the corresponding frequency, then voltage fluctuations should range between 0.1 Hz and 0.7 Hz. Hence, it can be assumed that:

$$\omega_e - \omega_j \approx \omega_e \quad \text{and} \quad \omega_e + \omega_j \approx \omega_e \quad (1.21)$$

Hence, the error on the reactance of the network can be considered as negligible. This demonstrates that the RMS method can be used for simulations including wave energy devices.

1.4 Grid operators' requirements

1.4.1 Introduction

The power fluctuations which may be generated by most oscillating wave energy converters without significant amounts of energy storage or without suitable control strategies may have a negative impact on the power quality of the local grid to which the wave farms will be connected. However, the grid operators must ensure that this impact remains negligible to the customers. Hence, a certain number of requirements defining the maximum tolerated impact and intended to the power plant owners were progressively developed by grid operators and/or energy authorities. They can usually be found in the form of grid codes (e.g. as in Ireland and the UK) or as decrees (e.g. as in France and Spain).

This section describes the different power quality criteria used in this thesis for assessing this impact, as well as requirements in terms of reactive power control in order to mitigate it. These descriptions are adapted from a book chapter written in collaboration with Joe MacEnri, formerly with a subsidiary of the Irish distribution system operator, ESBI [28].

1.4.2 Short-duration root-mean-square (RMS) voltage variations

There exist three different types of short-duration RMS voltage variations, namely voltage sag, swell and interruption, as described in IEEE standard 1159-2009 [29]. These variations are qualified as instantaneous, momentary or temporary depending on their duration, as shown in Table 1.2.

	Typical duration	Definition	Typical amplitude (pu)
Instantaneous	0.5-30 cycles	Sag	0.1-0.9
		Swell	1.1-1.8
Momentary	0.5-30 cycles	Interruption	≤ 0.1
	30 cycles-3 s	Sag	0.1-0.9
		Swell	1.1-1.4
Temporary	≥ 3 s-1 min	Interruption	≤ 0.1
		Sag	0.1-0.9
		Swell	1.1-1.2

Table 1.2: Classification of short-duration root-mean-square (RMS) voltage variations

Momentary as well as temporary voltage sag and swell are of particular interest with respect to power quality studies focusing on wave energy applications.

Voltage sag

According to IEEE 1159-2009, a voltage sag or dip (these words being interchangeable), is a decrease in RMS voltage between 0.1 pu and 0.9 pu. Voltage sags are traditionally induced by faults, the starting of large motors or by the switching of heavy loads. However, power fluctuations generated by wave farms may also be responsible for sags in sufficiently weak networks.

Voltage swell

Voltage swell is a voltage rise between 1.1 pu and 1.8 pu for a duration ranging from 0.5 cycles to 1 min. In opposite fashion to voltage sags, they are caused by load decrease, either load switching off or load shedding, or by the switching on of a large capacitor bank. However, similarly to sags, they may also be caused by the reflection of wave power fluctuations on the electrical power output of a wave farm.

1.4.3 Flicker

Introduction

Applying a varying voltage to a light bulb can result in significant light intensity variations, thus causing a potential visual disturbance. Although it is normal that voltage may vary

during the day, due for example to load switching or to motor starting, the impact of these fluctuations must be limited in order not to represent any disturbance to the customers. A statistical index of visual disturbance was developed in order to evaluate the level of annoyance caused by light intensity variations on the average individual. This index, called flicker level, can be evaluated over 10 minutes (short-term) or 2 hours (long-term), and is expressed as Pst and Plt respectively. In this thesis, only the short-term flicker level Pst evaluated over 10 minutes is analysed.

To ensure that visual disturbance remains negligible to the customer, grid operators limit either 1) the individual contribution in terms of flicker which a power plant is allowed to emit or 2) the total flicker level at the connection point. These limits enforced by several grid operators will be detailed and discussed in Chapter 4.

Flicker is a phenomenon which can have very significant consequences on customers' comfort and health. It has been recognised since the 1960s that flicker may potentially represent a risk to individuals prone to photosensitive epilepsy [30]. Besides, flicker can also induce electrical equipment malfunction, as well as non-negligible physical deterioration which may reduce significantly its lifetime. According to [31], the performances of control systems using electronics drives have been reported to be adversely affected by excessive and repeated voltage variations. In addition, the influence of these variations on rotating machines speed/torque control may for instance cause temperature rise and motor overloading issues. As wave farms can induce such rapid voltage variations with a significant amplitude, flicker is an issue of particular interest in the context of the large-scale grid integration of wave energy.

Evaluation

Flicker level is usually evaluated based on the perception of light intensity variations [32]. The lighting equipment considered in this standard is an incandescent light bulb. This may represent a worst case scenario regarding a number of lighting equipment types such as LEDs or compact fluorescent lamps, given their lower flicker response to low-frequency voltage modulation [33,34]. However, in the absence of widely agreed guidelines or standards on the flicker response of different types of lighting and electrical equipment, the recommendations established by IEC standard 61000-4-15 were retained for developing the flickermeter used in the studies presented in this thesis.

1.4.4 Voltage step

A voltage step is a sudden voltage variation as illustrated in Figure 1.16. In addition to be potentially detrimental to the quality of the electricity supplied to the customers, this type of variation may also affect the stability of the generators located close to the electrical element at the origin of the disturbance. A voltage step may be caused for instance by the switching on or off of a power plant, as well as by its unexpected disconnection.

1.4.5 Voltage control

Power plants of significant power capacity are usually required to provide so-called ancillary services, for instance in the form of local voltage control. Under normal operating conditions, the voltage control at a local level is usually achieved by controlling the reactive power flow to or from the plant. Power electronic converters, likely to be present in a majority of wave device designs, may help meeting this requirement.

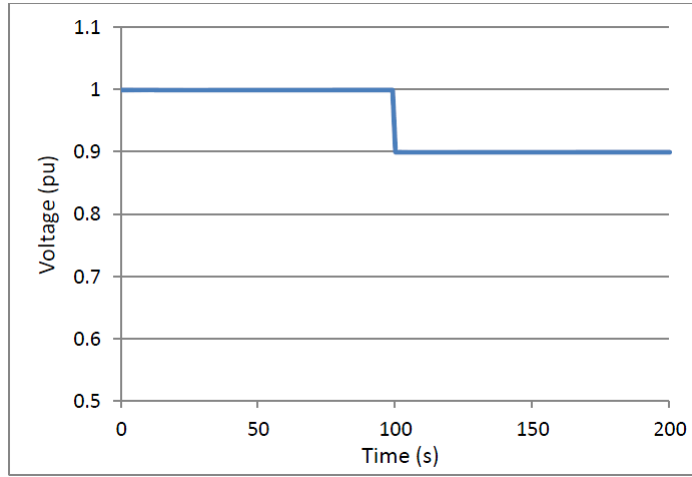


Figure 1.16: Illustration of a 10% voltage step

Different methods are available for maintaining the voltage within allowed limits as specified in grid codes: power factor control, reactive power control, direct voltage control or any combination of these. In the Republic of Ireland for instance, power factor control requirements are enforced for wind farms depending on the characteristics of their connection point: Figure 1.17a shows for instance the power factor capability required from wind farms connected to an existing substation up to 38 kV and Figure 1.17b presents the power factor capabilities required from those connected at a 38 kV node with no existing load customers or at a 110 kV node.

1.4.6 Influence of the grid strength on power quality

In power quality analyses, only a small part of a large network is analysed. Hence, the rest of the network is usually modelled by means of an ac voltage source in series with an impedance. This impedance corresponds to the Thevenin impedance \bar{Z}_S which can be expressed as:

$$\bar{Z}_S = R_S + jX_S \quad (1.22)$$

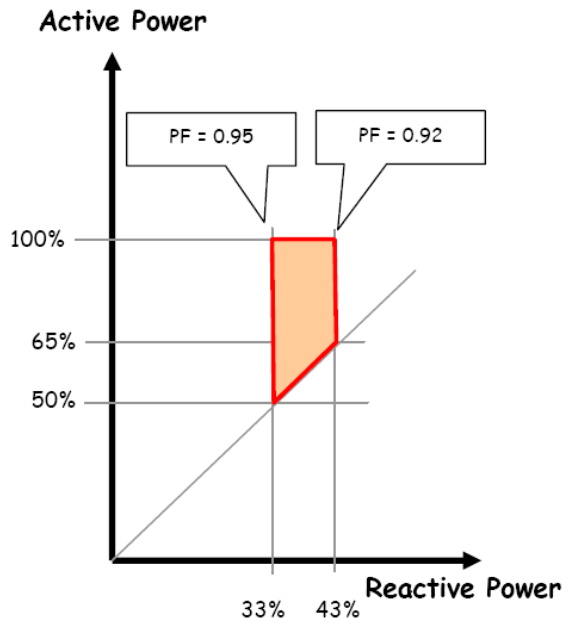
where R_S and X_S are the Thevenin resistance and reactance respectively. This impedance can be calculated from the short-circuit level S_{sc} and from the impedance angle Ψ_k at the point of connection between the local grid and the rest of the network which can be expressed respectively as:

$$S_{sc} = \sqrt{3}VI_{sc} = \frac{V^2}{Z_S} \quad (1.23)$$

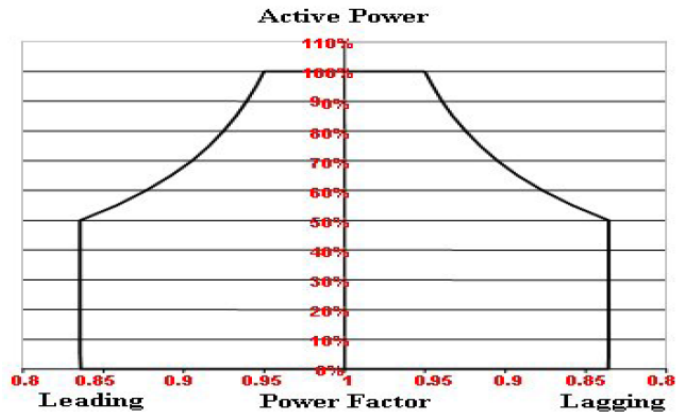
where V is the line voltage and

$$\Psi_k = \arctan\left(\frac{X_S}{R_S}\right) \quad (1.24)$$

Both the short-circuit level S_{sc} and the impedance angle Ψ_k , or alternatively the impedance \bar{Z}_S , are relevant indicators of the sensitivity of a given network to power fluctuations. The voltage fluctuations induced by power fluctuations injected into a network qualified as “strong” can be considered as negligible, whereas they are significant on a “weak” network.



(a) Connection to an existing substation up to 38 kV



(b) Connection at a 38 kV node with no existing load customers or at a 110 kV node

Figure 1.17: Requirements with respect to the power factor (top) and to the reactive power (bottom) as enforced in the Republic of Ireland [35]

Although there is no general definition of the grid strength, the amplitude of the induced voltage fluctuations decreases in an inverse proportion to the short-circuit level S_{sc} . Hence, a strong network is characterised by a sufficiently high short-circuit level S_{SC} . Consequently, the impact on the network is often studied as a function of the ratio of the short-circuit level to the apparent rated power of an installation, which is usually referred to as the short-circuit ratio. This will be detailed in the next chapter. The influence of the impedance angle Ψ_k is however more complex, as will be detailed in Chapter 4.

In practice, rural distribution grids such as those supplying the west coast of Ireland or the north of Scotland have a lower short-circuit level than most of the other coastal regions in Europe. This is due to the fact that these rural networks are supplied by low voltage distributions grids which have a usually a lower level of interconnection. In addition, the coastal areas are usually relatively remote from higher voltage networks as illustrated in Figures 1.18a and 1.18b which show the transmission network in Ireland and in Scotland

enforced in order to mitigate this impact. It showed that areas such as the west of Ireland and the north of Scotland may be more vulnerable to power quality issues than most other coastal regions. The next chapter will detail the state-of-the-art regarding the topics addressed in this thesis.

Chapter 2

State-of-the-art

2.1 Introduction

This thesis investigates four main topics. Firstly, the impact of a wave farm on the power quality of the local electrical network to which it is connected is analysed comprehensively. Then, the electrical design of wave farms is discussed in terms of minimum ratings required for different elements of the farm in terms of energy losses. The third topic of this thesis regards two flicker estimation laws in relation to the impedance angle Ψ_k and to the farm rated power. Finally, the generic modelling of ocean energy devices (including both wave and tidal current devices) is addressed.

The generic modelling of ocean energy converters was the initial focus of this work. However, with data becoming available as a result of the FP7 European project entitled CORES which is described in Chapter 4, this scope was modified in order to produce comprehensive studies on the impact of a wave farm on power quality. It is hoped that in the fullness of time, the results obtained through these case studies will be used as a benchmark for the validation of a generic model currently under development at HMRC.

2.2 Impact of a wave farm on the power quality of its local network

Only a limited number of case studies exist to date on the impact of a wave farm on its local network. In addition, it is difficult to draw general conclusions as these cases studies present numerous differences, which fall mainly into the eight categories as detailed below.

2.2.1 Modelling of the individual power profile

Experimental data on the power output of wave energy devices in real seas is very scarce and usually not publicly available. To date, with the exception of the work presented in this thesis, only two studies have detailed the impact of a wave device on its local grid based on experimental data of the power profile [39, 40]. Both these studies focus on a point absorber.

Hence, a majority of studies are based on raw sea-state data (either measured or generated numerically) which are used as input to numerical wave device models which present a high level of detail with respect to all the energy conversion stages [41, 42]. However, developing such models is very time-consuming and requires a large range of skills, in particular in hydrodynamics and mechanical engineering, areas in which electrical

engineers may have a limited knowledge. In addition, as this method is based on raw sea-state data, it is somewhat uncertain as the accuracy of the dynamic models has not been evaluated as yet in the absence of field measurements. Several other alternative approaches to the use of highly detailed wave device models were identified. One of them, which was developed in the framework of this thesis, consists of creating a fluctuating power profile composed of an average value and of a series of sinusoidal signals of different amplitudes and frequencies as will be detailed in the next chapter. Finally, a last approach consists in modelling the vertical motion of oscillating wave devices without significant storage means as being in phase with the sea surface vertical velocity, thus assuming that the wave device floats approximately on the sea surface at all times [43]. However, unlike these studies, the power output of wave devices is modelled in this work from experimental time series data generated in the framework of project CORES, as mentioned earlier.

2.2.2 Computation of the total wave farm power output

The power output of a wave farm may be computed based on a sufficiently accurate knowledge on both the sea surface elevation as a function of time at each position where a wave device is located and on the mechanical reaction of the power take-off mechanism to the sea conditions of the type of wave device considered. This type of computation usually provides results with a high level of detail which is however unnecessary in the case of power system studies. Hence, less sophisticated and time-consuming methods for estimating the power output of several wave devices are expected to be sufficient.

One of these methods consists of applying time delays to the individual power profile generated by a wave device in order to obtain a reasonable estimation of the power profiles of other wave devices [44]. This technique does not take into account wave dispersion, which implies that waves of different frequencies travel at different speeds. This means that the power profile of a wave device included in a wave farm cannot be exactly similar to this of another wave device. However, it is deemed sufficient for power system studies. Hence, a method based on time delays was used in this thesis and is described in Chapter 4.

2.2.3 Wave device technology

In the studies which are not based on experimental power profiles, the exclusive use of point absorber devices in power system studies may be partly explained by the fact that they represent the most simple design to model numerically compared to the other types of wave device. It seems that no study based on overtopping devices exists while only one study has dealt with the power quality of OWCs [45]. It is based on a small onshore OWC prototype located on the island of Islay, UK and addressed the level of flicker generated by this wave device.

This relative lack of knowledge on the power quality of different wave device types represents a barrier to the objective assessment of each technology from a grid integration perspective. It is one of the objectives of this thesis to investigate this gap regarding floating oscillating water columns.

2.2.4 Generator control strategy and storage means

In all the studies which are not based on experimental power profiles, the drive-train does not include any storage means and the generator is operated in fixed speed mode. In this mode, inertial storage not being available, the mechanical power peaks are directly transformed into electrical power peaks. Hence, this constitutes a worst case from a power

quality perspective.

However, using storage (either through dedicated means or in the form of variable speed mode) may greatly enhance the quality of the wave farm power output. Operating the generator in variable speed mode has already proved to be very efficient in the case of wind farms [25]. The flicker generated by the LIMPET oscillating water column operated in variable speed mode was detailed [45]. However, the absence of results regarding the fixed speed operation means that the power quality of these two modes cannot be compared. Another approach consists of including dedicated storage means in the design of a wave device [39]. In this study, several control strategies regarding the use of a bench of supercapacitors for limiting the flicker generated by a point absorber are detailed. The common point between these two studies is the use of storage for limiting the flicker generated by a wave device, either by using the variable speed mode as in the former, or by using dedicated storage means in the latter. However, it appears from these two studies that comparing the power quality of two different devices is not trivial, in particular if their storage mechanisms are of different nature and present different characteristics. However, the influence of storage on a power profile may be modelled generically by a first-order low-pass filter [46]. The time constant τ_s of this filter is assumed to be equal to the inertia time constant in the case of mechanical and hydraulic storage means. Hence, describing storage in this manner may facilitate the comparison between different devices from a power quality perspective. The accuracy of this proposed modelling approach is evaluated in this thesis. It is also used to estimate the minimum time constant τ_s required for meeting the flicker requirements.

2.2.5 Wave climate and sea-state

The existing studies which are described in this chapter present simulation results based on a single sea-state, which is rarely representative of the most energetic conditions at a given site. This thesis however provides results for different sea-states corresponding to a low, a medium and a high energy level, which are intended to be representative of a wide range of typical energy levels around the world.

2.2.6 Layout of the farm

The farm orientation compared to the dominant wave direction, as well as its layout, are important criteria regarding the quality of its power output. However, in most existing studies, both these criteria are fixed so their influence on the grid impact of the wave farm is not studied.

The impact of modifying the orientation of a linear array compared to the dominant wave direction by a variable angle was investigated [42]. However, only the variance of the farm power output as a function of this angle was studied, which does not enable the establishment a direct link between this variable angle and usual power quality criteria. In this thesis, the influence on power quality of the farm orientation compared to the dominant wave direction, as well as the influence of the device layout are analysed. In addition, the analysis of worst case conditions from a power quality perspective is included in the case studies, which has never been previously addressed. The worst case conditions correspond to the case where a linear array is orientated perpendicularly to the dominant wave direction, which leads to the simultaneous generation of power peaks by a number of the generators belonging to this array. This type of situation may occur in the case of a test site where different devices are structured into a linear array facing the dominant wave direction. This orientation, by enabling each device of the array to benefit from

similar sea conditions (thus limiting the inter-device hydrodynamic interactions) enables a fair comparison of the performances of different devices. However, this type of situation may also occur in the case where the wave direction changes significantly and becomes perpendicular to a linear array.

2.2.7 Short-circuit ratio and impedance angle Ψ_k

The short-circuit ratio of a fluctuating power source, which was defined in Chapter 1 as the ratio of the short-circuit level S_{sc} to the rated power S_n of the installation, is a relevant criterion for estimating the impact which this power source may have on its local network. This ratio was introduced in the context of the grid integration of wind farms and is also applicable in the case of wave farms, although its relevance in this latter case is more limited due to the ambiguity on rated power. This method facilitates an assessment of the maximum power fluctuation which the farm may output as a ratio of the short-circuit level S_{sc} of the node to which the farm is connected. This maximum power fluctuation is assumed to be equal to the farm rated power S_n as a worst case, which is relevant in the case of a wind farm but slightly less in the case of a wave farm where the notion of rated power is more ambiguous. However, regardless the nature of the input power, the amplitude of the voltage fluctuations induced by a grid-connected installation decreases in an inverse proportion to the short-circuit level S_{sc} . Hence, the higher the short-circuit ratio is, the smaller the amplitude of the induced voltage fluctuations.

Empirical values with respect to the short-circuit ratio have been adopted in the context of good practice by the wind energy industry. For instance, wind farms used to be recommended to be connected to points whose short-circuit level is at least 25 times greater than the farm rated power S_n [25]. Further studies have proved that wind farms could be safely connected to nodes with a short-circuit ratio as low as 2 provided that a suitable power factor control is applied at the point of common coupling [47, 48].

In the case of a wave farm, studies to date have been performed almost exclusively for extreme values of the short-circuit ratio. In one case, studies based on a small size farm (whose rated power is approximately 1 MW) connected to a generic weak rural network were undertaken [42, 49] while in others a medium size farm (with a rated power equal to 20 MW) was connected to the Belmullet site in Ireland whose short-circuit level is relatively low [41, 50, 51]. Hence, all the studies presented in this paragraph were performed for a relatively low short-circuit ratio, equal to 3.3 in the three last studies.

Conversely, the short-circuit ratio is extremely high in the case of similar studies based on the same medium size wave farm connected to the bimep test site in Spain, whose short-circuit level is extremely high [41, 51]. The short-circuit ratio of the 20 MW farm in this case is equal 225, leading to negligible voltage fluctuations, as expected. In similar fashion, the flicker induced by a single point absorber connected to a node having a short-circuit level 610 times as high as its rated power proved also to be absolutely negligible [40].

An exception to the above observation must be made for a study [39] in which flicker analyses were performed using a generic flicker coefficient $C(\Psi_k)$, adapted from IEC standard 61400-21 [52] and independent of the short-circuit level at the point of connection. The impedance angle Ψ_k chosen for this study is equal to 30° , which corresponds to a worst case scenario in terms of flicker generation for an installation operated at unity power factor. This study, based on a 1 MW point absorber, showed that flicker level may be maintained below the limit enforced in France by using an actively controlled storage means of relatively small energy capacity. However, in the absence of a flicker summation

law, the flicker corresponding to a larger wave farm cannot be estimated from these results.

In addition to using different short-circuit ratios, all the studies presented in this section were generally performed for different impedance angles Ψ_k , which renders more complex the comparison of their results. In summary, it is not possible to extract from these studies the minimum short-circuit ratio above which power quality issues are not expected to arise from the connection of a wave farm, as has been done in the case of wind farms.

This thesis is expected to fill the gap by presenting the grid impact on a number of power quality criteria, namely the voltage step, the maximum and minimum voltages and the flicker level, of a wave farm connected to a node whose short-circuit level S_{sc} and impedance angle Ψ_k covers the entire range of typical values for these parameters.

2.2.8 Power quality criteria addressed and grid codes

Grid operators define a number of requirements applicable to grid-connected installations, and among them those related to electrical power quality, to ensure that power systems are operated in a safe and reliable way. Hence, power plant managers must prove that their power station complies with these requirements in order to be allowed grid connection.

The importance of complying with power quality requirements is essential as failing to meet them is a sufficient reason for any grid operator to deny grid connection applications. However, limits specified by these requirements may differ among different grid connection codes, rendering compliance with power quality requirements somewhat site-specific. A survey on the limits enforced with respect to several power quality criteria in different grid codes, recommendations and standards was conducted in order to extract the most stringent as well as the most permissive of these limits. As mentioned earlier, the power quality criteria identified for investigation are the voltage step, the maximum and minimum voltages as well as the short-term flicker level. These criteria are directly applicable and relevant to wave farms, contrary to others such as those concerning power ramp rates, which are inapplicable as such to wave farms and which are not considered in this study. The compliance test of the wave farm is based on both the most permissive as well as the most stringent limits in order to be representative of the requirements applied by a range of grid operators around the world. All these topics are addressed in Chapter 4.

2.3 Electrical design of a wave farm

A wave farm must be optimally designed in order to maximise the revenue it generates and to minimise its capital expenditure. This must be achieved among other factors by selecting equipment with suitable characteristics, such as rating and impedance. This selection should focus on maintaining regulatory voltage and flicker levels, on minimising the power losses as well as on avoiding a useless and costly over-rating of the farm's constituent components.

The minimum rating required from three particularly costly types of element, namely the VAr compensator, the submarine cables and the overhead line, are investigated in Chapter 5. The cost of these elements being highly dependent on their rating, this work will provide useful information for facilitating the sufficiently accurate modelling of a wave farm for techno-economical studies. The current absence of studies on this topic may lead to a significant error in the estimation of the capital expenditure of a wave farm, as the cost of cabling in a large offshore wind farm may represent up to 20% [53] of the total cost.

This topic is investigated as part of this thesis. Although the minimum rating for the VAR compensator can be defined from load flow simulations, the minimum rating required from the submarine cables can only be obtained through additional analyses focusing on its thermal loading. It is important to bear in mind that the current rating of cable is determined from the maximum temperature at which its different components can be safely operated. Hence, the transient nature of the cable temperature must be taken into account in the overall power system study.

However, the conventional method for estimating this rating is based on steady-state calculations (hence assuming a constant current) [54]. This type of calculation is not representative of, nor relevant to wave energy applications, considering the rapid current fluctuations generated by a wave farm compared to the very slow thermal dynamic response of a submarine cable, ranging usually between 2 min to 30 min [55–57]. Consequently, a suitable current rating, from a thermal loading perspective, is expected to be much less than the maximum instantaneous current which the cables carry, which could lead to significant savings in terms of capital expenditure. Based on these considerations, a novel method for estimating the temperature of the cables in the case of wave energy applications is proposed in this thesis. Finally, the power losses generated within the farm are also investigated as they represent a loss of revenue which, although being potentially significant, is usually not taken into account in techno-economical analyses.

In summary, the minimum ratings required from three particularly costly types of element, namely the VAR compensator, the submarine cables and the overhead line, are investigated in Chapters 5 and 6. The minimum current rating required from the submarine cables is analysed from a thermal loading perspective. A novel method is proposed which, contrary to conventional methods based on steady-state calculations, takes into account the current fluctuations induced by the waves. Finally, the power losses generated within the farm are also investigated as they represent a loss of revenue which is usually not taken into account in techno-economical analyses.

2.4 Estimation of flicker results

Flicker level may vary greatly depending on the number of devices included in a wave farm and on the short-circuit level and on the impedance angle of the node in the grid to which it is connected. Hence, it is important to define estimation laws which describe the relation of the flicker level with these parameters. Given that a wind farm is a fluctuating power source in similar fashion to a wave farm, the flicker estimation method defined with respect to this former type of power plant was assumed to represent a relevant starting point for the development of an estimation method applicable to wave farms. So far, two methods have been developed, one in relation to the short-circuit ratio (as defined in the IEC standard 61400-21) and one in relation to the number of wind turbines included in a wind farm, which is usually referred to as a flicker summation law (as defined in the IEC standard 61000-3-7 [58]).

According to the IEC standard 61400-21, the flicker level Pst generated by a wind farm is inversely proportional to the short-circuit level of the node to which it is connected. As this relation is independent of the nature of the input power, it is also directly applicable in the case of wave farms. This, however, is not the case regarding the flicker summation law defined in the IEC standard 61000-3-7. This summation law defines the flicker level generated by N wind turbines as the product of the individual flicker level Pst_i generated by each of these turbines times the square root of N given by:

$$Pst = Pst_i \sqrt{N} \quad (2.1)$$

This implies that the influence on lighting equipment of voltage fluctuations generated by each wind turbine add according to the square root of N as in (2.1). This is also partially true in the case of wave farms. For instance, N generators may output a power peak simultaneously, which may result in a power peak of significant amplitude. Obviously, the higher this number N is, the higher the probability becomes that a fraction of these generators output a power peak simultaneously. However, it is also expected that the power fluctuations generated by each wave device would tend to compensate themselves to some extent with those generated by other wave devices, as they may be out of phase. Hence, this would lead to a smoother power profile [59]. Consequently, the amplitude of voltage variations may also decrease as a function of the wave farm rated power. As this latter aspect is not taken into account in the flicker summation law described in the IEC standard 61000-3-7, investigations were conducted to develop a flicker estimation law in relation to the farm rated power which is suitable for wave energy applications. It is important to bear in mind that a considerable number of wave devices must be simulated for a wave farm of significant rated power. This law would, among others, facilitate a considerable reduction in the computing resources necessary for determining the flicker generated by large wave farms.

Finally, it appears that no estimation method has been defined yet with respect to the impedance angle Ψ_k which has however a fundamental influence on the level of flicker. Hence, an estimation law in relation to this variable has been developed in this thesis. These estimation laws are complementary to the existing estimation law in relation to the short-circuit ratio defined in the IEC standard 61400-21. The combination of these three laws is expected to greatly facilitate both the estimation of flicker with respect to different connection points and the dissemination of experimental results.

2.5 Generic modelling of ocean devices for power system studies

2.5.1 Introduction

As mentioned in the introduction chapter, power system simulators are the tool of choice for assessing the grid impact induced by any system changes. Dynamic models for most of the typical components of a power system are usually provided as built-in models which the user only needs to parameterise. This, however, is not the case for renewable power plants for which reliable models have been released in the last decade only in the best case [60], or are still lacking.

This section describes the experience gained from the wind energy industry in the field of numerical modelling. It will detail the reasons why the concept of generic modelling has emerged as a solution for the modelling of wind turbines and why this approach seems to be relevant as well in the case of ocean devices, including both wave and tidal current devices.

2.5.2 Experience of the wind energy industry

In the past, the lack of suitable models for renewable power plant (wind farms and solar panels in particular) hindered renewable power generation being taken into account in power system stability studies. This became obviously more and more unrealistic as

the penetration rate of these renewable sources increased. When they represented a non-negligible share of the energy mix in a number of countries, the lack of reliable dynamic models clearly became an issue to the further integration of renewables. In Ireland for instance, due to the inherent stability issues resulting from the small size of the power system, the absence of dynamic models ultimately forced the transmission system operator, Eirgrid, to establish a moratorium on the connection of wind turbines [61].

It is in this context that grid operators introduced, as early as 2003 [62], requirements as part of the grid connection process regarding for the provision of dynamic models. This requirement concerns renewable power plants of a significant rated power, typically exceeding 5 MW in Ireland [35]. As a result, most grid operators in industrialised countries now routinely require dynamic models. As an example, the future European grid code, which will come into force in 2014 in 34 countries, will include precise requirements on the dynamic models to be provided by power plant owners [22].

However, the experience of the wind energy industry proved that the modelling of wind turbines could be relatively complex and time-consuming. Eirgrid, the Irish transmission system operator, detailed the numerous issues arising from the integration into its power system simulator of 20 dynamic models received from wind farm developers. Despite joint efforts between the wind farm developers and its staff over a three year period of adapting and/or debugging the models, none performed appropriately as of 2007 [63].

Consequently, generic modelling has been highlighted as being a potential approach to solve the issues inherent to the specific modelling approach [63,64]. The generic modelling approach consists of defining a generic structure common to most wind turbines which includes all the dynamic features relevant to power system stability studies. This structure must be parameterised by device-specific data which the manufacturers have the ability to provide without prejudice to the commercial confidentiality of their products.

2.5.3 Application of generic modelling to ocean devices

The issues arising from the grid integration of ocean farms presents similarities as well as differences compared to those occurring in the case of wind farms. From this perspective, a comprehensive review of these issues highlighted the need for a generic model of ocean devices, as well as the complexity of this task [65].

The first generic model structure was composed of three conversion stages which consist of a front-end stage where the wave power is converted into mechanical power, of an optional intermediate stage in the case where hydraulic storage means are included in the design and of a last stage corresponding to the electro-mechanical energy conversion [66]. The input power to this model was simulated as an average water velocity to which a stochastic variation was applied for tidal turbines, which is representative of real conditions. In the case of wave devices, the model was presented in the case of sinusoidal sea conditions. Comparison with experimental results was however not conducted.

Based on these studies, the OES-IA, a branch of the International Energy Agency (IEA), decided to initiate research on the issue of generic modelling. It established a collaborative research project running between 2009 and 2010 which was intended to obtain a refined generic structure applicable to a majority of ocean devices. Its second objective was to collect data which the device developers have the ability to provide in order to parameterise this structure. The results of this work were released as a technical re-

port [46]. The results of the work conducted by the author of this thesis, who participated in this collaborative project, are presented in Chapter 8. This personal contribution took the form a developer survey and focused on refining the generic structure proposed at an initial stage of this research project in order to include the influence of control strategies on the power profile of an ocean device. This work has been updated in order to include the recommendations described in Chapter 7 regarding the evaluation of flicker.

Since the closure of the OES-IA collaborative project, research has focused on the implementation of the generic model developed as part of this research project. HMRC has, for instance, launched a R&D project called SEAGRID under the leadership of D. O’Sullivan and R. Alcorn. As part of this project, in which the author of this thesis participated regularly, further research on the implementation of the generic model described was conducted [67,68]. However, the implementation of a fully generic model is out of the scope of this thesis and will not be addressed in detail.

In summary, this field of research is still relatively embryonic, which can be explained by the very limited number of power system researchers working in the field of ocean energy and the early stage of development of the ocean energy industry. As of early 2013, no technical committee has planned yet to address the generic modelling of ocean energy systems. This is however likely to change thanks to the work of the IEC technical committee TC 114 [69] which focuses on international standards for marine energy conversion systems and should be followed with great attention in the coming few years.

2.6 Summary of the contributions of the thesis

2.6.1 Chapters 4 and 6

Two majors obstacles to the analysis of the grid impact of a medium-size wave farm have been highlighted. Firstly, most power system studies intended to analyse the impact on power quality of wave farms are based on wave device numerical models which have not been validated against experimental results. The studies presented in this thesis are, on the contrary, based on actual experimental power profiles generated by a quarter-scale OWC prototype deployed at sea over a three-month period.

Secondly, the existing case studies were performed by using different parameters, which makes it difficult to draw general conclusions. In order to fill this gap, two case studies were performed and are presented in Chapters 4 and 6. While the case study presented in Chapter 4 addresses the impact of a 20 MW farm included in a test site facility, the case study described in Chapter 6 focuses on a commercial wave farm rated up to 50 MW. These two case studies are based on five different production periods which correspond to five different sea-states. In three of these production periods, the generator is operated in fixed speed mode, while it is operated in variable speed mode in the other two. Different device layouts are used, as well as two different wave farm orientations compared to the dominant wave direction. Worst case conditions from a power quality perspective in terms of farm orientation are also analysed. The simulations are performed for the entire range of typical short-circuit levels and impedance angles Ψ_k , as well as for a farm rated power ranging between 20 MW and 50 MW. Finally, a comprehensive review of grid codes, regulations and standards has been undertaken to determine the most stringent as well as the most permissive limits enforced in terms of voltage step, maximum and minimum voltages and flicker level. The compliance of a wave farm is assessed with respect to these two types of limits in order to be representative of typical grid operators’ requirements enforced around

the world. Based on these case studies, the minimum short-circuit ratio above which the connection of a wave farm is unlikely to pose power quality issues is investigated.

2.6.2 Chapter 5

The minimum ratings required from two particularly costly types of element, namely the VAR compensator and the submarine cables, are investigated in Chapter 5. The cost of these elements is highly dependent on their rating and this work is expected to provide useful information for facilitating an accurate modelling of a wave farm for techno-economical studies. The current absence of studies on this topic may lead to a significant error in the estimation of the capital expenditure of a wave farm. The minimum current rating required from the submarine cables is analysed from a thermal loading perspective. A novel method is proposed which, contrary to conventional methods based on steady-state calculations, takes into account the current fluctuations induced by the waves. Given that the cables' thermal time constants are usually greater than the period range of the wave-induced current fluctuations, it may be expected that a suitable current rating, from a thermal loading perspective, is much less than the maximum instantaneous current which the cables carry. This could lead to significant savings in terms of capital expenditure. Finally, the power losses generated within the farm are also investigated.

2.6.3 Chapter 7

Two flicker estimation laws in relation to the farm rated power and in relation to the impedance angle which are suitable for wave energy applications were developed as part of this thesis. They are complementary to the existing estimation law in relation to the short-circuit ratio defined in the IEC standard 61400-21.

2.6.4 Chapter 8

The current absence of dynamic models may represent a barrier to the large-scale grid connection of ocean devices. A collaborative research project was launched in 2009 by the OES-IA, a branch of the International Energy Agency (IEA). Chapter 8 describes the results of a developers survey conducted by the author of this thesis in the context of this collaborative research project. This work was intended to refine an existing generic model structure in order to include the influence of the control strategies on the power output of a device, as well as to collect data to parameterise this structure.

The following chapter presents a simplified analytical case study whose main purpose is to illustrate the notions introduced in Chapter 1 regarding the power quality issues which may arise from the grid connection of a wave farm. It is also intended to serve as an introduction to the case studies presented in Chapters 4 and 6.

Chapter 3

Simplified analytical case study

This section intends to provide an introduction to the issues related to the integration of fluctuating power sources, such as wave farms, into the network. It will present a simplified analytical case study conducted at an early stage of this thesis.

3.1 The AMETS test site

The case study focuses on the national wave test site of Ireland named the Atlantic Marine Energy Test Site (AMETS). This test site is located off Belmullet, County Mayo (see Figure 3.1) and was selected in 2009 by the Irish government. Although the test site was initially expected to become operational in 2011, its development stage still remains purely conceptual. According to the Sustainable Energy Authority of Ireland (SEAI), manager of the project, the strategic purpose of the site is to assess the performances and survivability of pre-commercial wave energy devices in extreme open ocean conditions. Hence, the test site is not thought to be built before 2015 at least, once sufficiently robust designs will have been tested at other test sites presenting milder sea conditions.

The test site is planned up to a maximum generating capacity of 20 MW, although the initial lease was accorded for 10 MW only. It will include four berths, as shown in Figure 3.2, two located at 6.5 km from the shore and at 50 m water depth, the other two being located at 16 km offshore and at 100 m water depth. Voltage is stepped up offshore from 0.4 kV to 10 kV. An onshore substation, whose consumption was assumed to be equal

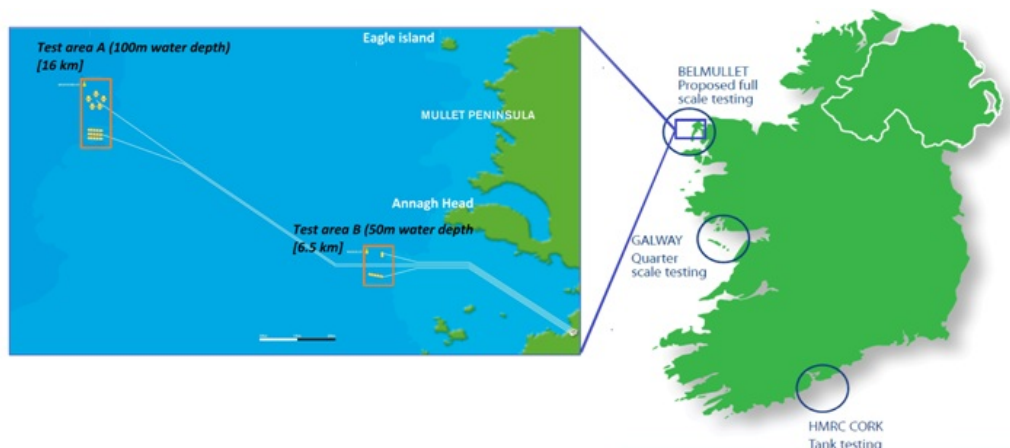


Figure 3.1: Location of the AMETS test site [70]

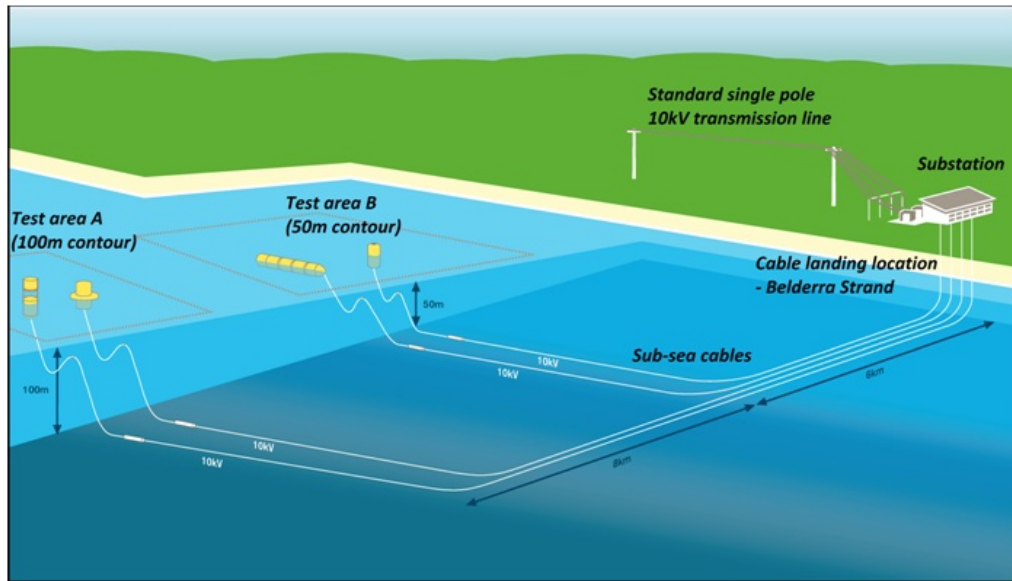


Figure 3.2: Conceptual layout of the test site [70]

to 0.10 MW at 0.95 power factor lagging (referring here as absorbing reactive power), steps then the voltage up again from 10 kV to 20 kV. Although this voltage stepping-up does not appear on the initial design of the test site, 10 kV lines are being progressively replaced all around Ireland by 20 kV lines. Hence, adapting the original configuration of the test site seemed relevant given that the test site will not become operational for a number of years. A 5 km overhead line connects the substation to the point of common coupling (PCC) with the rest of the network.

Considering that the Irish distribution system operator, ESB, requires wind farms connected to this type of connection point to control their power factor between 0.92 and 0.95 lagging, a VAR compensator was modelled at the PCC, maintaining a fixed power factor equal to 0.93 lagging. A transformer steps the voltage up from 20 kV to 38 kV at the location of Belmullet town, whose consumption (including this of its surroundings) was assumed equal to 2 MW at 0.95 lagging based on its number of inhabitants (approximately 15,000 according the latest census [71]). The rest of the national network is modelled by a constant voltage source (connected to the slack bus) in series with an impedance modelling the short-circuit level at the high-voltage side of the 20 kV/38 kV transformer.

3.2 Numerical modelling

3.2.1 Modelling of the electrical network

Wave farm's network

The geographical configuration of the wave farm as well as the electrical components ratings were modelled according to the design defined by the test site manager, ESBI, a branch of the Irish distribution system operator ESB. The numerical model of the farm which was developed under power system simulator PowerFactory is shown in Figure 3.3. The impedance values for the submarine cables as suggested in a consultancy study ordered by ESBI and conducted by HMRC were retained for their numerical modelling. The impedances of both the transformers and of the overhead line were defined based on typical values for these pieces of electrical equipment as found in manufacturer data sheets [72,73] or in specialised publications [74–76]. The values used for the positive-sequence impedance

	R_1 (Ω/km) ¹	X_1 (Ω/km) ¹	C_1 ($\mu\text{F}/\text{km}$) ²
Submarine cables	0.25	0.13	0.22
Overhead line	0.09	0.3	0

¹ series impedance

² shunt capacitance

Table 3.1: Positive-sequence impedance of the submarine cables and of the overhead line

	X_1 (pu)	P_T (kW)
Transformers	0.06 ¹	4

¹ per-unit value based on the apparent rated power of each transformer

Table 3.2: Positive-sequence impedance of the transformers

of each element of the model used in the study detailed in this chapter are presented in Tables 3.1 and 3.2. This model was used also for the studies detailed from Chapters 4 to 5.

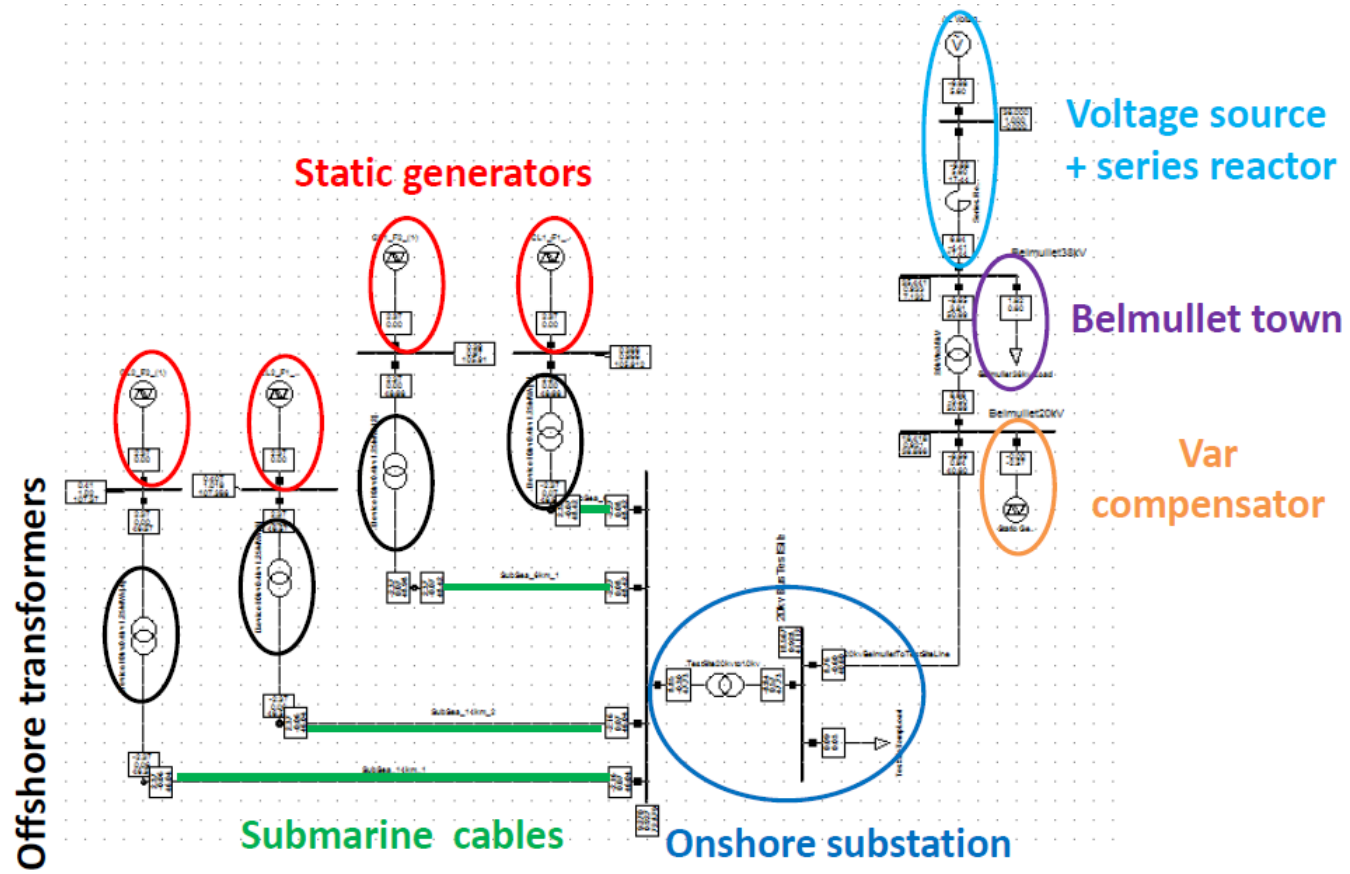


Figure 3.3: Model of the electrical network developed under PowerFactory

	Winter	Summer	Average
I_{sc} (kA)	3.9	3.0	3.45
X/R	3.1	2.9	3.0

Table 3.3: Short-circuit characteristics at the 110 kV connection point located at Bellacorick

Modelling of the rest of the network

The rest of the power system to which this local network belongs is modelled by means of an ac voltage source in series with a series reactor of impedance $\bar{Z}_S = R_S + jX_S$. The value of X_S and R_S , which are respectively the Thevenin reactance and resistance of the rest of the power system, can be calculated from the short-circuit level S_{sc} and the impedance angle Ψ_k as:

$$S_{sc} = \sqrt{3}VI_{sc} = \frac{V^2}{Z_S} = \frac{V^2}{\sqrt{R_S^2 + X_S^2}} \quad (3.1)$$

and

$$\tan(\Psi_k) = \frac{X_S}{R_S} \quad (3.2)$$

where I_{sc} is the short-circuit current. The voltage at the ac source terminals is maintained constant at all times at 1.0 pu, thus simulating an infinite grid.

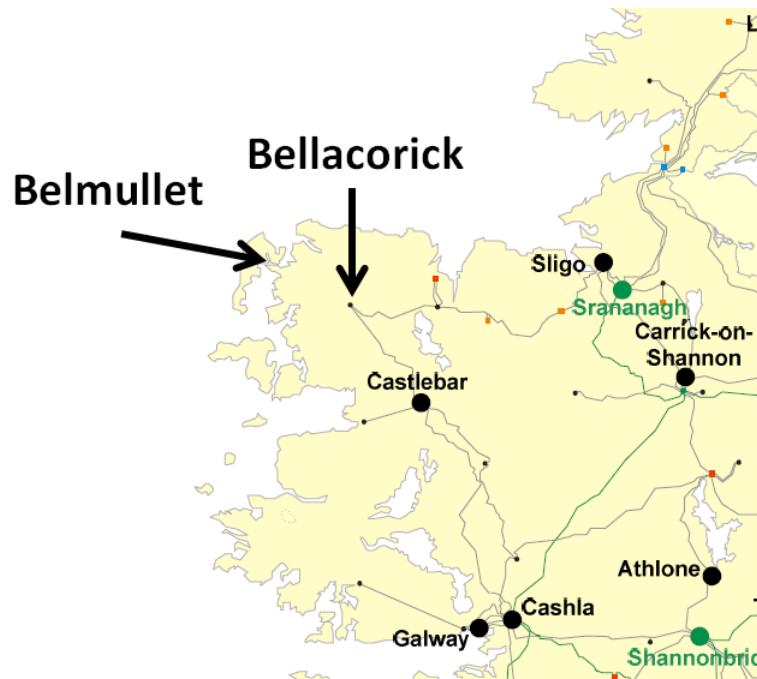
The short-circuit level S_{sc} at the high-voltage side of the 20/38 kV transformer was estimated from the short-circuit level S'_{sc} at the nearest 110 kV connection point and from the impedance Z of the overhead line and of the transformers between these two nodes, as:

$$S_{sc} = \frac{V^2}{\frac{V^2}{S'_{sc}} + Z} \quad (3.3)$$

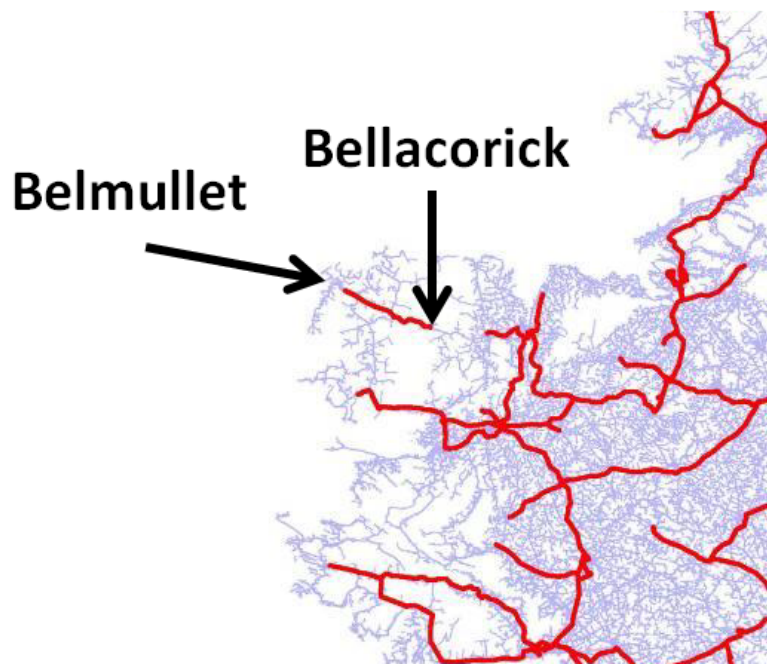
The 110 kV node supplying the Belmullet area is located at Bellacorick, County Mayo, as shown in Figure 3.4a. The Eirgrid's Transmission Forecast Statement 2012-2018 [36] indicates that the short-circuit level at this 110 kV node ranges between 3.9 kA (winter) and 3.0 kA (summer), with a X/R ratio ranging between 3.1 and 2.9 respectively, as summarised in Table 3.3. Average values of the short-circuit level and of the X/R ratio equal to 3.45 kA and to 3.0 respectively were selected for the study.

A single 38 kV overhead line, whose length was estimated to be equal to 35 km, connects the 110 kV node (located at Bellacorick) to the 38 kV node (located at Belmullet), as illustrated in Figure 3.4b which shows the 38 kV distribution system. The impedance between the 110 kV and the 38 kV nodes was estimated based on the typical impedance values for a 38 kV line and a 38/110 kV transformer. The current rating of the 38 kV line was selected as being equal to 340 A, which corresponds approximately 22 MW. This power level corresponds to the worst case scenario where the maximum electricity generation of the farm (equal to 20 MW) coincides with a negligible consumption of the local loads. As for the 38/110 kV transformer, the value provided by the Eirgrid's Forecast Statement was retained.

The Thevenin reactance X_S and resistance R_S at the high-voltage side of the 20/38 kV nodes were estimated to 21.4 Ω and 8.1 Ω respectively, corresponding to an impedance Z_S



(a) Transmission system



(b) 38 kV distribution system

Figure 3.4: Power system of the west of Ireland

equal to 22.9Ω and an impedance angle $\Psi_k=69.2^\circ$. These short-circuit characteristics are summarised in Table 3.4. Due to a lack of information on the power consumption along the Bellacorick-Belmullet line, it was not taken into account in the calculations. However, it is demonstrated in Appendix A that the error on the short-circuit level and on the impedance angle Ψ_k induced by this approximation is negligible.

R_S (Ω)	X_S (Ω)	Z_S (Ω)	Ψ_k ($^\circ$)
8.1	21.4	22.9	69.2

Table 3.4: Short-circuit characteristics at high voltage side of the 20/38 kV transformer

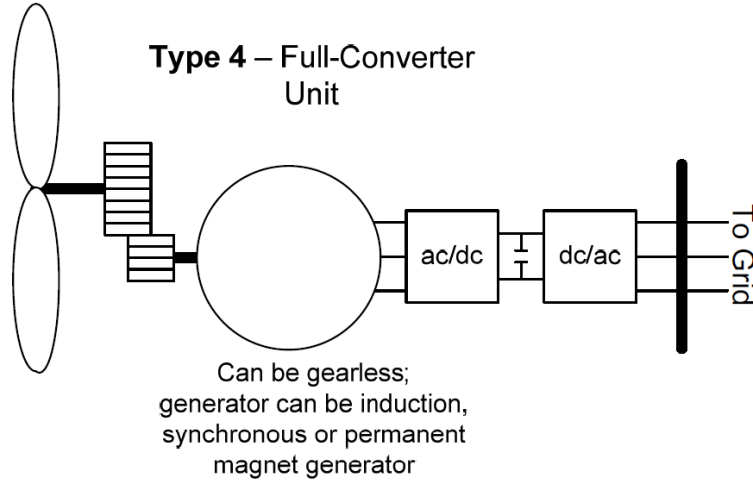


Figure 3.5: Generator connected through a fully-rated power electronic converters

3.2.2 Modelling of the wave energy devices

Generator model

The wave energy devices are simulated as generators connected through fully-rated power electronic converters, as illustrated in Figure 3.5. They were modelled by means of the “static generator” model, equivalent to a controlled current source, provided as part of the PowerFactory package. The control frame which was developed to control the power output of each generator included in the model is shown in Figure 3.6.

The “P-input” block outputs the reference active power P_{ref} of the static generator, from which its reactive power reference Q_{ref} is calculated by the “Reactive.Power” block. The generators were operated in fixed power factor mode, whose power factor reference was maintained to unity during the simulations. This type of operation was expected to be beneficial as it reduces power losses within the submarine cables as well as the need for the VAR compensator to supply reactive power to the farm.

However, as the static generators are modelled as current sources, the active and reactive power references P_{ref} and Q_{ref} must be expressed in terms of current references. In order to facilitate the calculations, these current references are expressed in terms of direct and quadrature components of the current, referred to as i_d and i_q respectively. These terms correspond to the phase currents i_a , i_b and i_c to which the dq-transform is applied as:

$$\begin{bmatrix} i_d \\ i_q \end{bmatrix} = \begin{bmatrix} \cos(\Phi) & \cos(\Phi - \frac{2\pi}{3}) & \cos(\Phi + \frac{2\pi}{3}) \\ -\sin(\Phi) & -\sin(\Phi - \frac{2\pi}{3}) & -\sin(\Phi + \frac{2\pi}{3}) \end{bmatrix} \begin{bmatrix} i_a \\ i_b \\ i_c \end{bmatrix} \quad (3.4)$$

where Φ is the angle between the direct axis and the axis corresponding to phase a . The dq-transform enables the expression of the three ac phase currents i_a , i_b and i_c as two dc currents i_d and i_q . These dc currents represent the projection of the ac currents onto two axes rotating at the same angular speed as the ac variables. Given that the voltage mea-

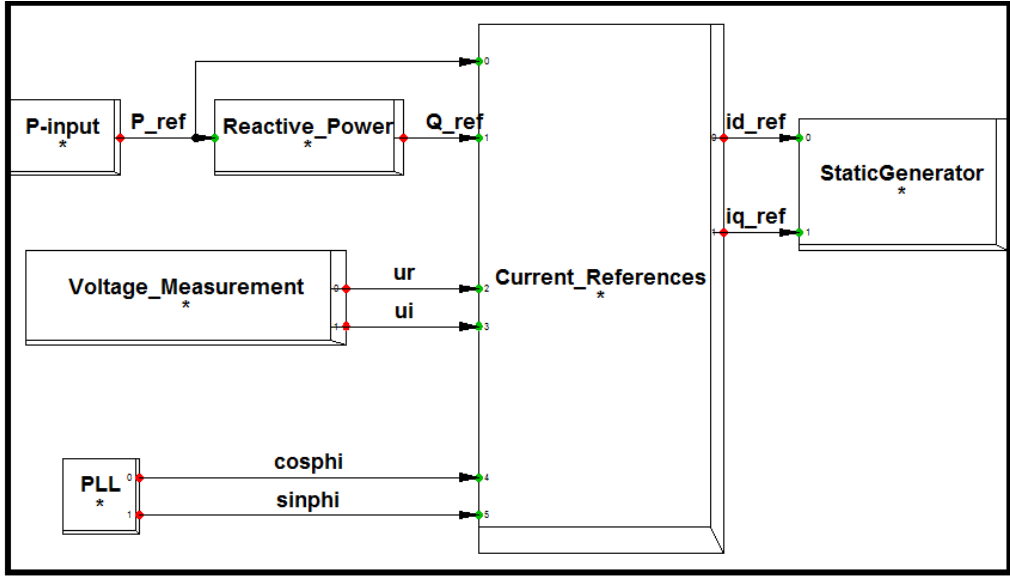


Figure 3.6: Control frame used for the static generator models

surement tool (corresponding to the block “Voltage_Measurement” in Figure 3.6) included in PowerFactory measures the real and imaginary components of the voltage, referred to as v_r and v_i , the real and imaginary components of the current i_r and i_i must be defined in the first place. These components are linked to the active and reactive power reference P_{ref} and Q_{ref} as:

$$\begin{aligned} S &= P_{ref} + jQ_{ref} = vi^* \\ &= (v_r + jv_i)(i_r - ji_i) = v_r i_r + v_i i_i + j(v_i i_r - v_r i_i) \end{aligned} \quad (3.5)$$

Hence, the real and imaginary current components i_r and i_i can be defined as:

$$\begin{aligned} i_r &= \frac{P_{ref}}{v_r} - \frac{v_i}{v_r^2 + v_i^2} (v_i P_{ref} - Q_{ref}) \\ i_i &= \frac{v_r}{v_r^2 + v_i^2} (v_i P_{ref} - Q_{ref}) \end{aligned} \quad (3.6)$$

Finally, the direct and quadrature current components i_d and i_q can be expressed as:

$$\begin{aligned} i_d &= i_r \cos(\Phi) + i_i \sin(\Phi) \\ i_q &= -i_r \sin(\Phi) + i_i \cos(\Phi) \end{aligned} \quad (3.7)$$

The angle Φ is measured in PowerFactory by a phase-locked loop (corresponding to the “PLL” block in Figure 3.6).

Power profile

Four static generators were used to represent four wave energy devices (or four array of devices) outputting a simplified fluctuating power output consisting of an average power P_{avg} and of three sinusoidal terms. The power profile $P(t)$ can be expressed as follows:

$$P(t) = P_{avg} + B \left[A_1 \sin \left(\frac{2\pi t}{T_{w1}} + \alpha_w \right) + A_2 \sin \left(\frac{2\pi t}{T_{w2}} + \alpha_w \right) + A_3 \sin \left(\frac{2\pi t}{T_{w3}} + \alpha_w \right) \right] \quad (3.8)$$

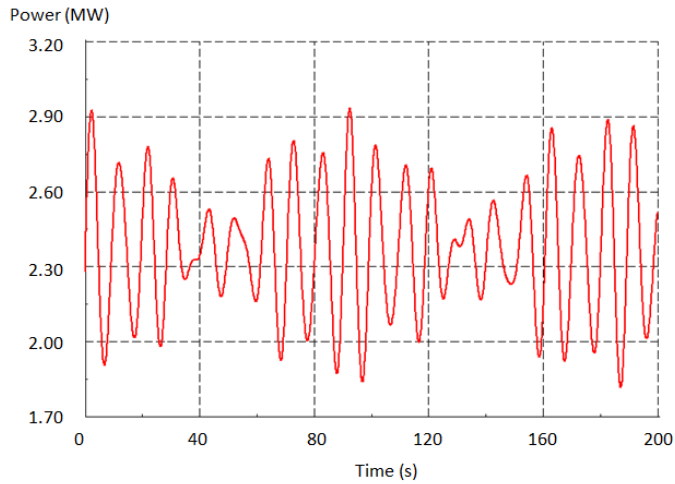


Figure 3.7: Individual power profile of a generator ($P_{avg}=2.5$ MW and $B=100\%$)

where B is a percentage ranging between 0% and 100%, constants A_i are the amplitudes of the power fluctuations, T_{w_i} are their periods, t is the time and α_w is a random phase shift intended to simulate the effect of devices aggregation on the farm power output (more details on the aggregation method are given in Section 3.2.3). The values of these parameters are described in Table 3.5 and an oscillogram of the resulting power profile for $P_{avg}=2.5$ MW, $B=100\%$ and $\alpha_w=0^\circ$ is shown in Figure 3.7. This corresponds to a total average active power equal to 10 MW, to which three sinusoidal terms, which represent the power fluctuations induced by the waves, are added. The power fluctuations of greatest amplitude are expected to range between 1.5 s and 10 s, considering that a wave device generates electrical power ideally twice per wave cycle and that the wave period of interest from a electricity generation perspective ranges between 3 s and 20 s. The periods of the three sinusoidal terms included in (3.8) were selected arbitrarily from this period range: periods T_1 , T_2 and T_3 are equal to 10 s, 7 s and 9 s respectively. The relatively low amplitudes, also chosen arbitrarily, for these sinusoidal terms contribute to create a power profile representative of a wave farm in which a significant amount of storage is available and/or consisting of a sufficiently large number of devices.

Parameter	Value or range
P_{avg}	0 MW-5 MW
B	0%-100%
A_1	0.3 MW
A_2	0.1 MW
A_3	0.2 MW
T_{w_1}	10 s
T_{w_2}	7 s
T_{w_3}	9 s

Table 3.5: Parameters used to define the electrical power profile

3.2.3 Aggregation of devices

The smoothing effect on the farm power output due to the aggregation of several wave energy devices was investigated. This was modelled by using different values of the phase shift α_w , which is included in (3.8), for each of the static generators. These phase shifts were generated randomly between 0° and 360° using the Matlab function “rand” which

creates uniformly distributed pseudo-random numbers. The script used to generate a single phase shift α_w is:

$$\alpha_{w_i} = rand \times 360^\circ \quad (3.9)$$

In order to study the sensitivity of the results with respect to the phase shift values, ten different phase shift sets, whose values are shown in Table 3.6, were created. A reference set for which all phase shifts are set to zero, which is referred to as “ref” in the table, was also created to enable the comparison between the cases benefiting and those not benefiting from the aggregation effect.

Set	Generator 1	Generator 2	Generator 3	Generator 4
1	0	42.3	106.8	114.8
2	0	152.7	182.8	30.8
3	0	94.5	288.4	10.5
4	0	334.4	262.9	175.9
5	0	208.3	85.4	165.2
6	0	346.7	196.9	187.6
7	0	83.4	176.0	224.7
8	0	244.5	142.4	132.3
9	0	355.7	13.6	318.7
10	0	328.8	286.6	35.5
ref	0	0	0	0

Table 3.6: Phase shift α_w ($^\circ$) for the 11 sets used in the study

3.3 Grid code requirements

The compliance of the idealised wave farm with respect to the grid code requirements of the Irish distribution operator, ESB, was assessed [35]. Given that no requirement has been issued for marine energy converters as yet in Ireland, as it is also the case in many other countries, the compliance was assessed based on the requirements applied to wind farms. This seems relevant due to the similarities between these two types of power plants, both in terms of power fluctuations and generator type. The grid compliance of the wave farm with respect to the maximum amplitude of the voltage variations, to the voltage limits and to the flicker level were investigated, as well as additional aspects.

3.3.1 Maximum amplitude of the voltage variations

Rapid voltage variations may deteriorate the local power quality as well as introduce a certain degree of instability in a power system which justifies the enforcement of limits regarding their amplitude. The rapid voltage variations potentially generated by a wave farm, including the voltage step due to a loss of connection, were analysed and compared to the limits defined by the Irish grid operator.

This grid operator indicates that generators must be able to remain connected up to a voltage step of 10%. In addition, the distribution code mentions also that “*the Distribution System [...] shall be designed to enable normal operating frequency and voltages supplied to customers to comply with European Standard EN 50160:1995*”. The limit recommended in this standard [77] in terms of rapid voltage variations is equal to 4% under normal

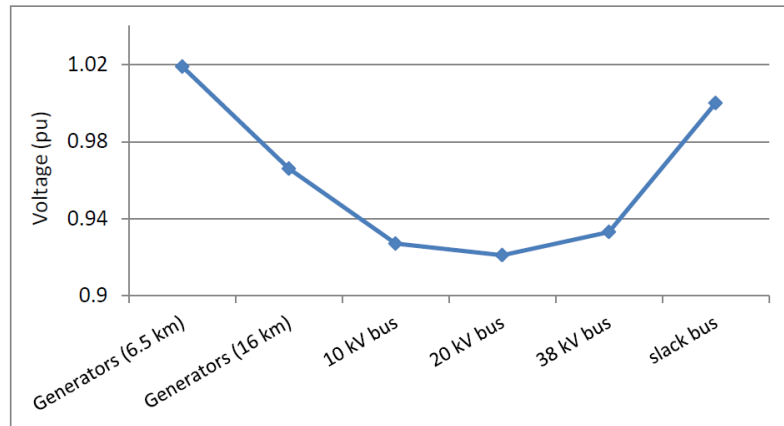


Figure 3.8: Voltage profile between the generators and the slack bus

conditions. This standard indicates also that a maximum voltage variation up to 6% can be tolerated under “certain circumstances”.

3.3.2 Voltage limits

The upper voltage limit at the point of common coupling is equal to 1.11 pu whereas the lower limit depends on operating conditions. Considering the typical voltage range defined in EN 50160 which is equal to $\pm 10\%$, a lower limit equal to 0.90 pu was arbitrarily chosen for assessing the grid compliance of the farm with respect to voltage limits.

3.3.3 Flicker

The Irish grid operator requires that the contribution of a wave farm in terms of flicker level is less than 0.35. This represents the lowest limit a grid operator can enforce [58].

3.4 Results

3.4.1 Load flow results

A static load flow study was conducted for a farm power output equal to 10 MW, the initial expected rated power of the wave farm.

Voltage profile

Due to the injection of active power, the voltage increases at the busses located close the farm. It decreases then to reach its lowest value at the 20 kV bus where the substation is connected, which is emphasised by the action of the VAR compensator at the PCC. The voltage at all nodes in both the offshore and onshore networks is maintained within a $[-8\%; +2\%]$ range, which seems reasonable for operating all the different pieces of electrical equipment under normal conditions.

Power losses

Losses represent 8% of the active power generated by the farm, which is significant. The submarine cables account for 86% of these losses, while the overhead line accounts for the remaining 14%, as shown in Figure 3.9. This predominance of the losses in the cables was expected given their high resistance (equal to 1.6Ω for the 6.5 km cables and to 4.0Ω for the 16 km cables) compared to the resistance of the overhead line (equal to 0.45Ω only).

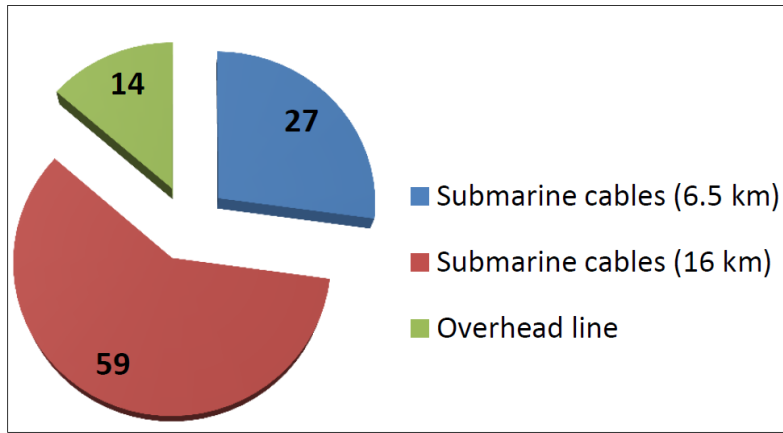


Figure 3.9: Distribution of the power losses over the different pieces of electrical equipment

Voltage variations

Two types of voltage variations potentially generated by a wave farm were investigated: those generated by its fluctuating power output, and referred to as rapid voltage fluctuations, and the voltage step induced by the sudden disconnection of one or more generation units.

- Rapid voltage fluctuations

For the purpose of this study, a wave farm including little to no means of storage was envisaged. This means that its minimum power output was assumed to be equal to zero. Hence, the maximum voltage fluctuation it may output is defined as the absolute value of the voltage difference between the case where it generates its maximum power and the case where its power output is equal to zero as:

$$\Delta V = |V(P_{max}) - V(0)| \quad (3.10)$$

It must be observed that the amplitude of a voltage fluctuation induced by a power fluctuation depends on the short-circuit circuit level S_{sc} and of the impedance angle Ψ_k of the node to which the wave farm is connected. Hence, as the maximum voltage fluctuation is analysed for an increasing rated power of the farm at Belmullet, it seems judicious to study this variation as a function of the farm's short-circuit ratio which is defined as the ratio of the short-circuit level S_{sc} to the farm's apparent rated power S_n as:

$$\text{short-circuit ratio} = \frac{S_{sc}}{S_n} \quad (3.11)$$

Considering that the wave devices are operated at unity power factor, the apparent rated power is equal to the rated active power. The results presented in Figure 3.10 show that this voltage difference increases as a function of the power capacity, although a slight decrease is observed around a short-circuit ratio equal to 30, which corresponds to a farm's active power equal to 2 MW. This can be explained by a reversal in the active power direction between the voltage source and the 38 kV bus to which a 2 MW load is connected: once the farm power capacity reaches this value and covers the load's consumption entirely, the voltage source is no longer needed to supply active power but rather to absorb it.

It appears that the maximum amplitude of a voltage fluctuation may exceed 4% for a short-circuit ratio less than 11. Exceeding the 10% limit above which generators are no longer required to remain connected is also exceeded for a short-circuit ratio less than 4,

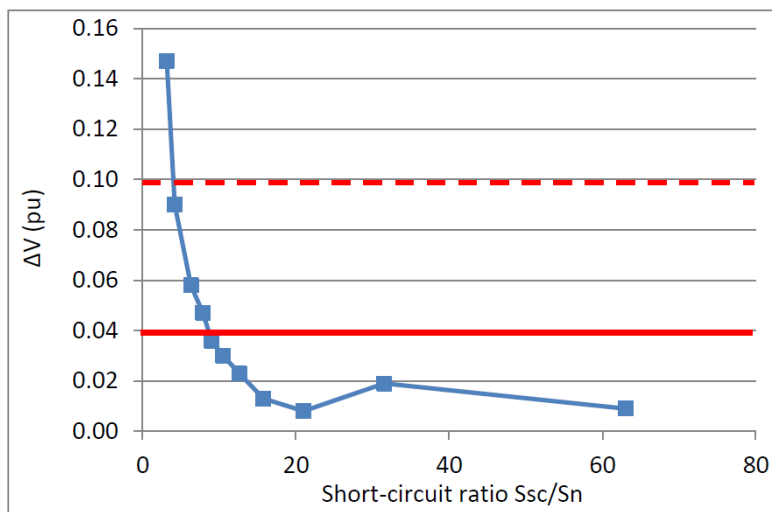


Figure 3.10: Maximum voltage difference induced at the PCC as a function of the farm's short-circuit ratio

although it is not sure whether this type of voltage fluctuation can actually be considered as a voltage step. Hence, the connection of a wave farm operated under the conditions described in the study may induce a significant deterioration of the power quality, and may as well introduce a certain level of risk concerning the stability of the local network for wave farms whose short-circuit ratio is less than 4.

– Voltage step

The disconnection of one or more generators (or array of generators) was simulated by disconnecting the submarine cables which connect them to the onshore substation. Given that one of the most probable causes of generation unit loss is the occurrence of a short-circuit with one or more of the cables, this simulation scenario reproduces the grid operator's reaction. Figure 3.11 shows that the amplitude of the voltage step induced by the sudden disconnection of one or more generators is always smaller than 10% for the 10 MW farm. The entire loss of the farm does not thus pose any stability issue in this case. This, however, may prove to be a problem for a wave farm of higher power capacity as it is the case for a 20 MW farm if two or more generation units are lost.

Voltage limits

The application of the 0.93 lagging power factor at the PCC makes the voltage decrease as a function of the farm power output. This trend is similar to what may be observed in a two-bus system for which the voltage variation ΔV_{2bus} at one bus compared to the voltage V at the other can be approximately defined as:

$$\Delta V_{2bus} = \frac{PR + QX}{V} \quad (3.12)$$

This equation means that, in the case considered in this work where the reactive power Q flowing from the PCC to the ac voltage source is defined based on the power factor pf as:

$$Q = -P\sqrt{\frac{1}{pf^2} - 1} \quad (3.13)$$

the voltage fluctuation ΔV may become negative for a sufficiently great active power P . In the case where the reactance X is particularly high between the two busses, which is also

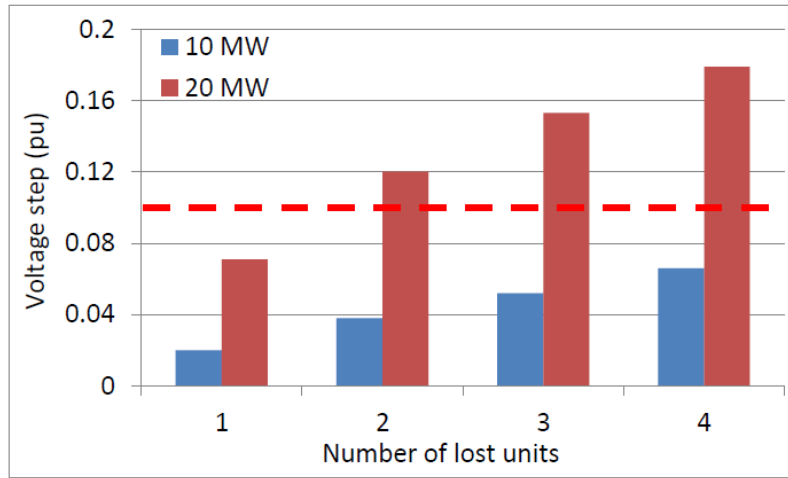


Figure 3.11: Voltage step induced at the PCC as a function of the number of lost units for two farm average power values

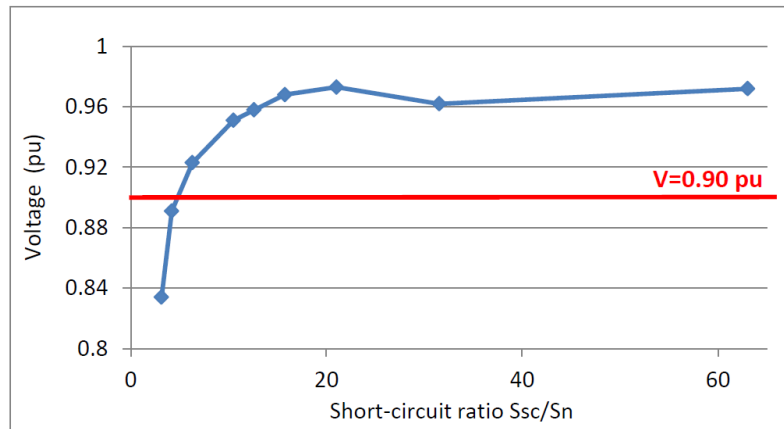


Figure 3.12: Minimum voltage at the PCC as a function of the farm's short-circuit ratio

the case here (the Thevenin reactance X_S is equal to 21.4Ω), negative voltage fluctuations ΔV_{2bus} are induced by active power peaks of any amplitude, which is in good agreement with what is observed in this work.

Hence, the maximum voltage is obtained when the farm outputs no power and is equal to 0.981 pu, thus remaining well within the $[-10\%;+11\%]$ range defined by the grid operator. Figure 3.12 shows on the contrary that the minimum voltage may be less than the lower limit from a short-circuit ratio less than 4 if the power factor at the PCC is not suitably modified.

3.4.2 Quasi-steady simulations

Quasi-steady simulations were performed based on the electrical power profile described in Section 3.2.2. The average power P_{avg} of each of the four generators is set to 2.5 MW which corresponds to a total active power of 10 MW. This power level corresponds to a short-circuit ratio of 6.3.

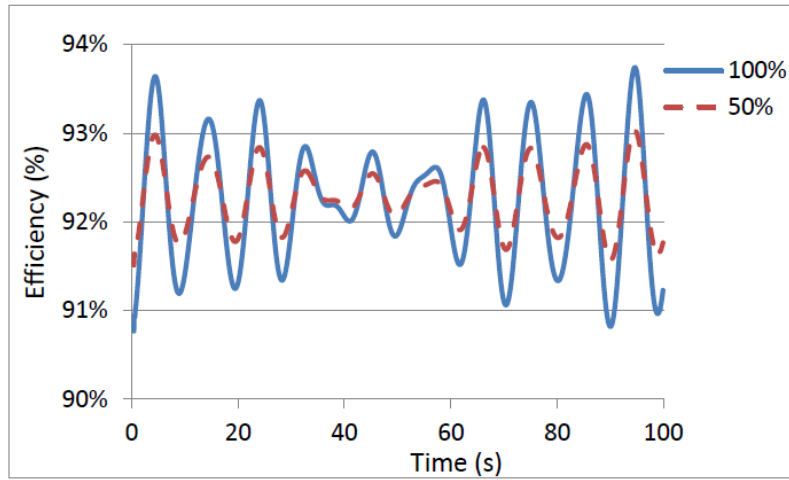


Figure 3.13: Profile of the efficiency of the farm's electrical network for two values of factor B

Efficiency of the network

The efficiency ζ of the farm's network going from the generators up to the point of common coupling was calculated as:

$$\zeta(t) = 1 - \frac{P_G(t) - P'_L(t) - P_{PCC}(t)}{P_G(t)} \quad (3.14)$$

where $P_G(t)$ is the sum of the generators' individual power output at time t , $P'_L(t)$ is the instantaneous consumption of the substation and $P_{PCC}(t)$ is the power received at the PCC. The efficiency profile is shown in Figure 3.13. It can be observed that the efficiency fluctuates around an average value equal to 92%, corresponding to the 8% power losses found in section 3.4.1. The deviation of the efficiency $\zeta(t)$ from its average value is significant, ranging between 89% and 94% when the power fluctuation amplitude is maximal ($B=100\%$). This deviation amplitude decreases as a function of the power fluctuation amplitude, as illustrated by the case where $B=50\%$ in Figure 3.13.

Flicker

The flicker level generated at the PCC by each of the 11 phase shift sets was investigated. The flickermeter used for this study is described in more detail in Chapter 4 along with its compliance tests as well as with additional tests performed with experimental data. Figure 3.14 shows that Pst is relatively variable depending on the phase shift set considered. It must also be noted that flicker may be relatively close to the maximum allowed level enforced by the Irish grid operator and equal to 0.35. However, it remains below this limit for all of the phase shift sets considered. It may be argued that this may no longer be the case though for wave farms with a greater rated power, although increasing this parameter tend also to render the farm power profile smoother. However, this aspect was not considered as it appears that no solution to the load flow problem exists when the farm's average power is greater than or equal to 20.7 MW. Increasing the maximum power which the farm may inject in the relatively weak grid to which it is connected generates incompatible initial load flow conditions. This was observed with PowerFactory and is demonstrated analytically in the next paragraphs by means of a simplified network model.

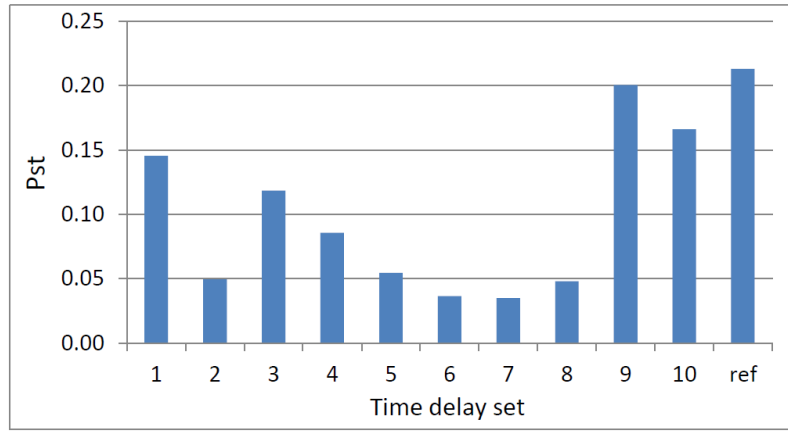


Figure 3.14: Flicker level at the PCC corresponding to the different phase shift sets

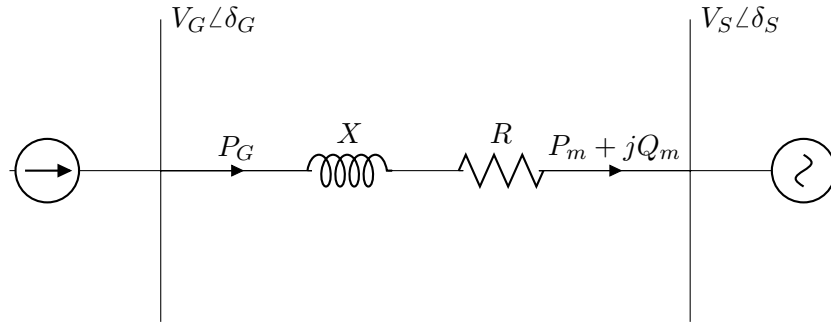


Figure 3.15: Simplified two-bus network

This absence of load flow solution can be explained by means of a simple network representing approximately the network considered in this study in which the loads as well as the VAr compensator are not included for the sake of simplicity. Hence, this network can be represented as a two-bus system as illustrated in Figure 3.15.

The voltage \bar{V}_G corresponds to the voltage at the terminals of the offshore generators, and the resistance R and the reactance X are the equivalent impedances of the network. Hence, the voltage \bar{V}_S of the ac voltage source can be expressed as:

$$\begin{aligned}\bar{V}_S &= \bar{V}_G - j\bar{I}X \\ &= \bar{V}_G - j\left(\frac{\bar{S}_m}{\sqrt{3}\bar{V}_S}\right)^* X\end{aligned}\quad (3.15)$$

thus neglecting the magnetising losses in the transformer. Hence:

$$V_S^2 = V_s^* \bar{V}_G - jX \frac{\bar{S}_m^*}{\sqrt{3}} \quad (3.16)$$

Considering that $\bar{V}_S = V_x + jV_y$ and $\bar{V}_G = V_G$, the previous equation can be rewritten as:

$$\begin{aligned}V_S^2 &= V_x^2 + V_y^2 = (V_x - jV_y)V_G - jX \frac{(P_m - jQ_m)}{\sqrt{3}} \\ &= V_x V_G - jV_y V_G - jX \frac{P_m}{\sqrt{3}} - X \frac{Q_m}{\sqrt{3}}\end{aligned}\quad (3.17)$$

Regrouping the real and imaginary terms together gives the two following equations:

$$\begin{cases} V_x^2 + V_y^2 = V_x V_G - X \frac{Q_m}{\sqrt{3}} \\ V_y V_G = -X \frac{P_m}{\sqrt{3}} \end{cases} \quad (3.18)$$

$$\begin{cases} V_x^2 - V_x V_G + V_y^2 + X \frac{Q_m}{\sqrt{3}} = 0 \\ V_y = -\frac{X P_m}{\sqrt{3} V_G} \end{cases} \quad (3.19)$$

This leads to:

$$V_x^2 - V_G V_x + \left(\frac{X P_m}{\sqrt{3} V_G} \right)^2 + X \frac{Q_m}{\sqrt{3}} = 0 \quad (3.20)$$

The solutions of this second order polynomial in V_x can be expressed as:

$$V_x = \frac{V_G \pm \sqrt{V_G^2 - 4 \left[\left(\frac{X P_m}{\sqrt{3} V_G} \right)^2 + X \frac{Q_m}{\sqrt{3}} \right]}}{2} \quad (3.21)$$

In order to obtain a valid solution for the real voltage term V_x , the following condition must be satisfied:

$$V_G^2 \geq 4 \left[\left(\frac{X P_m}{\sqrt{3} V_G} \right)^2 + X \frac{Q_m}{\sqrt{3}} \right] \quad (3.22)$$

$$\frac{V_G^2}{4} \geq \left(\frac{X P_m}{\sqrt{3} V_G} \right)^2 + X \frac{Q_m}{\sqrt{3}} \quad (3.23)$$

$$X \frac{Q_m}{\sqrt{3}} \leq \frac{V_G^2}{4} - \left(\frac{X P_m}{\sqrt{3} V_G} \right)^2 \quad (3.24)$$

$$Q_m \leq \frac{\sqrt{3} V_G^2}{4X} - \frac{X}{\sqrt{3}} \left(\frac{P_m}{V_G} \right)^2 = Q_{max} \quad (3.25)$$

This equation means that the reactive power consumption Q_m of the electrical network must be less than a defined limit Q_{max} for a valid load flow solution to exist. Assuming that the voltage $V_G \approx 1.0$ pu, this reactive power consumption is calculated approximately as:

$$\begin{aligned} Q_m &= 3XI^2 = 3X \left(\frac{P_G}{\sqrt{3} V_G} \right)^2 \\ &= 3 \times 41.0 \left(\frac{P_G}{\sqrt{3} \cdot 1.0 \times 38 \times 10^3} \right)^2 \end{aligned} \quad (3.26)$$

Figure 3.16 shows both the reactive power consumption Q_m and the maximum limit Q_{max} . It appears clearly from this figure the condition $Q_m \ll Q_{max}$ is no longer satisfied when the farm's active power P_G is approximately greater than 15 MW. This means that no valid load flow solution exists above this power level. This is in a relatively good agreement with what is observed with PowerFactory, where no load flow can be calculated from an active power P_G equal to 20.7 MW.

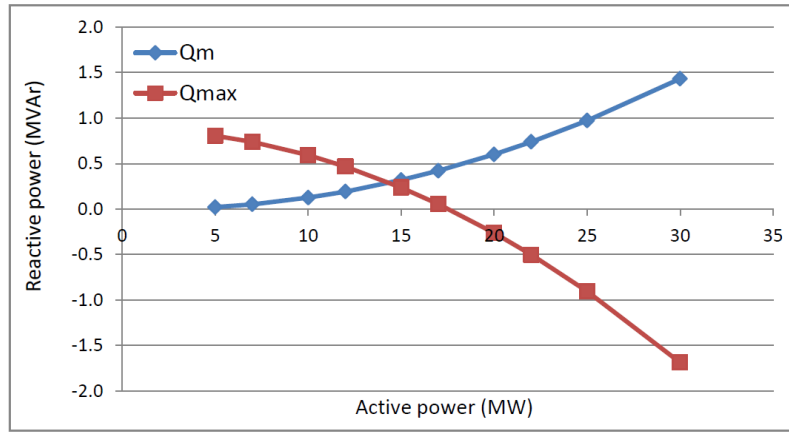


Figure 3.16: Reactive power consumption of the network Q_m and maximum limit Q_{max} as a function of the farm’s active power P_G

3.5 Conclusions

This chapter presents a simplified analytical case study conducted in the early stages of this thesis. It investigates the grid compliance of an idealised 10 MW farm with respect to the voltage limits, the maximum amplitude of the voltage variations and the flicker level requirements as defined by the Irish distribution system operator, ESB. Additional aspects such as power losses, and the voltage profile are also presented.

It was demonstrated that the 10 MW farm is not compliant with respect to the maximum amplitude of the voltage variations, as a voltage difference exceeding 4% may be induced by the power fluctuations generated by the wave farm. The requirements in terms of voltage limits as well as in terms of flicker level were on the contrary met, although both these limits may be exceeded for a farm of a slightly greater rated power. The loss of the entire farm proved not to represent a stability issue in terms of voltage step, although, in similar fashion to the voltage limits and flicker level, this may no longer be proved true for farms of higher rated power. Further studies on the grid compliance of a wave farm were conducted and are presented in Chapters 4 and 6. In these latter studies, the electrical power profile of each of the generators included in the model was modelled based on experimental time series.

The overall efficiency of the network up to the PCC was shown to be equal to 92% on average with significant deviation when the fluctuating power profile of the farm is taken into account. Hence, power losses fluctuate around 8% which is relatively significant. More detailed studies on power and energy losses based on the experimental time series mentioned in the previous paragraph were conducted and are presented in Chapter 5.

The wave farm compliance was assessed based on the grid code requirements defined by the Irish grid operator. It may interesting however to reflect on the relevance of these requirements, and in particular on these regarding the power factor, the amplitude of the voltage variations and the flicker level. Applying a lagging power factor is intended to mitigate the voltage rise induced by the power flow reversal, itself created by the connection of a power plant to the distribution network. However, this may on the contrary induce greater voltage variations if the farm is connected to a sufficiently reactive network, as it is the case in this study. Hence, the selection of the power factor to be applied at the PCC should be based on different criteria than those currently used by the grid operator.

Otherwise, this may hinder the grid integration of renewable power plants to be connected at the distribution level. This aspect is discussed in more detail in Chapters 4 and 6.

Another point which should be discussed regards voltage variations as induced by the power fluctuations of a wave farm. They may be extremely rapid compared to the power fluctuations either generated or absorbed by more conventional power plants or loads respectively. Hence, it would be interesting to define whether wave farm power fluctuations should be qualified as rapid voltage fluctuations or as voltage steps, with all the consequences this may have on the assessment of the farms' compliance with current grid code requirements. Determining the impact these fluctuations have on generator stability may help getting rid of this ambiguity.

Finally, it may be interesting to reconsider the flicker limit as imposed by the Irish grid operator. This operator enforces currently the most stringent limit recommended by IEC standard 61000-3-7 in terms of flicker level, while other grid operators enforce more permissive limits as described in Chapter 4. In addition, although this very stringent limit is applied for the individual contribution of a wave farm, no limit is specified regarding the total flicker level not to be exceeded at a given connection point. However, using a limit in terms of total flicker level, in complement to the individual limit, may help maximise the power capacity that can be connected to a given point. For instance, in locations where a low background flicker level is present before the connection of a wave farm, the flicker level limit assigned for the farm may be increased accordingly. In conclusion, it is possible that the excessive requirements of the Irish grid operator on that matter may hinder the large-scale development of the ocean energy industry in Ireland.

Chapter 4

Grid impact of a medium size wave farm

4.1 Introduction

As mentioned in the state-of-the-art, it is difficult to draw general conclusions from the limited number of existing studies on the grid impact of a wave farm as they present numerous differences. Hence, a comprehensive grid impact analysis regarding a 20 MW wave farm was conducted. The results are presented in this chapter.

4.2 Modelling

4.2.1 Modelling of the electrical network

Figure 4.1 shows a schematic overview of the grid model used for this study. It is based on the concept design of the Atlantic Marine Energy Test Site (AMETS) off Belmullet, Ireland [70] which was presented in Chapter 3. As this test site presents design characteristics common to current and planned test sites developed in the UK (WaveHub [78] and EMEC [79]) and in Spain (bimep [80]), it can be considered to represent a typical test site.

It includes the wave farm's network, the existing local network and the rest of the national/regional power system, modelled as a 38 kV voltage source in series with an impedance \bar{Z}_S . The simulations were performed for different short-circuit ratios and impedance angles Ψ_k . This is achieved by varying the values of the Thevenin resistance R_S and reactance X_S . The short-circuit level S_{SC} considered in this study ranges between 58 MVA and 14 GVA, which corresponds to an impedance Z_S ranging between 25Ω and 0.1Ω respectively.

Four impedance angles Ψ_k equal to 30° , 50° , 70° and 85° as specified in IEC standard 61400-21 were used. These impedance angles cover the entire range of typical values. For the sake of comparison, compliance tests with respect to power quality requirements were performed for five different test sites whose characteristics are shown in Table 4.1. Three additional, arbitrarily selected sites on the west coast of Ireland were also investigated in order to provide a more comprehensive overview of the power quality impact all over the island. The locations of all these sites are shown in Figure 4.2.

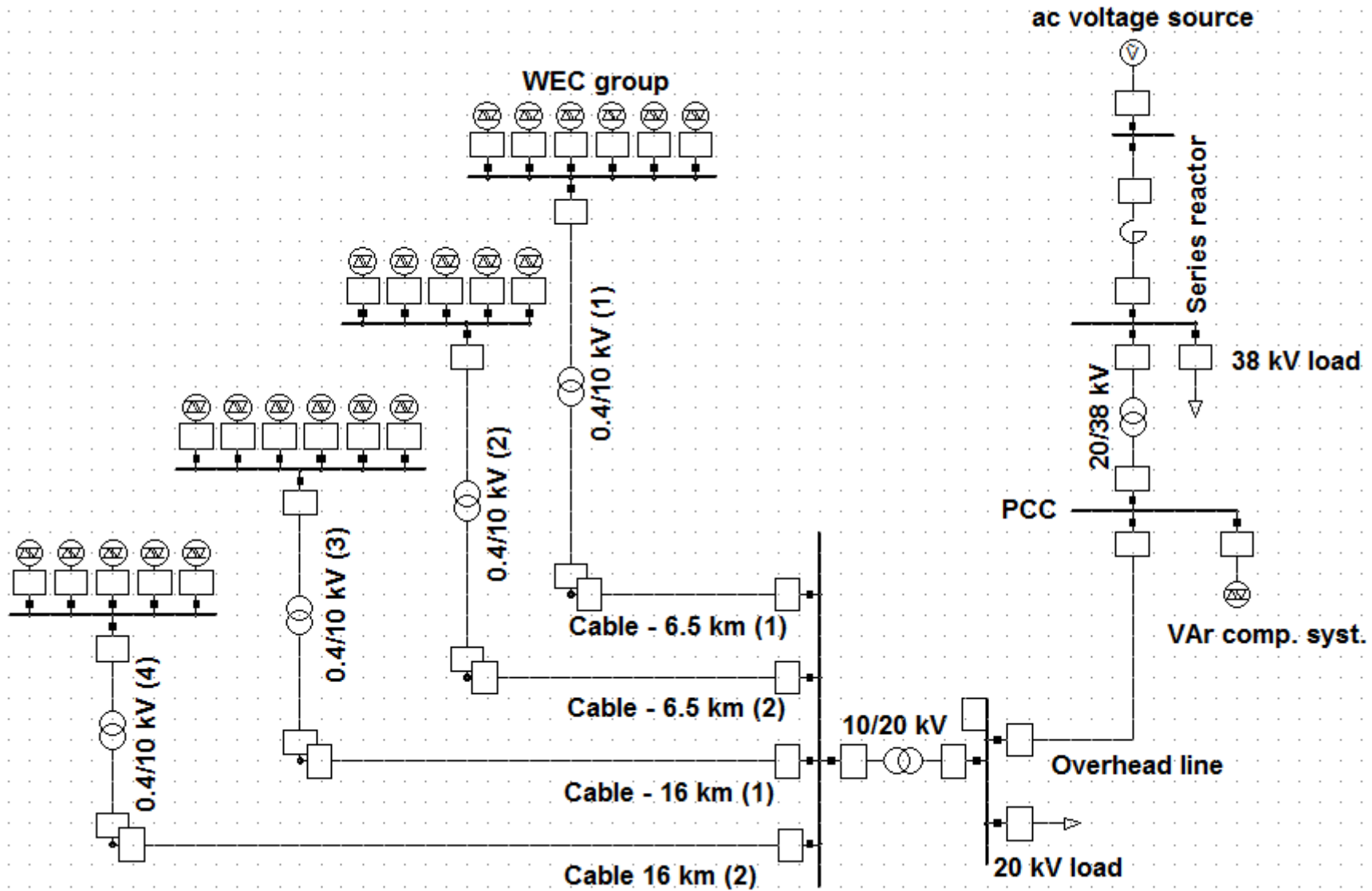


Figure 4.1: Schematic overview of the electrical network model



Figure 4.2: Location of the different potential sites. 1-Belmullet, 2-Achill Island, 3-Grallagh, 4-Killard, 5-Dingle, 6-Doory

Both the Sustainable Energy Authority of Ireland (SEAI) [70] and the WestWave consortium [81] envisage the connection of a wave farm at Belmullet for their respective projects. Achill Island and Killard are two other potential locations which are investigated by the latter. Killard, located relatively close to a large coal-fired power plant as well as to a 400 kV connection point, presents a higher short-circuit level and impedance angle than any of the other Irish sites, whose low short-circuit levels are typical of the sparsely populated, rural areas of the north-west of Ireland. The WaveHub is a test site currently in operation in Cornwall, UK, which is awaiting the installation of its first devices. It is also located at a small distance from a 400 kV connection point, which justifies its high short-circuit level. The Spanish Biscay Marine Energy Platform (bimep) presents the strongest grid both in terms of short-circuit level and impedance angle and will be located off the Basque country. All of these test sites are currently designed or planned to be operated for a maximum power capacity of 20 MW.

In addition to these official test sites, three additional sites off the Irish western coast which present also high wave energy resources were investigated as mentioned earlier. These potential sites are located off Grallagh, close to Clifden, County Galway, off Doory and off Dingle, both in County Kerry. It must be noted that, due to similarities in terms of power system architecture and of typical short-circuit levels between the rural areas of Ireland and of Scotland, the results obtained for Belmullet, Achill Island, Grallagh and Doory are expected to be relatively similar to those of potential sites located in this latter region. This parallel is interesting to establish as these two regions present the highest wave energy potential in Europe.

It must be noted that, with the exception of the bimep test site whose characteristics were provided by courtesy of the Basque Energy Agency, Ente Vasco de la Energia, the short-circuit level and impedance angle at the other sites are estimated. This estimation is based on the short-circuit level $S_{SC_{110}}$ and impedance angle at the closest 110 kV (for the Irish test sites) or 400 kV (for the WaveHub) connection point, as provided by their respective grid operators [36, 37]. However, the test sites are connected at distribution level, either at 38 kV in the case of the Irish test sites, or at the 33 kV level in the case of

Test site	Country	S_{SC} (MVA)	S_{SC}/S_{farm}	Ψ_k ($^\circ$)
Achill Island	Ireland	57	2.9	67
Belmullet	Ireland	63	3.2	69
Grallagh	Ireland	85	4.4	68
Doory	Ireland	97	5.0	73
Killard	Ireland	160	8.2	81
Dingle	Ireland	191	9.8	80
WaveHub	UK	626	32.3	78
bimep	Spain	4500	232.0	90

Table 4.1: Short-circuit characteristics at the terminals of the different potential test sites

the WaveHub. Hence, the short-circuit level at the distribution level node must take into account the impedance between this node and the transmission level node. This impedance is assumed to consist mainly of the impedance \bar{Z}_T of one or more transformers and of the impedance \bar{Z}_L of one or more overhead lines. The impedances at the WaveHub and bimep terminals are converted into equivalent impedances at 38 kV, which corresponds to the voltage level used in the network model. In the case of the Irish test sites, the equivalent impedance \bar{Z}_S is thus calculated as:

$$\begin{aligned}\bar{Z}_S &= \bar{Z}_{SC_{110}} \left(\frac{38 \cdot 10^3}{110 \cdot 10^3} \right)^2 + \bar{Z}_T + \bar{Z}_L \\ &= \frac{110 \cdot 10^3}{\sqrt{3} \bar{I}_{SC_{110}}} \left(\frac{38 \cdot 10^3}{110 \cdot 10^3} \right)^2 + \bar{Z}_T + \bar{Z}_L\end{aligned}\quad (4.1)$$

where $\bar{I}_{SC_{110}}$ is the short-circuit current at the 110 kV level. The transformers impedance for both the Irish test sites and the WaveHub is estimated from data available from grid operators and from typical values, as is the per kilometer impedance of overhead lines [72–76].

The impedance of the overhead lines connecting the different test sites is calculated from the product of this per kilometer impedance by the length of each overhead line. In the case of the Irish test sites, the length of the different overhead lines connecting the 110 kV node to the 38 kV node is estimated based on the 38 kV network map shown in Figure 3.4b.

In the case of the WaveHub, information at the closest 400 kV connection point only was available. This connection point, which is named “Indian Queens”, is shown in Figure 4.3. A 132 kV overhead line whose length is estimated at 46 km connects this node to the town of Hayle, where the voltage is stepped down to 33 kV. The equivalent impedance \bar{Z}_S for the WaveHub can thus be expressed as:

$$\begin{aligned}\bar{Z}_S &= \bar{Z}_{SC_{400}} \left(\frac{38}{400} \right)^2 + \bar{Z}_{T_{132/400}} \left(\frac{38}{132} \right)^2 + \bar{Z}_L \left(\frac{38}{132} \right)^2 + \bar{Z}_{T_{33/132}} \left(\frac{38}{33} \right)^2 \\ &= \frac{400}{\sqrt{3} \bar{I}_{SC_{400}}} \left(\frac{38}{400} \right)^2 + \bar{Z}_{T_{132/400}} \left(\frac{38}{132} \right)^2 + \bar{Z}_L \left(\frac{38}{132} \right)^2 + \bar{Z}_{T_{33/132}} \left(\frac{38}{33} \right)^2\end{aligned}\quad (4.2)$$

where $\bar{I}_{SC_{400}}$ is the short-circuit level at the 400 kV level, $\bar{Z}_{T_{132/400}}$ is the impedance of the 132/400 kV transformer expressed at the 132 kV level, \bar{Z}_L is the impedance of the 132 kV overhead line and $\bar{Z}_{T_{33/132}}$ is the impedance of the 33/132 kV transformer expressed at the 33 kV level.



Figure 4.3: Southern part of the British 400 kV transmission system

The power factor applied at the point of common coupling (PCC) is equal to unity in the base case, according to typical grid operators’ requirements. Simulations were also performed for different power factors to study the influence of this parameter on voltage and flicker level.

4.2.2 Discussion on the modelling method

The method described in the previous section to estimate approximately both the equivalent short-circuit level S_{SC} and the equivalent impedance angle Ψ_k at the high voltage side of the 20/38 kV transformer does not take into account the consumption of the loads between this node and the 110 kV (or 400 kV) connection point, as this data is usually unavailable. This leads however to a negligible underestimation of both the impedance angle Ψ_k and of the short-circuit level S_{SC} for both the UK and Irish test sites, as demonstrated in Appendix A.

4.2.3 Summary

In summary, this model is intended to represent a typical wave farm connected to nodes presenting a typical range of short-circuit ratios and impedance angles Ψ_k .

4.2.4 Modelling of the wave farm power output

Experimental data

Experimental data in the form of electrical power output time series were provided as an outcome of the project CORES, standing for “Components for Ocean Renewable Energy Systems”. This FP7 European collaborative research project focused on the development of new concepts and components for power-take-off, control, moorings, risers, data acquisition and instrumentation for floating wave devices [82]. The project itself was based on a floating OWC-type system and spanned over more than 3 years, between April 2008 and December 2011. The quarter-scale OWC prototype used in the project was deployed offshore from March to May 2011.

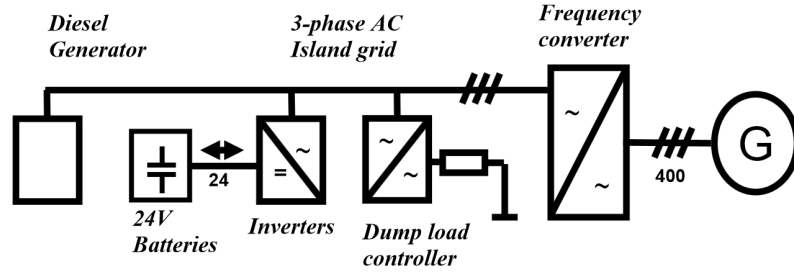
The device was connected to a small on-board island grid independent from the national electrical network. Figure 4.4a shows the on-board operating and monitoring system. The on-board grid was maintained by three fully-rated power electronic converters and the generated power was used to charge the on-board battery system, or dissipated in resistive load banks. A variable-frequency converter and a diesel generator were also included. Figure 4.4c shows the electrical system included in the prototype while Figure 4.4b shows the OWC deployed offshore.



(a) On-board operating and monitoring system



(b) Prototype deployed in Galway Bay, Ireland



(c) Electrical system of the prototype

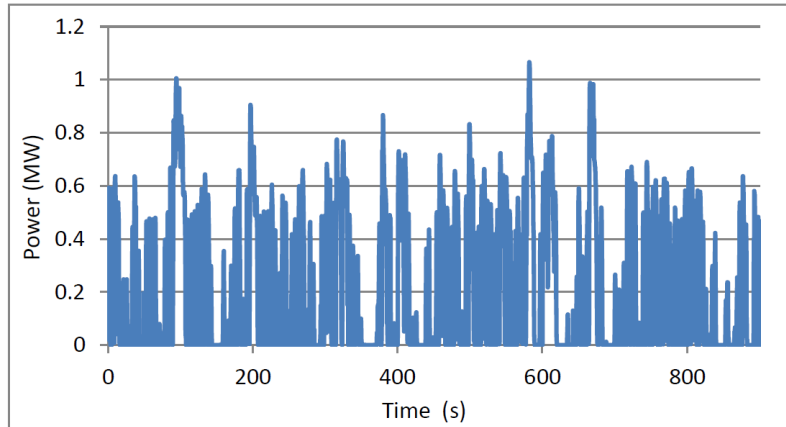
Figure 4.4: OWC quarter scale prototype used in project CORES

Production period	Full-scale H_s (m)	Full-scale T_z (s)	Energy level
A	5.0	8.4	high
B	2.1	5.6	medium
C	1.1	7.0	low

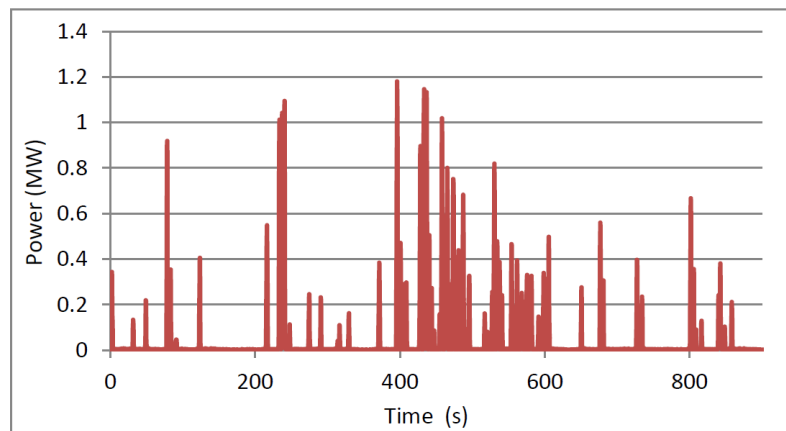
Table 4.2: Characteristics of the different production periods

The project has allowed the ocean energy research community to gain significant practical experience in the deployment, operation, maintenance of offshore ocean energy converters. It has also generated a considerable amount of time series data on a number of parameters, including electrical parameters at a high temporal resolution of 0.1 s. Contrary to most available data which is averaged over a sea-state, a season or even a year, the CORES electrical power time series data can be scaled and used directly for grid impact studies. Three time series, whose characteristics are shown in Table 4.2, were selected in order to represent high, medium and low energy sea-states, and are referred to as “production periods A, B and C” in the rest of this thesis. The scatter diagram of the Belmullet test site is shown in Figure 4.5.

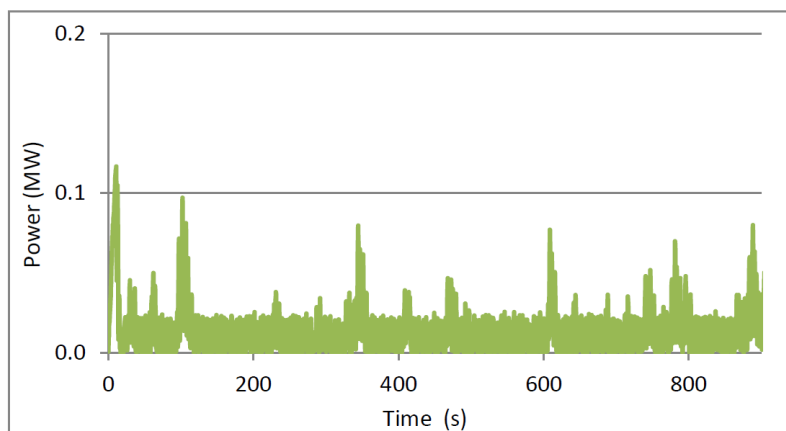
During these three production periods, the generator was operated in constant speed control mode which implies that, unlike in variable speed operation, inertial energy storage by means of speed control is not available. As a result, mechanical power peaks are converted directly into electrical power peaks, which is expected to represent a worst case from a power quality perspective. Figures 4.6a to 4.6c show the full-scale equivalent electrical power time series for each production period.



(a) Production period A



(b) Production period B



(c) Production period C

Figure 4.6: Individual power profiles for production periods A, B and C

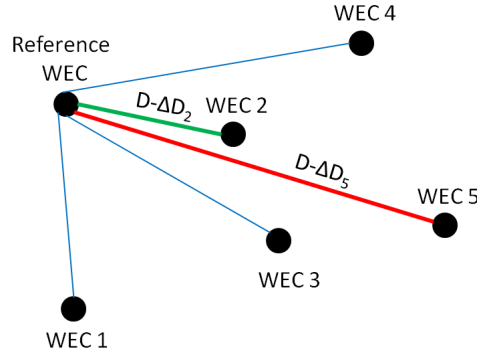


Figure 4.7: Schematic illustration of the time delay estimation method

$$v_g = \frac{gT_e}{4\pi} \quad (4.4)$$

As mentioned in Chapter 1, the use of the energy period T_e , as opposed to the more common parameters such as the peak period T_p or the zero-crossing period T_z , is justified as being more representative of the energy propagation speed between two WECs. Each time delay ΔT and ΔT_i is thus calculated as:

$$\Delta T = \frac{D}{v_g} = \frac{4\pi D}{gT_e} \quad \text{and} \quad \Delta T_i = \frac{\Delta D_i}{v_g} = \frac{4\pi \Delta D_i}{gT_e} \quad (4.5)$$

Half of the wave devices are to be located at 16 km from the shore while the remaining half will be placed at a closer distance of 6.5 km, as indicated in Chapter 3. Hence, it is necessary to take this difference in terms of distance into account by adding another time delay $\Delta T'$ to ΔT_{total} for the generators connected to the 6.5 km long cable as:

$$\Delta T_{total} = \Delta T - \Delta T_i + \Delta T' \quad (4.6)$$

If $\Delta T'$ were calculated in similar fashion to ΔT_{total} , that is based on the 10 km distance and on the typical wave group velocity v_g , it would be of the order of magnitude of thousands of seconds. However, the maximum duration of the experimental time series data provided as an outcome of the CORES project is much shorter. It was thus decided to set $\Delta T'$ to a value greater the time delay ΔT but reasonably small in order to perform sufficiently long power system simulations. This value was set arbitrarily to 110% of the time delay ΔT . This eliminates the possibility of two generators located 10 km apart outputting the same power profile.

As mentioned in Chapter 1, information on the energy period T_e for each of the production periods considered was supplied as part of the CORES project in the form of the mean zero-crossing period T_z to which T_e is proportional by a factor ranging between 0.71 and 0.83 with respect to the Belmullet test site [13]. An average value of 0.77 was selected for the studies. Five different time delay sets were used in order to model five different device layout combinations. The maximum and minimum voltage values retained for the study are defined as the maximum and minimum values obtained over these five simulations respectively. In similar fashion, the maximum flicker levels retained for the study are the maximum values obtained over these five simulations as well.



Figure 4.8: Wave power rose in western Europe [84]

Farm orientation compared to the dominant wave direction

Two different orientations of the farm with respect to the dominant wave direction were also simulated in order to determine the impact of this parameter on the quality of the farm power output. Although the wave direction is relatively constant throughout the year, it may vary widely over shorter periods of time that are yet long enough to give rise to power quality issues. This is illustrated by Figure 4.8 which presents the distribution of the wave power with respect to the dominant wave direction off western Europe.

The two orientations considered in this work constitutes a best and a worst case with respect to power quality. In the worst case, the wave front propagates perpendicularly to the alignment axis of the wave group, hitting all the WEC group laterally, as shown in Figure 4.9a. This orientation will thus be referred to as “lateral orientation” in the rest of this thesis. In this case, wave devices connected to the same cable generate the same power profile as it is the case for Generators A and C, while Generator B, connected to another cable has a different power profile. This is illustrated in Figures 4.10b, 4.10d and 4.10f. The power transported by a particular submarine cable is thus not smoothed as all the generators output the same power peak at the same time. As a result, power variations are expected to be higher in amplitude, and so are the voltage variations. However, generators connected to two different submarine cables show a power profile shifted by a defined time delay. Hence, the beneficial power smoothing effect expected from device aggregation is minimal here.

In the other case, considered as a best case from a power quality perspective, the wave front propagates in parallel to the alignment axis of the WEC group, as shown in Figure 4.9b. The corresponding orientation will be referred to as “frontal orientation”. In this case, all generators connected to the same submarine cable show a different power profile which is shifted by a different time delay. The power profile of generators connected to different submarine cables is similar though. For instance, Generators A and B present

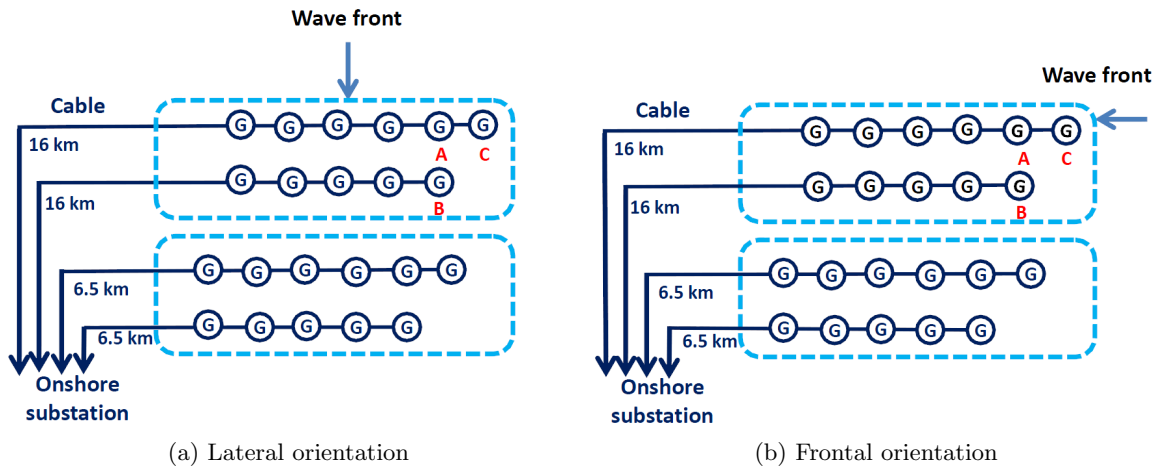


Figure 4.9: Schematic diagrams of the farm indicating the two orientations (compared to the dominant wave direction) considered in this work

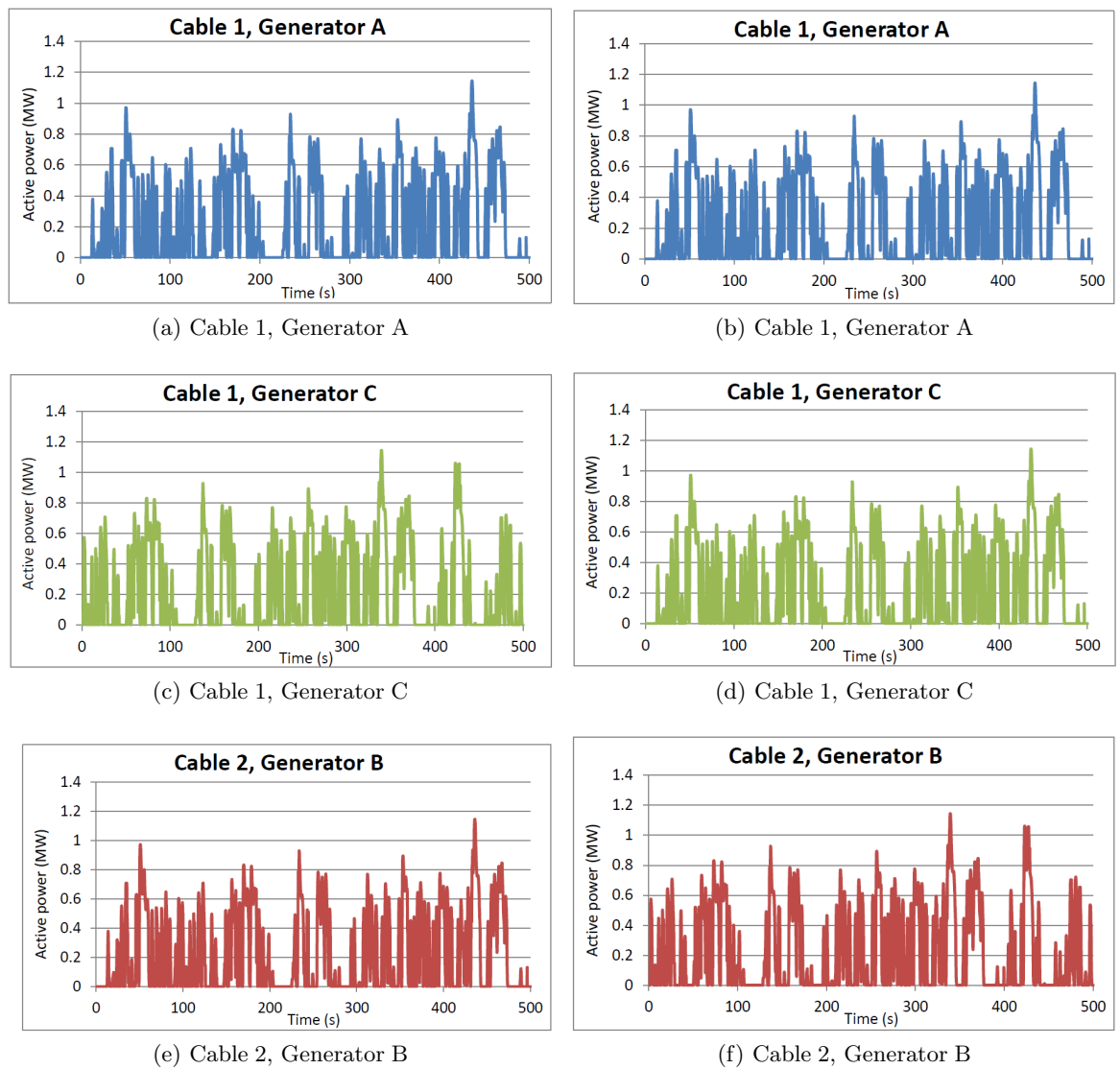


Figure 4.10: Individual power profiles of three generators indicated in Figures 4.9a and 4.9b for the frontal (left) and for the lateral (right) farm orientation

the same power profile as they are connected to two different submarine cables, whereas the power profile of Generator C, which is connected to the same cable as Generator A, is different. This is illustrated in Figures 4.10a, 4.10c and 4.10e. Hence, the beneficial power smoothing effect expected from device aggregation is more important in this case.

4.3 Theoretical analysis

In order to provide a benchmark for the results obtained with the power system simulator “PowerFactory”, theoretical load flow analyses, based on a simplified form of the power system considered in this work, were performed. An algorithm, developed and implemented in Matlab for the purpose of this thesis, is based on the Newton-Raphson algorithm typically used for solving load flow problems.

4.3.1 Introduction

The farm’s electrical network includes four submarine cables of different lengths. In order to simplify the load flow problems, a modified version of the considered electrical network was created for the purposes of this theoretical study in which the length of each cable (originally equal to either 6.5 km or 16 km) is replaced by an average length of 11.25 km. In this case, the voltage $V_G \angle \delta_G$ at all of the four generators’ busses is equal, provided that these generators output the same amount of power. This approach seems relevant as the difference in terms of voltage at the PCC between the original model and the simplified model is negligible for a majority of the short-circuit ratios and impedance angles Ψ_k considered, as shown in Figure 4.11, and does not exceed 0.8% for the weakest networks. The diagram of the corresponding electrical network is shown in Figure 4.12.

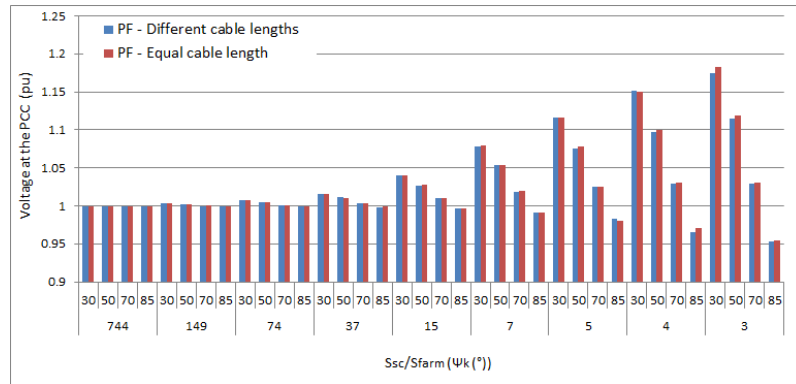


Figure 4.11: Voltage at the PCC as obtained from the original electrical network model and from the simplified model where all the cable lengths are equal

This network can be reduced to the approximately equivalent system shown in Figure 4.13. In this figure, $\bar{Z}_G = R_G + jX_G$ is the equivalent impedance of the part of the electrical network going from the generators up to the point of common coupling, excluding the impedance corresponding to the load L' and to the two parallel capacitances of each submarine cables. Given that this model is used for studying the grid impact of the farm when it outputs its maximum active power, the active and reactive power consumptions of the load can usually considered as negligible compared to the powers flowing through bus $B_{L'}$. In addition, given the high impedance of the parallel capacitances compared to the series impedance of the submarine cables, their presence was assumed to have little influence on the local voltages.

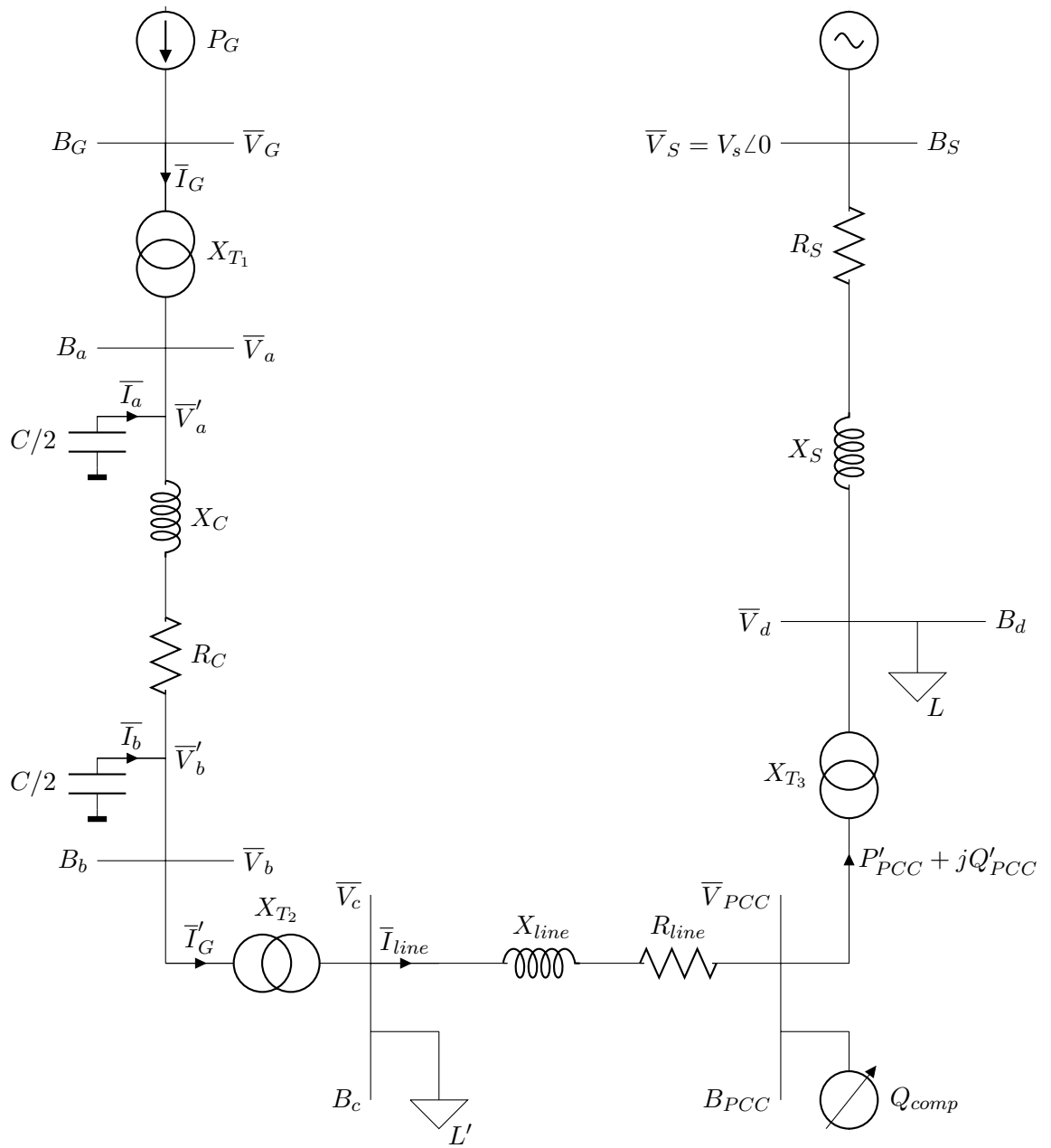


Figure 4.12: Electrical diagram of the entire network considered in this work

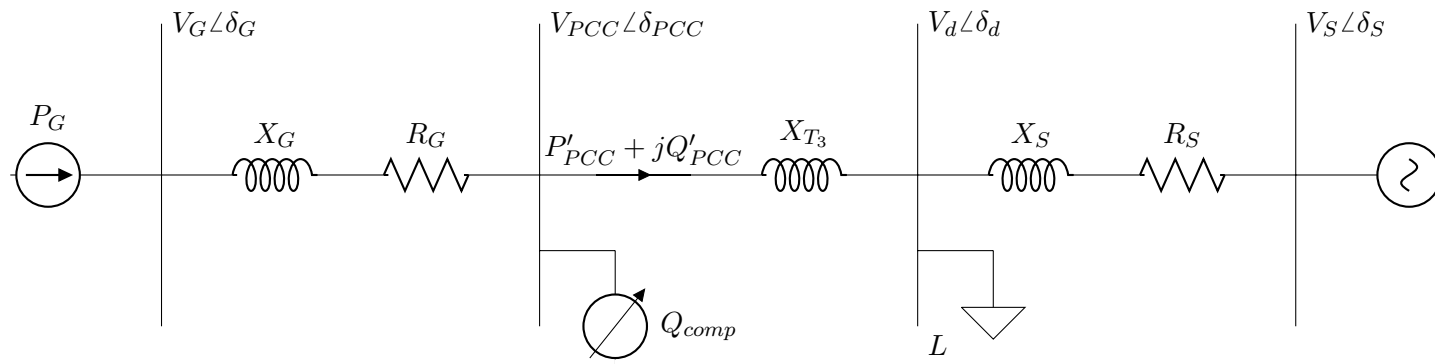


Figure 4.13: Simplified form of the electrical network used for the theoretical load flow analyses

Bus	Number	Known parameter	Bus type	Variable to be assumed
B_S	1	V_S, δ_S	slack bus	-
B_L	2	P_L, Q_L	PQ	V_L, δ_L
B_{PCC}	3	$Q'_{PCC}=0$ MVar	PQ	$V_{PCC}, \delta_{PCC}, Q_{comp}$
B_G	4	$P_G, Q_G=0$ MVar	PQ	V_G, δ_G

Table 4.3: Summary of the considered load flow problem

In the case where the voltage at the PCC is to be determined when the farm is disconnected, for instance for evaluating the maximum voltage step induced by a sudden disconnection of the wave farm, the model shown in Figure 4.14 is used. Both models working on the same principle, the general description of the method used in this work for solving the load flow problems is applicable to both. However, for the sake of clarity and concision, the method is detailed only for the first model which is used to determine the voltage at the PCC when the farm outputs its maximum active power.

The load flow problem must be solved by an iterative method as it contains too many unknowns, as shown in Table 4.3. The Newton-Raphson algorithm, which is commonly used in power system simulators, was selected to perform the theoretical analyses.

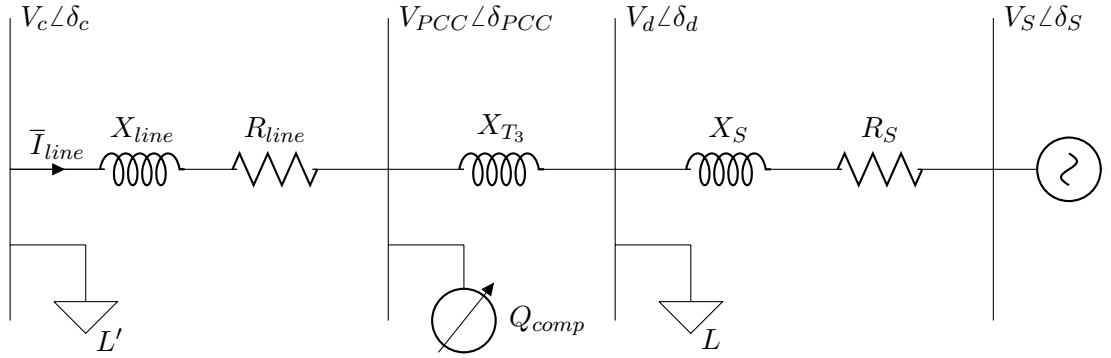


Figure 4.14: Electrical diagram of the network considered in this work in the case where the farm is disconnected

4.3.2 The Newton-Raphson algorithm applied to load flow problems

Introduction to the classical form of the Newton-Raphson algorithm

The Newton-Raphson method, named after Isaac Newton and Joseph Raphson, consists of an algorithm intended to determine iteratively the root α of a real-valued function f :

$$f(\alpha) = 0 \quad (4.7)$$

Alternatively, (4.7) can be approximately determined by its first order Taylor series in x_0 as:

$$\begin{aligned} f(\alpha) &= f(x_0) + f'(x_0)(\alpha - x_0) \\ 0 &= f(x_0) + f'(x_0)(\alpha - x_0) \end{aligned} \quad (4.8)$$

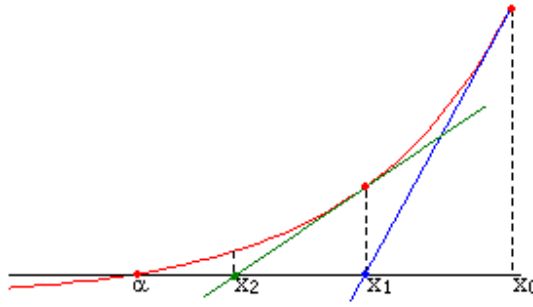


Figure 4.15: Illustration of the Newton-Raphson method for the estimating the root α

Iterations on the abscissa x are performed to find the value of the root α , as illustrated in Figure 4.15. Although it may happen that the algorithm does not converge, and thus does not provide the solution to a given problem, it has proven to be relatively robust with respect to load flow problems. The roots x_j can be expressed mathematically as:

$$x_{j+1} = x_j - \frac{f(x_j)}{f'(x_j)} \quad (4.9)$$

The iterations are stopped when the difference between the terms x_{j+1} and x_j is less than a pre-defined limit ϵ_x , which can be expressed as:

$$|x_{j+1} - x_j| \leq \epsilon_x \quad (4.10)$$

Application to load flow problems

The Newton-Raphson method is usually very efficient in solving load flow studies which may present usually a large number of unknowns in terms of voltages V_i , angles δ_i , and powers P_i and Q_i at each node i of the system. The application of the method for a root x and a function f as described in the previous section can be generalised to a number of unknowns x_i contained in an array \mathbf{x} , and for a number of function f_i contained in an array \mathbf{f} , which can be expressed as:

$$\mathbf{x} = \begin{bmatrix} x_1 \\ \vdots \\ x_n \end{bmatrix} \quad (4.11)$$

and

$$\mathbf{f} = \begin{bmatrix} f_1 \\ \vdots \\ f_n \end{bmatrix} \quad (4.12)$$

In the case of load flow problems, the unknowns x_i are the voltage V_i and the angle δ_i of each PQ node i , the other unknowns being calculated afterwards once these variables are defined. The corresponding array of unknowns \mathbf{x} can be expressed as:

$$\mathbf{x} = \begin{bmatrix} \delta_2 \\ \vdots \\ \delta_n \\ V_2 \\ \vdots \\ V_n \end{bmatrix} \quad (4.13)$$

The functions f_i , which are equal to zero provided that the correct values for the unknowns x_i are found, represent the difference in terms of both active and reactive power at each node (as calculated by the algorithm at a given iteration) and the scheduled active and reactive powers. The array \mathbf{f} , referred to as the mismatch array in this thesis, can be expressed as:

$$\mathbf{f} = \begin{bmatrix} \Delta P_2 \\ \vdots \\ \Delta P_n \\ \Delta Q_2 \\ \vdots \\ \Delta Q_n \end{bmatrix} \quad (4.14)$$

The parameters of the slack bus, whose index i is equal to 1, must not be included in the iteration process, as its voltage is known. Hence, calculations are performed for busses whose index i is greater than or equal to 2. The active and reactive powers P_i and Q_i flowing through each node i can be expressed as a function of the voltages at bus i and at its neighbour bus(es) k , as well as from the admittance \bar{Y}_{ik} between each of these busses, as shown below:

$$\begin{aligned} P_i + jQ_i &= \bar{S}_i = \bar{V}_i \bar{I}_i^* \\ &= \bar{V}_i \left(\sum_{k=1}^n \bar{Y}_{ik} \bar{V}_k \right)^* \\ &= \bar{V}_i \sum_{k=1}^n \bar{Y}_{ik}^* \bar{V}_k^* \end{aligned} \quad (4.15)$$

The admittance \bar{Y}_{ik} can be decomposed into a real part and an imaginary part as:

$$\bar{Y}_{ik} = G_{ik} + jB_{ik} \quad (4.16)$$

Hence, the power balance equations described in (4.15) can be rewritten as:

$$\begin{aligned} P_i + jQ_i &= \bar{V}_i \sum_{k=1}^n \bar{Y}_{ik}^* \bar{V}_k^* \\ &= \sum_{k=1}^n |\bar{V}_i| |\bar{V}_k^*| e^{j\delta_{ik}} (G_{ik} - jB_{ik}) \end{aligned} \quad (4.17)$$

The active and reactive powers P_i and Q_i flowing through each node i can be calculated by separating the real terms from the imaginary terms in (4.17) as:

$$P_i = \sum_{k=1}^n |V_i||V_k|(G_{ik}\cos\delta_{ik} + B_{ik}\sin\delta_{ik}) = P_{G_i} - P_{D_i} \quad (4.18)$$

$$Q_i = \sum_{k=1}^n |V_i||V_k|(G_{ik}\sin\delta_{ik} - B_{ik}\cos\delta_{ik}) = Q_{G_i} - Q_{D_i} \quad (4.19)$$

where P_{G_i} and P_{D_i} are the scheduled active powers generated and absorbed at node i respectively. In similar fashion, Q_{G_i} and Q_{D_i} are the scheduled reactive powers generated and absorbed at node i . The powers P_i and Q_i being recalculated at each iteration (v), they should be expressed $P_i^{(v)}$ and $Q_i^{(v)}$. At each iteration, the mismatch between these scheduled power and the powers $P_i^{(v)}$ and $Q_i^{(v)}$ as calculated by the algorithm is evaluated within the mismatch array \mathbf{f} which can finally be expressed as:

$$\mathbf{f}^{(v)} = \begin{bmatrix} P_2^{(v)} - P_{G_2} - P_{D_2} \\ \vdots \\ P_n^{(v)} - P_{G_n} - P_{D_n} \\ Q_2^{(v)} - Q_{G_2} - Q_{D_2} \\ \vdots \\ Q_n^{(v)} - Q_{G_n} - Q_{D_n} \end{bmatrix} \quad (4.20)$$

As mentioned earlier, the derivative of $\mathbf{f}^{(v)}$ is necessary for the calculations. This derivative consists of a sum of partial derivatives of powers $P_i^{(v)}$ and $Q_i^{(v)}$ with respect to the voltages V_i and the angles δ_i , which can be expressed as:

$$\frac{\partial P_i}{\partial \delta_i} = \sum_{\substack{k=1 \\ k \neq i}}^n |V_i||V_k|(-G_{ik}\sin\delta_{ik} + B_{ik}\cos\delta_{ik}) \quad (4.21)$$

$$\frac{\partial P_i}{\partial V_i} = \sum_{\substack{k=1 \\ k \neq i}}^n |V_k|(G_{ik}\cos\delta_{ik} + B_{ik}\sin\delta_{ik}) + 2|V_i|G_{ii} \quad (4.22)$$

$$\frac{\partial Q_i}{\partial \delta_i} = \sum_{\substack{k=1 \\ k \neq i}}^n |V_i||V_k|(G_{ik}\cos\delta_{ik} + B_{ik}\sin\delta_{ik}) \quad (4.23)$$

$$\frac{\partial Q_i}{\partial V_i} = \sum_{\substack{k=1 \\ k \neq i}}^n |V_k|(G_{ik}\sin\delta_{ik} - B_{ik}\cos\delta_{ik}) - 2|V_i|B_{ii} \quad (4.24)$$

$$\frac{\partial P_i}{\partial \delta_k} = |V_i||V_k|(G_{ik}\sin\delta_{ik} - B_{ik}\cos\delta_{ik}) \quad (k \neq i) \quad (4.25)$$

$$\frac{\partial P_i}{\partial V_k} = |V_i|(G_{ik}\cos\delta_{ik} + B_{ik}\sin\delta_{ik}) \quad (k \neq i) \quad (4.26)$$

$$\frac{\partial Q_i}{\partial \delta_k} = -|V_i|(G_{ik}\cos\delta_{ik} - B_{ik}\sin\delta_{ik}) \quad (k \neq i) \quad (4.27)$$

$$\frac{\partial Q_i}{\partial V_k} = |V_i|(G_{ik}\sin\delta_{ik} - B_{ik}\cos\delta_{ik}) \quad (k \neq i) \quad (4.28)$$

Finally, the array of unknowns $\mathbf{x}^{(v+1)}$ at the $(v + 1)$ th iteration can be expressed as:

$$\mathbf{x}^{(v+1)} = \mathbf{x}^{(v)} - \left(\mathbf{J}^{(v)}\right)^{-1} \mathbf{f}^{(v)} \quad (4.29)$$

where $\mathbf{J}^{(v)}$ is the Jacobian matrix of array $\mathbf{f}^{(v)}$ which can be written as:

$$\mathbf{J}^{(v)} = \begin{bmatrix} \frac{\partial P_2^{(v)}}{\partial \delta_2} & \cdots & \frac{\partial P_2^{(v)}}{\partial \delta_n} & \frac{\partial P_2^{(v)}}{\partial V_2} & \cdots & \frac{\partial P_2^{(v)}}{\partial V_n} \\ \vdots & & \vdots & & & \vdots \\ \frac{\partial P_n^{(v)}}{\partial \delta_2} & \cdots & \frac{\partial P_n^{(v)}}{\partial \delta_n} & \frac{\partial P_n^{(v)}}{\partial V_2} & \cdots & \frac{\partial P_n^{(v)}}{\partial V_n} \\ \frac{\partial Q_2^{(v)}}{\partial \delta_2} & \cdots & \frac{\partial Q_2^{(v)}}{\partial \delta_n} & \frac{\partial Q_2^{(v)}}{\partial V_2} & \cdots & \frac{\partial Q_2^{(v)}}{\partial V_n} \\ \vdots & & \vdots & & & \vdots \\ \frac{\partial Q_n^{(v)}}{\partial \delta_2} & \cdots & \frac{\partial Q_n^{(v)}}{\partial \delta_n} & \frac{\partial Q_n^{(v)}}{\partial V_2} & \cdots & \frac{\partial Q_n^{(v)}}{\partial V_n} \end{bmatrix} \quad (4.30)$$

The iterations are stopped when the difference between the scheduled active and reactive powers, equal to $P_{G_i} - P_{D_i}$ and to $Q_{G_i} - Q_{D_i}$ respectively, and the powers $P_i^{(v)}$ and $Q_i^{(v)}$ calculated by the algorithm is less than a pre-defined limit ϵ , which can be expressed mathematically as:

$$|f_i^{(v)}| \leq \epsilon \quad \forall i \quad (4.31)$$

Iterative algorithm regarding the reactive power generation/absorption of the VAR compensator

Using the Newton-Raphson algorithm requires to know the active and reactive powers flowing to or from each PQ node i . However, this is not the case in the load flow problem considered in this study, as the reactive power absorption/generation of the VAR compensator which is connected to the PCC depends on the active and reactive power flowing from the farm's electrical network. Hence, it cannot be defined prior to the iterative process. In order to solve this problem, a second iterative algorithm was developed to be used in conjunction with the Newton-Raphson algorithm.

This additional iterative algorithm is intended to determine the amount of reactive power Q_{comp} to be either generated or absorbed by the VAR compensator. The principle of this algorithm consists of assuming an initial value for the amount of reactive power Q_{comp} , solving the load flow problem based on this value, calculating then the actual reactive power either absorbed or generated by the farm's electrical network from which a more refined estimation of the actual value of Q_{comp} is determined. Based on this new value of Q_{comp} , another load flow is solved and so on until the difference between the value of Q_{comp} at the $(w + 1)$ -th and at w -th iterations is less than a pre-defined limit ϵ_Q . This algorithm can be summarised as:

```

While  $|Q_{comp}^{(w+1)} - Q_{comp}^{(w)}| \geq \epsilon_Q$ 
  While  $|f_i^{(v)}| \geq \epsilon$ 
    Solve load flow by means of the Newton-Raphson algorithm
  End
  Compute the VAR compensator's reactive power generation/absorption  $Q_{comp}$ 
End

```

4.3.3 Application to the different load flow problems considered in this thesis

The theoretical load flow analyses performed with the algorithm described in the previous section are based on the simplified network model shown in Figure 4.13. The admittance matrix $\bar{\mathbf{Y}}$, the array of unknowns \mathbf{x} and the mismatch array \mathbf{f} applicable to this network are described in the following sections.

Admittance matrix $\bar{\mathbf{Y}}$

The admittance matrix $\bar{\mathbf{Y}}$ corresponding to the simplified form of the electrical network considered in this thesis can be expressed as follows:

$$\begin{aligned} \begin{bmatrix} \bar{I}_1 \\ \bar{I}_2 \\ \bar{I}_3 \\ \bar{I}_4 \end{bmatrix} &= \begin{bmatrix} \bar{Y}_{12} & -\bar{Y}_{12} & 0 & 0 \\ -\bar{Y}_{12} & (\bar{Y}_{12} + \bar{Y}_{23}) & -\bar{Y}_{23} & 0 \\ 0 & -\bar{Y}_{23} & (\bar{Y}_{23} + \bar{Y}_{34}) & -\bar{Y}_{34} \\ 0 & 0 & -\bar{Y}_{34} & \bar{Y}_{34} \end{bmatrix} \begin{bmatrix} \bar{V}_1 \\ \bar{V}_2 \\ \bar{V}_3 \\ \bar{V}_4 \end{bmatrix} \\ &= \begin{bmatrix} \frac{1}{\bar{Z}_S} & -\frac{1}{\bar{Z}_S} & 0 & 0 \\ -\frac{1}{\bar{Z}_S} & \left(\frac{1}{\bar{Z}_S} + \frac{1}{\bar{Z}_{T_3}}\right) & -\frac{1}{\bar{Z}_{T_3}} & 0 \\ 0 & -\frac{1}{\bar{Z}_{T_3}} & \left(\frac{1}{\bar{Z}_G} + \frac{1}{\bar{Z}_{T_3}}\right) & -\frac{1}{\bar{Z}_G} \\ 0 & 0 & -\frac{1}{\bar{Z}_G} & \frac{1}{\bar{Z}_G} \end{bmatrix} \begin{bmatrix} \bar{V}_1 \\ \bar{V}_2 \\ \bar{V}_3 \\ \bar{V}_4 \end{bmatrix} \end{aligned} \quad (4.32)$$

where $\bar{Z}_S = R_S + jX_S$, $\bar{Z}_G = R_G + jX_G$ and $\bar{Z}_{T_3} = jX_{T_3}$.

Array of unknowns \mathbf{x}

Given that all the busses in the electrical network can be considered as PQ nodes with the exception of the slack bus, the array of unknowns \mathbf{x} at the v -th iteration can be expressed as:

$$\mathbf{x}^{(v)} = \begin{bmatrix} \delta_2^{(v)} \\ \delta_3^{(v)} \\ \delta_4^{(v)} \\ V_2^{(v)} \\ V_3^{(v)} \\ V_4^{(v)} \end{bmatrix} \quad (4.33)$$

The typical ‘‘flat start’’ method was used to initialise the Newton-Raphson algorithm. It consists of assuming that all the angles δ_i and all the voltages V_i equal to 0° and 1.0 pu respectively at all the PQ nodes. Hence, the array of unknowns $\mathbf{x}^{(0)}$ prior to the first iteration can be expressed as:

$$\mathbf{x}^{(0)} = \begin{bmatrix} 0 \\ 0 \\ 0 \\ 1.0 \\ 1.0 \\ 1.0 \end{bmatrix} \quad (4.34)$$

Mismatch array \mathbf{f}

Based on the scheduled active and reactive power flowing to or from each node, as defined in Table 4.3, the mismatch array $\mathbf{f}^{(v)}$ at each iteration corresponding to the studied electrical network can be expressed as:

$$\mathbf{f}^{(v)} = \begin{bmatrix} P_2^{(v)} - P_L \\ P_3^{(v)} \\ P_4^{(v)} - P_G \\ Q_2^{(v)} + Q_L \\ Q_3^{(v)} - Q_{comp}^{(v)} \\ Q_4^{(v)} \end{bmatrix} \quad (4.35)$$

The initial value of the VAr compensator's reactive power absorption/generation Q_{comp} is set to 0 MVar.

Computation of the amount of reactive power absorbed by the wave farm

The farm's electrical network, with the exception of the generators, is represented as load. Considering that the generators operate at unity power factor, the total current \bar{I}_G flowing from them can be expressed as:

$$\bar{I}_G = \frac{P_G}{\sqrt{3} \bar{V}_G} \quad (4.36)$$

The voltages \bar{V}_a and \bar{V}_b at the busses B_a and B_b respectively can be calculated as:

$$\bar{V}_a = \bar{V}_G - j(X_{T1}) \frac{\bar{I}_G}{4} \quad (4.37)$$

$$\bar{V}_b \approx \bar{V}_a - \frac{\bar{I}_G}{4} (R_c + jX_c) \quad (4.38)$$

Assuming that $\bar{V}'_a \approx \bar{V}_a$, the current \bar{I}_a flowing from the capacitance $C/2$ can be expressed as:

$$\bar{I}_a = \frac{\bar{V}_a}{\sqrt{3} \bar{Z}_{C/2}} \quad (4.39)$$

where the shunt impedance $Z_{C/2}$ can be expressed as:

$$Z_{C/2} = \frac{1}{2\pi \frac{C}{2} f_e} = \frac{1}{\pi C f_e} \quad (4.40)$$

and f_e is the grid frequency. The corresponding reactive power Q_a generated by the capacitance $C/2$ of a single submarine cable can be expressed as:

$$Q_a = -3Z_{C/2} I_a^2 \quad (4.41)$$

In similar fashion, the current I_b can be calculated by assuming that $\bar{V}'_b \approx \bar{V}_b$ as:

$$\bar{I}_b = \frac{\bar{V}_b}{\sqrt{3} \bar{Z}_{C/2}} \quad (4.42)$$

which corresponds to an amount of reactive power Q_b equal to:

$$Q_b = -3Z_{C/2} I_b^2 \quad (4.43)$$

The current flowing through the series reactance X_c of the submarine cables is equal to $4\bar{I}_a + \bar{I}_G$, so the reactive power absorbed by this impedance is equal to:

$$Q_c = 3X_c |4\bar{I}_a + \bar{I}_G|^2 \quad (4.44)$$

Finally, the reactive power Q_{cable_i} absorbed by the four submarine cables is equal to:

$$Q_{cable} = 4Q_a + 4Q_b + Q_c \quad (4.45)$$

As defined by the load convention, a positive value of the reactive Q_{cable} corresponds to the cable absorbing reactive power, while a negative value corresponds to the cable generating reactive power. The total active power lost by the four submarine cables can be expressed as:

$$P_{cable} = 3R_c |4\bar{I}_a + \bar{I}_G|^2 \quad (4.46)$$

The current \bar{I}'_G flowing through bus B_b can be calculated as:

$$\bar{I}'_G = \bar{I}_G + 4(\bar{I}_a + \bar{I}_b) \quad (4.47)$$

Hence, the voltage \bar{V}_c at bus B_c can be calculated as:

$$\bar{V}_c = \bar{V}_b - jX_{T_2} \bar{I}'_G \quad (4.48)$$

where X_{T_2} is the reactance of the 10/20kV transformer. The reactive power Q_{T_2} absorbed by the 10/20kV transformer is equal to:

$$Q_{T_2} = 3X_{T_2} \bar{I}'_G{}^2 \quad (4.49)$$

It is necessary to calculate the current $\bar{I}_{L'}$ flowing to the load L' to obtain the current \bar{I}_{line} flowing through the overhead line. This current can be calculated from the active and reactive powers $P_{L'}$ and $Q_{L'}$ absorbed by the load as:

$$\bar{I}_{L'} = \left(\frac{P_{L'} + jQ_{L'}}{\sqrt{3} \bar{V}_c} \right)^* \quad (4.50)$$

The current \bar{I}_{line} flowing in the overhead line is thus equal to:

$$\bar{I}_{line} = \bar{I}'_G + \bar{I}_{L'} \quad (4.51)$$

The active and reactive powers P_{line} and Q_{line} absorbed by the overhead line can be calculated as:

$$P_{line} = 3R_{line} \bar{I}_{line}^2 \quad (4.52)$$

and

$$Q_{line} = 3X_{line} \bar{I}_{line}^2 \quad (4.53)$$

Finally, the active and reactive powers P_{PCC} and Q_{PCC} flowing from the overhead line to the PCC can be calculated as:

$$P_{PCC} = P_G - P_{cable} - P_{line} - P_{L'} \quad (4.54)$$

and

$$Q_{PCC} = -(Q_{T_1} + Q_{cable} + Q_{T_2} + Q_{line} + Q_{L'}) \quad (4.55)$$

The reactive power Q_{comp} which must be generated by the VAR compensator is thus equal to $-Q_{PCC}$.

Summary

This section introduced the Newton-Raphson method with which load flow problems are usually solved. The application of this method to the load flow problem considered in this thesis was detailed, as well as a simplified load flow programme developed as part of this thesis which is intended to provide a sanity check for the results obtained with PowerFactory.

4.4 Studied variables

As mentioned earlier, power plant managers must prove that their power plant complies with a number of requirements, and among them standards related to power quality, in order to be allowed grid connection. The following three power quality criteria, which are directly applicable to wave farms and were analysed at the PCC, are examined in this work:

- voltage step
- voltage limits (maximum and minimum)
- short-term flicker level Pst

The limits specified for each of these power quality criteria may differ among different grid connection codes. A survey on several grid codes, recommendations and standards was conducted in order to extract the most stringent as well as the most permissive limits currently enforced. The compliance tests applied to the wave farm is based on both these types of limit in order to be representative of the requirements enforced by a large number of grid operators around the world.

4.4.1 Voltage step

The switching on, or off, of a power generation plant induces an instantaneous voltage increase or decrease, also called voltage step, as illustrated in Figure 4.16. This step must be limited below a specified amplitude to prevent any stability issue on, or deterioration of other pieces of electrical equipment connected to the grid. Numerical values for this limit found in four different grid codes and recommendations are shown in Table 4.4.

Code, standard or recommendation	Region/country	Limit
TAB-2008	Germany	2%
ESB's Distribution Code	Republic of Ireland	10%
National Grid's Code and ER-P28	Great Britain	1%
Nordic Grid Code	East Denmark, Norway, Sweden and Finland	3%

Table 4.4: Voltage step limits

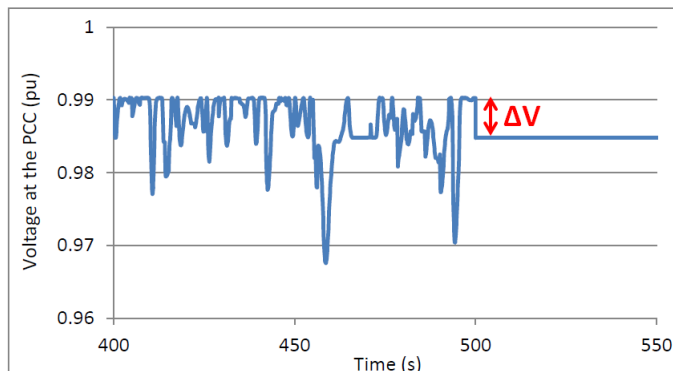


Figure 4.16: Illustration of the voltage step induced by the disconnection of a wave farm

The TAB [85], standing for Technische Anschlussbedingungen für den Anschluss an das Mittelspannungsnetz (Technical Connection Requirements for the Connection at Distribution Level), constitutes a common reference for grid operators in Germany regarding the connection at the medium voltage networks. This document recommends that the amplitude of rapid voltage changes should not exceed 2%. The ESB’s Distribution Code [35] is the official grid code of the Irish distribution system operator, ESB. In this code, although no requirement is dedicated to voltage step, it is indicated that generators connected at the 110 kV level and whose power capacity exceeds 2 MW are required to remain connected up to a voltage step not exceeding 10%. Given the increasing number of distributed generation plants connected at distribution level, this requirement is expected to be applied at the 38 kV level as well, which is the voltage level considered in this work. Hence, a limit equal to 10% was considered. The British National Grid’s Code [86], some of whose requirements are based on the Engineering Recommendation P28 [87], requires that the amplitude of a voltage step is limited to 1%. Finally, the Nordic grid code is a common reference for the grid operators belonging to the former NORDEL group, i.e. East Denmark, Norway, Sweden and Finland [88].

As it was described above, the limits defined in the British and Nordic grid codes, as well as in the German recommendation TAB concerns the maximum tolerated amplitude of a voltage step induced on the local network. On the contrary, the limit defined in the Irish grid code regards the maximum amplitude of a voltage step after which the power generation plant must remain connected. This means that exceeding the former limit may lead to a potential deterioration of the local power quality, while exceeding the latter may have potentially serious implications on the operation and control of a power generation plant, and consequently on the stability of the region powered by this plant.

Regarding the limits, the strictest 1% limit specified in the British grid code is applied to “step changes which may occur repetitively”. Although this statement is not accompanied by a numerical value to determine the exact meaning of “repetitively”, it is not believed to be applicable to the connections or disconnections of a wave farm, whose number is expected to be limited in time and restricted to events such as transitions between stand-by and normal operation (and vice versa), emergency stops due to storm conditions, and faults. Hence, the TAB limit of 2% represents the strictest requirement applicable to a wave farm, closely followed by the 3% limit defined in the British and Nordic grid codes. The compliance of the wave farm with the voltage step requirement was thus assessed based on the 2% limit, which represents the most stringent limit and on the 10% limit mentioned in the Irish distribution code, which constitutes the most permissive limit, as summarised in Table 4.5.

	most permissive	most stringent
Voltage step limit (pu)	10%	2%

Table 4.5: Most permissive and most stringent voltage step limits

4.4.2 Voltage limits

Under normal conditions, the voltage at the point of common coupling between the wave farm and the rest of the network must remain within a specified voltage range defined by lower and upper limits. This section presents an overview of the different limits which are enforced by the grid operators or recommended in different standards.

The limits defined in standard EN 50160 [77] are the most permissive with an allowed voltage range spanning from -10% to +10% during 95% of the week, thus allowing voltage to go well below or above these values. However, the authors of this standard acknowledge that a narrower range of $\pm 5\%$ may prevent voltage to be maintained at either the lower or the upper limit for prolonged periods. Hence, standard EN 50160 should be considered as defining minimum requirements which may not always prove to be sufficient to maintain an acceptable level of power quality. The ENTSO-E “Network Code Applicable to All Generators” [22] also defines allowed voltage ranges including a temporal limitation for either the lower or upper ranges, or both, as shown in Table 4.6. This code gathers the minimum requirements applicable in 34 different European states from 2014. This code specifies that more stringent limits may also be issued by regional or national grid operators if deemed necessary. Current regional and national limits were thus also investigated for the sake of completeness and are summarised in Table 4.7.

The application of time limitation is however relatively ambiguous in the case of a wave farm which may induce regular voltage excursions of very limited duration. Although the concept of time limitation is intended to avoid the voltage to be maintained persistently below or above the nominal range for periods of time sufficiently long to damage power quality significantly, it does not prevent voltage levels regularly reaching excessively low or high values for short periods of time, which can have very negative consequences in terms of power quality. Hence, requirements in terms of voltage range may need to be adapted

Synchronous area	Voltage range (pu)	Time period for operation
Continental Europe	0.85-0.90	60 minutes
	0.90-1.118	unlimited
	1.118-1.15	variable, but not less than 20 minutes
Nordic	0.90-1.05	unlimited
	1.05-1.10	60 minutes
Great Britain	0.90-1.10	unlimited
Ireland	0.90-1.118	unlimited
Baltic	0.85-0.90	30 minutes
	0.90-1.12	unlimited
	1.12-1.15	20 minutes

Table 4.6: Allowed voltage ranges as defined in the ENTSO-E “Network Code for All Generators” [22]

in the perspective of wave energy grid integration to ensure sufficient power quality. However, this is beyond the scope of this chapter whose overall objective is to determine the compliance of a wave farm based on a number of current power quality requirements. On the other hand, determining the compliance of a wave farm based on the strict reading of current grid code requirements would not only be taking an unreasonable advantage of their ambiguity, inapplicability or irrelevance in the context of wave farms grid connection, but would also result in failing to assess its actual impact. A reasonable compromise between these two stances was adopted in this chapter by considering only the voltage ranges for which no time limitation is applied. This can be considered as conservative conditions from a power quality perspective as a wave farm inducing the voltage at the PCC to be less than the lower limit or to exceed the upper limit would be deemed to have failed the compliance test.

Code, standard or recommendation	Region/country	Lower limit (pu)	Upper limit (pu)
ESB's Distribution Code [35]	Republic of Ireland	-10% ¹	+11% ²
National Grid's Code [86]	Great Britain	-6%	+6%
Regulation of 25/09/2000 [89]	Poland	-10%	+5%
Contrat d'accès au réseau public (detailed conditions for grid connection) [90]	France	-10% ³	+10% ³
Technical regulation 3.2.5 [91]	Denmark	-10%	+10%
ENTSO-E Network Code [22]	Nordic area	-10%	+5%
	Baltic area	-10%	+12%

Table 4.7: Voltage limits

¹ Variable according to operating conditions

² Depending on nominal voltage level

³ Information limited to a voltage level of 230 V

Both the most stringent and the most permissive sets of voltage limits were considered in the compliance test, namely -6% and +5%, and -10% and +12% respectively as summarised in Table 4.8, in order to reflect the diversity of voltage limit requirements.

	most permissive	most stringent
Lower voltage limit (pu)	-10%	-6%
Upper voltage limit (pu)	+12%	+5%

Table 4.8: Most permissive and most stringent voltage limits

4.4.3 Flicker level

Introduction

Grid codes usually define the flicker limit in terms of the individual contribution of a power plant to the total flicker level at the point of common coupling, or in terms of the total flicker level at the PCC, as shown in Table 4.9. However, determining the flicker compliance of a wave farm based on only one of these two limits is irrelevant. Using the total flicker level at the point of common coupling as the base for any compliance test necessitates having sufficient information on the flicker level prior to the connection of the wave farm, which is usually unavailable. On the other hand, using the flicker emission limit of $Pst=0.35$ for assessing grid compliance may be unrealistic as, with the exception

Code, standard or recommendation	Region/country	Flicker level Pst	Type
ESB's distribution code	Republic of Ireland	0.35	individual
National Grid's code	Great Britain	1.0	total
IEC 61000-3-7	N/A	0.35 ¹	individual
		0.8	total
Nordic Grid Code	Norway, Sweden, Finland, East Denmark	1.0	total

Table 4.9: Flicker level limits

¹ Minimum emission limits for a voltage level between 1 kV (excluded) and 35 kV (included)

	Most permissive	Most stringent
Pst	1.0	0.35

Table 4.10: Most permissive and most stringent flicker limits

of the Republic of Ireland, this constitutes the minimum flicker emission limit which a grid operator is recommended to enforce, as defined in IEC 61000-3-7.

The standard defines also a method to determine the individual flicker limit to be assigned to a power plant. This limit represents a fraction of the total allowed flicker emission at the connection point, which is estimated from the percentage of the plant's rated power compared to the total, already installed power capacity connected at this point. However, this method may lead to unrealistically low flicker emission limits for installations having a small rated power, which is the reason why a minimum flicker emission limit equal to 0.35 is defined.

The most stringent as well as the most permissive flicker limits equal to 0.35 and 1.0 respectively were selected for the compliance test, as summarised in Table 4.10. A total flicker level at the point of common coupling smaller than 0.35 indicates that flicker is not an issue and that the farm complies with the flicker level requirements in any case. A flicker level ranging between 0.35 and 1.0 indicates on the contrary that flicker may be an issue. In this case, detailed information on the background voltage variations at the connection point considered are needed to draw more definitive conclusions. Exceeding the 1.0 flicker level limit implies that the farm fails definitively to comply with the flicker level requirements even with a minimum pre-connection flicker level.

4.5 Flickermeter design

4.5.1 Standards

IEC 61000-4-15

The computation of flicker level from voltage time series has been strictly defined in the IEC standards 61000-4-15 [32] and 61400-21 [52]. The former standard defines the overall design of a flickermeter while the latter describes a number of modifications to be brought to this design for the analysis of flicker induced by wind farms. Flickermeters can be

Variable	Numerical value
κ	1.74802
λ	$2\pi \times 4.05981$
ω_1	$2\pi \times 9.15494$
ω_2	$2\pi \times 2.27979$
ω_3	$2\pi \times 1.22535$
ω_4	$2\pi \times 21.9$

Table 4.11: Indicative filter parameter values for a 230 V lamp in a 50 Hz system

implemented either in a hardware or a software form and compute flicker severity levels from voltage time series which may be generated either from field experiments or from numerical simulations.

A flickermeter consists of 5 functional blocks, as shown in Figure 4.17. Blocks 1 to 4 compute the instantaneous flicker level from voltage time series, whereas Block 5 computes the statistical index of flicker, Pst , referred to as flicker severity or flicker level. More specifically, by scaling down the RMS voltage amplitude to a per-unit value with respect to the time series mean RMS value, Block 1 extracts the fluctuations from the voltage time series. This enables also the generalised use of the flickermeter for any voltage level. Luminous intensity produced by an incandescent light bulb for a given voltage fluctuation is then obtained by squaring the input voltage in Block 2. Blocks 3 and 4 simulate the physical human perceptibility to light intensity variations by means of filters whose parameters were defined based on experiments on groups of individuals. Perceptibility curves similar to this shown Figure 4.18 were produced as an outcome of these experiments.

Two filters, whose transfer functions were developed based on these perceptibility curves, emulate the human perceptibility. One filter reproduces the response of the eye to light intensity variations, while another simulates the brain reaction to the nervous signals generated by the eye. The resulting filter included in Block 3 presents the following transfer function $F(s)$:

$$F(s) = \frac{k\omega_1 s}{s^2 + 2\lambda s + \omega_1^2} \frac{1 + s/\omega_2}{(1 + s/\omega_3)(1 + s/\omega_4)} \quad (4.56)$$

where s is the Laplace transform operator. The IEC standard 61000-4-15 provides indicative values, which are shown in Table 4.11, for the parameters of these filters with respect to a 230 V lamp used in a 50 Hz system.

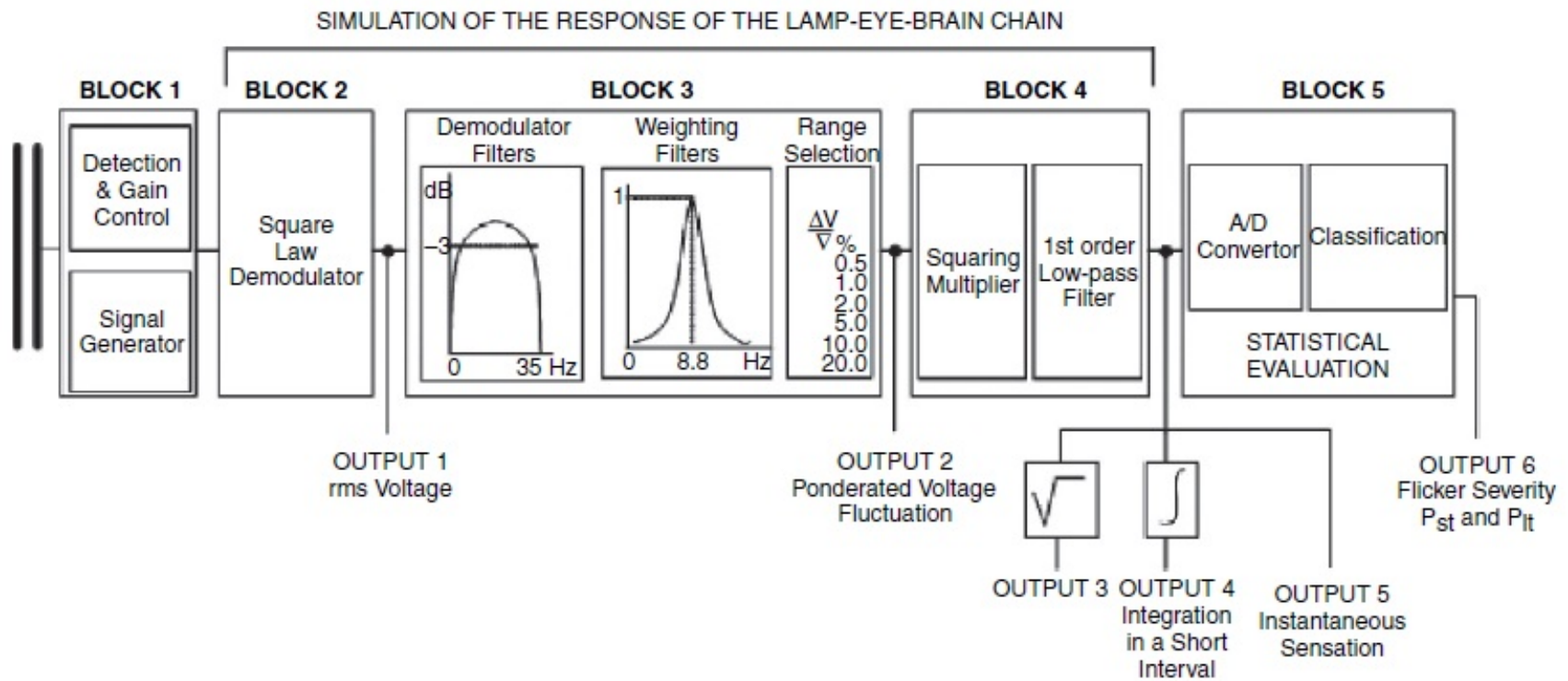


Figure 4.17: Functional representation of the IEC flickermeter [32]

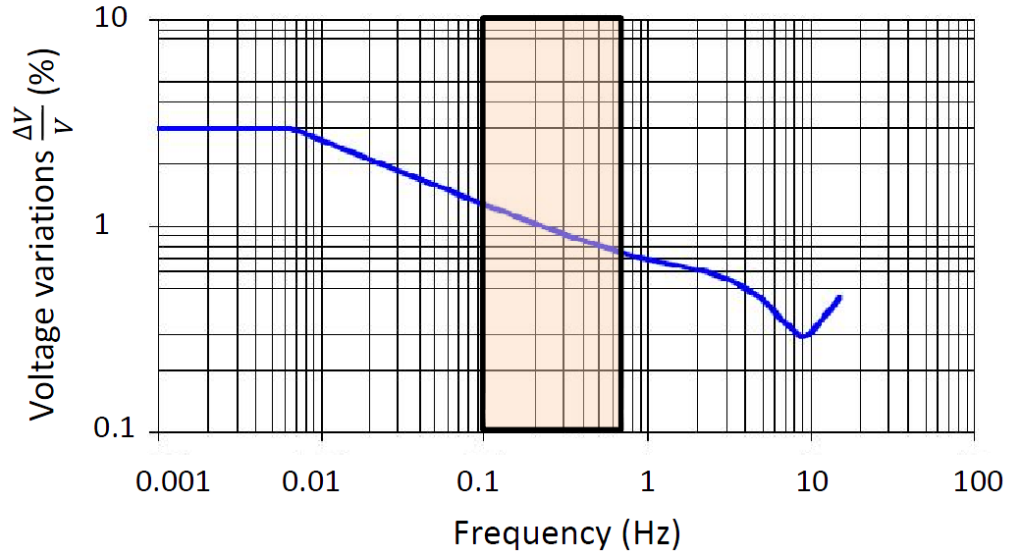


Figure 4.18: Amplitude of sinusoidal voltage variations giving a flicker level P_{st} equal to unity. The orange-shadowed area indicates the frequency range of the voltage fluctuations potentially induced by a wave farm.

IEC 61400-21

As small voltage variations as induced by wind farms are not taken into account accurately enough with the base design of the flickermeter described in the IEC standard 61000-4-15, the IEC standard 61400-21 recommends to increase the number of classes of the classifier contained in Block 5 from 64 to 6400. Consequently, the suitable number of class necessary for wave energy applications was investigated, as detailed in the next section.

4.5.2 Development and compliance with the IEC standard 61000-4-15

A flickermeter was built in Matlab for the purpose of this thesis according to the design specifications of IEC standards 61000-4-15 and 61400-21. In addition, this flickermeter includes the “empty class” feature designed by Alcorn [45] which is intended to help produce a sufficiently smooth cumulative probability function (CPF), necessary for obtaining sufficiently accurate results. It consists of interpolating the ordinate of any empty class based on the ordinate of surrounding non-empty classes.

Different tests were performed to evaluate the accuracy of this flickermeter. First, a test focusing on the number of classes to be used in the classifier of Block 5 was conducted. Results showed that the number of classes recommended by the IEC standard 61400-21 in the case of wind farms and equal to 6400 seems also suitable for wave energy applications. Table 4.12 presents the flicker level obtained from three different production periods and computed with four different numbers of classes. Results are stable from this number of classes which was thus retained for the studies.

In addition to analysing the number of classes, compliance tests as defined in the IEC standard 61000-4-15 were also performed. They consist of three different tests. The first two tests address the accuracy of the instantaneous flicker perceptibility measured at Output 5, as shown in Figure 4.17. Hence, these tests concerns Blocks 1 to 4 only and are performed by applying a set of periodic voltage time series of strictly defined frequency f_{test} and amplitude ΔV_{test} to the flickermeter. A set of values for these parameters for

Production period	Number of classes				
	64	3200	6400	12800	25600
A	1.582	1.417	1.416	1.415	1.415
B	0.102	0.093	0.093	0.093	0.093
C	1.132	1.015	1.015	1.015	1.015

Table 4.12: Flicker level computed with several numbers of class

which the maximum instantaneous flicker perceptibility is equal to unity is supplied in the standard. This type of test is performed for both sinusoidal and rectangular voltage time series. The standard stipulates that a flickermeter is compliant if the maximum value of Output 5 is equal to unity provided that the amplitude ΔV of the corresponding voltage time series ranges between $\pm 5\%$ of the reference amplitude ΔV_{test} . The difference between the voltage amplitude for which the maximum instantaneous flicker perceptibility is equal to unity and the reference amplitude defined in the IEC standard 61000-4-15 will be referred to as $\delta_{\Delta V}$.

The results with respect to both sinusoidal and rectangular voltage time series are shown in Table 4.13a and Table 4.13b. They demonstrate that the part of the flickermeter consisting of Blocks 1 to 4 is compliant with the IEC standard 61000-4-15 as an instantaneous flicker perceptibility equal to unity ($\pm 1\%$) is obtained for an amplitude difference $\delta_{\Delta V}$ of the input voltage variations varying between -3% to $+2\%$ of the indicative values provided in the standard, thus less than the maximum allowed level equal to $\pm 5\%$.

The compliance test for Block 5 is somewhat different. In this case, the standard requires that a flicker level Pst approximately equal to unity with an allowed error of $\pm 5\%$ is obtained for a rectangular voltage time series whose amplitude ΔV and frequency f are exactly equal to its indicative values. The results shown in Table 4.14 demonstrates that Block 5 is also compliant with the IEC standard 61000-4-15 and presents a high level of accuracy as the error on Pst ranges between -1% and 3% , thus also within the allowed error range equal to $\pm 5\%$.

In summary, besides being compliant with the IEC standard 61400-15, the flickermeter designed for the purpose of this thesis can be considered as presenting a high overall accuracy.

4.6 Detail on the simulations and methodology

The studies were performed using 11 different short-circuit levels S_{SC} , 4 distinct impedance angles Ψ_k , and 3 production periods with different levels of wave energy. In addition, two different wave farm orientations and 5 device layout combinations were also used, leading to a total of 1320 simulations. Table 4.15 sums up the different values used for each parameter. In addition, three different power factors, namely 0.92 and 0.95 lagging (referring here as absorbing reactive power) as well as unity were applied at the PCC to study the influence of this parameter on the maximum and minimum voltage limits as well as on the maximum flicker level obtained at this node.

The following sections detail the simulations performed regarding the voltage step, the voltage limits and the flicker level.

f_{test} (Hz)	$\delta_{\Delta V}$ (%)	f_{test} (Hz)	$\delta_{\Delta V}$ (%)
0.5	-1	10	0
1	-3	10.5	0
1.5	-1	11	0
2	0	11.5	1
2.5	-1	12	1
3	-1	13	1
3.5	-1	14	1
4	-1	15	1
4.5	-1	16	1
5	0	17	0
5.5	-1	18	-1
6	-1	19	-1
6.5	0	20	0
7	0	21	0
7.5	0	22	0
8	0	23	0
8.8	0	24	0
9.5	0	25	0
		33.33	0

(a) Sinusoidal

f_{test} (Hz)	$\delta_{\Delta V}$ (%)	f_{test} (Hz)	$\delta_{\Delta V}$ (%)
0.5	-1	10	-1
1	-1	10.5	0
1.5	-1	11	0
2	-1	11.5	0
2.5	-1	12	0
3	-1	13	-1
3.5	-1	14	0
4	0	15	0
4.5	-1	16	1
5	0	17	0
5.5	0	18	-2
6	0	19	0
6.5	0	20	1
7	0	21	-1
7.5	0	21	2
8	-1	23	0
8.8	-1	24	0
9.5	0	33.33	-3

(b) Rectangular

Table 4.13: Results of Blocks 1 to 4 to the compliance tests

Rectangular changes per minute	Pst
1	1.02
2	1.03
7	1.02
39	1.02
110	1.00
1620	0.99
4000	1.03

Table 4.14: Results of Block 5 to the compliance test

Parameter	Value
Series reactor impedance Z_S (Ω)	0.1, 0.5, 1, 2, 3, 4, 5, 10, 15, 20, 25
Equivalent short-circuit ratio	744, 149, 74, 37, 25, 19, 15, 7, 5, 4, 3
Short-circuit impedance angle Ψ_k ($^\circ$)	30, 50, 70 and 85
Production periods (energy level)	A (high), B (medium), and C (low)
Wave farm orientation	frontal and lateral
Device layout combination	1 to 5

Table 4.15: Value range used for each parameter

4.6.1 Voltage step

Electrical model

The voltage step study was performed by means of load flow studies. As dynamic models are not required for this type of study, a simplified electrical model based on only four static

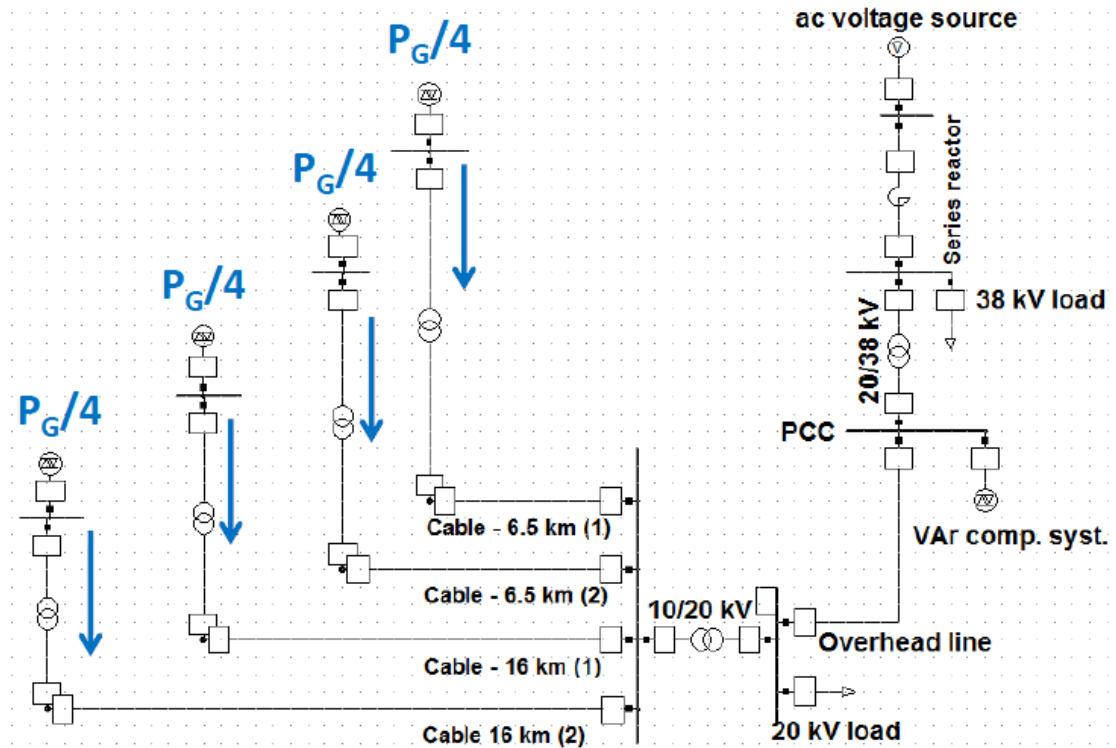


Figure 4.19: Simplified PowerFactory electrical model of the farm as used for the voltage step analysis

generators was used, as shown in Figure 4.19. All the other parameters remain as described in Section 4.2.1. The farm power output P_G , to which each of the four generators contribute in an equal manner, is defined according to the values described in the next section. The voltage step at the PCC is defined as the difference between the voltage obtained when the farm outputs its maximum power (for a given production period) and the voltage when the onshore 10/20 kV transformer is disconnected from the network, thus representing a mains loss for the farm's offshore electrical network. This event represents a worst case as the entire farm is then lost: this may occur for instance in the case of a failure of the 10/20 kV onshore transformer, or if the integrity of all the cables is deteriorated simultaneously.

Determination of worst case conditions

The disconnection of a wave farm at the time when it outputs its maximum power represents worst case conditions regarding the amplitude of the voltage step induced at the PCC. The load flow simulations were thus performed based on a farm power output equal to 20 MW (in order to represent the extreme case) as well as based on the maximum power output generated by the farm in each of the production periods A, B and C and for both farm orientations. This study in this last case was limited to a single time delay set: time delay set 1 was chosen arbitrarily. Table 4.16 shows the maximum power values of the different power profiles considered.

This scenario was selected as, besides providing the maximum voltage step amplitude, it seems also realistic that a failure within the farm internal network may occur at peak power, due for instance to pieces of equipment switching off or tripping if their power rating is exceeded.

	Production period		
	A	B	C
Frontal orientation	15.3	7.5	0.8
Lateral orientation	16.5	15.5	1.3

Table 4.16: Maximum power (MW) in the power profiles generated for production periods A to C, and for both farm orientations (time delay set 1)

Given the similarity in terms of maximum power between production period A in frontal orientation and production period B in lateral orientation, as well as the small difference between the maximum powers of period C for both orientations, four values only were considered for the farm power P_G besides 20 MW (equal to its rated power): 16.5 MW, 15.5 MW, 7.5 MW and 1.0 MW. Each of the static generator outputs a power equal to a quarter of P_G .

4.6.2 Voltage limits

Contrary to the voltage step analysis, both the voltage limits and the flicker level are determined from dynamic simulations. Both the maximum and minimum voltages were investigated and compared to the limits defined in Section 4.4. As mentioned earlier, five different time delay sets were used to simulate different layouts of the devices within the farm. The maximum and minimum voltages for given impedances Z_S , impedance angles Ψ_k , production periods and wave farm orientations were defined respectively as the maximum and minimum values over all these five simulations.

4.6.3 Flicker level

The flicker level was determined from the same voltage time series as used for the voltage limits analysis. These time series were then processed by the flickermeter developed for the purpose of this thesis. In similar fashion to the voltage limits analysis, the flicker corresponding to a given impedance Z_S , impedance angle Ψ_k , production period and wave farm orientation is defined as the maximum flicker obtained over the five time delay sets considered in this study.

4.7 Compliance with power quality requirements

4.7.1 Voltage step

Maximum farm power output (20 MW)

Figure 4.20 shows the maximum voltage step induced by the loss of a farm outputting 20 MW at the moment of its disconnection as a function of the short-circuit ratio and of the impedance angle Ψ_k . Both the results obtained with PowerFactory and those obtained with the simplified load flow programme developed for the purpose of this study (which are labelled “Theoretical” in the figures) are in good agreement, as the maximum error is equal to 2% only.

The results indicate that a voltage step exceeding the limit of 2% may be induced by the disconnection of a wave farm connected to a connection point whose short-circuit ratio is less than or equal to 37 (i.e. 722 MVA in this case). This is generally greater than the

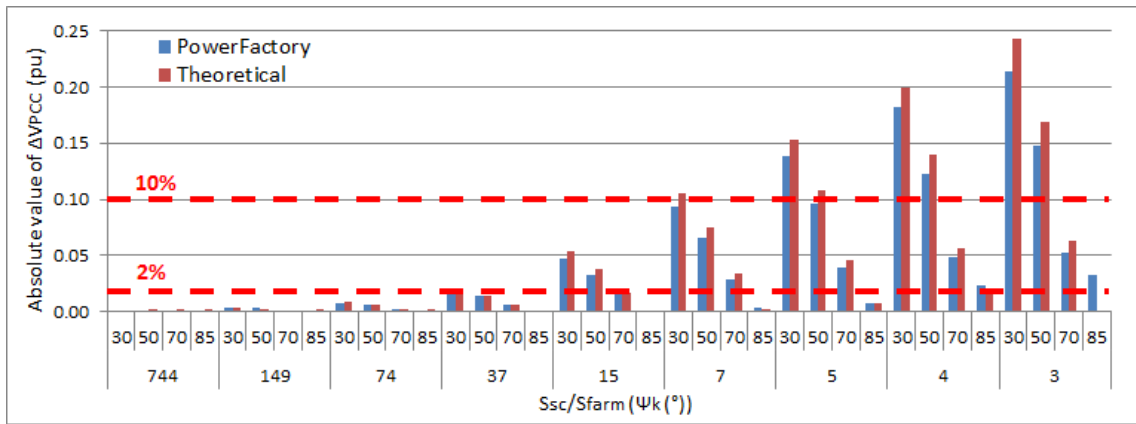


Figure 4.20: Maximum voltage step amplitude versus short-circuit level ratio and impedance angle, as obtained with PowerFactory and the load flow programme (labelled “Theoretical”)

typical short-circuit ratio of most connection points, and especially much greater than the short-circuit ratio of the connection points located in the west of Ireland, as indicated in Table 4.1. Hence, such a voltage step may be considered as an issue.

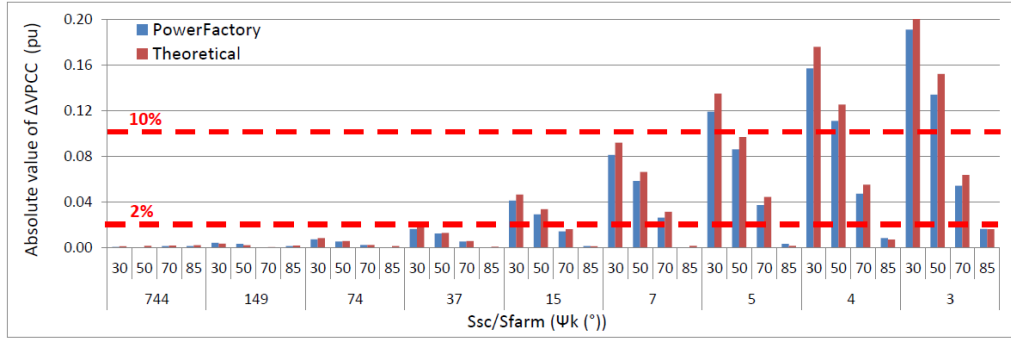
The 10% limit is exceeded for relatively weak grids with connection points whose short-circuit ratio is smaller than or approximately equal to 5 (i.e. 97 MW). This concerns still a majority of the potential Irish test sites considered in this study, thus indicating that the loss of a wave farm may represent an issue for the stability of the local power system. This threat is to be taken all the more seriously as weak grid areas present typically a more fragile stability due to the relatively limited number of generators being usually required to power these networks. In this case, the stability of a part of the power system is maintained by a single generator whereas several generators would have ensured this role in stronger grid areas. Hence, this may increase considerably the influence which a significant voltage step may have on the rotor stability of this isolated generator.

Maximum farm power output corresponding to different production periods

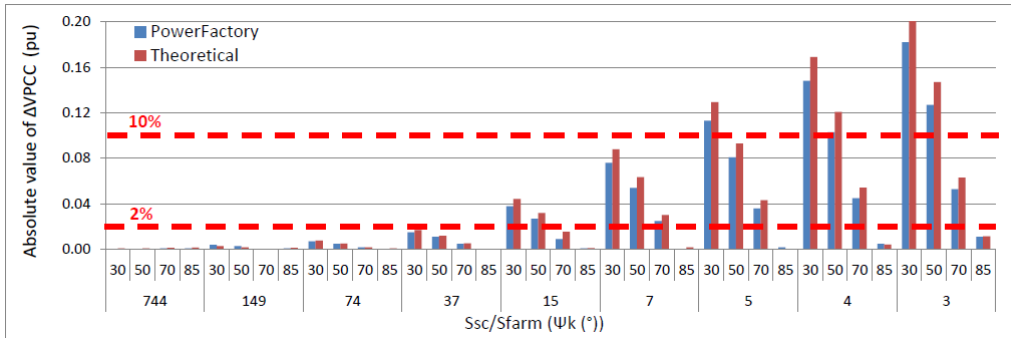
The same study was performed based on the maximum power values obtained from the different production periods considered, as shown in Figures 4.21a to 4.21d. It can be observed that the amplitude of the induced voltage step is still significant in the case of production periods A and B for a number of connection points, even though the maximum power level corresponding to production period B in the lateral orientation represents only 37% of the maximum rated power. This indicates that the disconnection of a wave farm even in moderate sea conditions may induce a voltage step of significant amplitude on relatively weak networks whose short-circuit ratio is less than or equal to 5, which covers the majority of the sites located on the west of Ireland. On the contrary, the induced voltage step is negligible for period C, which was expected from the very low values corresponding to its maximum power levels with both farm orientations.

Level of error

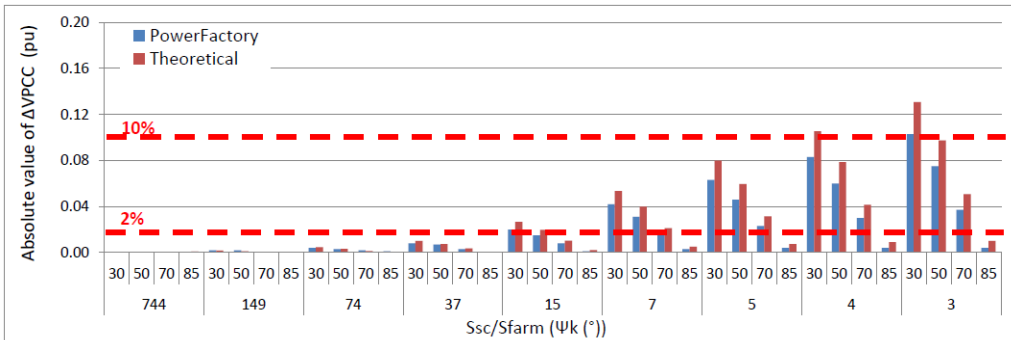
Both the results obtained with PowerFactory and those obtained with the simplified load flow programme are in good agreement, with an error not exceeding 3% for production



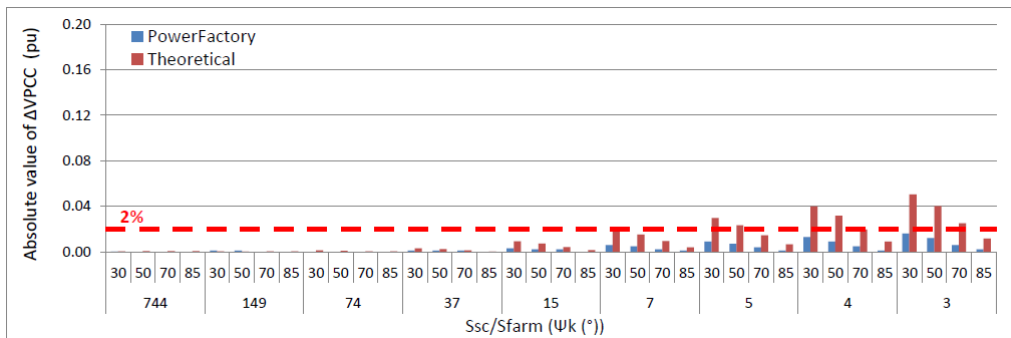
(a) $P_G=16.5$ MW (period A, lateral orientation)



(b) $P_G=15.5$ MW (period A, frontal orientation & period B, lateral orientation)



(c) $P_G=7.5$ MW (period B, frontal orientation)



(d) $P_G=1.0$ MW (period C, both orientations)

Figure 4.21: Absolute value of the maximum voltage step obtained for different values of the farm power output P_G , as a function of the short-circuit ratio and of the impedance angle

periods A and B. However, the error is greater (3.4%) for production period C. It is interesting to investigate the nature of the different sources inducing this error. This rapid analysis focuses on the type of network and on the conditions under which the maximum level of error (equal to 3.4%) is observed, that is for a short-circuit ratio is equal to 3, an impedance angle Ψ_k is equal to 30° , and a farm power output equal to 1 MW.

In this case, no error on the voltage corresponding to the case where the farm is disconnected is observed between the results obtained with PowerFactory and those obtained with the simplified load flow programme. Hence, the error is entirely due to the case where the farm outputs 1 MW. A fraction of this error equal to 0.9% is due to the simplifications performed for obtaining the theoretical model which consists of:

- assuming an equal cable length of 11.25 km,
- neglecting the influence of the onshore substation’s power consumption on its local voltage,
- simulating the power consumption of the 38 kV load as constant.

The loads are indeed modelled by default in PowerFactory as being voltage-dependent. Their voltage dependence law is defined as:

$$P = P_0 \left(\frac{V}{V_0} \right)^{1.6} \quad (4.57)$$

$$Q = Q_0 \left(\frac{V}{V_0} \right)^{1.8} \quad (4.58)$$

where P_0 and Q_0 are the active and reactive power corresponding to the nominal voltage V_0 . It is interesting to note that the maximum level of error corresponds to the lowest value of the farm power output P_G (equal to 1 MW). In this case, the power consumption of the onshore substation, which is equal to 0.1 MW, is no longer negligible compared to the power flow coming from the farm, contrary to what is assumed in the simplified load flow programme.

As 0.9% of error is due to the simplifications done for the model used with the simplified load flow programme out of the 3.4% observed in the worst case, the algorithm itself can be assumed to be responsible for an error level equal to 2.5%. This error level, although relatively low, was expected from the limitations of the Newton-Raphson algorithm themselves: the classical form of the algorithm, usually considered as very efficient for large transmission systems, is known for being relatively less robust in the case of weak distribution networks [92], as it is the case here. However, this is this type of algorithm which is used in the simplified load flow programme while PowerFactory uses another form of the Newton-Raphson algorithm for this type of networks, which is based on current equations rather than on power equations.

Immunity levels

Table 4.17 summarises the maximum short-circuit ratio up to which a voltage step of significant amplitude can be induced by the sudden disconnection of a farm outputting its maximum power for the different production periods considered.

Limit (%)	Production periods			Limit (%)	Production periods		
	A	B	C		A	B	C
2	15	15	N/A	2	15	15	N/A
10	5	3	N/A	10	5	5	N/A

(a) Frontal orientation

(b) Lateral orientation

Table 4.17: Highest short-circuit ratio up to which the network is affected

It must be noted that the monotonically decreasing trend of the voltage step amplitude as a function of the impedance angle Ψ_k is typical of unity factor operation: when a different value of power factor is applied, this trend may no longer be monotonic, as shown later in Section 4.7.2 on voltage limits.

It appears that the sudden disconnection of an approximately 20 MW-rated wave farm may induce of voltage step whose amplitude is greater than or equal to 2% up to a short-circuit ratio less than or equal to 37 for grids with a low impedance angle Ψ_k . However, it is important to bear in mind that this impedance angle has a strong influence on the amplitude of the induced voltage step, limiting it to 3% only for $\Psi_k=85^\circ$ in the case of the lowest short-circuit ratio considered in this study and equal to 3, while it is as high as 22% for $\Psi_k=30^\circ$.

Exceeding the 10% voltage step limit may also be an issue, but for a more limited number of potential connections points whose short-circuit ratio is less than or equal to 5. However, if their impedance angle Ψ_k is greater than or equal to 70° , such a voltage step cannot be induced by the sudden disconnection of a 20 MW-rated farm. Hence, they can be considered as immune to this issue.

Another point which must also be noticed concerns the influence of the wave farm orientation on the voltage step amplitude at the PCC. Voltage steps of higher amplitude are observed when the lateral orientation is used compared to the frontal orientation. This is explained by the higher level of maximum power generated in the former orientation due to the greater number of generators outputting the same power output simultaneously.

Table 4.18 indicates whether the test sites considered in this study may be affected or not by a voltage step exceeding the limit of 2%. None of this test site is considered to be affected by a voltage step exceeding the 10% limit.

Generally-speaking, it must be borne in mind that a connection point presenting any of the short-circuit ratio and impedance angle considered in this study may not necessarily exist in practice. For instance, it is unlikely that a connection point whose impedance angle can be considered as low (equal to 30° for instance) may present a high short-circuit ratio equal to 37. This means that, even though this study highlighted that a voltage step of 2% could be induced at a node whose short-circuit ratio is equal to 37 and whose impedance angle is equal to 30° , in practice, this type of node is unlikely to be found in a real power system. However, data being unavailable regarding the typical combinations of short-circuit level and impedance angle, the results with respect to all the possible combinations are presented. Another point which must be borne in mind regards the power transfer capacity at nodes whose low short-circuit ratio and low impedance angle. The power transfer capacity, which is usually low at this type of nodes, may constitute the main obstacle regarding the connection of a 20-MW rated wave farm. Data being unavailable

Test site	2%	10%
Achill Island	affected	immune
Belmullet	affected	immune
Grallagh	affected	immune
Doory	affected	immune
Killard	immune	immune
Dingle	immune	immune
WaveHub	immune	immune
bimep	immune	immune

Table 4.18: Results of the compliance test of the different test sites considered in this study with respect to the most stringent (2%) and to the most permissive (10%) voltage step limits

as well regarding this criterion, it was not taken into account to filter the results presented in this study.

Summary

In conclusion, exceeding the 2% voltage step limit represents an issue for all the test sites supplied by a relatively weak network whose short-circuit ratio is smaller than 37, regardless of their impedance angle Ψ_k . Most potential test sites located off the west coast of Ireland were determined to be potentially affected by this issue.

Exceeding the 10% voltage limit may be considered as a potential issue for a more limited number of connection points, and presenting both a short-circuit ratio less than or equal 5 and an impedance angle Ψ_k less than 70° . It was emphasized that inducing a voltage step whose amplitude exceeds this limit may pose a threat for the stability of this type of particularly weak networks as in Ireland for instance, generators are not required to remain connected after this type of event. However, the usually limited power transfer capacity at these nodes having both a low short-circuit ratio as well as a low impedance angle may constitute the main obstacle to the grid connection of a 20-MW rated farm.

4.7.2 Voltage limits

Both the maximum and minimum voltages are investigated and compared to the limits defined in Section 4.4. As mentioned earlier, five different time delays were used to simulate different layouts of the devices within the farm. The maximum and minimum voltages for given impedances Z_S , impedance angles Ψ_k , production periods and wave farm orientations are defined respectively as the maximum and minimum values over all these five simulations.

It is important to mention that the voltage at the point of common coupling never remains persistently outside the allowed range, as shown in Figure 4.22a and 4.22b. These two figures present the voltage profile at the point of common coupling under worst case conditions, that is for production period A with a lateral farm orientation, combined with the lowest short-circuit ratio as well as with the lowest impedance angle Ψ_k considered in this study which are equal to 3 and 30° respectively. These two figures correspond to the extreme power factors considered in this study which are equal to 0.92 lagging and unity.

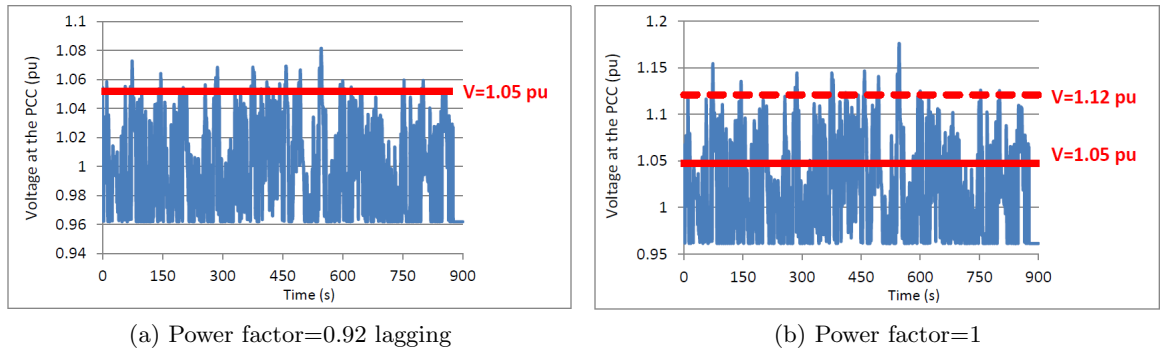


Figure 4.22: Voltage profile at the PCC under worst case conditions for two different values of the power factor

Although voltage may remain few seconds to few tens of second above or below the limits (in particular with respect to the most stringent limits), these voltage excursions still remain classified, as defined in the standard IEEE-1159-2009, as “voltage sag” and “voltage swell” respectively. However, considering the repeated number of times a wave farm may generate voltage sag or swell episodes over a relatively short timescale of the order of magnitude of tens of seconds, it may seem appropriate to define a more suitable denomination for characterising this type of voltage disturbances. However, the development of power quality criteria adapted to wave devices is out of the scope of this thesis.

Maximum voltage

Figure 4.23 shows the maximum voltages obtained during a simulation as a function of the short-circuit ratio. For the sake of clarity, the abscissa axis was limited to a maximum value of 100. As expected, voltage converges towards the value imposed by the ac voltage source, 1.0 pu. In addition, its deviation from this value decreases as the impedance angle Ψ_k increases which is typical of the operation at unity power factor. For impedance angles up to 70° , deviation is positive (maximum voltage is greater than 1.0 pu), whereas it is negative for $\Psi_k=85^\circ$. This trend will be explained in more detail later in this section.

The results shown in Figure 4.23 demonstrate that swell may occur under medium and high energy level sea conditions in networks whose short-circuit level and impedance angle is sufficiently low. Although the voltage remains within narrow limits for production period C (the minimum deviation below the nominal value is less than -4%), it can exceed 1.05 pu for both production periods A and B, the 1.12 pu upper limit being exceeded for production period A only. Table 4.19 shows the short-circuit ratio above which voltage swell is no longer an issue for 30° networks, representing the worst case scenario with respect in the case where unity power factor is maintained at the PCC.

However, in similar fashion to the amplitude of a voltage step, the maximum voltage is highly dependent on the impedance angle Ψ_k . Table 4.20 shows for instance the maximum voltage obtained under worst case conditions, namely production period A with the lateral farm orientation) for the four impedance angles considered in this study. It is clear that networks whose impedance angle is greater than or equal to 70° are not affected by voltage swell, voltage remaining below 1.05 pu at all times. Hence, none of the site taken as example is affected. An impedance angle of 50° leads to voltage exceeding 1.05 pu, but maintained below 1.12 pu, for networks whose short-circuit ratio is smaller than 7. How-

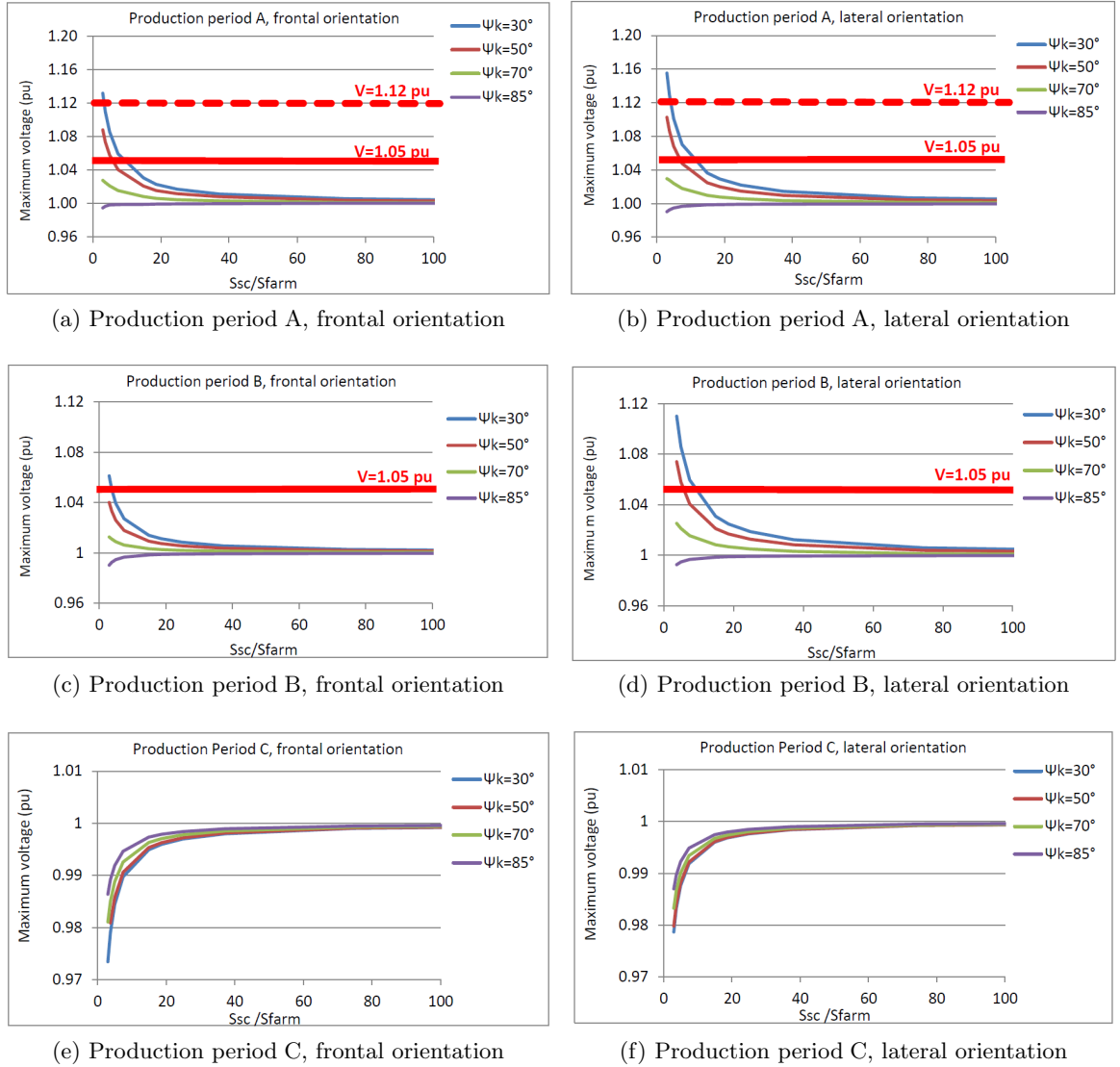


Figure 4.23: Maximum voltage for the different production periods and farm orientations considered as a function of the short-circuit ratio

Limit (pu)	Production periods		
	A	B	C
1.05	9	4	immune
1.12	3.5	immune	immune

(a) Frontal orientation

Limit (pu)	Production periods		
	A	B	C
1.05	11	10	immune
1.12	4	immune	immune

(b) Lateral orientation

Table 4.19: Short-circuit ratio above which voltage swell is not an issue

Limit (pu)	Ψ_k ($^{\circ}$)			
	30	50	70	85
1.05	4	7	immune	immune
1.12	11	immune	immune	immune

Table 4.20: Short-circuit level above which voltage swell is not an issue under worst case conditions (production period A, lateral orientation)

Test site	+5%	+12%
Achill Island	immune	immune
Belmullet	immune	immune
Grallagh	immune	immune
Doory	immune	immune
Killard	immune	immune
Dingle	immune	immune
WaveHub	immune	immune
bimep	immune	immune

Table 4.21: Results of the compliance test of the different test sites considered in this study with respect to the voltage swell limits

ever, this type of network can be considered as immune to voltage swell in regions where the most permissive limit 1.12 pu is enforced. As regards the test sites considered as examples in this work, none of them is affected by voltage swell, as summarised in Table 4.21.

These results were compared to those obtained with the simplified load flow programme developed for the purpose of this thesis. In similar fashion to the voltage step study presented in Section 4.7.1, the calculation of the voltage at the PCC with this programme is based on the maximum power output of the wave farm for a given production period. Table 4.22 presents the maximum absolute value of the error between the results obtained with PowerFactory and those obtained with the simplified load flow programme. These results are similar, but not equal to those presented in Section 4.7.1 which discussed the error with respect to the voltage step analysis. This is explained by the fact that in the previous study, only one time delay set was used whereas five of them are used in this study. The error level remains relatively low, indicating a relatively good agreement between the results obtained from the two different tools.

Production period	A	B	C
Frontal orientation	3.5	3.0	3.7
Lateral orientation	2.0	2.1	

Table 4.22: Maximum absolute error (%) between the results obtained with PowerFactory and those obtained with the simplified load flow programme

Minimum voltage

A study similar to this presented in the previous section was conducted concerning the minimum voltages obtained for the three different production periods and for the two farm orientations considered in this study. In this case again, both the results obtained with PowerFactory and with the simplified load flow programme are in good agreement.

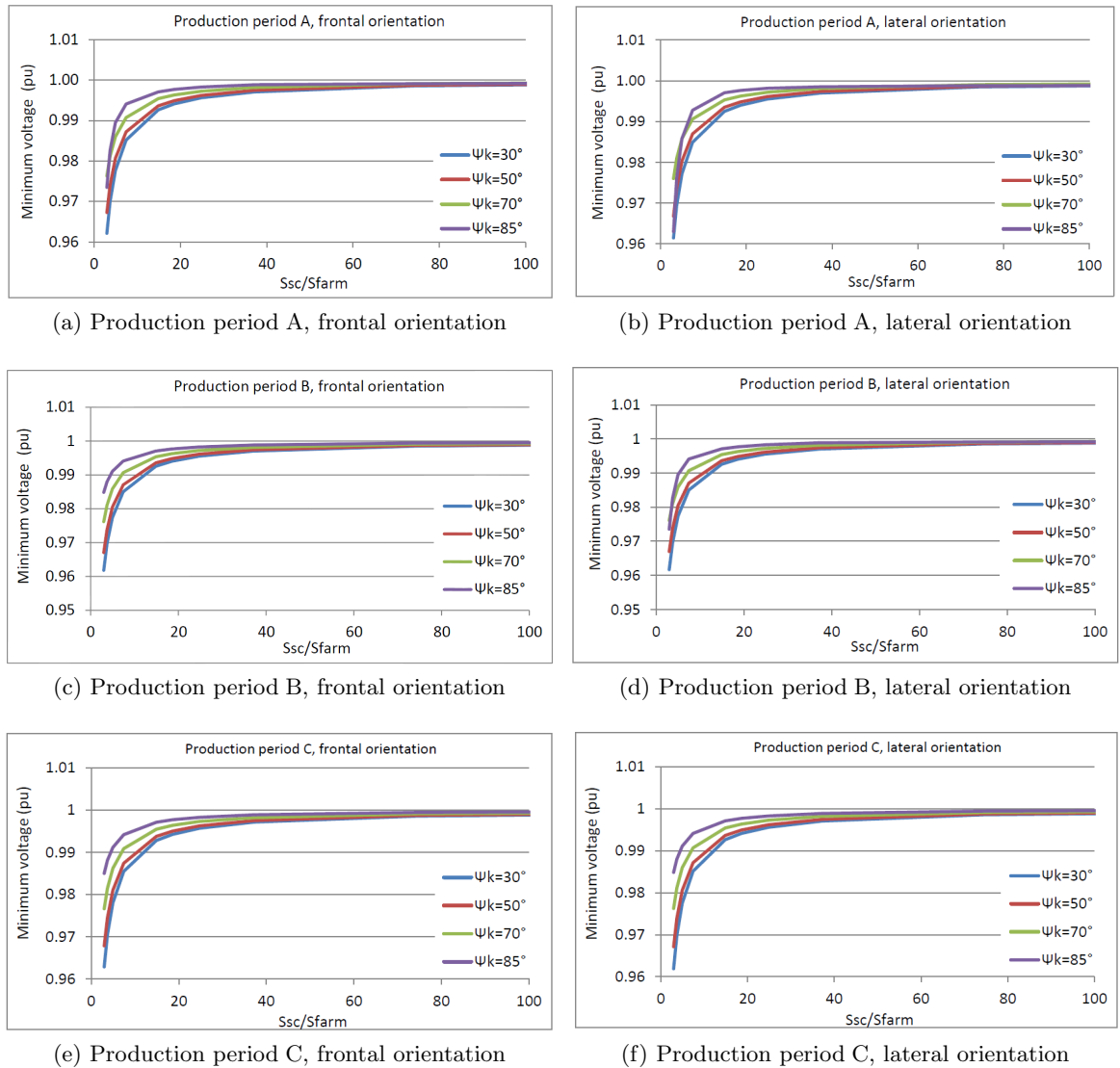


Figure 4.24: Minimum voltage for different production periods and farm orientations as a function of the short-circuit ratio

Figure 4.24 demonstrates that voltage sag is not an issue in this case as voltage remains above 0.96 pu for any combinations of the short-circuit ratio and of the impedance angle considered in this study. Hence, none of the test sites considered as examples in this work is affected by this issue, as summarised in Table 4.23.

Power factor control

The two previous studies showed that a limited number of connection points may be affected by a voltage swell issue whereas voltage sag was no issue for any of the potential connection points considered. This voltage swell issue can be mitigated by applying a lagging power factor at the PCC by means of the controlled VAR compensator, as opposed to a unity power factor as used in the previous studies. This strategy is actually enforced by the Irish distribution system operator ESB in the case of wind farms connected to the distribution network. Typically, connecting a power plant of significant power capacity to this type of low voltage networks induces a voltage rise due to the direction reversal of the active power flow. This voltage rise can be counteracted by reactive power flowing

Test site	-6%	-10%
Achill Island	immune	immune
Belmullet	immune	immune
Grallagh	immune	immune
Doory	immune	immune
Killard	immune	immune
Dingle	immune	immune
WaveHub	immune	immune
bimep	immune	immune

Table 4.23: Results of the compliance test of the different test sites considered in this study with respect to the voltage sag limits

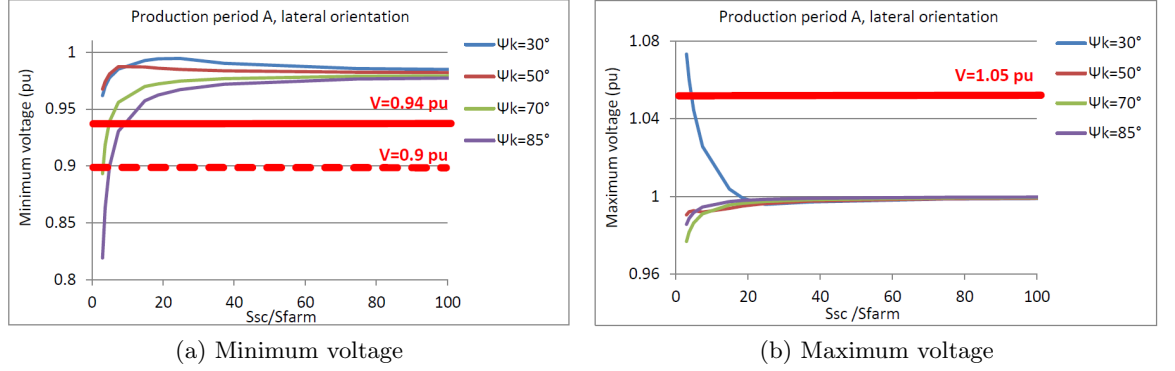


Figure 4.25: Minimum and maximum voltages obtained for production period A, lateral orientation, 0.92 power factor lagging, as a function of the short-circuit ratio

in the opposite direction. Figure 4.25b shows that the maximum voltage obtained for the worst case conditions (namely production period A with the lateral farm orientation) is actually reduced below the most permissible limit when a 0.92 lagging power factor is applied. Applying a lagging power factor has the additional advantage to reduce flicker level significantly in networks with an impedance angle less than or equal to 70° , as detailed in next section.

However, this method has its limitations, which are described here based on a simplified two-bus electrical network which is presented in Figure 4.26. As described in (3.12), the voltage drop ΔV_{2bus} through the impedance $\bar{Z} = R + jX$ between busses B_1 and B_2 can be expressed as:

$$\Delta V_{2bus} = \frac{PR + QX}{V_1} \quad (4.59)$$

where P and Q are the active and reactive power flowing through the impedance \bar{Z} . Hence, the voltage variation ΔV_{2bus} is equal to zero provided that the following condition is met:

$$\frac{P}{Q} = -\frac{X}{R} \quad (4.60)$$

This condition shows that this method is efficient only as long as the ratio of the impedances $\frac{X}{R}$ is of the order of magnitude of the ratio of the powers $\frac{P}{Q}$. Assuming that

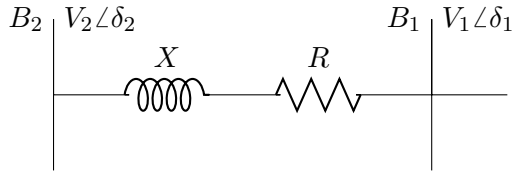


Figure 4.26: Simplified two-bus system

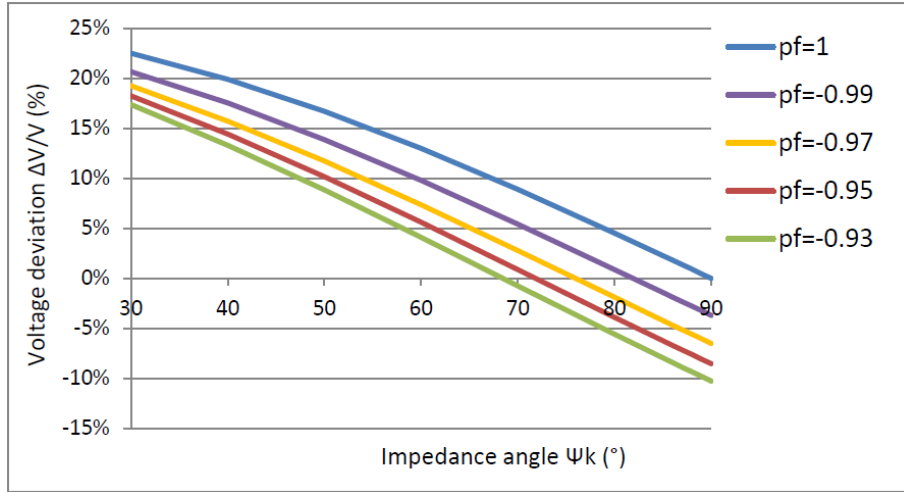


Figure 4.27: Theoretical voltage deviation for $P=15$ MW as a function of the impedance angle Ψ_k (short-circuit ratio=3)

the amount of reactive power Q flowing from bus B_1 to bus B_2 is defined from a fixed power factor pf which can be expressed as:

$$pf = \frac{P}{\sqrt{P^2 + Q^2}} \quad (4.61)$$

Hence, (4.59) can be re-written as:

$$\begin{aligned} \frac{P}{P\sqrt{\frac{1}{pf^2} - 1}} &= \frac{X}{R} \\ \sqrt{\frac{1}{pf^2} - 1} &= \frac{R}{X} \end{aligned} \quad (4.62)$$

Figure 4.27 shows the voltage drop ΔV for $P=15$ MW and for a short-circuit ratio equal to 3. This figure shows that in the case where a lagging power factor is applied, the voltage drop ΔV may be negative for the connection points having a sufficiently high impedance angle Ψ_k . This means that the voltage at the bus B_1 is greater than the voltage at the bus B_2 . Consequently, the voltage corresponding to a peak of active power is less than the voltage corresponding to the case where the farm power output is equal to 0 MW, which is precisely what is observed for the voltage with respect to an impedance angle Ψ_k equal to 85° as shown in Figures 4.24a to 4.24f. This effect is amplified by using an increasingly lagging power factor, as illustrated in Figure 4.25a.

In summary, the application of a fixed power factor at the PCC can be considered as a reasonable strategy provided that the power factor is suitably selected according to the impedance angle Ψ_k . The beneficial effect of a lagging power factor at the PCC is

undeniable for weak networks having a low impedance angle equal to 50° . As shown in Figure 4.25b, networks whose impedance angle is equal to 50° become immune to voltage swell as a result of this control strategy. However, this technique has little effect on the networks whose impedance angle is equal to 30° , due to the highly resistive nature of the impedance. Hence, this technique should be applied with discernment, and the power factor selection should be based on the network impedance angle rather than on the voltage level of the point of common coupling and on the presence or not of other customers as it is currently done, for instance in the Republic of Ireland. In addition, applying a lagging power factor may induce significant low voltage level at the connection points whose impedance angle is greater than or equal to 70° , as illustrated in Figure 4.25a. Hence, operating at unity power factor should be preferred in this case.

Comparison with the results obtained from the simplified analytical case study presented in Chapter 3

It is interesting to compare the results obtained with this detailed case study regarding the Belmullet test site to those obtained with the simplified analytical case study described in Chapter 3. In the latter, the electrical power output of a group of wave devices was modelled as a sum of an average power P_{avg} and of sinusoidal terms. The power factor applied at the PCC was equal to 0.93 lagging, so the results obtained in this study for a power factor equal to 0.92 lagging were retained for the comparison.

The simplified study indicated that no voltage swell may be observed if a medium-size farm were to be connected at this type of node, which is also the conclusion of the detailed study. In addition, the results of the simplified study indicated that the voltage may be less than the lower limits enforced by the Irish grid operator and equal to 0.90 pu. The minimum voltage was estimated to 0.84 pu in the simplified study, while it is equal to 0.91 pu (thus slightly above the lower limit) in the detailed study. Hence, the simplified study provided a reasonable estimate of the maximum and minimum voltages to be expected in terms of voltage at the Belmullet test site.

Summary

Both the maximum and minimum voltages reached at the point of common coupling under the influence of a 20 MW-rated wave farm were investigated. The results obtained with PowerFactory were compared to those obtained with the simplified load flow programme developed for the purpose of this thesis and showed good agreement.

The results were also compared to the most permissive as well as to the most stringent voltage limits enforced in different countries. It was demonstrated that the voltage may be less than the most stringent lower limit (and close to the most permissive lower limit) in the case where the power factor at the PCC is sufficiently low. In similar fashion, the voltage may also exceed both the most stringent as well as the most permissive upper limits in this case. However, the application of a suitably selected power factor was found to be an efficient mitigation means with respect to both the voltage sag and swell issues.

The power factor should be selected based on the impedance angle Ψ_k . A lagging power factor was recommended to be applied if the wave farm is to be connected to points with low impedance angles Ψ_k up to 50° . On the contrary, a unity power factor should be applied for higher impedance angles greater than 70° .

Limit	Ψ_k ($^\circ$)			
	30	50	70	85
0.35	17	13	6	immune
1.0	6	4	immune	immune

Table 4.24: Short-circuit ratio above which flicker is not an issue

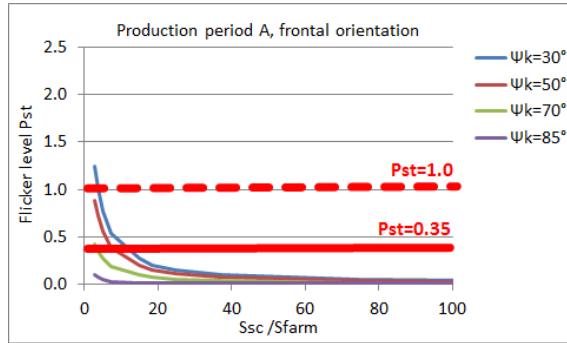
However, it seems that no grid operator defines requirements in terms of power factor based on the impedance angle Ψ_k of the connection point to which a power generation plant is connected. In the Republic of Ireland for instance, the power factor range for which a wind power plant is expected to operate depends only on the topography of the grid connection, including criteria such as the voltage level of the point of common coupling, and the existence or not of other customers connected to the same feeder or to parallel feeders. As a result, wind farms connected directly to the 110 kV level or connected at the low voltage side of a 38/110 kV transformer (without parallel connections of other customers) are expected to operate for a large range of power factor (both lagging and leading) while wind farms connected at lower voltage levels are required to operate at a power factor between 0.92 and 0.95 lagging. The strategy adopted by the Irish grid operator is to mitigate the voltage rise induced by the direction reversal of the active power flow in a distribution feeder due to the connection of a power generation plant at this level. As detailed in this work, although this strategy may be efficient for connection points with an impedance angle equal to 50° , it may not be sufficient for connection points with an impedance angle equal to 30° , and be even counterproductive regarding connection points with an impedance angle at least equal to 70° compared to operating at unity power factor. The requirements in terms of power factor may thus need to be modified to facilitate a safer integration of wave farms to the distribution grids.

In addition, the simplified study presented in Chapter 3 was shown to provide a reasonable estimate of the trends to be expected in terms of voltage at the Belmullet test site.

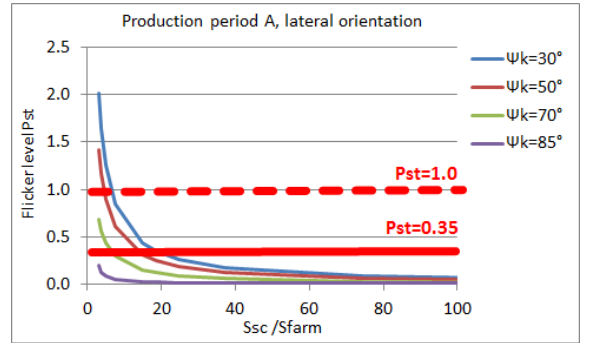
4.7.3 Flicker level

Flicker level exceeding its limit represents an issue for both production periods A and B, its level remaining below 0.35, the most stringent limit, for production period C although being non-negligible, as shown in Figures 4.28a to 4.28f. The short-circuit ratios above which flicker is not an issue are presented in Table 4.24. The results indicated in this table demonstrate that flicker is an issue which may be more important than voltage swell as a larger number connection points are potentially affected by an excessive flicker level than by voltage swell, as was shown in Table 4.20.

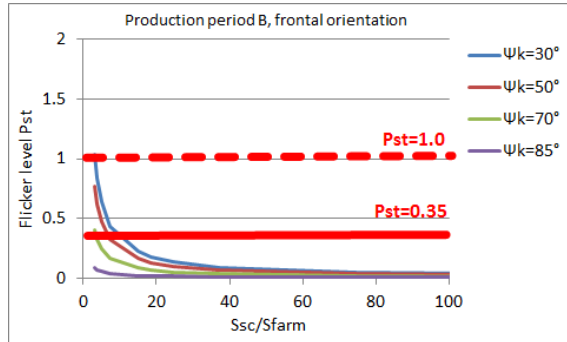
Connection points with lower impedance angles of 30° to 50° can mostly be considered as potentially affected by an excessive flicker level if unity power factor is applied at the PCC. The short-circuit ratio above which flicker is below the most stringent limit is equal to 17 and to 13 for the 30° and 50° connection points respectively. However, these short-circuit ratios are relatively greater than the typical short-circuit ratio for this type of connection points. The short-circuit ratio required for preventing flicker from exceeding the most permissive limit is equal to 5 only, which remains however very significant for this type of connection points. In conclusion, if a unity power factor is to be maintained at the PCC, and if no mitigations means are employed, most of the 30° to 50° connection points must be considered as potentially affected by an excessive flicker level.



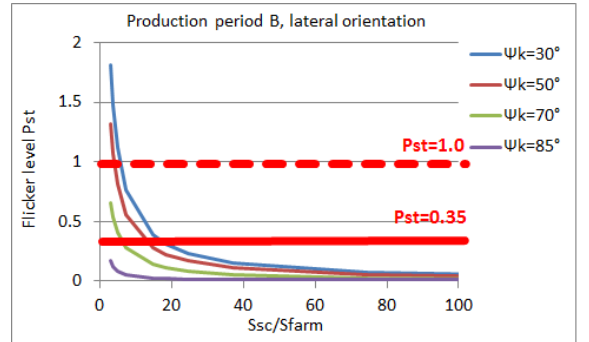
(a) Production period A, frontal orientation



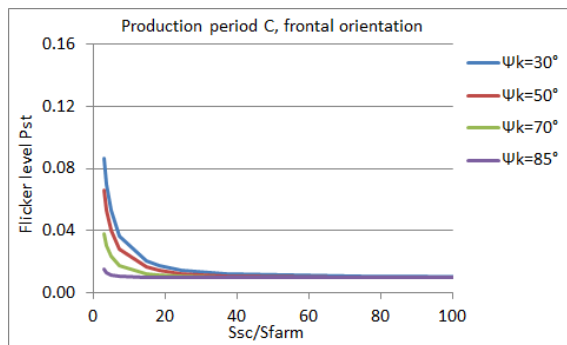
(b) Production period A, lateral orientation



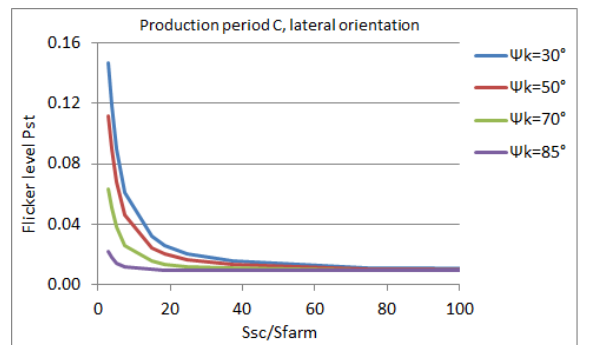
(c) Production period B, frontal orientation



(d) Production period B, lateral orientation



(e) Production period C, frontal orientation



(f) Production period C, lateral orientation

Figure 4.28: Maximum flicker level for different production periods and both farm orientations as a function of the short-circuit ratio

The situation is more complex for networks whose impedance angle is equal to 70° , as, although flicker level is always maintained below unity, it can be far greater than 0.35, thus constituting a potential issue. Flicker is however no issue for those connection points whose short-circuit ratio is greater than 6. It is interesting to note that this is the case only for the two strongest Irish connection points, namely Dingle and Killard, as well as the WaveHub and the bimep. The flicker in the rest of the test sites selected as examples being greater than 0.35, a wave farm connected to these sites could be considered as failing to meet the flicker requirements, as the most stringent limit is enforced in Ireland. More generally speaking, 70° connection points can be considered as potentially failing to meet the flicker requirements. This may be the case if the flicker level exceeds the individual emission limit (if any) and/or whether the plant's contribution makes the total flicker level at the PCC exceeds the total limit assigned to this node. A short-circuit ratio greater than 6 is thus recommended for the connection to 70° points, the use of mitigation means being necessary otherwise. Finally, 85° points can be considered as immune to the flicker issue as flicker remains below the most stringent limit regardless of the short-circuit ratio.

It is interesting to note that the lateral farm orientation corresponds to the worst case conditions in terms of flicker level for a given production period, as it was for the voltage step and for the voltage limits analyses. This tends to indicate that the voltage peaks of higher amplitude generated with this orientation have more influence on the farm's flicker level than the higher number of voltage fluctuations created when the frontal orientation is used. Further analyses on this aspect are presented in Chapter 7.

Finally, it is also interesting to observe that a short-circuit ratio equal to 5 only is necessary to prevent the flicker induced by the wave farm considered in this study from exceeding unity when a unity power factor is applied at the PCC. In comparison, it used to be recommended to connect wind farms to nodes whose short-circuit ratio was at least equal to 25 [25]. This difference can be explained by the lower perceptibility of wave-induced voltage fluctuations, due to their typically lower frequencies compared to those generated by wind farms.

Power factor control

Power factor control at the PCC is expected to be an efficient means for mitigating flicker. As mentioned in the previous section, applying a lagging power factor at the PCC can, in certain cases, reduce the amplitude of the voltage fluctuations induced by the injection of fluctuating power, thus reducing flicker as well. More specifically, it was found that wind farms could be connected to nodes with a short-circuit ratio equal to 3 without leading to a flicker level exceeding unity [47], whereas a short-circuit at least equal to 25 used to be recommended for operation at unity power factor, as mentioned in the previous section.

The results obtained in this study show as well that applying a lagging power factor can help reduce flicker level for connection points having an impedance angle up to 50° or 70° , as expected. Figure 4.29a shows the flicker level obtained under worst case conditions, namely production period A with the lateral farm orientation, for the minimum short-circuit ratio equal to 3. The figure shows the results obtained for the three power factors considered in this study, namely: unity, 0.95 and 0.92 lagging. It is clear from this figure that a dramatic flicker level decrease can be obtained for connection points with a low impedance angle up to 50° . Applying a 0.92 lagging power factor leads even to decrease the flicker down to a level extremely close to 0.35 in the 50° case. The short-circuit ratio above which flicker is no longer an issue with respect to the most stringent limit in this

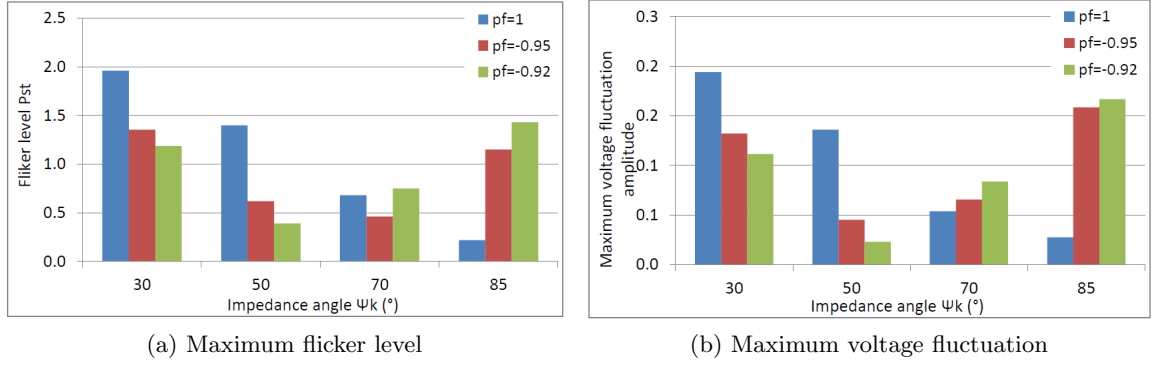


Figure 4.29: Flicker level and maximum voltage amplitude ΔV under worst case conditions for different impedance angles Ψ_k and for different power factors (pf)

particular case decreases from 13 to only 3, which, although remaining a high short-circuit level value for most 50° connection points, can be exceeded by some of them.

This significant decrease does not however prevent flicker level from exceeding unity in the 30° case. The short-circuit level above which flicker is no longer an issue in this case presents a dramatic decrease from 17 to 3.5, but this remains still greater than the short-circuit ratio of an overwhelming majority of 30° connection points. Hence, applying a lagging power factor is not considered as an efficient solution for reducing the flicker level in this case. Finally, applying a unity power factor at nodes whose impedance angle Ψ_k is equal to 85° is recommended, as applying a lagging power factor makes the flicker level increase for this type of nodes. As expected from these observations, the connection of a medium-size wave farm to some of the sites considered in this study may give rise to flicker issues, as summarised in Table 4.25.

The trend of the flicker level as a function of the impedance angle Ψ_k is similar to the trend observed with respect to the maximum amplitude which a voltage fluctuation may present, as shown in Figure 4.29b. This maximum amplitude ΔV is calculated as the difference between the maximum voltage minus the minimum voltage obtained during a simulation with PowerFactory as:

$$\Delta V = \max(V(t)) - \min(V(t)) \quad (4.63)$$

Although such voltage fluctuation may or may not occur during a simulation, estimating this maximum amplitude gives an insight into the actual amplitude of the voltage fluctuations generated by the wave farm. Further analysis focusing on this topic are detailed in Chapter 7.

Comparison with the results obtained from the simplified analytical case study presented in Chapter 3

It is not possible to compare directly the results obtained for Belmullet from this study to those obtained with the simplified analytical case study presented in Chapter 3. The flicker analysis in this latter study was performed for a wave farm whose power oscillates closely around 10 MW whereas the amplitude of the voltage fluctuations are more important in the experimental time series. In addition, the power profile of the farm as defined in the simplified study is much smoother than this based on the experimental time series.

Test site / Pst limit	0.35	1.0
Achill Island	affected	immune
Belmullet	affected	immune
Grallagh	affected	immune
Doory	affected	immune
Killard	immune	immune
Dingle	immune	immune
WaveHub	immune	immune
bimep	immune	immune

Table 4.25: Immunity status of different test sites with respect to flicker level compliance test (provided that a suitable power factor is applied at the PCC)

However, it is worth comparing their order of magnitude. The maximum flicker level Pst was estimated to be equal to 0.21 in the simplified analytical case study, whereas it was evaluated to range between 0.5 (frontal orientation) and 0.6 (lateral orientation) in the detailed study. This shows that, despite important modelling differences in terms of farm power profiles, the results obtained from the simplified analytical case study already gave a reasonable insight on the order of magnitude of the flicker level generated. However, this difference emphasises the importance of experimental data in evaluating the impact of wave energy on the grid.

Summary

In conclusion, flicker may be maintained below even the most permissive limit by means of power factor control. However, flicker level may remain very high for 30° networks for which the beneficial effect of this type of control strategy is limited. On the contrary, a dramatic flicker level decrease is observed for 50° networks, rendering flicker level close to the most stringent limit under worst case conditions. It is recommended however to maintain a unity power factor at the PCC for connection points whose impedance angle Ψ_k is greater than 70° to prevent both voltage sag and flicker level increase. In addition, mitigation means, such as storage, may be necessary for 70° connection points whose short-circuit ratio is smaller or equal to 6. Connection points whose impedance angle is about equal to 85° are not affected by excessive flicker level.

The results of the study presented in this chapter were compared to the results obtained from the simplified analytical case study which was presented in Chapter 3. Despite important modelling differences in terms of farm power profiles, the results of the simplified analytical case study were demonstrated to provide a reasonable insight into the order of magnitude of the flicker level generated by a wave farm.

4.7.4 Summary

The work presented in this section details the grid impact of a 20 MW-rated wave farm with respect to the three following power quality criteria: voltage step amplitude, voltage limits and flicker level. Power system simulations were performed for the typical range of short-circuit ratio and of impedance angle Ψ_k .

The results of these simulations were compared to those obtained from the simplified analytical case study presented in Chapter 3 in terms of maximum and minimum voltages as well as in terms of flicker level. The results obtained from this simplified study proved to be reasonably close to those obtained from the detailed study with respect to the max-

imum and minimum voltages. Although the conclusions regarding the flicker level cannot be compared directly, the results of the simplified analytical case study were demonstrated to provide a reasonable insight into the order of magnitude of the flicker level generated by a wave farm, despite important modelling differences in terms of farm power profiles. Hence, the simplified analytical case study was demonstrated to constitute an interesting starting point for the grid impact assessment of a wave farm before more detailed analyses are undertaken.

The results presented in this chapter show that flicker seems to be a major issue as it effectively determines the minimum short-circuit ratio required for avoiding power quality issues. More specifically, this study shows that point of a connection with an impedance angle as low as 30° can be affected by voltage step, voltage swell and flicker issues. Wave farms without further mitigation means than power factor control at the point of common coupling are not recommended to be connected to this type of nodes. This recommendation is based on power quality considerations, but seems doubly justified by the expected equipment overloading issues due to the typically low power transfer capacity available on low voltage distribution networks to which these points usually belong. Connection points with an impedance angle of 50° are also affected by these issues if their short-circuit ratio is smaller than 15, but they can be mitigated to a certain extent by applying a lagging power factor. This technique may in many cases render the wave farm compliant with the specified power quality requirements.

However, in the case where the most stringent flicker limit is enforced, additional mitigation means such as storage would be required, as it would be the case for farms connected to a 70° connection point, whatever the applied power factor value at the point of common coupling, if the short-circuit ratio is smaller than 6. Connection points whose impedance angle is equal to 85° are not affected by any of these issues.

More generally speaking, the results imply that:

- Medium size wave farms can be safely connected to relatively weak grids (down to 50°), provided that the power transfer capacity is sufficient and that a suitable power factor control is applied. The possible utilisation of 50° connection points is very interesting for regions or countries having a relatively weak power system, as it is the case in developing and some emerging countries. This potential utilisation is also interesting for providing power to partially damaged electrical power systems, for instance in the case of natural disasters or of man-made events [93].
- In addition, it appears that wave farm owners may not necessarily need initially to connect their plants to a very strong connection point which may be located very far inland, as it is the case in the rural areas of Ireland and Scotland. Hence, they may avoid the costly installation of a long overhead line between the test site's onshore substation and the inland connection point. From a financial point of view, this means that the expensive power system reinforcement necessary for facilitating the large scale integration of wave farms can be postponed until the wave energy industry reaches a certain degree of commercial maturity. This represents a major asset for the wave energy community as it will enable the different stakeholders to gain confidence in the technology before important investments are required.

It seems interesting at this stage to discuss the relevance of the requirements currently enforced by the grid operators, in particular in terms of flicker. Although flicker seems usually limited to 0.8-1.0, the Irish grid operator enforces a limit equal to 0.35 which corresponds to the lowest limit which may be enforced by a grid operator, as recommended

by the IEC standard 61000-3-7. This decision may be based on the assumption that the background flicker in distribution networks, as measured prior to the connection of a wave farm, may be already relatively high. However, this assumption may not be easily verifiable as this type of data is usually unavailable. The sole publication mentioning the level of background flicker monitored at an Irish location (more specifically at Strangford Lough) during three months indicates it is usually below 0.5, with a couple of occasions where the value reaches 1 [94].

It is important to note that the voltage level, the short-circuit ratio level and the impedance angle Ψ_k of the connection point at which these background flicker measurements were performed are very low and equal to 11 kV, to 10.7 MVA and to 50° respectively. Hence, the background flicker level as measured at a 20 kV node whose short-circuit ratio is at least equal to 3 (as it is the case for the sites taken as examples in this study) may be expected to be significantly lower. In addition, the frequency range of the voltage fluctuations induced by a wave farm is expected to be sensibly different from the typical frequency range of switching loads or starting motors at the origin of background flicker. Hence, as these two types of flicker contributions do not add algebraically, it may thus be expected the total flicker level as generated by a wave farm and by other loads or generators connected in the local area would be lower than the algebraic sum of these two types of contributions as analysed separately. These two reasons may lead to the conclusion that the very stringent requirement in terms of flicker level as enforced by the Irish grid operator may be relaxed without being detrimental to the customers.

In addition, the results presented in this study show that flicker exceeds this very stringent limit of 0.35 for a large number of short-circuit ratio/impedance angle combinations. Most connection points located off the west coast of Ireland where the wave energy resource is abundant were demonstrated to be potentially affected by flicker exceeding this limit while remaining below the most permissive limit equal to unity. Hence, if this requirement in terms of flicker level regarding the distribution systems is not relaxed, the large-scale development of the wave energy industry in this country may be significantly impeded.

4.8 Effect of wave farm direction and device layout within the farm

4.8.1 Introduction

This section investigates the influence of the farm orientation as well as the influence of device layout on power quality with respect to the maximum and minimum voltages, as well as to the flicker level.

4.8.2 Voltage limits

The wave farm orientation relative to the dominant wave direction has a strong influence on the extreme voltages reached during a simulation. Power peaks of higher amplitude are reached with the lateral orientation than with the frontal orientation, as mentioned previously. Consequently, the lateral orientation induces larger voltage deviations from the nominal value compared to the case where the frontal orientation is used. However, as expected, this difference between the two orientations decreases with both the short-circuit ratio and the impedance angle of the connection point. Figures 4.30a to 4.30c shows the maximum observed difference between the frontal and the lateral orientations for each of the production periods. Although this difference is negligible for production period C

(not exceeding 0.7%), it is significantly more important for production periods A and B for which a maximum difference up to 6% and 8% respectively can be observed for the weakest networks. This is very significant, especially compared to the voltage limits considered in this study which are equal to [-6%;+5%] for the most stringent limit and to [-10%;+12%] for the most permissive.

The influence of the farm direction is considered as negligible when the voltage difference between the maximum voltage obtained from the lateral orientation and this obtained from the frontal orientation is smaller than 1%. Under worst case conditions represented by production period A, the short-circuit ratio above which this condition is met ranges between 15 and 10 for 30° and 50° connection points respectively. Considering that their typical short-circuit ratio is much smaller, the influence of the wave farm orientation remains significant for most of these connection points. However, it is negligible for connection points whose impedance angle is greater than or equal to 70°.

The device layout has a lesser influence than the farm orientation. The influence of this parameter is defined by investigating the maximum voltage difference among all the maximum voltages obtained for the five time delay sets. Results showed that this difference is significant for 30°-50° connection points only, while it is smaller than 1% for connection points whose impedance angle is greater than or equal to 70°. This is illustrated in Figures 4.31a to 4.31f.

Given that the difference between different farm orientations, and to a lesser extent between different device layouts, may be significant, these parameters may be key factors with respect to the compliance of the farm to voltage limit requirements. This is for instance illustrated in Figures 4.32a and 4.32b. Although the most permissive limit may be exceeded when the lateral orientation is used, this is not the case when the frontal orientation is. More generally, the maximum voltage is significantly reduced when the frontal orientation is used.

4.8.3 Flicker level

In similar fashion to maximum voltage, the influence of the wave farm orientation on the flicker level is more important than that of the device layout. Figures 4.33a to 4.33c show the maximum flicker level difference between the frontal and lateral orientations. This difference can be very important for production periods A and B, as ranging around unity for the weakest grids. This emphasises the fact that the farm orientation and the device layout may be key factors with respect to the compliance of the farm to flicker requirements.

Figures 4.34a and 4.34b illustrate this fact: although the flicker level exceeds the most permissive limit for a relatively large number of short-circuit ratio/impedance angle combinations with the lateral orientation, none of them exceeds this limit with the frontal orientation.

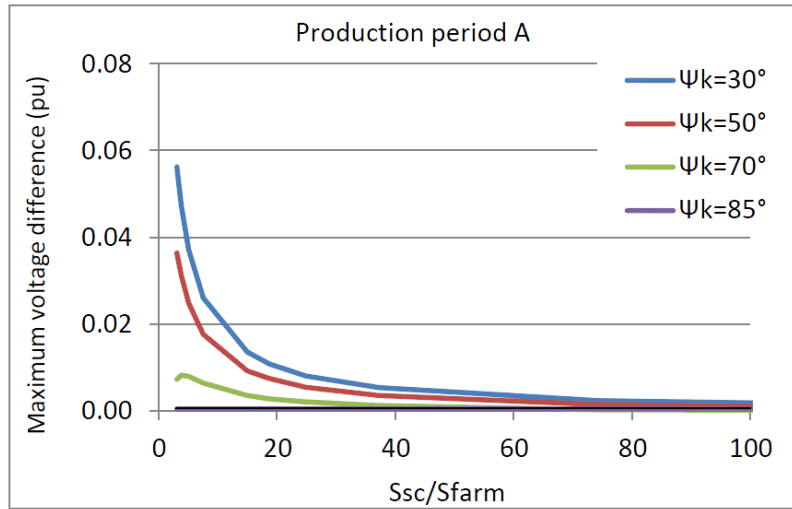
The farm orientation is considered to have a negligible influence when the maximum observed difference is smaller than 10% of the most permissive limit, i.e. 0.1. From this perspective, connection points whose impedance angle is as high as 85° are not significantly affected by the farm orientation, considering their typically high short-circuit level. The influence of the farm orientation becomes negligible above a short-circuit ratio of 13 for 70° connection points. The high value of the minimum short-circuit ratio for which it is negligible for both 30° and 50° connection points, being equal to 35 and 25 respectively,

means that the orientation has always a significant influence on the flicker level at these connection points.

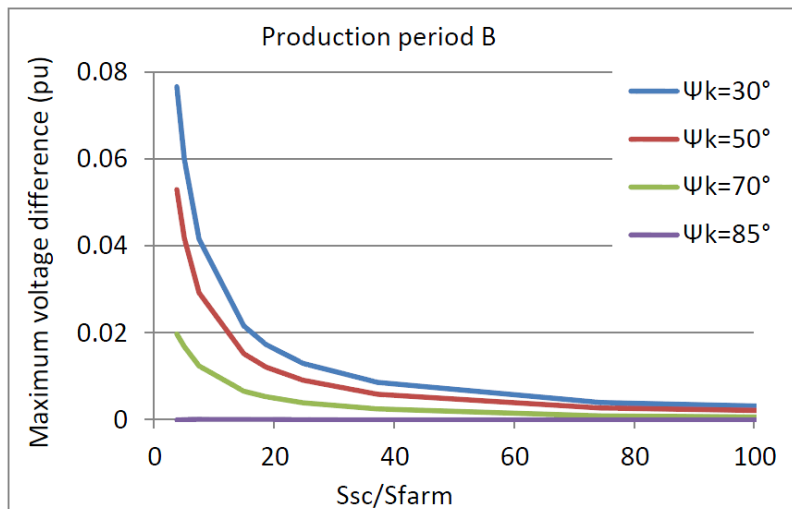
The device layout has also a lesser influence than that of the farm orientation on the flicker level for most short-circuit ratio/impedance angle combinations, as shown in Figures 4.35a to 4.35f. The maximum flicker difference obtained among the different production periods can be as high as 0.24 with the frontal orientation and 0.18 with the lateral orientation (the two of them occurring for production period A) for these weak connection points. These two values are significant compared to the most stringent emission limit of 0.35. The influence of device layout for 30° to 50° connection points can be considered as almost always significant, considering that the short-circuit of most of these points may be smaller than 5. On the contrary, the influence of the device layout is negligible for connection points whose impedance angle is greater than or equal to 70° .

Summary

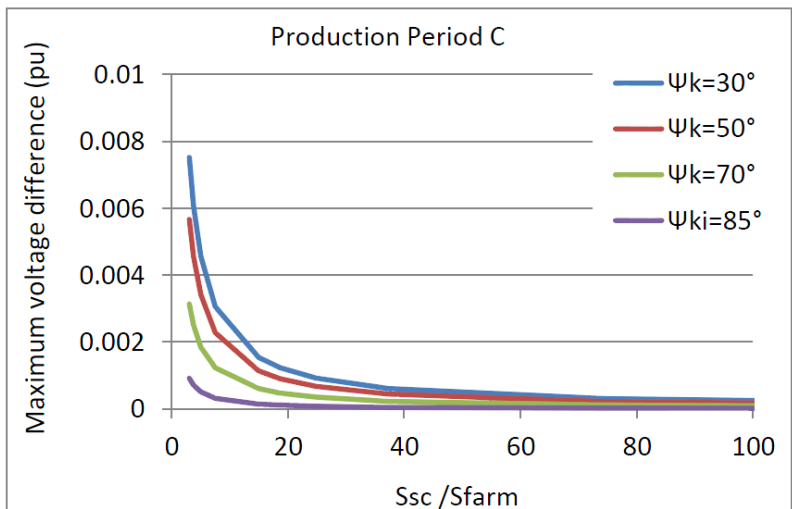
In conclusion, the orientation of the wave farm has a very strong influence on the flicker level at the PCC for connection points up to 70° , whereas the influence of the layout of the devices within the farm is rather limited to connection points up to 50° . Their influence on voltage is more limited. Wave farm orientation can be a determining factor in the wave farm success or failure in complying with power quality requirements. Hence, this aspect should be taken into account in designing an optimal wave farm in addition to the energy capture optimisation which is usually the only aspect considered at early design stages. The influence of the farm orientation is always significant for 30° - 50° connection points, considering their typically low short-circuit levels, whereas it ceases being significant from a ratio higher than 13 for 70° points and has no influence on 85° points. The device layout has an influence on a majority of connection points whose impedance angle Ψ_k ranges between 30° and 50° , whereas this factor is negligible for connection points whose impedance angle is greater than 70° .



(a) Production period A

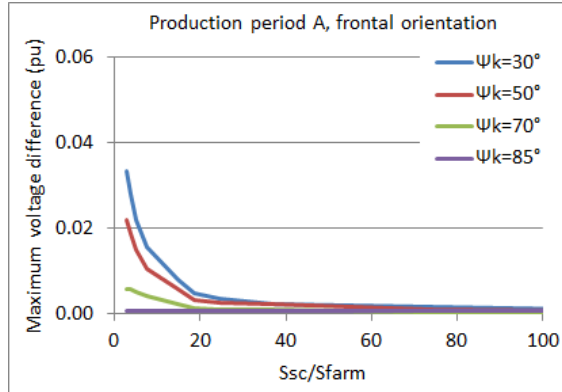


(b) Production period B

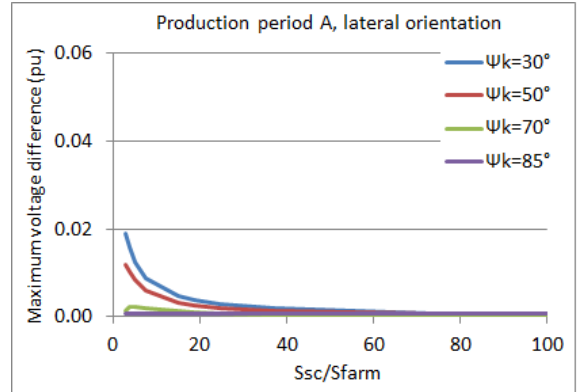


(c) Production period C

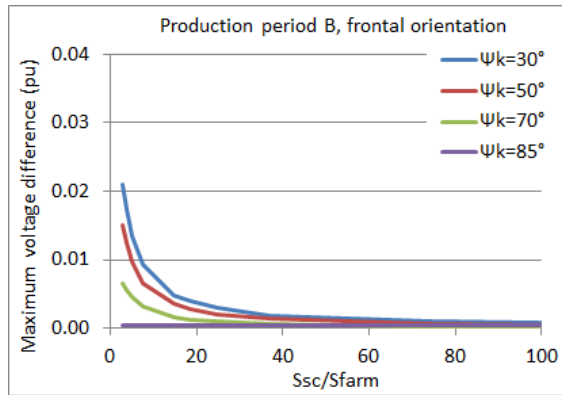
Figure 4.30: Maximum difference in terms of maximum voltage between the frontal and the lateral orientations



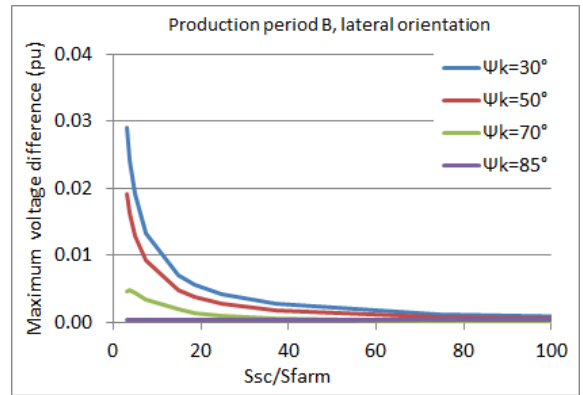
(a) Production period A, frontal orientation



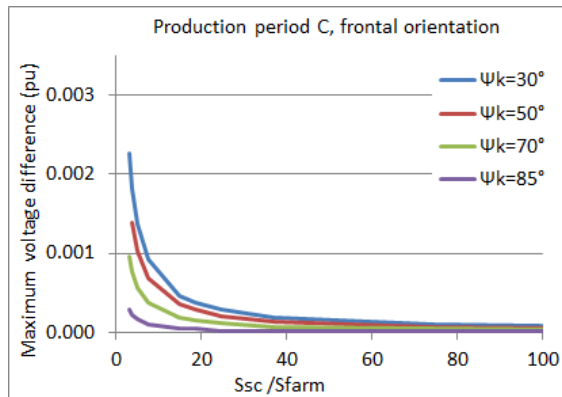
(b) Production period A, lateral orientation



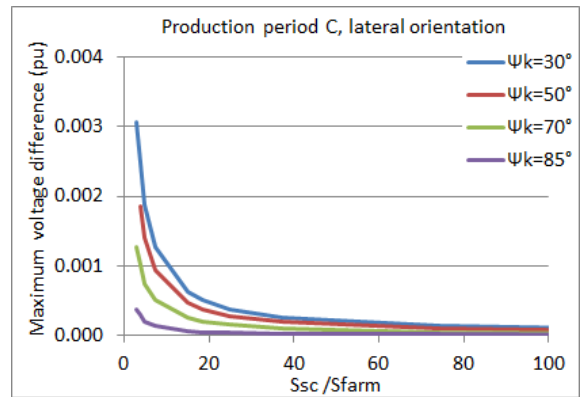
(c) Production period B, frontal orientation



(d) Production period B, lateral orientation

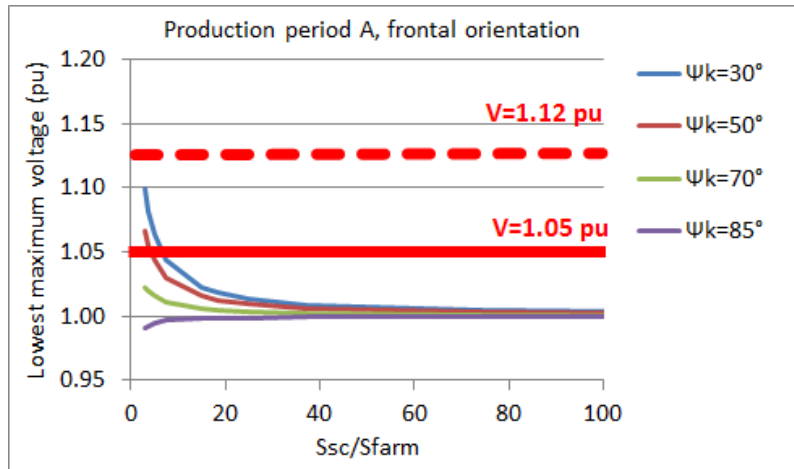


(e) Production period C, frontal orientation

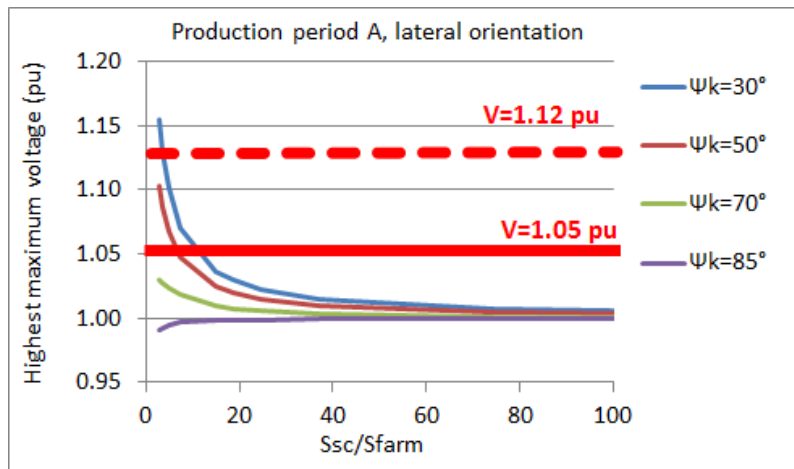


(f) Production period C, lateral orientation

Figure 4.31: Maximum difference in terms of maximum voltage among the different device layouts for both farm orientations

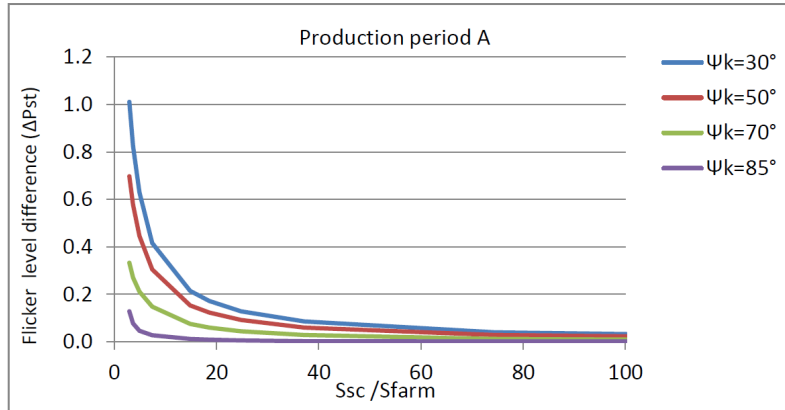


(a) Lowest maximum voltage, (frontal orientation)

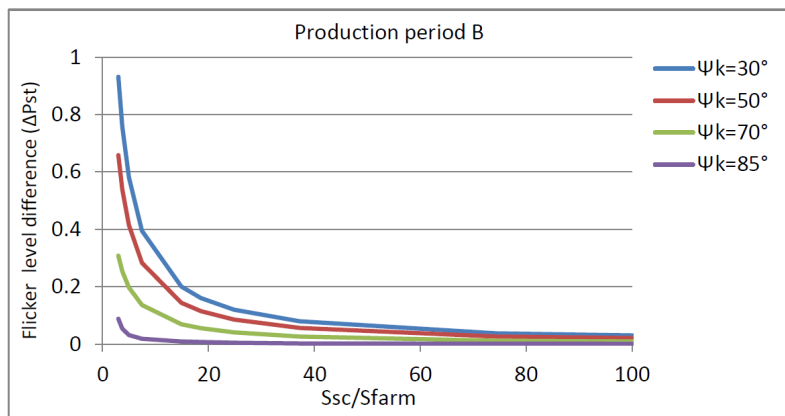


(b) Highest maximum voltage (lateral orientation)

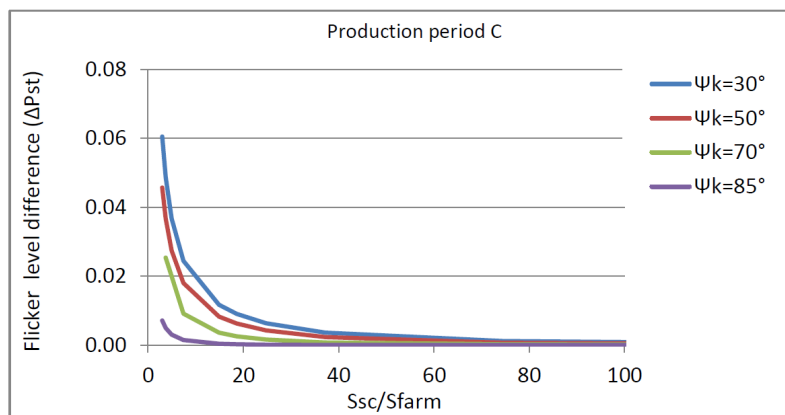
Figure 4.32: Lowest and highest values reached by the maximum voltage for production period A



(a) Production period A

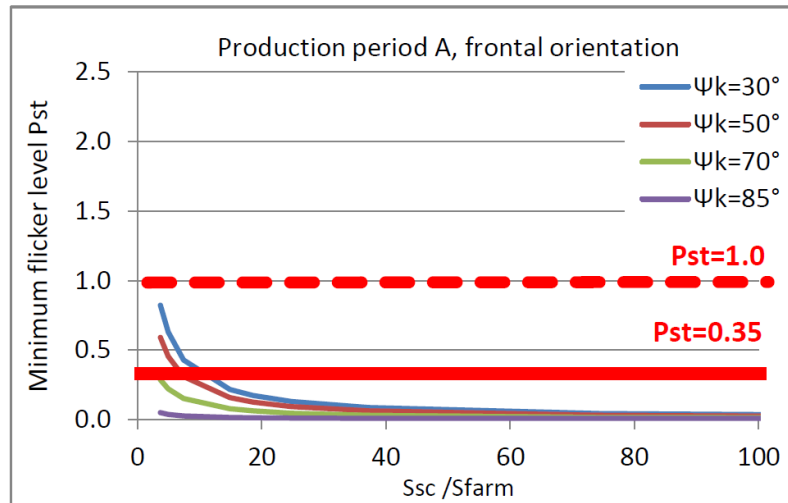


(b) Production period B

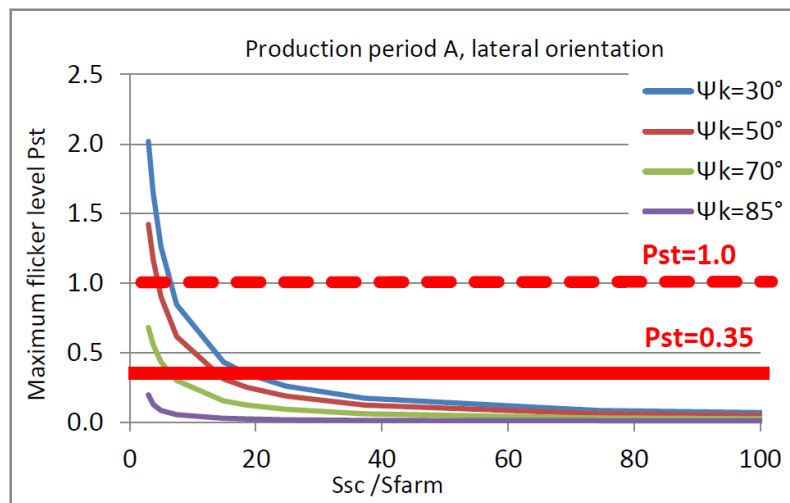


(c) Production period C

Figure 4.33: Maximum flicker level difference between the frontal and the lateral farm orientations

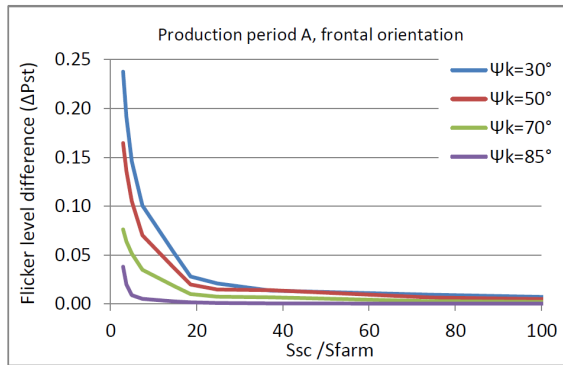


(a) Frontal orientation

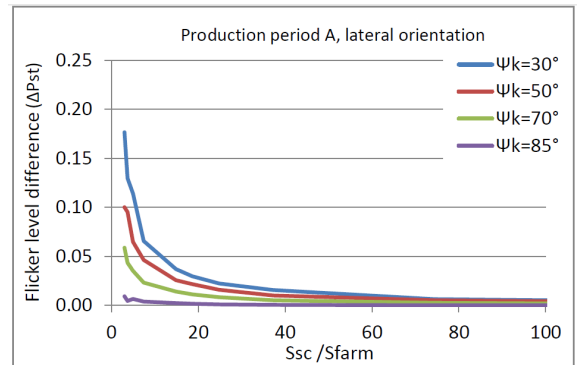


(b) Lateral orientation

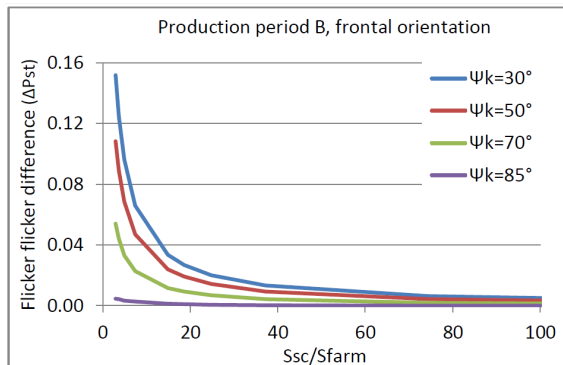
Figure 4.34: Lowest and highest maximum flicker level for production period A (frontal and lateral farm orientations)



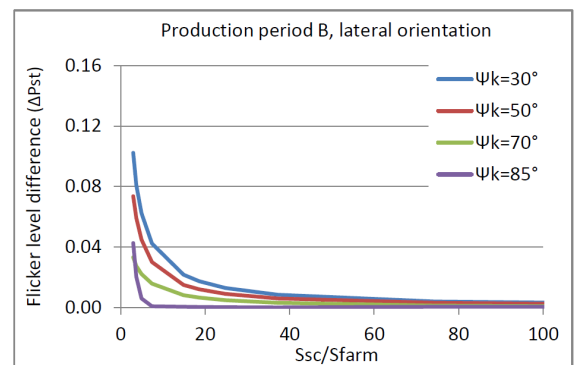
(a) Production period A, frontal orientation



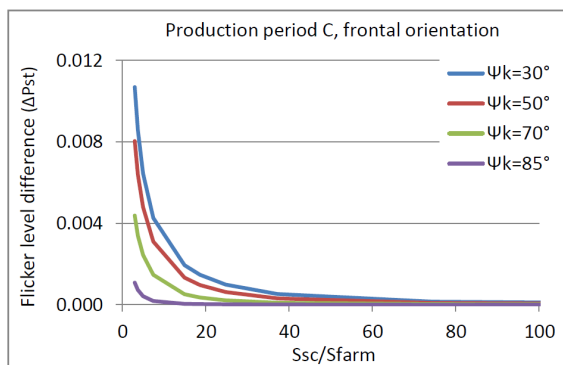
(b) Production period A, lateral orientation



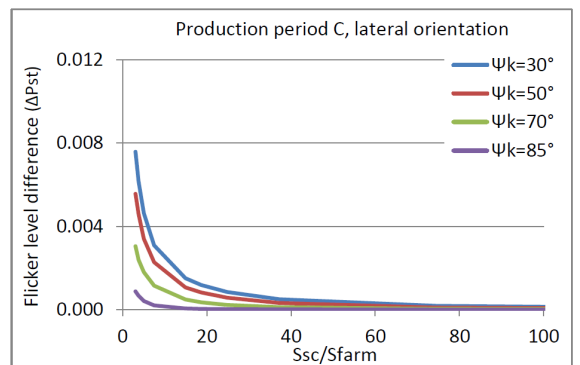
(c) Production period B, frontal orientation



(d) Production period B, lateral orientation



(e) Production period C, frontal orientation



(f) Production period C, lateral orientation

Figure 4.35: Maximum flicker level difference among the different device layouts

4.9 Conclusions

The work presented in this chapter details the grid impact of a 20 MW-rated wave farm according to the three following power quality criteria: voltage step amplitude, voltage limits and flicker level. Power system simulations were performed for the typical ranges of short-circuit ratio and impedance angle Ψ_k . The results obtained with PowerFactory were compared with those obtained with a simplified load flow programme developed for the purpose of this thesis and showed good agreement.

The results of these detailed simulations were also compared to those obtained from the simplified analytical case study presented in Chapter 3 in terms of maximum and minimum voltages as well as in terms of flicker level. This latter study, in which the farm's power profile is modelled by means of sinusoidal terms, was demonstrated to provide an interesting starting point for the grid impact assessment of a wave farm before more detailed analyses are undertaken.

Flicker was demonstrated to be a major issue as it effectively determines the minimum short-circuit ratio required for avoiding power quality issues. However, power factor control was demonstrated to be an efficient means of mitigation in most cases. In others, additional means such as storage may be necessary.

More generally speaking, the results imply that medium size wave farms can be safely connected to relatively weak grids (down to 50°), provided the power transfer capacity is sufficient and that suitable power factor control is applied. In addition, it appears that wave farm owners may not necessarily need to connect their plants initially to a very strong connection point which may be located very far inland, as it is the case in the rural areas of Ireland and Scotland. Hence, they may avoid the costly installation of a long overhead line between the test site's onshore substation and the inland connection point. From a financial point of view, this means that the expensive power systems reinforcement necessary for facilitating the large scale integration of wave farms can be postponed until the wave energy industry reaches a certain degree of commercial maturity. This represents a major asset for the wave energy community as it will enable the different stakeholders to gain confidence in the technology before important investments are required.

However, major questions remain concerning the maximum farm power capacity up to which a wave farm can be connected safely to the distribution network from a power quality perspective. This power capacity limit represents the transition point towards a fully mature technology used in large, high voltage offshore farms. Its estimation would contribute to establishing a long-term vision of the wave energy industry development. In this perspective, the impact on the grid of a 50 MW-rated wave farm is investigated in Chapter 6.

The relevance of the very stringent requirement in terms of flicker, as currently enforced in the Republic of Ireland, was discussed. It was concluded that, based on the results presented in this chapter, the current flicker limit, equal to 0.35, may be relaxed without being detrimental to the customers. In addition, the results showed that the flicker generated by a medium size wave farm may exceed this limit of 0.35 for a large number of short-circuit ratio/impedance angle combinations. Hence, not relaxing this limit may impede significantly the large scale development of the wave energy industry in this country.

Finally, this chapter presented results concerning the influence on power quality of the farm orientation (compared to the dominant wave direction) and of the device layout. The

influence of these parameters was demonstrated to be significant on the voltage and on the flicker for connection points whose impedance angle does not exceed 50° and 70° respectively. The wave farm orientation can be a determining factor in the wave farm success or failure in complying with power quality requirements. Hence, this aspect should be taken into account in the design of wave farm in addition to the energy capture optimisation which is usually the only aspect considered at early design stages.

Designing a wave farm optimally is a complex process which necessitates meeting requirements of many different types: technical, economical, environmental, etc. However, the number of studies focusing on the design of a wave farm from an electrical engineering perspective is extremely limited. In addition, they are generally based on a constant farm power output, in similar fashion to wind farms design studies. This does not take into account the effect of the power fluctuations induced by the waves and may thus lead to a significant level of error when defining the minimum rating required from the farm's electrical elements. In this perspective, a detailed analysis was undertaken regarding the minimum rating of the submarine cables and of the VAR compensator, while addressing also the losses in the system. The results of this analysis are presented in the next chapter.

Chapter 5

Design of a wave farm's electrical network

5.1 Introduction

A wave farm must be optimally designed in order to maximise the revenue it generates and to minimise its capital expenditure. This may be achieved among others by selecting equipment with suitable characteristics, such as rating and impedance. This selection should focus on maintaining regulatory voltage and flicker levels, on minimising the active power losses as well as on avoiding over-design and costly over-rating of the farm's elements.

Based on the same wave farm model as described in Chapter 4, the minimum rating of two types of expensive pieces of equipment, namely the VAr compensator and the submarine cables, are investigated in terms of reactive power and current respectively. These ratings are defined as the smallest reactive power or current level for which a given farm's element is operated safely, for instance without exceeding the maximum permissible temperature in the case of the cables, and by meeting the power factor requirements at all times for the VAr compensator.

Both the inductive and capacitive ratings of the VAr compensator are investigated, as well as the influence on these ratings of two major farm design parameters, namely the length of both the submarine cables and the overhead line.

The minimum current rating of the cables is investigated from a thermal loading perspective. This chapter highlights that the present rating determination methods, being based on steady-state calculations, may no longer be realistic in the case of wave energy applications, due to the relatively large current fluctuations generated by wave farms. Additional methods intended to take the thermal dynamic response of the cables into account were developed in the context of this thesis and are presented in this chapter. The third and last study of this chapter focuses on the active power losses dissipated within the farm, and more especially on their distribution over the different pieces of equipment as well as on the loss of revenue they represent.

5.2 VAr compensator

5.2.1 Methodology

The cost of a VAr compensator is highly dependent on its rating, which must then be carefully selected. Both the minimum required levels of reactive power it must absorb and

Test site	Cable length (km)	Estimated line length (km)
AMETS(Ireland)	6.5 to 16	5 (38 kV)
bimep (Spain)	3.4 to 5.9 [95]	N/A
EMEC (UK)	4.7 to 8.0 [79] ¹	unknown
SEM-REV (France)	23 [96] ¹	unknown
WaveHub (UK)	16 [78]	N/A

¹ estimated

Table 5.1: Cable and line length at different test sites (either planned, under development or in operation)

generate are investigated in this work. The VAR compensator maintains power factor at a fixed level at the PCC which is selected as unity for this study, this type of operation being typical for wind farms. However, in the case of a wave farm, the distance between the generators and the PCC is considerably increased, which is expected to increase as well the level of reactive power absorption and generation required from the VAR compensator.

Load flow simulations were performed in PowerFactory in order to determine the reactive power consumption of the farm’s electrical network. The results are detailed by type of element in Section 5.2.3. The minimum required ratings in terms of reactive power generation and absorption required from the VAR compensator are determined from these results. Two cases are considered. In the first case, the farm outputs its rated power equal to 20 MW: reactive power absorption by the farm’s electrical network is thus maximal, and so is the reactive power generation required from the VAR compensator. In the second case, the farm outputs no power, which implies that the series reactive power losses are negligible. In this case, the shunt reactive power generation from the cables is predominant, hence the amount of reactive power to be absorbed by the VAR compensator is maximal.

Considering that the submarine cables and the overhead line are expected to be the major reactive power elements, the results were expected to be highly dependent on their length. The study was thus performed for cable lengths ranging between 5 km and 30 km, and for line lengths ranging between 5 km and 20 km. These values are deemed representative of the typical length of the submarine cable(s) and of the overhead line included in the design of different test sites whose characteristics are shown in Table 5.1.

5.2.2 Theoretical analysis

Introduction

The reactive power consumption of each element of the wave farm’s electrical network was calculated based on two different methods in order to validate the results. It is computed based on the load flow analyses in PowerFactory and it is also estimated using the simplified load flow programme developed for the purpose of this thesis and presented in Chapter 4.

In addition, the reactive power consumption of each element was calculated from an approximate method using analytical formulae in order to facilitate the interpretation of the trends observed in the different graphs. The principle of this approximate method is detailed in the following section.

Approximate method

The approximate method is based on the assumption that the voltage at all the busses in the system is equal to 1.0 pu and that their angles is equal to 0° . This corresponds approximately to the results obtained with the “flat start” method typically used with the Newton-Raphson algorithm prior to any iteration. However, for the sake of simplification, the power consumption of the onshore substation, which is modelled by load L' connected at the high-voltage side of the 10/20 kV bus, was not taken into account in the calculations. This should lead to a negligible error in compared to the two iterative methods based on the Newton-Raphson algorithm.

The principle of the approximate method consists of calculating the reactive power consumption of each element of the network from the generators up to the PCC. This is done by calculating the value of the apparent power \bar{S}_i flowing through a bus i based on the apparent power \bar{S}_{i-1} flowing through the bus $i - 1$ located upstream minus the active and reactive power losses \bar{S}_{losses_i} due to the impedance located between the two busses $i - 1$ and i as:

$$\bar{S}_i = \bar{S}_{i-1} - \bar{S}_{losses_i} \quad (5.1)$$

The reactive power consumption Q_{series} of each series element of impedance $\bar{Z} = R + jX$ is calculated as:

$$Q_{series} = 3XI^2 = 3X \left(\frac{\bar{S} - 3\bar{Z} \left(\frac{\bar{S}}{\sqrt{3}V} \right)^2}{\sqrt{3}V} \right)^2 \quad (5.2)$$

where I is the current flowing through the impedance, and V is the voltage at its terminals which is assumed to be equal to 1.0 pu/ 0° . The reactive power consumption Q_{shunt} of the two shunt capacitances $C/2$ of a cable can be expressed as:

$$\begin{aligned} Q_{shunt} &= -3ZI^2 = -3\frac{V^2}{Z} \\ &= -3V^2 2\pi C f_e = -6V^2 \pi C f_e \end{aligned} \quad (5.3)$$

where f_e is the frequency of the power system supply.

5.2.3 Results

Transformers

Figures 5.1a to 5.1d show the reactive power consumption of the 0.4/10 kV transformers for all the three methods described in the previous section. The results obtained with PowerFactory are labelled “PowerFactory”, those obtained with the simplified load flow programme are labelled “Theoretical” and those obtained with the approximate method are labelled “Approximation”.

The results obtained with PowerFactory as well as those obtained with the simplified load flow programme indicate that the reactive power consumption of the 0.4/10 kV transformers decreases as a function of the cable length. On the contrary, the curve corresponding to the approximate method indicates a constant reactive power consumption. As this method assumes that the voltage at all the busses is equal to 1.0 pu/ 0° , the decreasing trend observed for both the results obtained with the iterative methods can be assumed

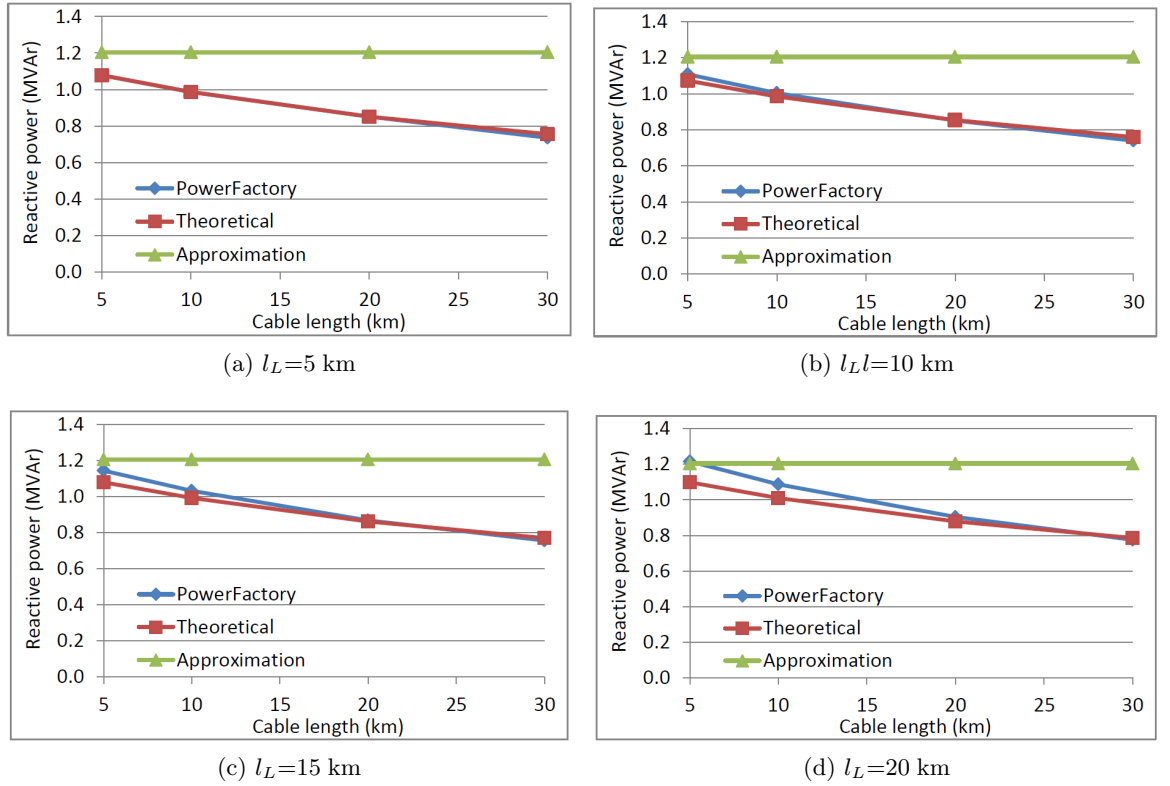


Figure 5.1: Reactive power consumption of the 0.4/10 kV offshore transformers for different values of the overhead line's length l_L

to be due to the increase of the voltage at the transformers' terminals as a function of the cable length. The amount of reactive power consumed by the offshore transformers ranges between 0.7 MVAR and 1.2 MVAR depending on the cable length considered. As the influence of the line length on the voltage at the transformers' terminals is negligible, the influence of this parameter on the reactive power consumption of the 0.4/10 kV offshore transformers is also negligible.

This predominance of the cable length influence can be illustrated by the difference in terms of reactive power consumption compared to the case where the line is 5 km long. These results are shown in Table 5.2a. It should be noted that the maximum difference which can be observed in terms of reactive power consumption when the line length is multiplied by 4 (from 5 km to 20 km) does not exceed 14% compared to the 5 km case. This correspond to 0.14 MVAR only. In comparison, the maximum difference which is observed when the cable length is multiplied by 6 (from 5 km to 30 km) is equal to 44% compared to the case where the cable is equal to 5 km, as shown in Table 5.2b.

Results similar to those presented for the 0.4/10 kV transformers are observed for the 10/20 kV transformer, as shown in Figures 5.2a to 5.2d. The reactive power consumption of the 10/20 kV onshore transformer decreases also as a function of the cable length, which is indicated by both the theoretical and simulation results, as well as by the results obtained from the approximate method. Two factors can be responsible for this trend: the voltage increase at the transformer's terminals and the power losses in the cables which make the apparent power flowing through the transformer decrease as a function of the cable length. This decrease is indeed very significant, as illustrated in Figure 5.3 which presents the apparent power flowing from the overhead line through the PCC as a function

Cable length (km)	Line length (km)		
	10	15	20
5	3%	7%	14%
10	2%	5%	10%
20	0%	2%	5%
30	0%	2%	4%

(a) Comparison with the case where the overhead line is 5 km long

Cable length (km)	Line length (km)			
	5	10	15	20
10	-9%	-10%	-11%	-13%
20	-23%	-26%	-28%	-31%
30	-34%	-37%	-39%	-44%

(b) Comparison with the case where the submarine cable is 5 km long

Table 5.2: Increase in terms of reactive power consumption for the 0.4/10 kV transformer

Cable length (km)	Line length (km)			
	5	10	15	20
5	2.1	2.2	2.2	2.3
10	2.0	2.0	2.0	2.1
20	1.7	1.7	1.7	1.7
30	1.4	1.4	1.4	1.5

Table 5.3: Reactive power consumption (MVar) of all the transformers included in the farm's electrical network

of the cable length for a line length equal to 5 km. Additional simulations based on a line length equal to 10 km, 15 km and 20 km gave similar results.

The results obtained from the approximate method are relatively close to the results obtained through the Newton-Raphson method. It is important to bear in mind that with the approximate method, the voltage at any bus of the network is assumed to be equal to 1.0 pu $\angle 0^\circ$. Hence, it can be concluded that the decreasing trend observed regarding the reactive power consumption of the 10/20 kV transformer is induced mainly by the power losses in the cables. In conclusion, the reactive power consumption of both the offshore and the onshore transformers was demonstrated to be highly dependent on the cable length, the overhead line length having a much lesser influence as expected. This is illustrated in Table 5.3 which presents the total reactive power absorption of all the transformers included in the farm's electrical network for the considered cable and overhead line lengths.

Submarine cables

As shown in Figure 5.4, the submarine cables generate more reactive power than they consume when the farm power output P_G is equal to zero, as the consumption of the cables is negative. The results obtained with all the methods used in this study are in good agreement. In this case, the VAr compensator must absorb reactive power. The reactive power generation Q_{cable} of the cables increases linearly as a function of their length, which proves that the influence of the series reactance is negligible in this case. The proportional factor between the shunt impedance of the cable and its length l_C can thus be defined from:

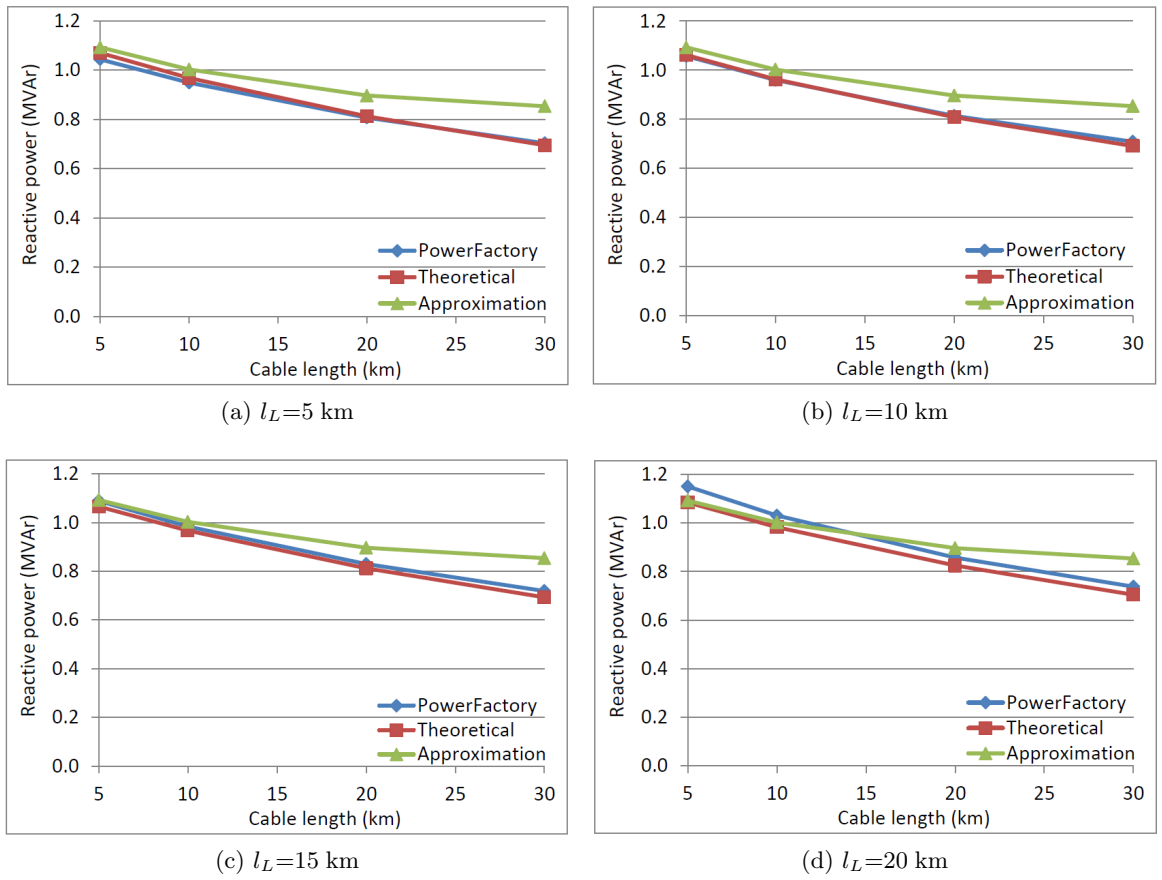


Figure 5.2: Reactive power consumption of the 10/20 kV onshore transformer for different values of the overhead line's length l_L

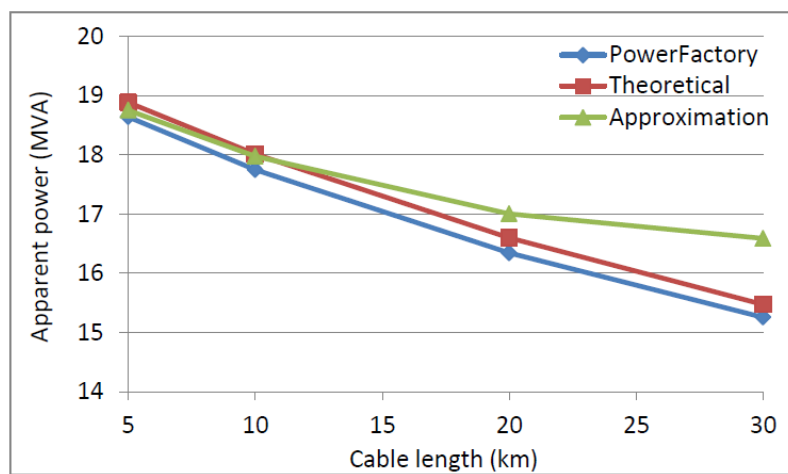


Figure 5.3: Apparent power flowing from the overhead line through the PCC as a function of the cable length

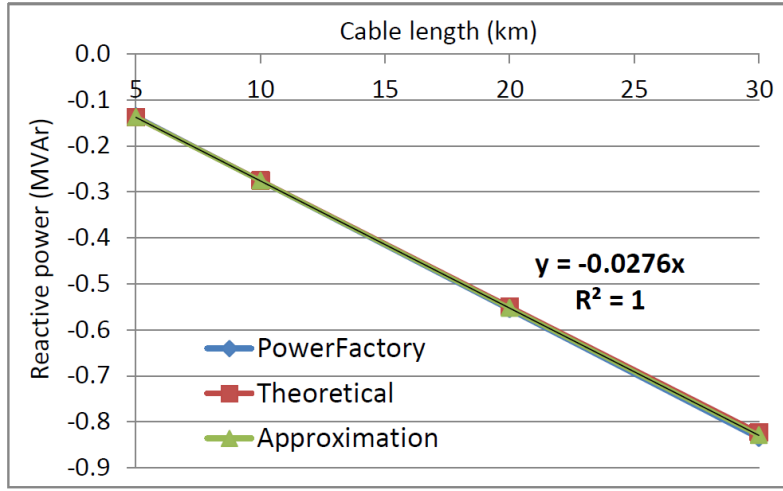


Figure 5.4: Reactive power consumption of the cables as a function of their length ($P_G=0$ MW)

$$Q_{C_{shunt}} = -4 \times 3Z_C I^2 = -4 \times 3V^2 2\pi C_{km} f_e l_c = -24V^2 \pi C_{km} f_e l_c \quad (5.4)$$

so the proportionality factor is equal to:

$$-24V^2 \pi C_{km} f_e = -24 \left(\frac{10 \cdot 10^3}{\sqrt{3}} \right)^2 \pi \times 0.22 \cdot 10^{-6} \times 50 = -0.0276 \text{ MVar/km}$$

where C_{km} is the shunt capacitance per kilometer of the cable and the voltage V is assumed to be equal to 1 pu. The proportionality factor found in the simulation results is also equal to -0.0276 MVar/km.

The reactive power consumption of the cables ranges between -0.1 MVar to -0.9 MVar depending on the cable length considered. The length of the overhead line has a negligible influence on the reactive power consumption of the cables in this case, as it increases by only 0.02 MVar maximum when the value of the length is increased from 5 km to 20 km. Hence, it was not judged necessary to present the results as a function of the length of the overhead line.

On the contrary, the submarine cables consume more reactive power than they generate in the case when the farm outputs its rated power ($P_G=20$ MW) and for the entire length range considered in the study (5 km to 30 km). This is illustrated in Figures 5.5a to 5.5d. The results obtained with the three methods are in good agreement. The reactive power consumption of the cables, as defined with the approximate method, is calculated as:

$$\begin{aligned} Q_{cable} &= Q_{C_{shunt}} + Q_{C_{series}} \\ &= 4(-3V^2 2\pi C_{km} f_e l_c + 3X_{km} I_G^2 l_c) \\ &= 4 \left(-3V^2 2\pi C_{km} f_e l_c + 3X_{km} \left(\frac{\bar{S} - \left(3 \frac{\bar{S}}{\sqrt{3}V} \right)^2 \bar{Z}_{km} l_c}{\sqrt{3}V} \right)^2 l_c \right) \end{aligned} \quad (5.5)$$

where I_G and S are respectively the current and the apparent power flowing from the farm through each cable, and Z_{km} is the series impedance per kilometer of a single cable.

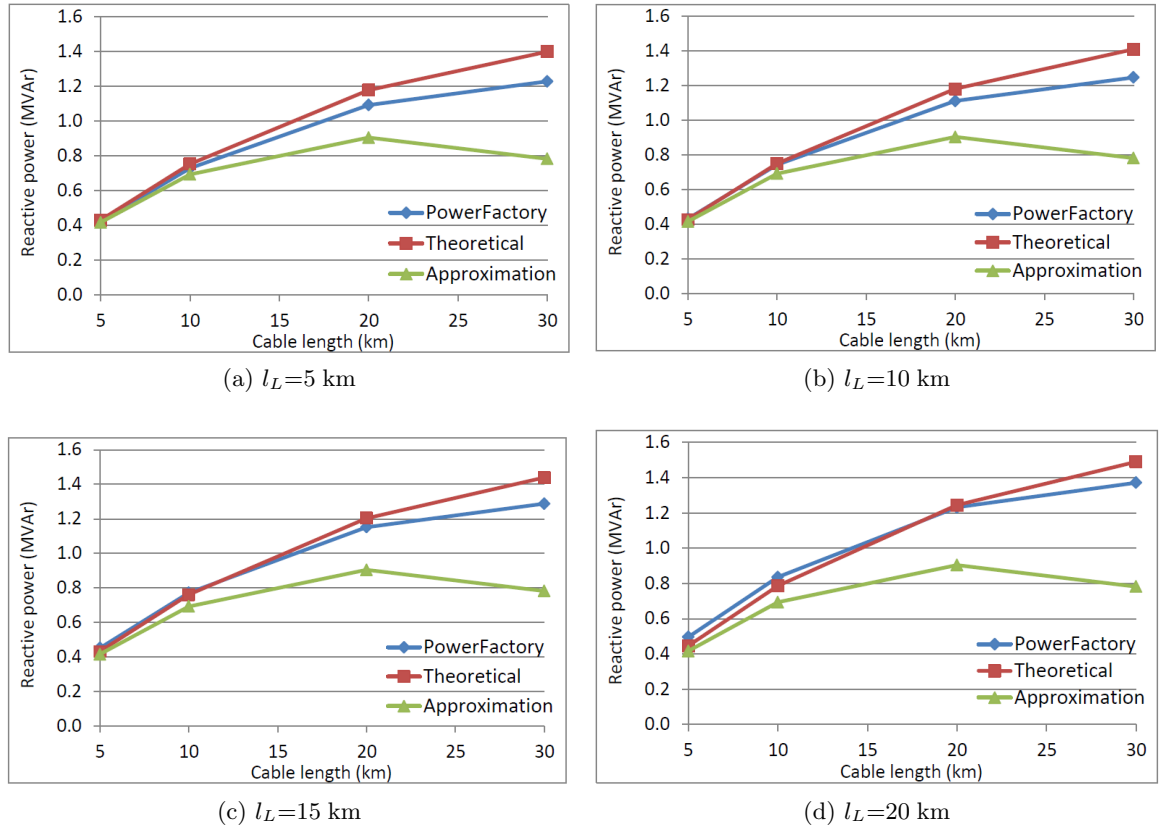


Figure 5.5: Reactive power consumption of the cables as a function of their length for different values of the overhead line length ($P_G=20$ MW)

It is interesting to observe that the reactive power consumption does not increase linearly as a function of the cable length, contrary to the case where the farm outputs a power P_G equal to 0 MW. This is of course explained by the fact that the reactive power consumption of the cable series reactance and the reactive power generation of the shunt capacitance are two opposite effects which are approximately of the same order of magnitude. The former was shown to prevail for distances less than 30 km, which corresponds to the maximum cable length considered in this study. However, the proportion of the reactive power generation by the shunt capacitance becomes more and more important as the cable length increases, which limits considerably the reactive power actually consumed by the cables.

The length of the overhead line has a negligible influence on the reactive power consumption of the cables in this case, as it increases by only 0.1 MVar maximum when the value of the length is increased from 5 km to 20 km, as shown in Table 5.4. The maximum amount of reactive power both absorbed and generated by the four submarine cables are summarised in Table 5.5.

Overhead line

As shown in Figure 5.6, the reactive power consumption of the overhead line increases linearly as a function of its length by a proportionality factor ranging between 0.17 MVar/km to 0.27 MVar/km depending on the cable length considered. These values are in agreement with the expected proportionality factor, which ranges between 0.22 MVar/km to 0.27 MVar/km according to the results obtained with the approximate method. This vari-

Cable length (km)	Line length (km)			
	5	10	15	20
5	0.4	0.4	0.4	0.4
10	0.8	0.8	0.8	0.8
20	1.2	1.2	1.2	1.2
30	1.4	1.4	1.4	1.5

Table 5.4: Total reactive power consumption (MVar) of the four submarine cables

	Reactive power (MVar)	
$P_G=0$ MW	-0.1	-0.9
$P_G=20$ MW	0.4	1.2

Table 5.5: Maximum amount of reactive power both absorbed and generated by the four submarine cables

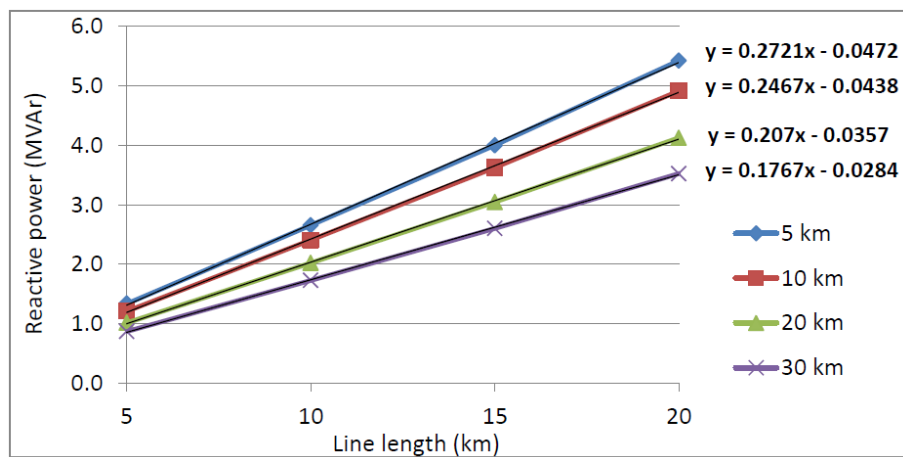


Figure 5.6: Reactive power consumption of the overhead line as a function of its length for several values of cable length

ability of the proportionality factor is due to the power losses in the cables which increase as a function of their length.

The results indicate also that the reactive power consumption of the overhead line decreases as a function of the cable length, as shown in Figures 5.7a to 5.7d. The results obtained through the approximate method being similar to those obtained with the two iterative methods, the decreasing trend observed for the reactive power consumption of the overhead line can be assumed to be due to the decreasing amount of apparent power flowing through the overhead line as the cable length increases (due to the power losses dissipated by the cables). This decrease can be significant, as the reactive power consumption of the overhead line may decrease by up to 36% when the cable length is increased from 5 km to 30 km, as shown in Table 5.6.

Depending on the length of the cables and of the overhead line, this latter element can consume between 0.9 MVar and 6.0 MVar, as shown in Table 5.7. Hence, the overhead line may constitute by far the element in the farm's electrical network which consumes the most important share of reactive power.

Cable length (km)	Line length (km)			
	5	10	15	20
10	7%	8%	8%	9%
20	22%	22%	23%	25%
30	32%	32%	33%	36%

Table 5.6: Decrease (%) in terms of reactive power consumption compared to the case where the submarine cables are 5 km long

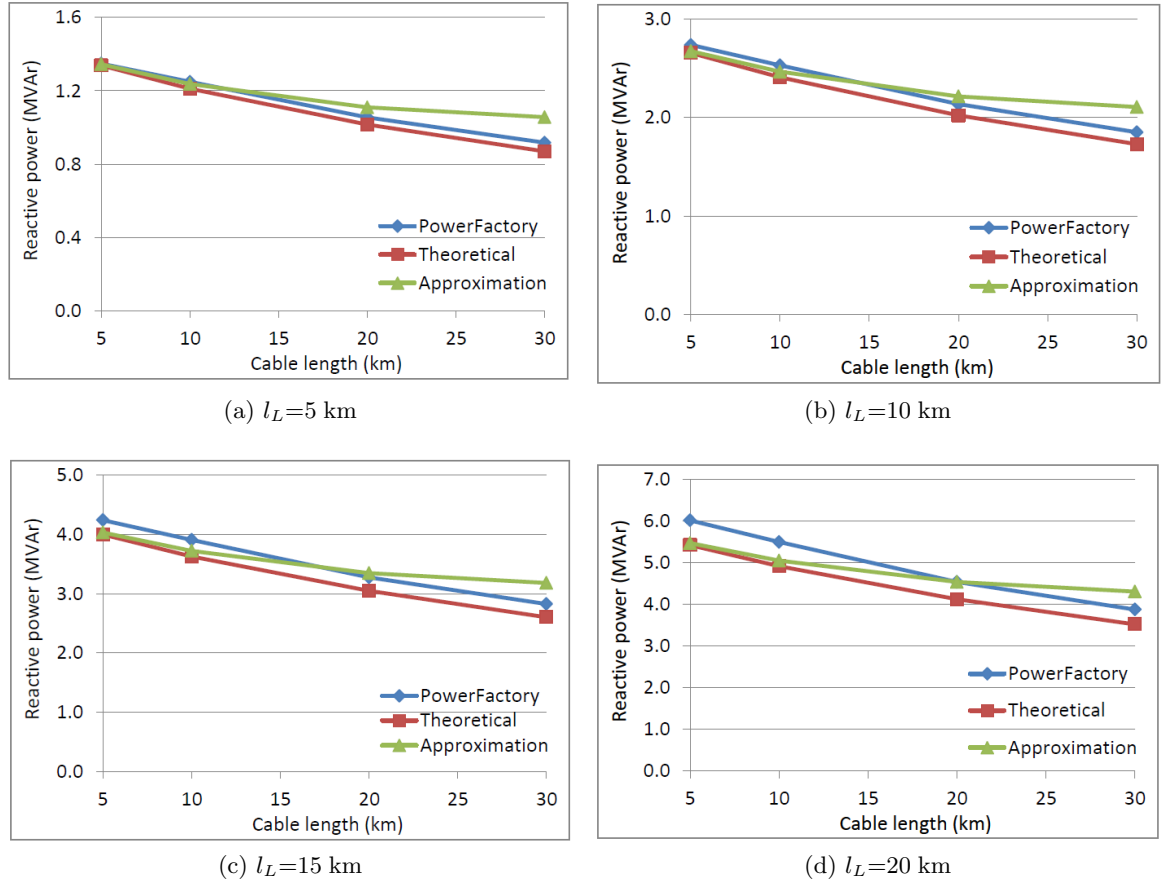


Figure 5.7: Reactive power consumption of the overhead line as a function of the cables' length for different values of its length ($P_G=20$ MW)

Cable length (km)	Line length (km)			
	5	10	15	20
5	1.3	2.7	4.0	5.4
10	1.2	2.4	3.6	4.9
20	1.0	2.0	3.0	4.1
30	0.9	1.7	2.6	3.5

Table 5.7: Reactive power consumption (MVar) of the overhead line for a number of line and cable length combinations

Line length (km)	20	-0.1	-0.2	-0.5	-0.8
	15	-0.1	-0.2	-0.5	-0.8
	10	-0.1	-0.2	-0.5	-0.8
	5	-0.1	-0.2	-0.5	-0.8
		5	10	20	30
Cable length (km)					

(a) $P_G=0$ MW

Line length (km)	20	9.0	8.4	7.5	6.7
	15	7.0	6.7	6.1	5.6
	10	5.4	5.3	4.9	4.6
	5	4.0	4.0	3.8	3.6
		5	10	20	30
Cable length (km)					

(b) $P_G=20$ MW

Table 5.8: Reactive power generated by the VAr compensator as a function of the length of the submarine cables and of the overhead line

Minimum ratings required from the VAr compensator

The results detailed in the previous section indicated that the farm's electrical network generates reactive power when the farm power output P_G is equal to zero, which the VAr compensator must absorb, while it consumes reactive power when the farm power output is sufficiently important, requiring the VAr compensator to generate reactive power in this case. Table 5.8a and 5.8b summarise the amount of reactive power to be generated by the VAr compensator as a function of the length of the cables and of the overhead line.

As expected, the influence of the cables prevails over that of the overhead line when the farm power output P_G is equal to zero. However, when its power output is equal to 20 MW, the amount of reactive power to be supplied by the VAr compensator is determined mainly from the length of the overhead line, while the length of the cables has a lesser, but still very significant, influence.

It may be practical to determine the share of the VAr compensator rating which corresponds to the reactive power consumption of each type of element for $P_G=20$ MW. The results are illustrated in Figures 5.8a to 5.8d. As shown in Figure 5.8a, if the test site is located at a short distance from a suitable connection point, thus requiring a short overhead line, the required rating can be approximately estimated from the expected reactive power consumption of the transformers and of the overhead line if the cables are sufficiently short. However, if the devices are to be located at a relatively long distance from the shore, the consumption of the cables must be taken into account, as shown in Figure 5.8b. If on the contrary the connection point is located far from the test site, the reactive power consumption of the overhead line constitutes between 50% and 75% of the rating required from the VAr compensator, as shown in Figures 5.8c and 5.8d. Hence, the rating can be roughly estimated based on the reactive power consumption of this latter element only in this case.

The results indicate that, under the conditions considered in this study, the VAr compensator is required to generate between 3.6 MVar and 9.0 MVar, and to absorb between 0.1 MVar and 0.8 MVar, as summarised in Table 5.9. Although the amount of reactive power to absorb is relatively small, the amount of reactive power which should be generated

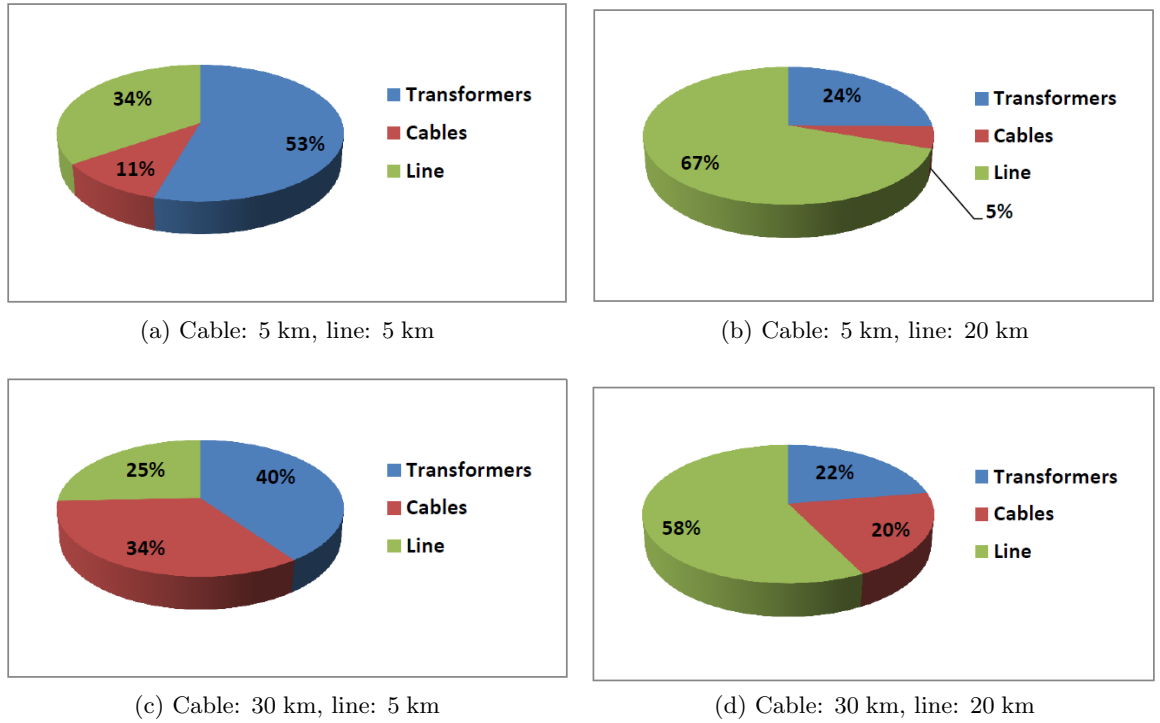


Figure 5.8: Distribution of the reactive power consumption of the farm’s network as a function of the type of its elements

Generation		Consumption	
Minimum	Maximum	Minimum	Maximum
3.6	9.0	0.1	0.8

Table 5.9: Maximum and minimum amount of reactive power either generated or absorbed by the VAR compensator

may become very large in the case of a wave farm including a sufficiently long overhead line. Hence, the cost corresponding to the purchase of a suitable VAR compensator may render the project less economically attractive. Consequently, it is not recommended to develop a test site at a medium voltage level if a suitable connection point is not available in the close neighbourhood. On the contrary, there is no limitation on the length of the cables with respect to the rating of the VAR compensator, as increasing this parameter decreases the overall reactive power consumption of the farm’s electrical network, due to the large apparent power losses it induces. However, this decreases dramatically the efficiency of the network. In addition, sufficiently long cables represent a large capacitance which may have a significant impact on the voltage at low load, that is when the series reactance has little influence.

5.2.4 Summary

The study presented in the first part of this chapter focused on the evaluation of the minimum rating required from the VAR compensator both in terms of reactive power generation and absorption. The length of the submarine cables was demonstrated to have a strong influence on both these two variables. The influence of the overhead line is also very important, and even prevails over that of the submarine cables when the farm power output is sufficiently high.

The results of the studies performed with PowerFactory were compared to the results obtained with the simplified load flow programme developed for the purpose of this thesis which was presented in Chapter 4. In addition, another method complementary to the previous two was developed to give a more precise understanding of the different physical phenomena at play. Generally speaking, the simulation results obtained with PowerFactory are in good agreement with the results obtained with the other two methods. The amount of reactive power to be absorbed by the VAr compensator is relatively small as it ranges between 0.1 MVar and 0.9 MVar depending on the cable length considered. On the contrary, the amount of reactive power to be generated is significant even in the case where both the cables and the overhead line are relatively short. This amount increases rapidly as a function of the overhead line length and ranges between 3.6 MVar and 9.0 MVar, depending on the length considered.

However, results showed that the amount of reactive power required from the VAr compensator, when the farm power output P_G is equal to 20 MW, decreases as a function of the length of the cables. This latter trend was explained by the fact that the apparent power S flowing from the cables through the 10/20 kV transformer and the overhead line decreases significantly as the length of the cables increases.

It was recommended to select preferably test sites where a point of connection is available at a relatively close distance from the onshore substation, in order to limit the minimum rating required from the VAr compensator in terms of reactive power generation. From this perspective, increasing the cable length was not considered as an issue, as the overall reactive power consumption of the farm's electrical network decreases as a function of this parameter. It must be borne in mind, however, that increasing the length of the cable decreases dramatically the efficiency of the network. Generally speaking, the length of the overhead line and of the cables should be minimised to limit both the infrastructure costs associated with the VAr compensator, the overhead line and the submarine cables. In addition, minimising their length minimises also the revenue loss occurring in the form of energy losses.

5.3 Current rating of the submarine cables

5.3.1 Introduction

The experience gained from the wind energy industry as well as studies focusing on wave energy have demonstrated that exploiting the entire amount of wave energy available at a given site, including during the periods presenting the most extreme wave conditions, may be detrimental from an economic perspective. Besides requiring a more robust wave device design, harnessing energy during the most energetic sea-states demands also a higher rated, and thus more expensive, power transmission subsystem, in particular regarding the submarine cables. A study suggests power generation curtailment during highly energetic conditions as a possible way to decrease the capital expenditure of a wind farm by reducing the rating of its cables. It demonstrates indeed that the optimal current rating, from an economical point of view, of the wind farm's export cable corresponds to a fraction of the farm rated power (which is equal to 89% under the conditions considered in this study) [97].

In similar fashion, it was demonstrated that the submarine cables of a wave farm may be significantly under-used if they are designed with respect to the most energetic sea conditions [98]. This study highlighted that the contribution of the most energetic sea-states to the annual electricity production may be relatively negligible. Hence, power generation

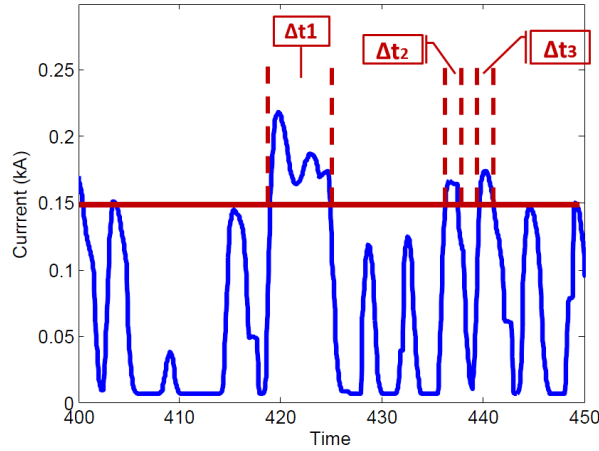
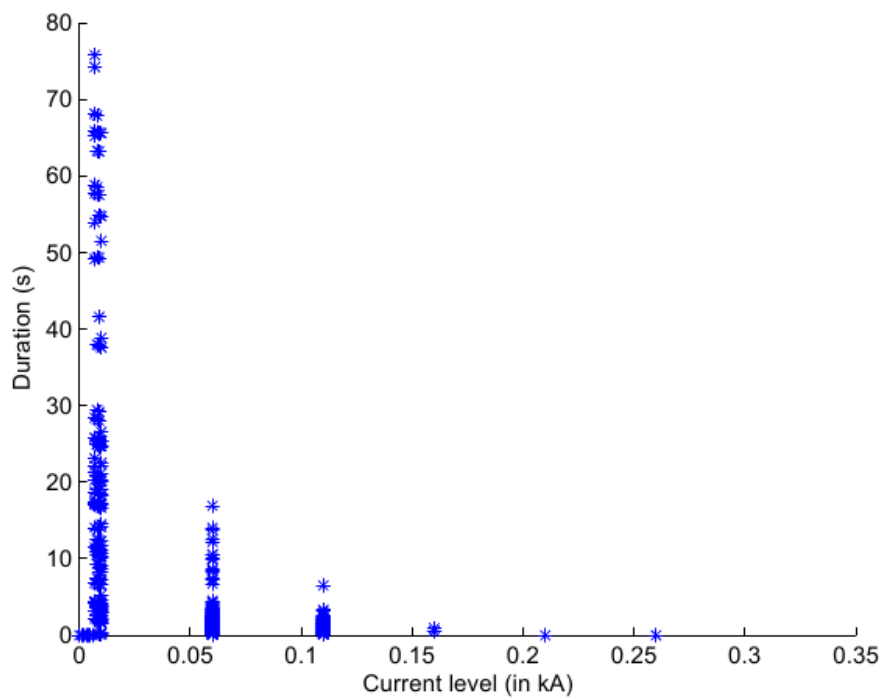


Figure 5.9: Illustration of the principle of the algorithm developed for evaluating the different time intervals during which the current is above a given level

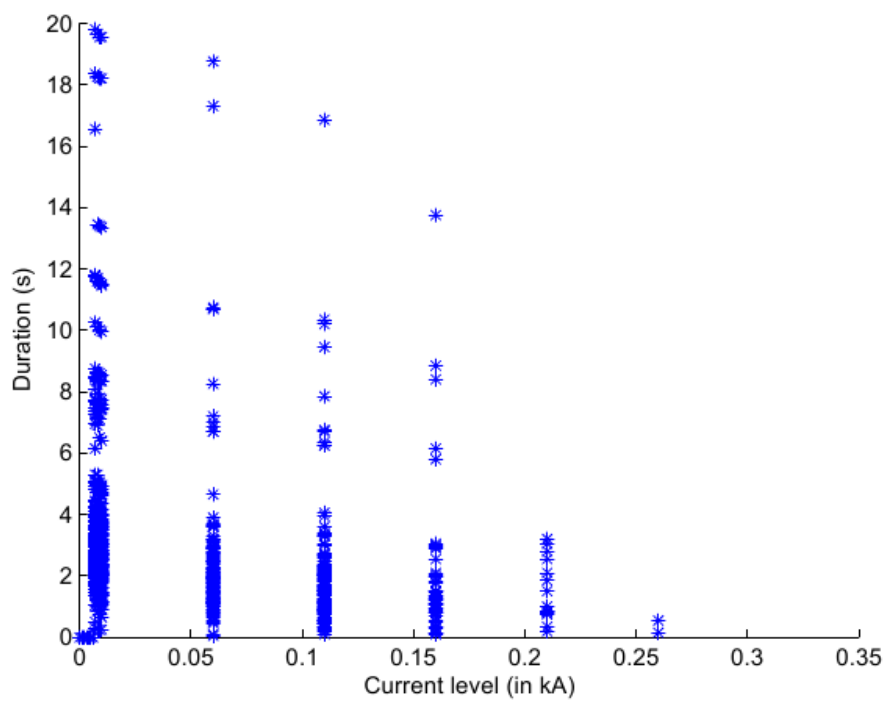
curtailment during these periods is proposed as a solution for limiting the costs related to the electrical infrastructure.

Another approach, which is complementary to the curtailment method, consists of estimating the minimum current rating required from the cables based on their dynamic thermal response. It is important to bear in mind that the current rating is determined from the maximum temperature at which the cable can be safely operated. Hence, temperature constitutes one of the main limiting factors for power transmission. However, the minimum current rating of a cable is usually determined based on *steady-state* calculations which are not representative of, nor relevant to wave energy applications, considering the rapid current fluctuations generated by a wave farm compared to the very slow thermal dynamic response of a submarine cable: indeed, typical thermal time constants range usually between 2 minutes and 30 minutes [56, 57]. Based on these observations, it can be expected that the steady-state temperature corresponding to a given current peak will never be reached, as the duration of these peaks may be very short.

The typical duration of the current peaks was verified by an algorithm developed for the purposes of this study and whose principle is illustrated in Figure 5.9. This algorithm determines the duration of the time intervals during which the current flowing through a cable is above a given level. This operation is repeated for a number of levels ranging between the minimum and the maximum current level observed in the time series. The results obtained with respect to the frontal and to the lateral farm orientations are presented in Figures 5.10a and 5.10b respectively. As expected, the current remains regularly at lower levels when the frontal orientation is used than when the lateral orientation is. However, the current flowing through one cable is greater when this latter orientation is used, which can be explained by the fact that a greater number of generators output the same power profile in this case. These figures show that the duration of the current fluctuations are of the order of tens of seconds only for current levels of significant amplitude. Consequently, it may be possible for a submarine cable to transport safely more current at an instant t than its steady-state rating indicates. This means also that the maximum current flowing through a cable is no longer a relevant criterion for the evaluation of its current rating.



(a) Frontal orientation



(b) Lateral orientation

Figure 5.10: Duration of the time intervals during which the current flowing through a cable is above a given current level

This study investigates the dynamic thermal response of the submarine cables implemented in the network model to the current time series corresponding to the production period A. The objective is to determine a minimum current rating for which the temperature of these cables does not exceed a limit which is defined in the following section.

The two methods developed for evaluating the current rating which are presented in this chapter are expected to have a significant impact on the capital expenditure of a wave farm, as the cabling cost may represent a significant share of the capital expenditure. More precisely, in the case of large offshore wind farms, the cost of cabling may represent up to 20% [53]. Hence, decreasing the rating of the cables, and thus their cost, may represent significant savings in terms of capital expenditure.

The first method is a simplified method from which an approximate value of the current minimum rating can be determined. The second method is more detailed and is based on the recommendations of the IEC standards 60287-1-1 [54] and 60287-2-1 [99]. The results obtained with both methods were compared.

5.3.2 Simplified method

Methodology

A simplified study was conducted initially, its results being then used as a benchmark for a more detailed study performed subsequently. The current time series as generated in PowerFactory were used. The thermal response of a submarine cable to a given current profile is estimated by means of a Simulink model shown in Figure 5.11. The model consists of a first order low-pass filter simulating the thermal response of the cable. As the temperature increase $\Delta\theta$ above the ambient temperature θ_{amb} is assumed to be proportional to the square of the current $I(t)$, the temperature θ of the cable is defined as:

$$\theta = \Delta\theta + \theta_{amb} = \frac{K_{\theta}I^2(t)}{1 + s\tau} + \theta_{amb} \quad (5.6)$$

where K_{θ} is a gain equal to:

$$K_{\theta} = \frac{\theta_f - \theta_{amb}}{(A_c I_{avg})^2} \quad (5.7)$$

and τ is the thermal time constant of the cable, θ_f is its temperature corresponding to a steady-state constant current equal to I_{avg} , which is the average current of the time series, and A_c is a percentage less than or equal to 100%. The idea underpinning the definition of gain K_{θ} consists of assuming that the temperature of a cable would rise from the ambient temperature θ_{amb} to a typical final operating temperature θ_f under the action of a constant current whose amplitude is equal to $A_c I_{avg}$, provided that the cable is rated at this current level. The average of the current times series for this study was selected as it was intuitively expected to be a more relevant criterion than the maximum current level. This model is based on the assumption that the cable can dissipate the heat it generates in the environment.

The simulations are performed in two steps. First, a constant current equal to $A_c I_{avg}$ is applied to the Simulink model in order to obtain the temperature θ_f . Once this temperature is reached, the current time series generated in PowerFactory is applied to the model to observe the effect of the current fluctuations on the temperature of the cables. This is illustrated in Figure 5.12 which shows the current input and its corresponding cable temperature for $A_c=100\%$. It must be noted from this figure that current fluctuations

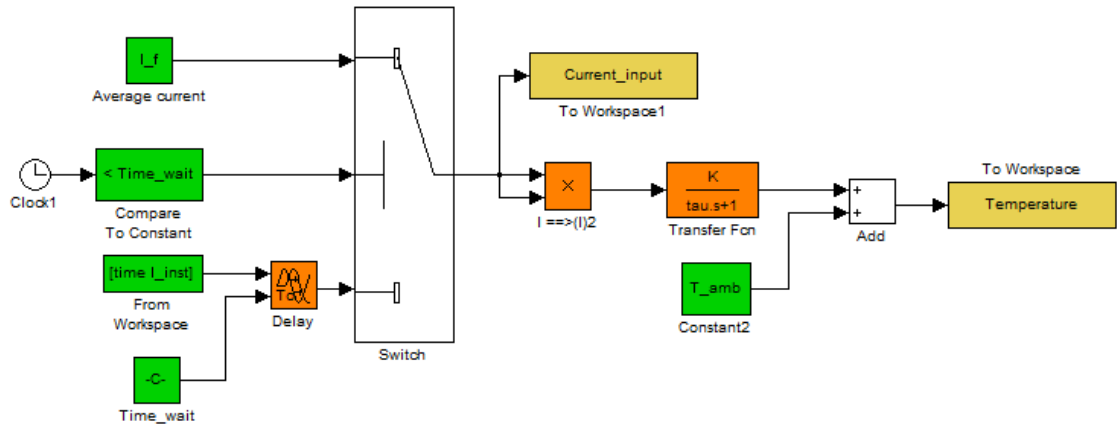


Figure 5.11: Cable thermal model developed in Simulink

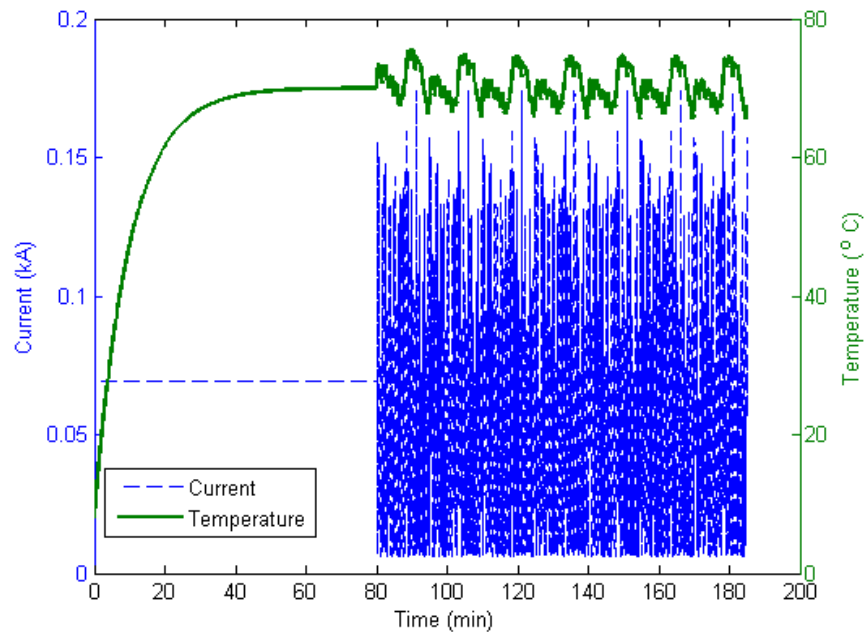


Figure 5.12: Current input $I(t)$ and resulting temperature θ for a cable rated to I_{avg}

which are sometimes three times greater than the average current level induce a limited temperature rise of approximately 6% of the final temperature only. This shows that a cable whose steady-state rating corresponds to a current level approximately equal or even smaller than I_{avg} could be used without exceeding the maximum permissible temperature.

The maximum temperature reached under the influence of the current fluctuations was recorded for a decreasing percentage A_c until it exceeds the maximum permissible temperature. The smallest percentage A_{cmin} for which the cable temperature does not exceed the maximum operating temperature determines the minimum current rating $A_{cmin} \times I_{avg}$ which could be selected for operating the cable under the sea-state conditions selected for the study.

An ambient temperature θ_{amb} equal to 10°C was selected based on typical sea water temperatures. This value was considered to be representative of the average external conditions at seabed level in North-West Europe, but it is assumed to be representative

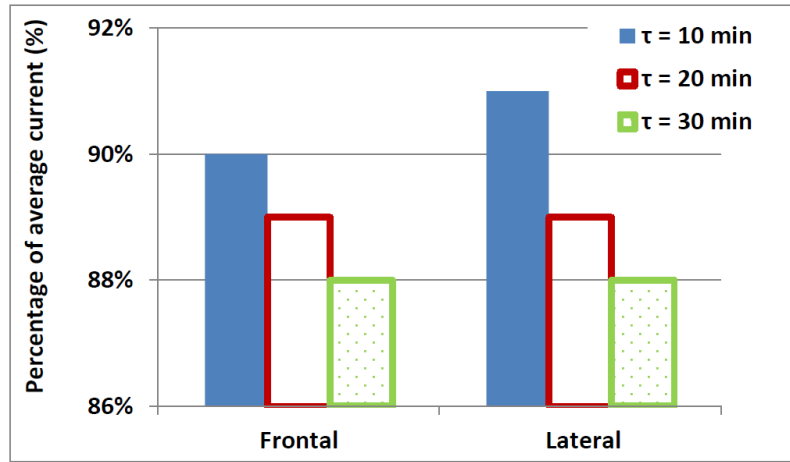


Figure 5.13: Minimum ratings in terms of percentage of the average current flowing through the cable for both wave farm orientations

also of a range of conditions at a number of locations. The final temperature θ_f must range between the ambient temperature and the typical operating temperature equal to 90°C for submarine cables. A value equal to 70°C was arbitrarily chosen for this parameter assuming the cable is operated at partial load, which is correct as the power output of the wave farm never reaches its rated power equal to 20 MW, as described in Chapter 4.

Results

The results indicated that the minimum percentage $A_{c_{min}}$ below which the temperature exceeds 90°C ranges between 88% and 91% of the current time series average I_{avg} . In other words, a cable could be rated to 88%-90% of the average current flowing through it. This is illustrated in Figure 5.13 which presents the minimum ratings in terms of percentage of the average current for both the frontal and the lateral farm orientations. The corresponding current rating represents only 21% to 22% of the maximum current flowing through the cable. Hence, this suggests that the submarine cables to be used for wave energy applications could be rated to current level even lower than the average current flowing through them. In addition, it must be noted that limiting the cable temperature to 90°C constitutes a worst case scenario, considering that the submarine cables may be operated at higher temperatures for periods of time which, although being limited, can be relatively long compared to the rapid temperature fluctuations induced by the observed current variations.

It is interesting to note that the results are relatively similar regardless of the thermal time constant τ used. This can be explained by the action of two opposite effects. On one hand, a greater thermal time constant simulates the response of a cable whose temperature is less responsive to current fluctuations, resulting in temperature fluctuations with a smaller amplitude. On the other hand, the temperature of this type of cable decreases also more slowly during current troughs. Consequently, the average temperature rises until a new equilibrium is reached. Figures 5.14a to 5.14d, which show the cable temperature for four different values of τ ranging between 2 min and 30 min, illustrate this phenomenon. Figure 5.14a shows the temperature profile of the cable for the smallest value of τ equal to 2 min which is presented for the sake of illustrating the two phenomena described in this paragraph. However, these results were not retained for the study, considering that such a quick response time is unrealistic regarding the large difference between the initial and the final temperatures, which are equal to 10°C and 70°C respectively.

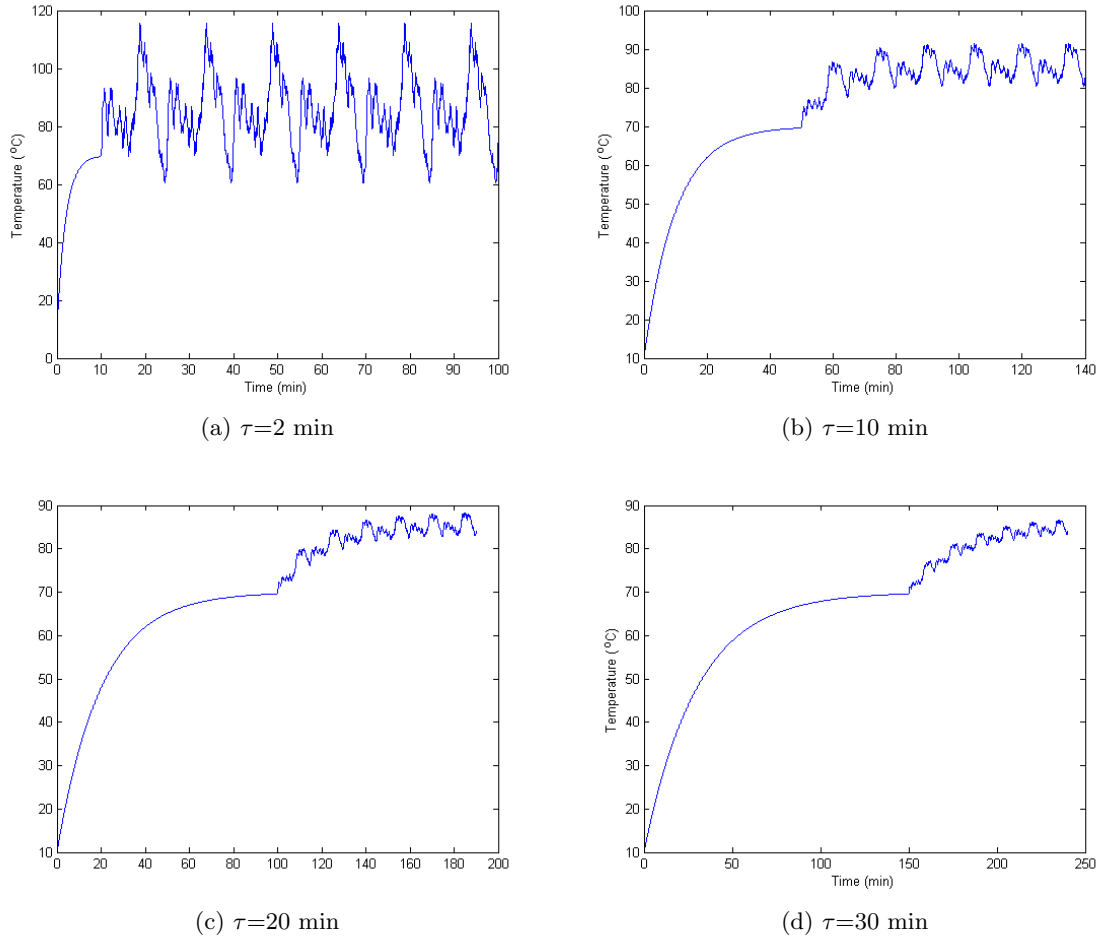


Figure 5.14: Temperature of the cable for different thermal time constant τ

Simulations were performed for both the frontal and the lateral farm orientations. The results showed that this criterion has an influence which is however very limited on the cable minimum rating, as shown in Table 5.10. This can be explained by the fact that the amplitude of the current fluctuations are relatively similar in both cases, even though they are slightly greater when the lateral orientation is used. The maximum current corresponding to each of these farm orientations is equal to 174 A for the frontal orientation and to 194 A for the lateral orientation.

τ (min)	Minimum current rating (A)	
	Frontal	Lateral
10	54.7	56.2
20	54.1	55.0
30	53.5	54.4

Table 5.10: Minimum current rating (A) as a function of the thermal time constant τ and of the farm orientations.

Summary

The results of the study conducted with the simplified method indicate that the average value of a current profile is a relevant indicator for the selection of a suitable cable rating from a thermal loading perspective. The simulations for which different values of the thermal time constants τ were used as well as simulations using two different wave farm orientations proved to give relatively similar results. This shows that the influence of both these parameters may be relatively limited. The results of the more detailed analysis conducted subsequently are presented in the next section.

5.3.3 Detailed method

Introduction

The calculations performed in this detailed study are based on the recommendations of IEC standards 60287-1-1 and 60287-2-1. This set of standards defines a method for determining the maximum current which may be carried by a cable under steady-state conditions. The method is based on the maximum permissible temperature rise $\Delta\theta$ above ambient temperature, and on the thermal properties of the different cable's parts.

A reverse approach is adopted in this study for determining the temperature increase $\Delta\theta(t)$ resulting from the application of a fluctuating current $I(t)$. A temperature rise $\Delta\theta_{cst}$ corresponding to a constant current $I = I(t)$ is calculated for each point of the current time series. Then, in similar fashion to the simplified study, the temperature rise $\Delta\theta(t)$ is modelled by filtering the profile of the temperature rise $\Delta\theta_{cst}$ by means of a first order low-pass filter whose time constant τ corresponds to the thermal time constant of the cable.

Characteristics of the cable

Table 5.11 shows the characteristics of the cable implemented in PowerFactory model. Its rating I_{rated} was initially selected based on the maximum current which may flow through each of the cables and which corresponds to the initial rated power P_{rated} of the Belmullet test site equal to 10 MW, as defined in Chapter 3. The corresponding maximum current is equal to:

$$I_{rated} = \frac{P_{rated}}{\sqrt{3}V} = \frac{10 \times 10^6}{\sqrt{3} \times 10 \times 10^3} = 144 \text{ A} \quad (5.8)$$

As shown in Figure 5.15, the cable includes three copper conductors insulated with cross-linked polyethylene (XLPE) and having each a copper screen. The sheath is made of polyethylene and the bedding of polypropylene yarn, as well as the serving. The surrounding armour is made of galvanised steel [100]. Additional data necessary to perform the calculations are however not indicated in the Nexans data sheet for this cable. Hence, it was estimated from additional data found in data sheets of other cables of similar structure, operating voltage and conductor size.

Methodology

As defined in IEC standard 60287-1-1, the steady-state temperature rise $\Delta\theta$ of a conductor above the ambient temperature θ_{amb} can be expressed as:

$$\begin{aligned} \Delta\theta = & (I^2 R + \frac{1}{2} W_d) T_1 + [I^2 R(1 + \lambda_1) + W_d] n T_2 \\ & + [I^2 R(1 + \lambda_1 + \lambda_2) + W_d] n (T_3 + T_4) \end{aligned} \quad (5.9)$$



Figure 5.15: Structure of the cable implemented in the PowerFactory model

Parameter	Definition	Numerical value
d_c	Conductor diameter	8.2 mm
S	Conductor cross-section	50 mm ²
V_n	Operating voltage	12/20 (24) kV
θ_c	Operating temperature	90°C
$t_{insulation}$	Nominal insulation thickness	5.5 mm
S_{screen}	Screen section	16 mm ²
t_{sheath}	Nominal outer sheath thickness	2.5 mm
t_{armour}	Armour thickness	3.15 mm
A_{buried}	Permissible current rating when buried	199 A

Table 5.11: Characteristics of the cable selected initially for the electrical network model

where I is the current flowing in one conductor (A), R is the resistance per meter (Ω/m), W_d is the dielectric loss per meter (W/m), T_1 , T_2 , T_3 and T_4 are the thermal resistances of different parts of the conductor (K.m/W), n is the number of conductors in the cable, λ_1 and λ_2 are the loss ratios in different parts of the conductor to the total losses in all the conductors. The dielectric loss is calculated as:

$$W_d = \omega C_W U_0^2 \tan \delta \quad (5.10)$$

where C_W is the capacitance per meter and per phase, U_0 is the line-to-neutral voltage and $\tan \delta$ is the loss tangent. The dielectric loss is induced by the variations of the electrical field in a dielectric material. This phenomenon can be considered as instantaneous compared to the simulation time step used in the study (equal to 0.05 s). Hence, although (5.10) was defined initially for steady-state conditions, it is considered as applicable in the case of the dynamic simulations performed here. Hence, the instantaneous dielectric loss is calculated from the instantaneous voltage amplitude $V(t)$ defined by the time series generated in PowerFactory, as shown by (5.11). The rest of the calculations was performed according to the recommendations of the IEC standards 60287-1-1 and 62087-2-1.

$$W_d(t) = \omega C_W V^2(t) \tan \delta \quad (5.11)$$

In similar fashion to the simplified study, the maximum permissible temperature was chosen equal to the operating temperature of 90°C. As mentioned earlier, this represents a worst case scenario, considering that the cable is designed to be operated at higher temperatures for limited periods of time. It is also interesting to note that by limiting the maximum permissible temperature to its nominal operating value, no additional thermal aging effect compared to the steady-state case (due to excessive temperatures) needs to be considered.

Parameter	Definition	Numerical value
T_1	Thermal resistance between conductor and sheath	0.4929 K.m/W
T_2	Thermal resistance between sheath and armour	0.0890 K.m/W
T_3	Thermal resistance of external serving	0.1827 K.m/W
T_4	External thermal resistance	0.6783 K.m/W
W_d ¹	Dielectric loss	0.0041 W/m
λ_1 ²	Loss ratio	$7.9151 \cdot 10^{-7}$
λ_2 ²	Loss ratio	$1.8093 \cdot 10^{-7}$
I^2R ²	Thermal losses from one conductor	19 W/m

¹ Instantaneous value calculated based on a constant voltage equal to 10 kV

² Instantaneous value calculated based on a constant current equal to 100 A

Table 5.12: Thermal parameters of the selected cable

Results

The different thermal parameters necessary for calculating the steady-state temperature rise above ambient temperature θ_{amb} were calculated according to the methods described in IEC standards 60287-1-1 and 62087-2-1. Their numerical values are shown in Table 5.12. Although the dielectric loss W_d and of the loss ratios λ_1 and λ_2 vary as a function of the voltage and of the current respectively, their numerical values corresponding to a constant voltage equal to 10 kV, and to a constant current I equal to 100 A are presented in this table as well in order to provide information on their order of magnitude. Due to copyright issues regarding the IEC standards used for the calculations, they will not be detailed in this thesis.

As expected from medium voltage cables with relatively small size conductors, the skin effect and the proximity effect proved to be negligible, as well as the dielectric losses W_d [101].

The results obtained with the detailed method presented here indicate the cable is clearly over-rated. Although the maximum current flowing through it is equal to 174 A for the frontal farm orientation, the temperature reached by this conductor (whose diameter is equal to 8.2 mm) is equal to 17°C only, as illustrated in Figure 5.16 which shows the temperature actually reached by the conductor (for several values of the thermal time constant τ), as well as the temperature predicted by the steady-state calculations as a function of the conductor diameter. This is much lower than the temperature limit defined in this study which is equal to 90°C. The very important difference which exists between the temperatures obtained with the steady-state and with the dynamic methods illustrates the lack of relevance of steady-state calculations regarding the evaluation of the cable thermal loading in the case of wave energy applications.

Further calculations indicated that the maximum permissible temperature of the conductor, equal to 90°C, is not exceeded for a conductor diameter greater than or equal to 2.5 mm to 2.6 mm, depending on the farm orientation and on the thermal time constant τ considered, as shown in Table 5.15. This is much smaller than the diameter of the cable selected initially which is equal to 8.2 mm. As found in the simplified study, both the farm orientation and the value of the time constant τ have a limited influence on the results. These results are summarised in Table 5.14.

The current rating corresponding to each of these diameter values is estimated from a polynomial approximation of a curve linking the current ratings of similar cables to the diameter of their conductors, which is presented in Figure 5.17a. This curve was created

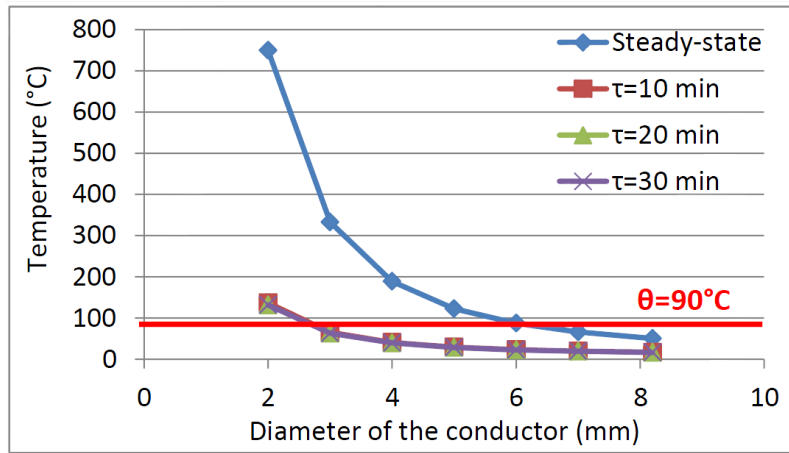


Figure 5.16: Temperature obtained from steady-state and dynamic calculations as a function the conductor diameter (lateral orientation)

τ (min)	Minimum conductor diameter (mm)	
	Frontal	Lateral
10	2.51	2.58
20	2.46	2.51
30	2.45	2.5

Table 5.13: Minimum conductor diameter required for different values of the thermal time constant and for both farm orientations

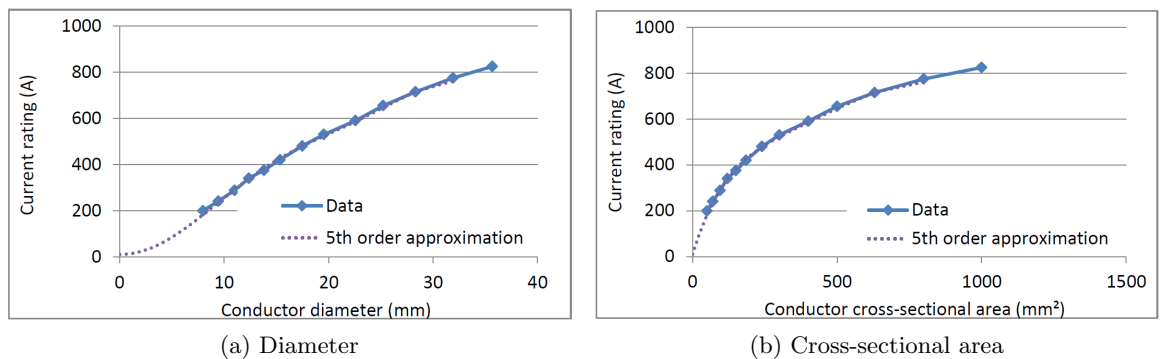


Figure 5.17: Typical cable current rating as a function of the conductor diameter and cross-sectional area

from the 5th order polynomial approximation of a curve linking the current rating to the conductor cross-section area, as shown in Figure 5.17b. In order to improve the accuracy of the polynomial approximation, a zero ordinate was added and approximated to zero, considering that the current level flowing through a conductor whose diameter converges to zero would also converge to zero. The curve is based on data found in manufacturers data sheets [102–104].

Based on the curve linking the current rating to the conductor diameter, it was found that the minimum current rating corresponding to the results found in this study ranges between 28.8 A and 29.7 A when the frontal orientation is used, and between 29.5 A and 30.8 A when the lateral orientation is used. Hence, the rating values range between only 15% and 17% of the maximum current flowing through the cable, equal to 175 A and to

τ (min)	Minimum current rating (A)	
	Frontal	Lateral
10	29.7	30.8
20	28.9	29.7
30	28.8	29.5

Table 5.14: Minimum current rating required from the conductor for different values of the thermal time constant and for both farm orientations

		Frontal	Lateral
Average current (A)		60.1	61.1
τ (min)	10	49%	51%
	20	47%	49%
	30	47%	49%

(a) Percentage of the average current

		Frontal	Lateral
Maximum current (A)		175	194
τ (min)	10	17%	16%
	20	17%	15%
	30	16%	15%

(b) Percentage of the maximum current

Table 5.15: Percentage of the minimum cable rating compared to the average and to the maximum current τ flowing through the cable

194 A when the lateral and the frontal farm orientation are used respectively, as summarised in Table 5.15. They also represent 47% to 51% of the average current equal to 60.1 A when the frontal orientation is used and equal to 61.1 A when the lateral orientation is. This shows that the average current level is a relevant indicator for estimating the minimum cable rating, thus confirming the outcomes of the simplified study.

However, the results described in this section must be considered pragmatically. In practice, the conductor diameter of the currently available medium voltage cables is usually greater than or equal to 8.2 mm, which is much greater than the diameter values recommended in this study. However, the methodology developed as part of this work may be applied to cables included in wave farms of greater rated power. As mentioned previously, the selection of suitably rated cables may lead to a significant decrease in terms of capital expenditure.

Discussion on the influence of the ambient temperature

As mentioned earlier, an ambient temperature equal to 10°C was selected for the study. This corresponds approximately to the temperature of the seabed which remains relatively constant throughout the year. However, it is important to study the sensitivity of the obtained results as a function of the ambient temperature, as the part of the cable which is located close to the onshore substation is expected to be either buried in the beach ground or exposed to the air. Hence, its minimum required rating varies as a function of the air temperature. The impact of solar radiation on this rating, which may be significant in the case of cables exposed to the air, is out the scope of this study.

For the sake of illustration, the temperature variations at Belmullet, Ireland are pre-

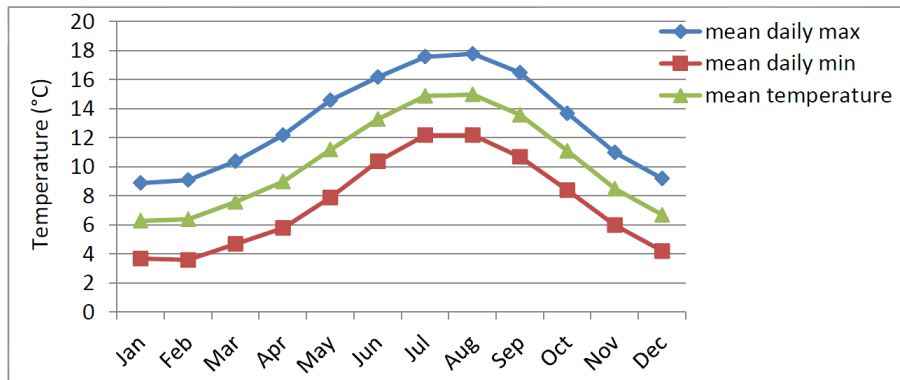


Figure 5.18: Mean daily maximum and minimum air temperatures, and monthly mean air temperature at Belmullet [105]

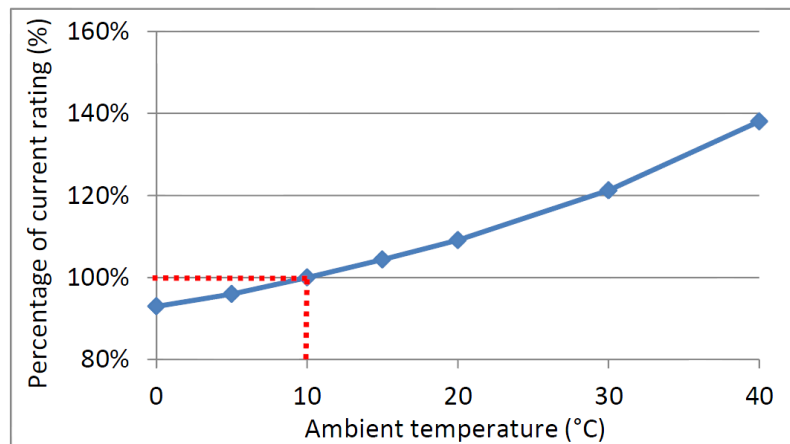


Figure 5.19: Percentage of the current rating compared to the case where the ambient temperature is equal to 10°C

sented in Figure 5.18. This figure presents the mean daily maximum and minimum temperatures as well as the monthly mean temperature as provided by MetEireann, the Irish meteorological office [105]. Although the temperature at this location does not usually exceed 18°C, the sensitivity of the results was analysed for an ambient temperature ranging between 0°C and 40°C for the sake of completeness. This study is based on a cable whose time constant τ is equal to 10 minutes. The current time series corresponds to a frontal farm orientation.

Figure 5.19 presents the results obtained in the form of a percentage compared to the current rating obtained for the case where the ambient temperature is equal to 10°C. It shows that the ambient temperature has a significant influence on the current rating which remains however relatively moderated for a temperature range from 0°C to 20°C as the corresponding difference in terms of rating does not exceed 10%. Hence, the results presented in this work provide a useful benchmark for the design of wave farms located in regions where the ambient temperature does not exceed 20°C. As regards the wave farms located in regions presenting higher temperatures, although the difference in terms of rating increases rapidly as a function of the ambient temperature, the results presented in this study constitute an interesting starting point for further studies.

5.3.4 Summary

This study investigated the minimum current rating required for a submarine cable from a thermal loading perspective. Both a simplified method and a detailed method were developed from this work and their results proved to be in good agreement. It was demonstrated that the average current is a relevant indicator for determining the minimum current rating required from a submarine cable. The results proved indeed that the cable could have been rated downwards to approximately half (47%-51%) of the average current flowing through it.

The wave farm orientation and the value of the thermal time constant τ were demonstrated to have a non-negligible influence on the results, although it is considered as relatively limited. The sensitivity of the results to the ambient temperature was also investigated. It was concluded that only a moderate difference with the results presented in this study could be observed for an ambient temperature ranging between 0°C and 20°C. In addition, although this difference is more significant for higher temperatures, the results presented in this study constitute an interesting starting point for further studies.

The study concluded that although cables of smaller ratings could be used with respect to the operating conditions considered in the study, the diameter of currently available cables at this voltage level is usually greater, which may lead to an unavoidable over-design. However, the methodology developed as part of this work is expected to be very relevant for analysing the minimum current rating of cables included in wave farms of greater rated power. This aspect is investigated in more detail in Chapter 6.

5.4 Power and energy losses

5.4.1 Introduction

Minimising energy losses is one of the key factors for power plant owners to maximise their revenue. This study investigates the constituent elements of the energy losses dissipated in a wave farm. The same wave farm model as used in Chapter 4 and in the previous section was also used for this study.

5.4.2 Methodology

Two studies focusing on losses were performed. The first one focuses on the power losses dissipated within the farm in order to determine the distribution of the losses over the different pieces of equipment of the farm, while the other is intended to determine the level of energy losses. Both studies are based on power system simulations performed for a short-circuit ratio equal to 3 and for an impedance angle Ψ_k equal to 30°. However, additional simulations performed for different values of the short-circuit ratio and of the impedance angle Ψ_k were shown to give similar results.

The power loss study was performed by means of a load flow analysis based on a farm power output equal to 14 MW. This represents an average value of the farm maximum power output reached with production periods A or B which ranges between 13 MW and 15 MW depending on the farm orientation and on the time delay set selected. The power losses were calculated by subtracting the power arriving at the PCC and the consumption of the substation load to the power generated by the farm as:

$$P_{losses} = P_G - P_{PCC} - P'_L \quad (5.12)$$

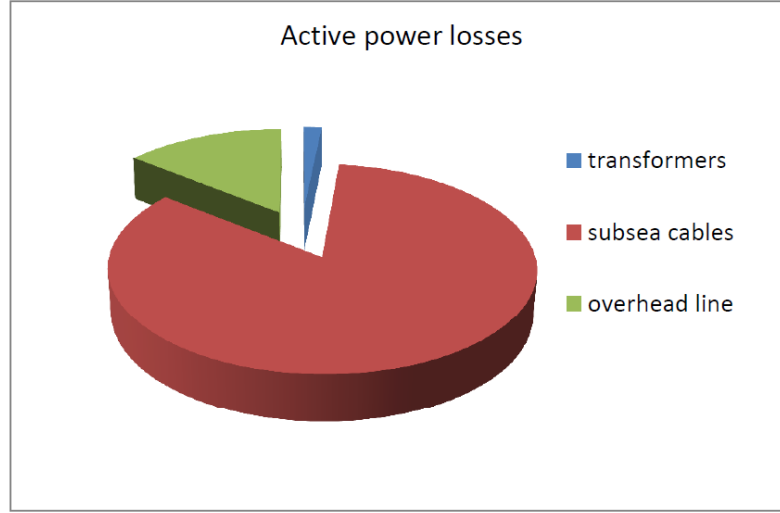


Figure 5.20: Power losses distribution over the different pieces of electrical equipment of the farm's electrical network

As regards the study focusing on the level of energy losses, time series corresponding to the three production periods A, B and C were used. This study was performed by means of simulations performed over a time period of 900 s. The energy losses are calculated by integrating the power losses over time, as:

$$\begin{aligned}
 E_{losses} &= \int_0^{900s} P_G dt - \int_0^{900s} P_{PCC} dt - \int_0^{900s} P'_L dt \\
 &= E_G - E_{PCC} - E'_L
 \end{aligned} \tag{5.13}$$

5.4.3 Power losses

The total power losses between the farm and the point of common coupling were found to represent 9.0% of the 14 MW output by the farm, as 1.26 MW are lost within the electrical network. This percentage is particularly significant and slightly greater than the percentage of the electric power transmission and distribution losses in Ireland which is equal to 7%, according to [106].

It was found that 84% of the active power losses is related to the submarine cables, whereas the overhead line accounts for 14% and the transformers for the remaining 2% of the losses, as illustrated in Figure 5.20. These results seem logical considering that the equivalent series resistance of the transformers is much smaller than the resistance of both the overhead line and the cables. In addition, the equivalent series resistance of the submarine cables is greater than the resistance of the overhead line which explains their greater contribution to the active power losses.

5.4.4 Energy losses

The results showed that the energy losses increase significantly with the sea-state energy level, as shown in Figure 5.21 for the three different production periods A, B, and C. Losses are negligible when production period C is used, which can be explained by the very low current level generated during this period compared to production periods A and B. It should also be noted that the wave farm orientation has a very strong influence on the level of losses. More specifically, the lateral orientation constitutes the worst case as a

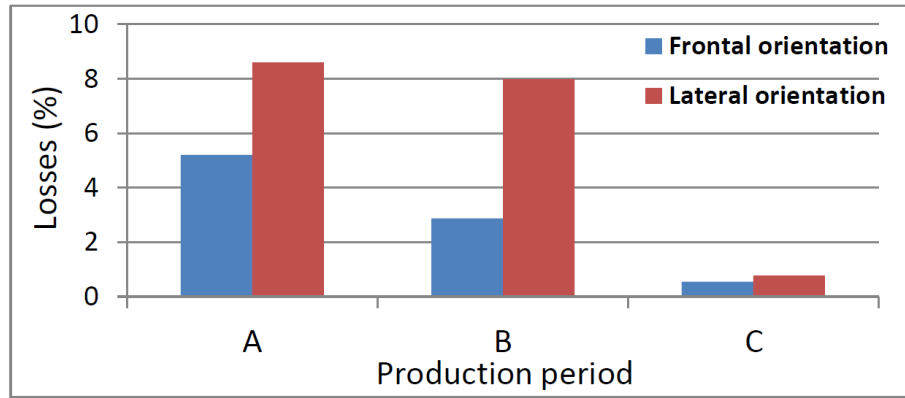


Figure 5.21: Percentage of losses for three different production periods and for the two farm orientations

	Production period		
	A	B	C
Losses increase (%)	63	177	45

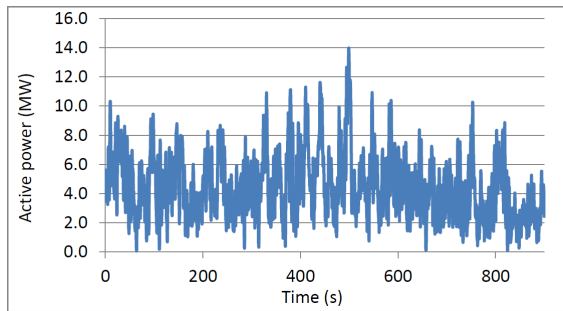
Table 5.16: Percentage of losses increase for the three different production periods between the lateral and the frontal farm orientations

losses increase ranging between 45% and 177%, as shown in Table 5.16, can be observed compared to the simulations in which the frontal orientation is used.

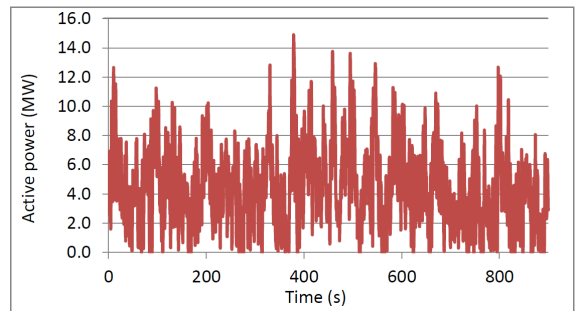
This can be explained by the greater current level reached regularly when the lateral orientation is used as shown in Figures 5.22a to 5.22f where the power profile at the PCC for each of these production periods is presented. In addition, the greater occurrence of these higher amplitude current peaks when the lateral orientation is used is also a factor that can increase power losses. It can be observed that the profiles of the farm power output corresponding to the production period A are relatively similar in terms of amplitude and number of occurrence of the highest power peaks for both orientations, as shown in Figures 5.22a and 5.22b. This may explain that the losses increase is moderate in this case, contrary to that of production period B, for which a large increase in terms of power losses is observed (177%). In this latter case, the profile of the farm power output is relatively different between the two orientations, as high amplitude power peaks occur much more regularly when the lateral orientation is used than when the frontal orientation is. As for production period C, the small amplitude of the power peaks limits the losses increase, although the difference between the power profile corresponding to each of the two orientations is significant in terms of amplitude and number of occurrence of the power peaks.

It is interesting to observe that the percentage loss seems to converge towards approximately 9%, thus matching the power loss percentage found in the load flow analysis and equal to 9.0%. This can be explained by the fact that the load flow case represents an extreme case compared to the dynamic simulations: in the former case, losses are maximal as the load flow is performed for a constant power output equal to the maximum power output of the farm (14 MW). Hence, it can be concluded that the maximum percentage of losses corresponding to a wave farm outputting a power up to 14 MW is equal to 9.0%.

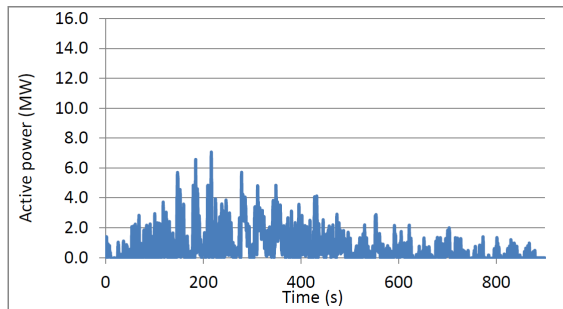
As mentioned earlier in this section, energy losses represent a direct loss of revenue for the wave farm's owners. For the sake of illustration, Figure 5.23b shows the theoretical



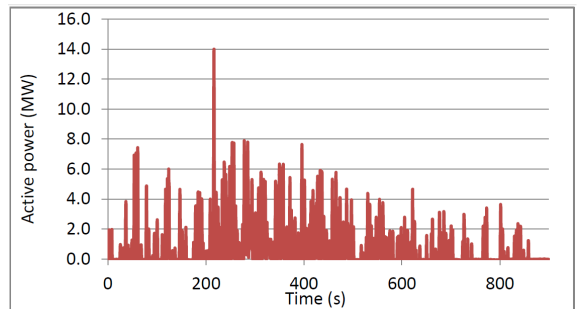
(a) Production period A, frontal orientation



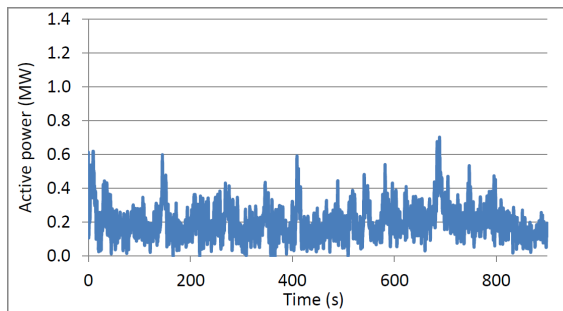
(b) Production period A, lateral orientation



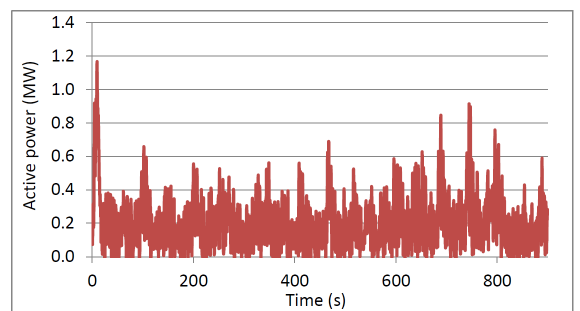
(c) Production period B, frontal orientation



(d) Production period B, lateral orientation



(e) Production period C, frontal orientation



(f) Production period C, lateral orientation

Figure 5.22: Profiles of the farm power output for different production periods and farm orientations

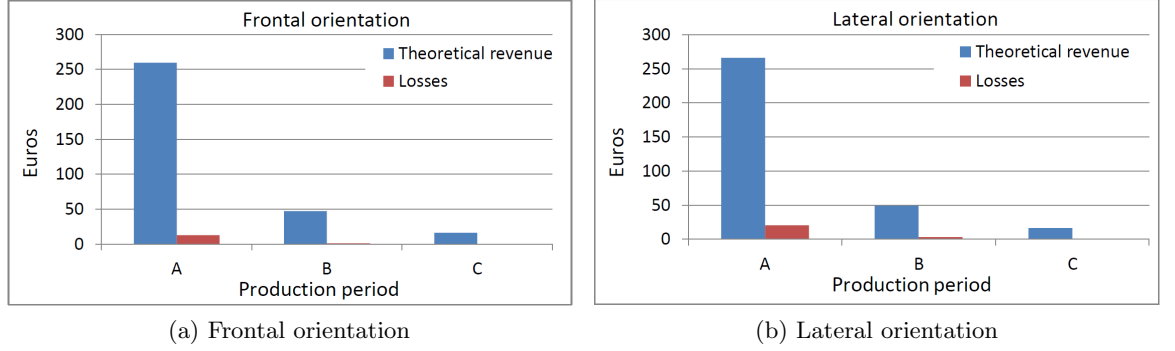


Figure 5.23: Theoretical revenue and losses

revenue generated over 900 s based on the farm’s power generation (excluding losses) and on the expected Irish feed-in tariff for wave electricity equal to 22c€/kWh [107] as:

$$\textit{Theoretical revenue} = \int_0^{900s} P_G dt \times 0.22 \times \frac{10^3}{3600} \quad (5.14)$$

and

$$\textit{Losses} = \int_0^{900s} P_{\textit{losses}} dt \times 0.22 \times \frac{10^3}{3600} \quad (5.15)$$

The relatively high level of losses observed in this study leads to a non-negligible revenue loss for the wave farm’s owner. Increasing the voltage level at which the farm is operated from 10 kV to 20 kV would decrease these power losses considerably. In addition, the 10/20 kV transformer connected at the onshore substation would no longer be needed. A load flow simulation was performed for a farm power output P_G equal to 14 MW using a modified version of the farm’s network (presented later in the next chapter) in which the cables are effectively operated at 20 kV. The percentage loss in this case is equal to 2.5%. This value corresponds to what may be expected, given that the current is divided by two in this case, which leads to power losses divided by four and thus to a theoretical percentage of losses equal to $9.0\%/4=2.3\%$. Hence, this simple modification of the wave farm design leads to a level of losses which is clearly more acceptable from a revenue perspective.

5.4.5 Summary

Energy losses were demonstrated to be significant and to represent up to 9.0% of the electricity generation under the conditions selected for the simulations. As expected, energy is mostly lost in submarine cables. In addition, the wave farm orientation was proven to have a strong influence on the level of losses, as the increase in terms of losses between the lateral and the frontal orientations was found to range between 45% and 177%, the lateral orientation representing the worst case.

It was recommended to operate the farm at 20 kV as this would lead to a significant decrease of the power losses percentage down to 2.3%. This would also avoid the need for a 10/20 kV transformer at the onshore substation.

It is important to note that the outcomes of both this study and of the study focusing on the submarine cables rating are complementary. This latter study focused on determining the minimum current level, and thus the minimum conductor diameter, for which the submarine cables should be rated. However, a smaller rating implies a reduction of

the conductor cross-sectional area, which increases its resistance, according to the law of Pouillet expressed as:

$$R = \frac{\rho_T l}{S_c} \quad (5.16)$$

where R is the resistance of the conductor, ρ_T is the material conductivity, l is the conductor's length and S_c is its cross-sectional area. Consequently, although minimising the cable rating of the submarine cables may lead to significant savings in terms of capital expenditure, it may also reduce significantly the revenue generated from the electricity sale. Hence, these two criteria are recommended to be taken into account for optimising the cable rating.

5.5 Conclusions

This chapter presented three different studies. The first study focused on the reactive power ratings of the VAr compensator located at the point of common coupling while the second focused on the current rating of the submarine cables. A third study investigating the losses dissipated within the farm's electrical network was also presented.

5.5.1 VAr compensator

The minimum ratings of the VAr compensator were found to range between 3.6 MVar and 9.0 MVar (generated), and 0.1 MVar and 0.8 MVar (absorbed). The ratings were demonstrated to be highly dependent on the length of both the cables and the overhead line. As the amount of reactive power to be generated by the VAr compensator may become very important for a sufficiently long overhead line, it was recommended to connect a wave farm at a location where a connection point sufficiently close to the farm is available, if at all possible.

5.5.2 Submarine cables

The second study, which focused on the minimum current rating of submarine cables, demonstrated that these cables could actually be safely designed, from a thermal loading perspective, for a current level approximately equal to the half of the average current flowing through them, more precisely ranging between 47% and 51% of this value. Selecting the cables rating based on the thermal loading approach may lead to a significant decrease in terms of capital expenditure, compared to basing the selection process on usual, steady-state calculations which are no longer relevant in the case of wave energy applications, due to the fluctuating nature of the current generated by wave farms. A simplified method, whose results were compared to the results of a more detailed study using dedicated IEC standards, was developed and presented. The results obtained with both studies proved to be in good agreement. They showed that the influence of the farm orientation and of the thermal time constant τ was non-negligible, but relatively limited. Finally, the sensitivity of the results to the ambient temperature was investigated. The results showed that a moderate difference is observed for an ambient temperature ranging between 0°C and 20°C compared to the case where the ambient temperature is equal to 10°C, which is the temperature selected for the study. In addition, although this difference is slightly more important for higher temperatures, the results presented in this study constitute however an interesting starting point in this case.

5.5.3 Losses

The third and last study investigated the power and energy losses dissipated in the farm's electrical network. It showed that power losses were dissipated mainly in the submarine cables and that the percentage loss compared to the total farm power output converges towards 9.0%, which is particularly significant. Hence, it was recommended to increase the voltage level at which the farm is operated from 10 kV to 20 kV to obtain a more reasonable percentage loss equal to 2.3%.

5.5.4 Discussion

The studies presented in this chapter as well as in the previous one were based on a typical model of wave farm intended to be used as a test site. However, although most developers have indicated that they intend to increase the available power capacity of their sites once the wave energy industry has reached the commercial phase, major questions remains concerning the feasibility of this project. First, it has been demonstrated that the impact of a medium size wave farm on the power quality may already exceed the regulatory limits. Hence, this aspect should be investigated in order to determine whether it may become a limiting factor to the expansion of the test site. Then, the thermal loading of the farm's electrical network elements may also limit the power capacity of a commercial site. The study presented in this chapter regarding the cables current rating was thus performed again for a wave farm of rated power up to 50 MW. The electrical network of this commercial wave farm is operated at 20 kV according to the recommendations issued in the third study focusing on the power losses.

Chapter 6

Analysis of the obstacles to the transformation of a test site into a commercial site

6.1 Introduction

Chapter 4 investigated the issues posed by the connection of a 20 MW-rated wave farm in terms of power quality. It was shown that flicker represented a serious problem in the case where a wave farm is connected to sufficiently weak networks, or if the power factor which the grid operator mandates at the PCC is not optimal.

Additional aspects regarding the relevance of the typical test site design were also discussed in Chapter 5. More specifically, the rating of the electrical elements as well as the energy losses within the farm's electrical network were analysed. It was suggested that the operating voltage of this particular farm's electrical network is stepped up from 10 kV to 20 kV to reduce the power losses within this network as well as to minimise the required rating for the VAr compensator. The previous chapters have investigated the aspects mentioned above with respect to a medium-size wave farm.

However, test sites are envisaged to be transformed into commercial sites once the wave energy industry has reached the commercial phase. Hence, it is interesting to discuss the feasibility of this project. This transformation will mainly consist of increasing the number of wave devices included in the farm. In addition, the device layout may also differ greatly between a test site and a commercial site as will be discussed later in this chapter. Two aspects are investigated: the impact on the power quality and the relevance of the wave farm design in terms of the current ratings of both the submarine cables and of the overhead line.

6.2 Methodology and models

6.2.1 Numerical grid model

The numerical model used for the studies presented in this chapter is shown in Figure 6.1. It is based on the model used in the previous chapters, with the following modifications to enable the connection of wave farm of greater rated power P_{rated} . First, the number of wave devices was increased up to 57, which corresponds to a rated power P_{rated} approximately equal to 50 MW, as shown in Table 6.1. The values of the rated power P_{rated} will be referred to as their rounded values in the rest of this thesis for the sake of clarity, in similar

Rated power P_{rated} (MW)	19.4	30.0	39.7	50.3
Number of devices	22	34	45	57
Rounded rated power P_{rated} (MW)	20	30	40	50
Short-circuit ratio	3.6	2.4	1.8	1.4

Table 6.1: Short-circuit ratio corresponding to a short-circuit level $S_{sc}=72$ MVA

Impedance Z_S at 38 kV (Ω)	5	10	15	20
Short-circuit level S_{sc} (MVA)	289	144	96	72

Table 6.2: Short-circuit levels S_{sc} considered in this study

fashion to Chapter 4. Then, the operating voltage for the submarine cables was increased from 10 kV to 20 kV, as recommended in the previous chapter. The characteristics of these cables in terms of impedance remained unchanged and the offshore transformers, initially stepping the voltage up to 10 kV, were modified to step the voltage up to 20 kV. The 10/20 kV transformer located at the substation was removed. The short-circuit levels considered in this study range from 72 MVA (corresponding to a series reactor impedance Z_S at 38 kV equal to 20 Ω) to 289 MVA (i.e. 5 Ω), as summarised in Table 6.2. However, the analysis of the results will focus mainly on the lowest short-circuit level of 72 MVA as a worst case scenario. This corresponds to a short-circuit ratio ranging between 3.6 to 1.4 for a wave farm with a rated power P_{rated} ranging between 20 MW to 50 MW, as shown in Table 6.1.

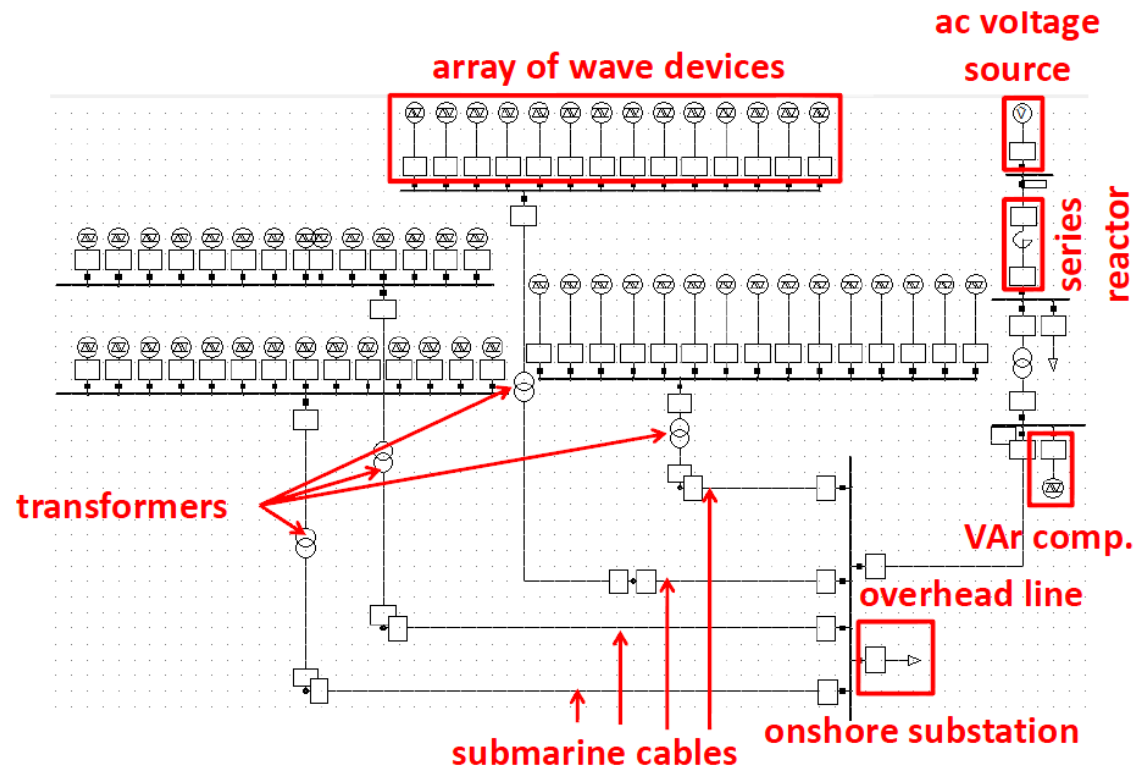


Figure 6.1: Numerical grid model used for the studies presented in this chapter

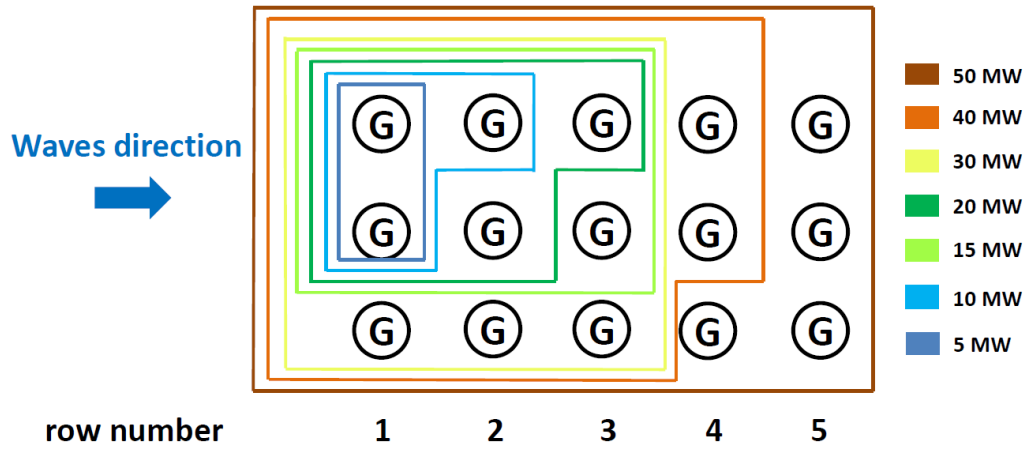


Figure 6.2: Illustration of the device layout of a single array for an increasing rated power P_{rated} . Each circle corresponds to the position of a generator within an array.

6.2.2 Device aggregation

Introduction

The device layout in the case of a test site is intended to enable the performance monitoring of each device under the best sea conditions. It is important to bear in mind that the performance assessment is more and more taken into account by funding agencies such as the Scottish Investment Bank [108] or the Saltire Prize [109]. Hence, each wave device or device array is expected to be located sufficiently far from the other devices belonging to the farm in order to limit mutual interferences. In addition, in order to benefit from the best sea conditions, no device should be positioned directly behind another device as it may reduce the amplitude of its incoming waves significantly. Consequently, it is very likely that the devices will be structured into linear arrays in the case of a test site. This corresponds to the lateral farm orientation described in Chapter 4 which is considered as a worst case in terms of power quality.

However, the device layout must be structured differently in the case of a commercial wave farm. The larger number of wave devices included in the farm implies that they will most likely be located sufficiently close to each other in order to minimise the cable length [95]. Hence, a linear array should no longer be envisaged in this case. On the contrary, more compact geometrical shapes, such as a square or a rectangle, seem more suitable. This modification in terms of device layout is also expected to reduce the impact of a wave farm on power quality by facilitating the generation of a smoother farm power output.

Device layout

The farm is modelled as four rectangular arrays similar to the sample shown in Figure 6.2. An increasing rated power P_{rated} is simulated by adding a defined number of wave devices to each array whose position in the array is defined as well. Figure 6.2 shows the number of devices included in the array, as well as their position within the array, as a function of the rated power P_{rated} . The studies were performed for four values of the rated power P_{rated} , namely 20 MW, 30 MW, 40 MW and 50 MW for which the corresponding number of devices is indicated in Table 6.1.

The time delays are defined as described in the following section and according to the

wave direction indicated in Figure 6.2. Given the symmetrical shape of the farm, similar results are obtained whether the wave direction indicated in this figure or a direction perpendicular to this one is used. Hence, only the results corresponding to the former wave direction are presented.

Time delays

The time delays are defined based on the method detailed in Chapter 4. However, this method implied that all devices in the array may be spaced at maximum 1000 m apart. Although this is reasonable with respect to a small size array consisting of up to 6 wave devices, as is the case in the work presented in Chapter 4, this is no longer applicable in the case of an array consisting of up to 15 devices. Hence, a modified method was developed.

As described in Chapter 4, the time delay ΔT_{total} applied to the power profile of a wave device depends on the energy period T_e of the sea-state corresponding to the production period under consideration, and on the distance D_{total} between a wave device and the reference device. In this chapter, this distance D_{total} is the sum of four different terms and can be expressed as:

$$D_{total} = D_{row}[(n_{row} - 1)(1 - a_{row}) + a_{pos} + a_{arr}] + D_c \quad (6.1)$$

The term D_{row} corresponds to the distance between each of the rows numbered from $n_{row} = 1$ to $n_{row} = 5$ in Figure 6.2 and which was chosen equal to 1000 m for the same considerations as discussed in Chapter 4. The factor a_{row} is a percentage ranging between 0% and 60% which was generated by using the function “rand” in Matlab as described in Chapter 3. The value of the percentage a_{row} is the same for wave devices belonging to the same row and is meant to capture the uncertainty associated with the position of each device.

The factor a_{pos} is also a randomly-generated percentage ranging between 0% and 10%. This term introduces a certain level of randomness with respect to the position of each individual device, as it is different for each. The last randomly-generated percentage a_{arr} is meant to prevent two generators belonging to two different arrays to output the same power profile in the case where they have the same parameters D_{row} , a_{row} and a_{pos} . In practice, this parameter is applied to one of the array located at 6.5 km from the shore and to one of the array located at 16 km from the shore. This percentage is equal for all the generators belonging to the same array.

The last term D_c corresponds to the distance of 10 km which separates the arrays located 6.5 km and 16 km from the shore. However, as described in Chapter 4, the duration of the experimental time series is not sufficiently long to use a time delay corresponding to 10 km. Hence, this distance D_c was arbitrarily chosen such as $D_c = D_{row} = 1000$ m. This eliminates the possibility of two wave devices located 10 km apart outputting the same power profile in the case where they present the same values for the factors a_{row} , a_{pos} and a_{arr} . Finally, the time delay ΔT_{total} is determined as:

$$\Delta T_{total} = \frac{D_{total}}{v_g} = \frac{4\pi D_{total}}{gT_e} \quad (6.2)$$

The resulting farm power profiles for a rated power P_{rated} equal to 50 MW are shown in Figure 6.3. As it can be observed from this figure, the device layout contributes in reducing the amplitude of the power peaks, as the maximum power does not exceeds 19.4 MW in this case. The maximum power reached in the case of other values of the rated power P_{rated} and for other production periods is shown in Figure 6.4.

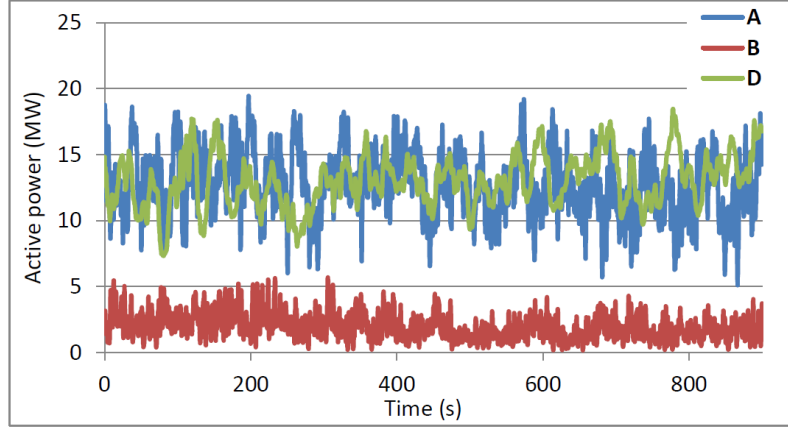


Figure 6.3: Profiles of the farm power output for four production periods A, B and D and for a rated power $P_{rated}=50$ MW

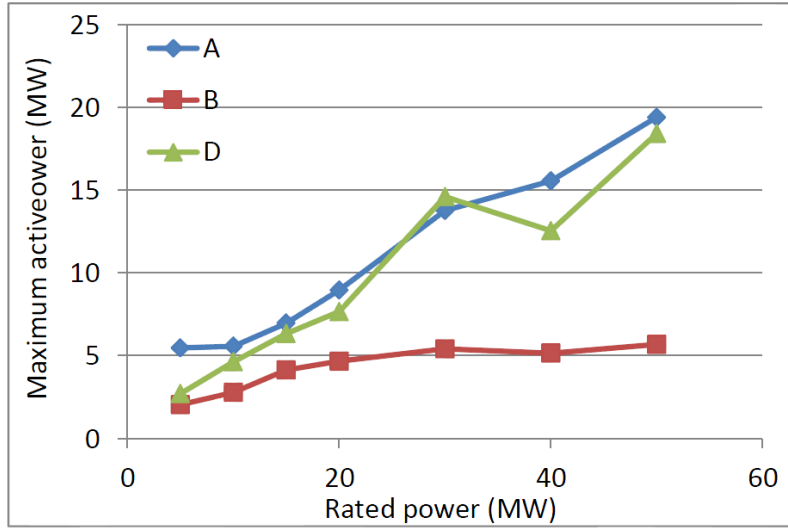


Figure 6.4: Maximum power as a function of the rated power P_{rated} for the three production periods A, B, and D

6.2.3 Power factor control

As the studies presented in the previous chapters indicated, the selection of a suitable power factor reference for the VAr compensator connected at the PCC may reduce the amplitude of the voltage fluctuations at this node dramatically. This helps also in reducing the flicker level. Simulations were performed for four values of the power factor reference, namely 0.92, 0.95, 0.97 lagging and unity. The results are detailed in Section 6.3.

6.2.4 Storage

Storage means may need to be included either in the wave device design or in the wave farm for smoothing their power fluctuations. Storage is modelled in this study by a first order filter of time constant τ_s whose transfer function F_s can be expressed as:

$$F_s(s) = \frac{1}{1 + s\tau_s} \quad (6.3)$$

The time constant τ_s of the filter facilitates the modelling of the storage means in a generic manner [46]. The minimum value of τ_f for which the farm is compliant with the

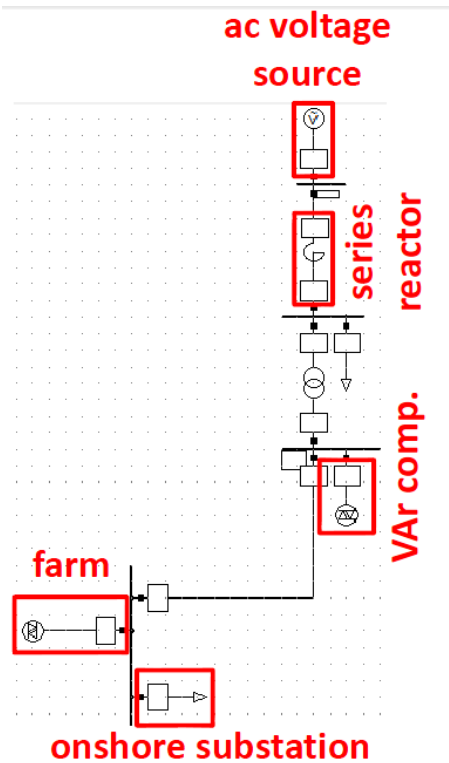


Figure 6.5: Numerical model used for the study focusing on storage

flicker requirement was compared to typical time constants provided in this document in order to determine the type of storage means required.

The generic storage means is implemented in the static generator connected at the onshore substation, as shown in Figure 6.5, and which represents the rest of the farm. This generator is controlled to output the reactive power profile corresponding to the reactive power flowing through the substation bus. Its active power profile corresponds to the active power flowing through the bus substation filtered by the generic storage means of transfer function F_s .

6.2.5 Generator control strategies

The two previous chapters used time series generated when the OWC prototype was operated in fixed speed mode, which constitutes a worst case scenario from a power quality perspective. However, variable speed operation has already demonstrated to be a very efficient way to reduce rapid power fluctuations in the case of wind turbines [25]. This beneficial aspect was also observed in the case of a single onshore OWC [45]. Although this type of operation requires the use of relatively costly power electronic converters, requirements such as the fault ride-through and the frequency response requirement will in any case require these power electronic converter systems in the device design. Hence, it is expected that variable speed operation will become the norm for wave devices having reached the commercial stage.

A study was conducted to compare the effect on several power quality criteria, namely the maximum and minimum voltages as well as the flicker level, of operating the wave devices in a variable speed mode. A production period during which the OWC prototype was operated in variable speed mode and in sea-state conditions similar to those corresponding to production periods A and B was selected. The characteristics of this production period,

Period label	Significant wave height H_s (m)	Energy period T_e (s)	Fixed/variable speed mode
A	5.0	10.9	fixed
B	2.1	7.3	fixed
D	4.5	8.8	variable

Table 6.3: Characteristics of the different production periods used for the power system simulations

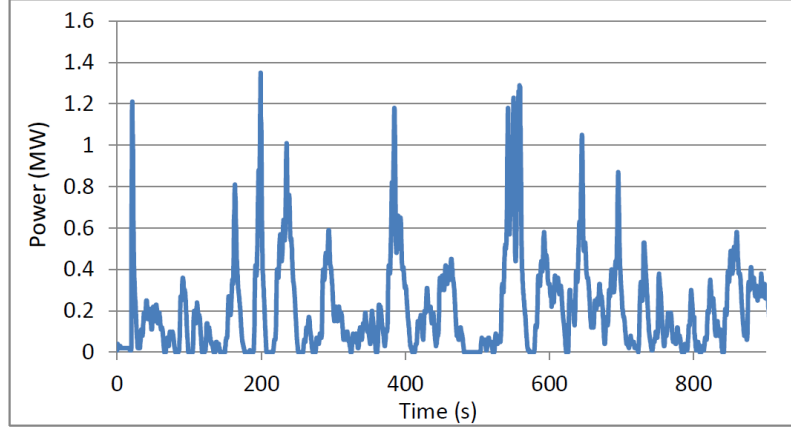


Figure 6.6: Individual power profile corresponding to production period D

referred to as production period D in the rest of this document, is shown in Table 6.3. The individual power profile corresponding to production period D is shown in Figure 6.6. The two most energetic production periods A and B used in the previous studies, in which the generator is operated in fixed speed mode, are taken as benchmarks for the results obtained with production period D.

In order to provide a sanity test for the results presented in this study, a virtual production period was created to represent the equivalent power profile of a generator operated in variable speed mode under the sea conditions encountered in production period A. The action of the inertial storage provided by the generator and the air turbine included in the OWC drive train was simulated by filtering the individual power profile of a wave device of production A by a first order filter whose transfer function $F_f(s)$ can be expressed as:

$$F_f(s) = \frac{1}{1 + s\tau_f} \quad (6.4)$$

where τ_f is the time constant of the filter which is equal to 1.7 s. This corresponds to the inertia of the air turbine [46]. The original (i.e. non-filtered) power profile as well as the resulting individual power profile is shown in Figure 6.7. The filtered power profile will be referred to as production period A'.

6.3 Grid compliance

Considering that production period A presents the farm maximum power as shown in Figure 6.4, the compliance of the wave farm with respect to the voltage limits requirements was investigated for this production period only. However, the flicker level corresponding to all the production periods is analysed.

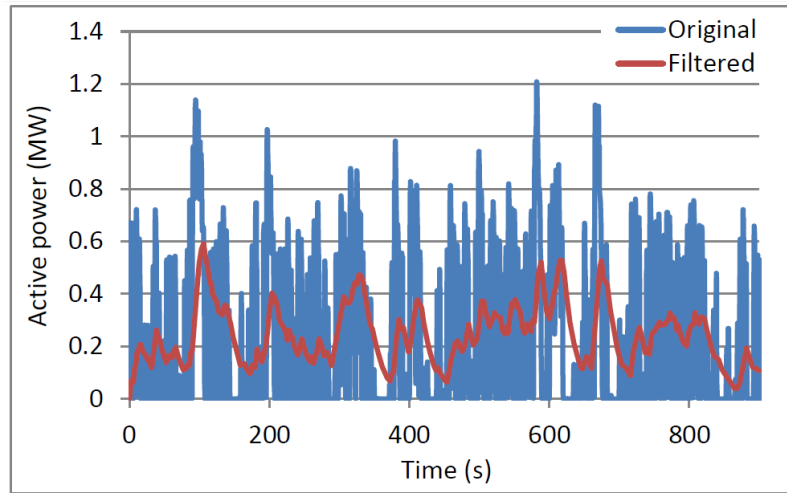


Figure 6.7: Original and filtered power profile of production period A

6.3.1 Voltage limits

Power factor control

Power system simulations were performed for four values of the reference power factor at the PCC, namely: 0.92, 0.95 and 0.97 (all lagging) and unity. The results presented in this section correspond to the lowest short-circuit level S_{sc} considered in this work and equal to 72 MVA. Hence, for each rated power P_{rated} and impedance angle Ψ_k , there are four maximum and four minimum voltages corresponding to the four power factor references. Among these four values, the one closest to unity is retained for the study, as it corresponds to the application of an optimal power factor reference at the PCC.

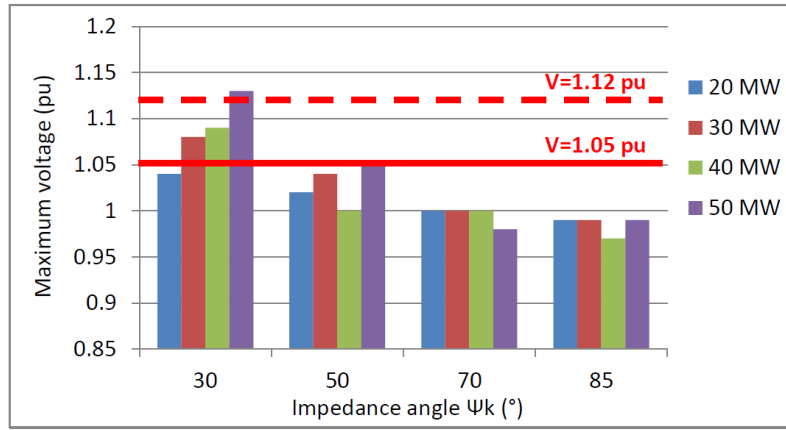
Figures 6.8a and 6.8b presents the maximum and minimum voltage obtained through this selection. It can be observed that, even when the maximum voltage is minimised by the application of an optimal power factor, it may still exceed (or be very close to) the most stringent limit equal to 1.05 pu in the case where the farm is connected to an impedance angle up to 50° . The most permissive limit, which is equal to 1.12 pu, may also be exceeded for a 50 MW-rated farm connected to a connection point whose impedance angle Ψ_k is equal to 30° .

As for the minimum voltage, Figure 6.8b shows that the voltage is less than the most stringent limit, which is equal to 0.94 pu, for a 50 MW-rated farm only, and is equal to the most permissive limit equal to 0.90 MW.

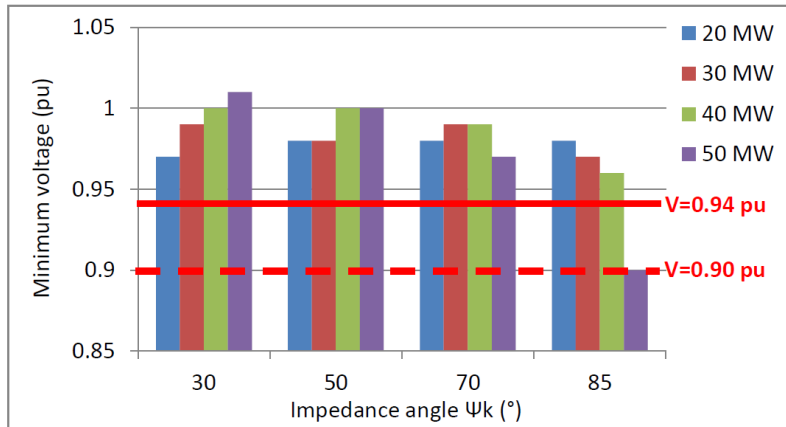
Hence, if a wave farm of significant rated power is connected at distribution level, power factor control may not always be sufficient for rendering this farm compliant with the voltage limits requirement.

Storage

Storage is an efficient means for reducing the amplitude of the voltage fluctuations at the PCC, as shown in Figure 6.9. This figure shows the voltage profile corresponding to different values of the storage means' time constant τ_s . However, in the case where the average voltage exceeds the upper limit or is less than the lower limit, then power factor control becomes necessary to decrease it. Figure 6.10 shows for instance the average voltage as a function of the farm rated power P_{rated} for different impedance angles Ψ_k for a power



(a) Maximum voltage



(b) Minimum voltage

Figure 6.8: Maximum and minimum voltages obtained for an optimal power factor

factor equal to unity. The red-shadowed area corresponds to the cases where the average voltage is greater than the most stringent limit, which is equal to 1.05 pu. In these cases, using storage means only cannot help rendering the wave farm compliant with the voltage limits requirement.

Based on the results presented in the previous section which showed that the voltage limits may be exceeded even with an optimal power factor, it may be concluded that exceeding the voltage limits (or generating a voltage less than the lower limit) may represent a serious issue if a sufficiently high-rated wave farm is connected to nodes whose impedance angle Ψ_k is relatively low. However, the usually low power transfer capacity available at this type of nodes is expected to represent the limiting factor for the increase of the farm rated power P_{rated} rather than power quality issues.

Variable speed mode

In similar fashion to the results obtained with the collective storage means, the results obtained when the generators are operated in variable speed mode confirm that, although storage is a very efficient means for reducing the voltage fluctuations, it is useless if the average voltage exceeds or is less than the limits allowed by the grid operator. Figures 6.11a and 6.11b show the maximum and minimum voltages obtained for production period D in which the generator is operated in variable speed mode, while Figures 6.12a and 6.12b show the maximum and minimum voltages obtained for production period A in which the

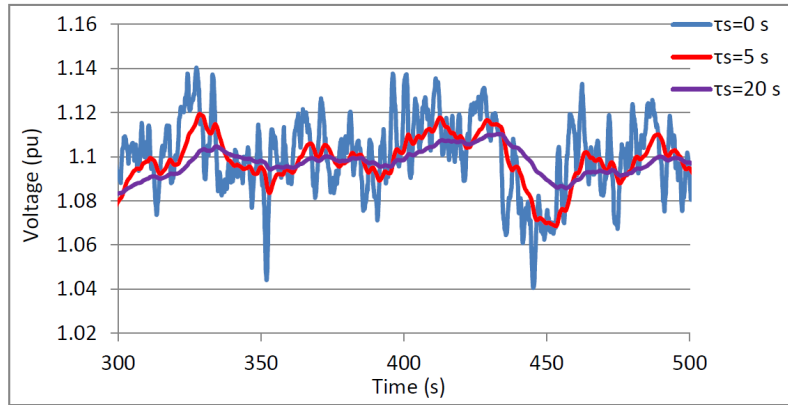


Figure 6.9: Voltage profile at the PCC for a number of values for the storage time constant τ_s

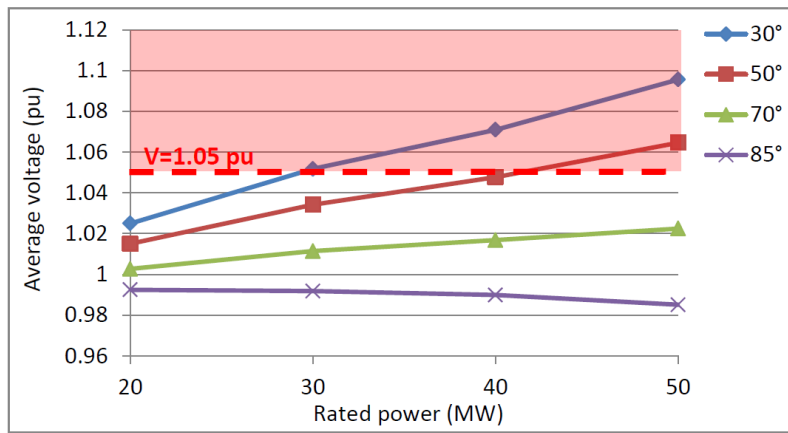


Figure 6.10: Average voltage as a function of the rated power P_{rated} for different impedance angles Ψ_k ($pf=1$)

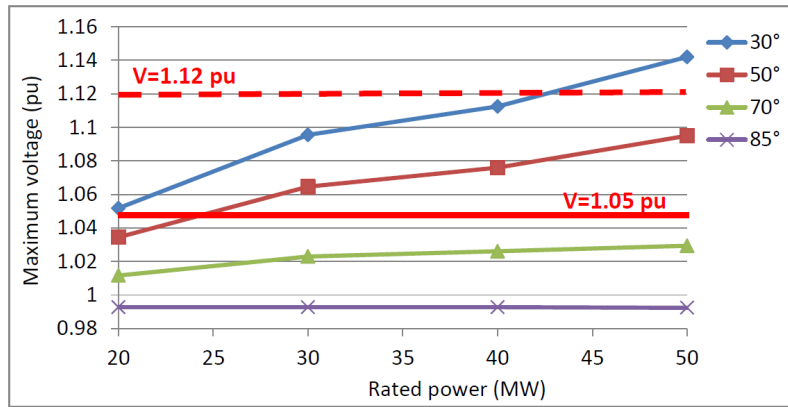
generator is operated in fixed speed mode. As both these production periods were recorded during sea-states having similar characteristics, the results corresponding to each of these periods can be reasonably compared. It appears clearly that in both cases, the most stringent as well as the most permissive limits may be exceeded if the wave farm rated power is sufficiently great. However, the beneficial effect of the variable speed operating mode is significant as the voltage deviation are slightly less excessive in the case of production period D than they are in production period A.

6.3.2 Flicker

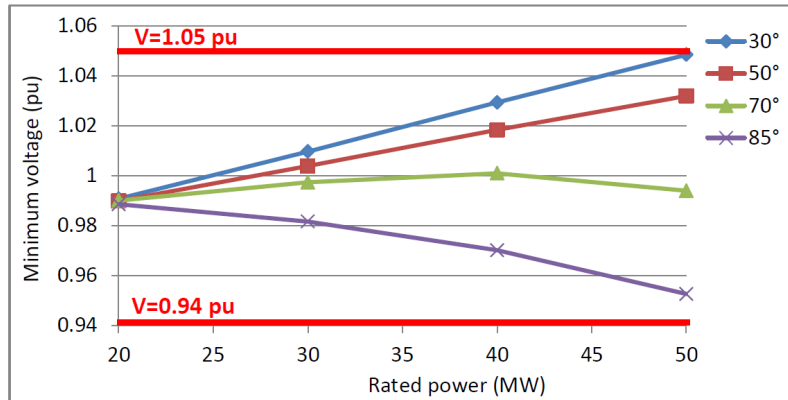
Power factor control

Power factor control is an efficient means for reducing the flicker level Pst below the most stringent limit equal to 0.35 in most cases, as shown in Figure 6.13. This figure presents the minimum flicker level generated by a 50 MW-rated wave farm for the four power factor references considered in this study which are equal to 0.92, 0.95 and 0.97 lagging as well as unity, and for the lowest short-circuit ratio considered in this study which is equal to 1.4.

The results show that power factor control is an efficient means for maintaining flicker level below the most stringent limit, with the exception of connection points with a impedance angle as low as 30° and with a low short-circuit level S_{sc} . However, as mentioned



(a) Maximum voltage



(b) Minimum voltage

Figure 6.11: Maximum and minimum voltages of production period D (variable speed) operated at unity power factor

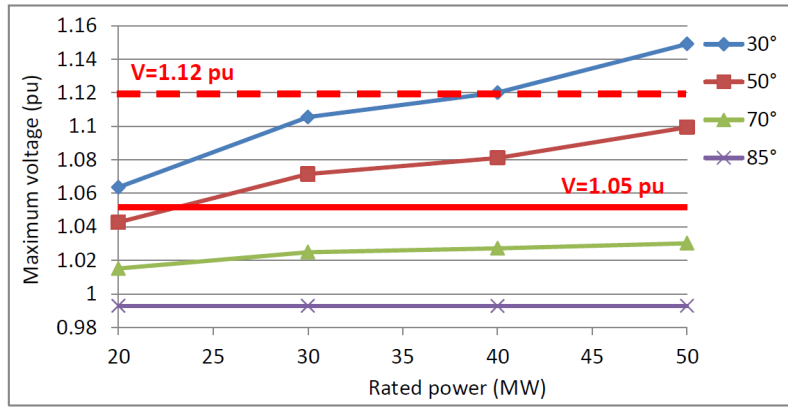
earlier, this type of connection points is not expected to be envisaged for the connection of a wave farm, given the usually low power transfer capacity available at these nodes.

Storage

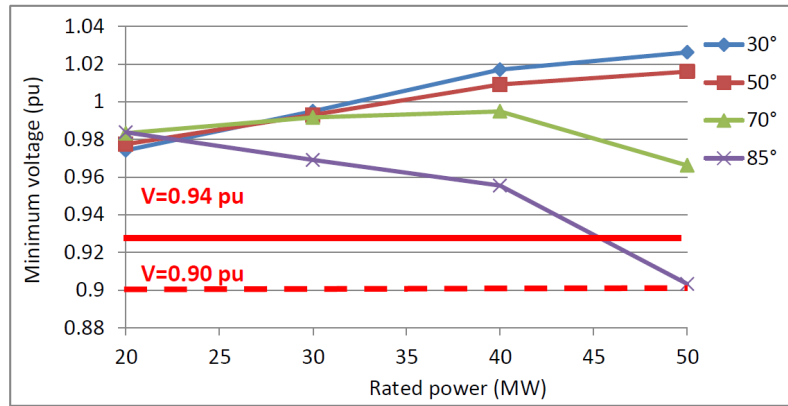
Storage is an efficient means for reducing the flicker level, as shown in Figure 6.14 which presents the flicker level generated by a 50 MW-rated wave farm at a relatively weak connection point whose short-circuit ratio is equal to 1.4 as a function of the impedance angle Ψ_k . In the case where the flicker level exceeds the most stringent limit equal to 0.35, it appears that a storage means of time constant τ_s equal to 1 second is sufficient to reduce the flicker level below this limit. This relatively low value corresponds to the time constant of a small size hydraulic accumulator [46].

Variable speed mode

Figure 6.15 shows the flicker level Pst as a function of the impedance angle Ψ_k for all the four production periods considered in this work. It can be observed that the flicker level generated by production period A' is very close to this generated by production period D. This proves that the method adopted for modelling energy storage is relevant and provides accurate results. In addition, assuming that these results are approximately equivalent to these corresponding to the use of a collective storage means of time constant $\tau_s=1.7$ s, they show good agreement with the results presented in Figure 6.14. It must be noted as well that using the variable speed mode decreases the flicker level much below the most



(a) Maximum voltage



(b) Minimum voltage

Figure 6.12: Maximum and minimum voltages of production period A (fixed speed) operated at unity power factor

stringent limit equal to 0.35. Hence, the variable speed mode seems to be a sufficient mitigation means for the connection of a 50 MW-rated wave farm.

6.3.3 Summary

The study presented in this section investigated the compliance of a wave farm rated up to 50 MW with the voltage limits and flicker level requirements. The wave farm was demonstrated to be compliant with the voltage limits requirement in almost all the cases considered, provided that a suitable power factor is applied at the PCC and that a storage means with a sufficient time constant τ_s is used, if necessary. In addition, the usually low power transfer capacity available at the nodes for which the farm may not be compliant constitutes the main obstacle to the connection of a wave farm at these nodes. Hence, conventional voltage control means, such as power factor control and the use of storage, proved to be sufficient for rendering a wave farm compliant.

It was also demonstrated that a minimal amount of storage was sufficient for reducing the flicker level below the most stringent limit equal to 0.35. This is in good agreement with the findings of [39]. Storage may be included as part of the individual wave device design, for instance by enabling the variable speed operation of the generator, or implemented as a collective means smoothing the farm power output. In both cases, a storage means whose time constant τ_s is approximately equal to one second is sufficient for reducing the flicker level below the most stringent limit. This value corresponds to the time constant

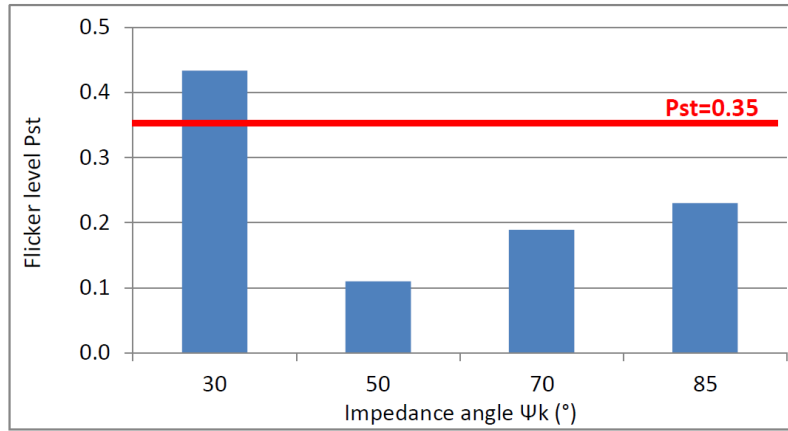


Figure 6.13: Minimum flicker level P_{st} obtained for the optimum power factor as a function of the impedance angle Ψ_k for a 50 MW-rated wave farm with a short-circuit ratio equal to 1.4

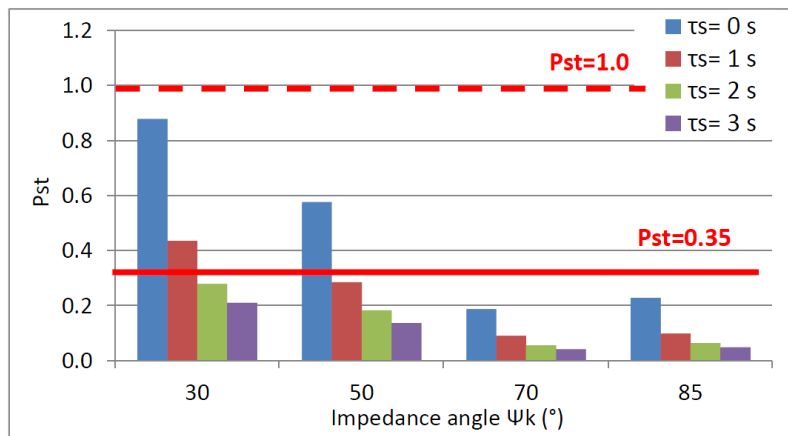


Figure 6.14: Flicker level P_{st} as a function of the impedance angle Ψ_k for a 50 MW-rated wave farm with a short-circuit ratio equal to 1.4 (production period A)

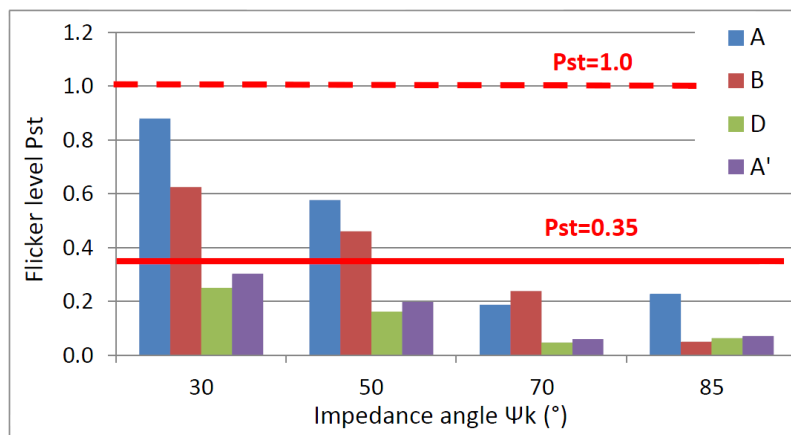


Figure 6.15: Flicker level P_{st} as a function of the impedance angle Ψ_k for all the four production periods considered in this work

Rated power P_{rated} (MW)	20	30	40	50
Average current (A)	32	50	67	81
Standard deviation (A)	17	23	26	27
Rating (A)	7	12	21	30
Rating/Average (%)	22	25	32	37

(a) 20 kV

Rated power P_{rated} (MW)	20	30	40	50
Average current (A)	65	99	133	163
Standard deviation (A)	33	46	52	55
Rating (A)	23	47	77	112
Rating/Average (%)	35	48	58	69

(b) 10 kV

Table 6.4: Results with respect to the original current profiles at 20 kV (top) and to the equivalent current profiles at 10 kV (bottom)

of a small hydraulic accumulator for instance. The power factor control at the PCC was also proven to be an efficient means for reducing flicker. However, it may not be always sufficient. In conclusion, power factor control, and also storage if necessary, are efficient means for rendering a 50 MW wave farm compliant with both the voltage limits and the flicker level requirements.

6.4 Current ratings of the cables and of the overhead line

6.4.1 Submarine cables

The same study as presented in Chapter 5, initially conducted for an approximately 20 MW-rated farm developed for testing purposes, was also performed based on the simulations obtained for a wave farm whose rated power P_{rated} ranges between approximately 20 MW and 50 MW.

It is important to bear in mind that in the model used in this chapter, the submarine cables are operated at 20 kV, contrary to the study presented in Chapter 5 in which they were operated at 10 kV. Hence, this renders the comparison between the results obtained in this study and those obtained from the study presented in Chapter 5 not straightforward. In order to facilitate this comparison, equivalent current profiles $I_{eq}(t)$ were created by multiplying the current profiles $I(t)$ obtained from the present study by two as this corresponds to current profiles generated by a wave farm rated between 20 MW and 50 MW in the case where the submarine cables were operated at 10 kV. This can be summarised as:

$$I_{eq}(t) = \frac{20}{10}I(t) = 2I(t) \quad (6.5)$$

The rating study was performed for both the original current profiles $I(t)$ at 20 kV and the equivalent current profiles $I_{eq}(t)$. The results of the study are summarised in Tables 6.4a and 6.4b. Table 6.4a shows the minimum current ratings required for each of the considered farm rated power P_{rated} , and the percentage of the average current they represent. Table 6.4b shows the results with respect to the equivalent current profiles at 10 kV while Table 6.5 recalls the results obtained from the study presented in Chapter 5.

Rated power P_{rated} (MW)	20
Average current (A)	60
Standard deviation (A)	47
Rating (A)	30
Rating/Average (%)	49

Table 6.5: Summary of the results obtained from the previous study presented in Chapter 5

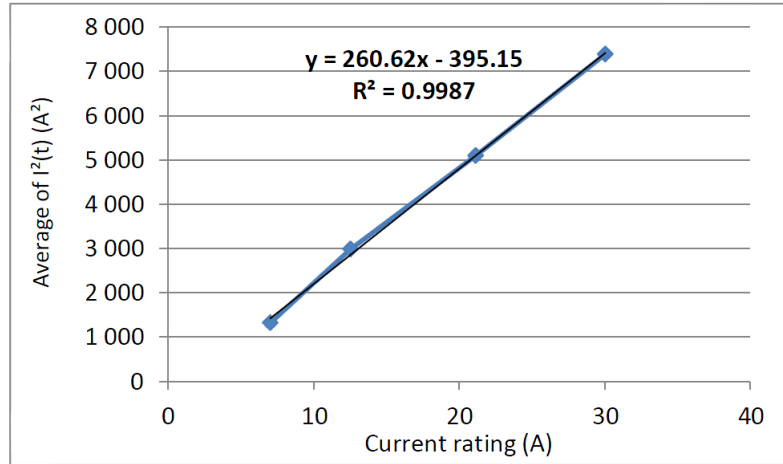


Figure 6.16: Average of the square of the current $I^2(t)$ as a function of the current rating I_{rating}

As expected, the ratio of the current rating I_{rating} to the average current I_{avg} is almost doubled between the original results (obtained for submarine cables operated at 20 kV) and the results corresponding to the 10 kV case. This can be explained by the fact that, by doubling the value of the current $I(t)$, the average current I_{avg} is also doubled. On the contrary, the current rating I_{rating} is determined based on the cable temperature, which is calculated from the square of the current $I(t)$. Hence, it is expected that it increases as a function of the square of the current $I^2(t)$, which is confirmed in Figure 6.16. This figure shows that the current rating I_{rating} is approximately proportional to the average of the square of the current $I(t)$. Hence, it can be assumed that doubling the current $I(t)$ leads to multiplying the current rating by approximately four. Consequently, the ratio of the current rating I_{rating} to the average current I_{avg} is expected to be almost doubled between the original current profiles and the corresponding current profiles at 10 kV, which is confirmed by the results.

The results concerning the original current profiles presented in Table 6.4a show that this ratio ranges between 22% and 37% for a farm rated between 20 MW and 50 MW. This corresponds to 8% to 17% only of the maximum current I_{max} flowing through the cable as summarised in Table 6.6. These results confirm that the average current is a relevant criterion for the estimation of a suitable rating for the submarine cables from a thermal loading perspective.

It is also interesting to compare the results obtained for the cases where the submarine cables are operated at 10 kV, both for the present study and the study detailed in Chapter 5. It can be noted that sensibly similar values in terms of average current are observed for a 20 MW-rated wave farm. The average current is equal to 65 A in the first case while it is equal to 60 A in the latter. However, the standard deviation is relatively

Rated power P_{rated} (MW)	20	30	40	50
Rating/Maximum (%)	8	10	14	17

Table 6.6: Ratio of the current rating I_{rating} to the maximum current I_{max}

Rated power P_{rated} (MW)	20	30	40	50
Rating/Maximum (%)	12	24	39	56

Table 6.7: Ratio of the current rating I_{rating} to the initial current rating (199 A)

different, being much greater in the previous study where it is equal to 47 A while it is equal to 33 A only in the present study. This is explained by the fact that current peaks of greater amplitude are observed in the previous study than in the present study due to the device layout. This is illustrated in Figures 6.17a and 6.17b which show the equivalent current profile at 10 kV obtained from the present study and the current profile obtained from the previous study respectively. This means that temperature fluctuations of greater amplitude are generated in the case of the previous study, which corresponds to the need for a greater current rating I_{rating} . Hence, these results show that a suitable device layout facilitates the reduction of the cables' minimum current rating as it decreases the amplitude of the current peaks.

The minimum ratings determined in this study represent between 12% to 56% of the initial current rating of the cables, which is equal to 199 A, as shown in Table 6.7. Consequently, the thermal loading of the cables is not expected to constitute a limiting factor to the increase of the farm rated power P_{rated} .

6.4.2 Overhead line

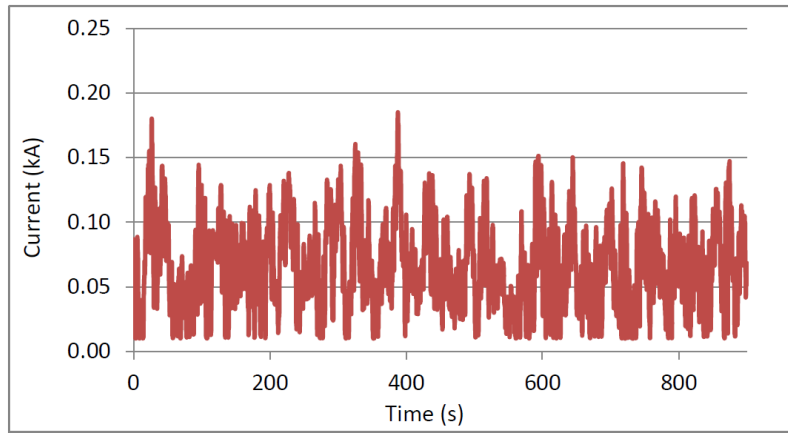
In the case of a overhead line directly exposed to the solar radiation, further calculations are necessary to determine the cables' temperature rise $\Delta\theta$ above ambient temperature. However, as these detailed calculations could not be performed due to time constraints, the order of magnitude of the minimum current rating for the overhead line was estimated based on the average current flowing through it. This last parameter was studied and compared to the rating of the line I_{rating} equal to 672 A. This rating was selected from manufacturers data sheets based on the condition that $I_{rating} \geq 577$ A as it corresponds to the theoretical maximum current which may flow through the overhead line, as detailed below:

$$I_{rating} \geq \frac{P_{max}}{\sqrt{3}V} = \frac{20 \cdot 10^6}{\sqrt{3} \cdot 20 \cdot 10^3} \geq 577 \text{ A} \quad (6.6)$$

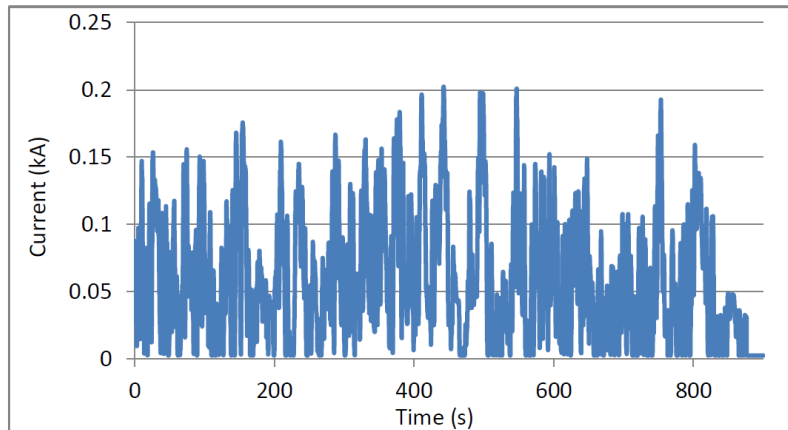
Table 6.8 shows the average current flowing through the overhead line as a function of the farm rated power P_{rated} , as well as the percentage it represents with respect to its initial current rating I_{rating} . This percentage does not exceed 51% for a rated power P_{rated} as high as 50 MW. Hence, the overhead line is not expected to be excessively loaded thermally speaking, so this should not constitute a limiting factor for the increase of the farm rated power P_{rated} .

6.4.3 Summary

This section investigated the minimum ratings required from the submarine cables as well as from the overhead line for avoiding their thermal overloading. The value of the ratio of



(a) Present study



(b) Previous study

Figure 6.17: Current profiles in a submarine cable corresponding to the case where the cables are operated at 10 kV for the present study (top) and for the previous study (bottom)

Rated power P_{rated} (MW)	20	30	40	50
Average current (A)	142	215	271	345
Average/Rating (%)	21	32	40	51

Table 6.8: Minimum current rating for the overhead line as a function of the farm rated power P_{rated}

the current rating I_{rating} to the average current I_{avg} was shown to decrease significantly between the present study and the study presented in Chapter 5. The increase of the operating voltage from 10 kV to 20 kV partly explains this decrease. This decrease is also due to the smoother current profile generated by an array laid out rectangularly with a larger number of devices, as it is the case for a commercial test site, than by a linear array corresponding to a test site as presented in Chapter 5. The minimum rating required for the submarine cables was shown not to exceed 37% of the average current flowing through them.

The average current flowing through a submarine cable was demonstrated to be a relevant criterion for the estimation of its minimum current rating, thus confirming the findings of Chapter 5. Based on this observation, a simplified analysis was conducted

regarding the thermal loading of the overhead line. It was shown that the average current flowing through it does not exceed 51% of its initial current rating. In conclusion, the thermal overloading of both the submarine cables and of the overhead line is not expected to constitute a limiting factor to the increase of the farm rated power P_{rated} .

6.5 Conclusions

This chapter investigated the compliance of a wave farm with respect to typical voltage limits and flicker level requirements. A 50 MW-rated farm was demonstrated not to pose any power quality issue with respect to these two criteria, provided that a suitable power factor is applied at the PCC and that storage (either in the form of a dedicated storage means or in the form of variable speed operation) is used in a complementary manner.

The minimum current ratings required from the submarine cables as well as from the overhead line were also investigated from a thermal loading perspective, based on the method developed in Chapter 5. The average current I_{avg} was confirmed to constitute a relevant criterion for the estimation of the minimum current rating for the submarine cables, as the ratio of the current rating I_{rating} to the average current I_{avg} ranges between 22% and 37%. This represents only 12% to 56% of the initial current rating of the cables, which is equal to 199 A. In similar fashion, the average current flowing through the overhead line was shown not to exceed 51% of its initial rating equal to 672 A. Hence, neither the submarine cables nor the overhead line should be over-loaded if the rated power P_{rated} of the farm increases up to 50 MW.

In conclusion, neither the power quality nor the thermal over-loading of the submarine cables and of the overhead line is expected to constitute an obstacle to the transformation of a test site into a commercial site. This means that a site designed for testing purposes does not necessarily require modifications and/or reinforcements of the farm's electrical network to be transformed into a commercial site of up to 50 MW. However, this does not take into account of course any power flow or stability constraints related to the wider network.

It is also important to note that the results indicated that voltage remains well within the limits and that flicker remains also well below its limit for this rated power. In addition, the current ratings of the submarine cables and of the overhead line is also well below their initial current rating. Hence, this means that a significantly greater rated power P_{rated} could possibly be envisaged for sufficiently strong networks.

The study presented in this chapter has required the generation of a considerable amount of data concerning the flicker level as generated by a wave farm of an increasing rated power P_{rated} , and connected to nodes in the grid having different short-circuit levels S_{sc} and impedance angles Ψ_k . These results were analysed in order to determine a method for estimating the flicker level Pst as a function of the farm rated power P_{rated} and of the impedance angle Ψ_k of the node to which it is connected. This work is presented in the next chapter.

Chapter 7

Estimation of the flicker level P_{st} in relation to the farm rated power P_{rated} and to the impedance angle Ψ_k at the connection point

7.1 Introduction

Given that a wind farm is a fluctuating power source in similar fashion to a wave farm, the flicker summation law defined with respect this former type of power plants was investigated in order to determine whether it is applicable to wave farms. In addition, as no flicker estimation method in relation to the impedance angle Ψ_k of the connection point had yet been defined, a method was developed in this thesis and is presented here.

7.1.1 Estimation of the flicker level P_{st} in relation to the impedance angle Ψ_k

According to the IEC standard 61400-21, the flicker level P_{st} of a wind turbine of apparent power $S_{n,i}$ can be expressed by means of a flicker coefficient $c(\Psi_k, v_a)$ independent of the short-circuit level S_{SC} of the node to which it is connected as:

$$P_{st_i} = c_i(\Psi_k, v_a) \frac{S_{n,i}}{S_{SC}} \quad (7.1)$$

The term v_a corresponds to the average wind speed at hub-height at a given site. However, although using the flicker coefficient $c(\Psi_k)$ facilitates the calculation of the flicker level P_{st} as generated at any short-circuit level S_{SC} , no relationship has been defined as yet regarding the estimation of the flicker level in relation to the impedance angle Ψ_k . However, this last variable has a strong influence on the resulting flicker level P_{st} , as it was shown in the case studies presented in Chapters 4 and 5. Hence, defining an estimation method in relation to the impedance angle Ψ_k is necessary to determine the flicker level P_{st} which could be generated when a wave farm is connected to different connection points. This topic is investigated and the results are presented in this chapter.

7.1.2 Estimation of the flicker level P_{st} in relation to the farm rated power P_{rated}

A flicker summation law, supposedly applicable to any grid-connected installations, is defined in the IEC standard 61000-3-7 as:

$$Pst_N = \sqrt[\alpha]{\sum_{i=1}^N Pst_i^\alpha} \quad (7.2)$$

where Pst_N is the flicker generated by N installations with an individual flicker level Pst_i . The value of the exponent α depends on “the characteristics of the main source of fluctuation”. Depending on the probability that the voltage fluctuations occur simultaneously, the IEC standard 61000-3-7 recommends to use values ranging between $\alpha=1$ (corresponding to a high level of probability) and $\alpha=4$ (corresponding to a low level of probability).

In the case of wind farms, the IEC standard 61400-21 recommends using of a value of α equal to 2. Using the flicker coefficient $c(\Psi_k)$ described in Section 7.1.1, the flicker summation law can be rewritten as:

$$Pst_N = \frac{1}{S_{SC}} \sqrt{\sum_{i=1}^N (c_i(\Psi_k, v_a) S_{n,i})^2} \quad (7.3)$$

Although this method has proven to provide accurate results in the case of a wind farm consisting of two turbines [110], no reference was found regarding the validation of this summation law in the case of a wind farm consisting of a greater number of turbines. This summation law means implicitly that the flicker generated by several wind turbines of similar characteristics increases monotonically with the number N of wind turbines as:

$$Pst_N = Pst_i \sqrt{N} \quad (7.4)$$

This means that the voltage fluctuations generated by each wind turbine add according to the square root of N . Although this is expected to occur in the case of wave farms as well, it is also expected that the power fluctuations generated by each wave device tend to compensate themselves and lead to a smoother power profile [59]. For instance, N generators may output a power peak simultaneously, which may result in a power peak of significant amplitude. Obviously, the higher this number N is, the higher the probability becomes that a fraction of the generators composing a wave farm output a power peak simultaneously. However, the amplitude of the voltage fluctuations may also decrease as a function of the wave farm rated power, as the power fluctuations generated by each wave device tend to compensate with these generated by the other devices. This latter aspect is not taken into account in the flicker summation law as described in the IEC standards 61000-3-7 and 61400-21.

The inapplicability of the flicker summation law defined in these standards is well illustrated by Figure 7.1 which shows the flicker level Pst at a connection point of short-circuit level $S_{SC}=72.2$ MVA and for a range of impedance angles Ψ_k . It appears clearly from this figure that there is no direct relation of proportionality between the flicker level generated by a 5 MW farm and farms of greater rated power multiples of 5. Hence, investigations were conducted to determine an estimation method in relation to the farm rated power P_{rated} .

7.2 Input data

The input data to the study presented in this chapter was generated as part of the case study presented in the previous chapter. In addition to the three production periods A, B

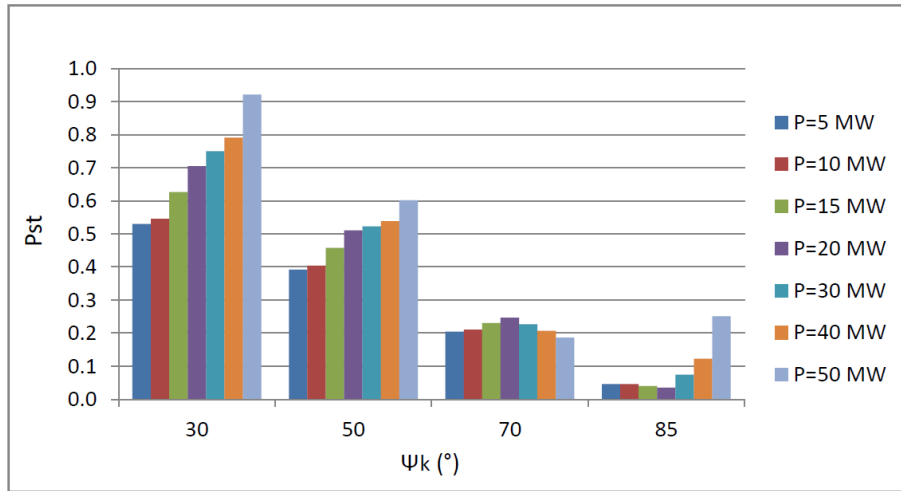


Figure 7.1: Flicker level P_{st} for a weak grid ($S_{SC}=72$ MVA) as a function of the impedance angle Ψ_k and for several values of the farm rated power P_{rated} (production period A)

Production period	Significant wave height H_s (m)	Mean zero-crossing period T_z (s)	Generator speed control mode
A	5.0	8.4	fixed
B	2.1	5.6	fixed
D	4.5	6.8	variable
E	4.5	7.8	variable

Table 7.1: Characteristics of the different production periods used for the power system simulations

and D already described in the previous chapter, an additional production period, referred to as production period E, is included in the study detailed in this chapter. The sea-state characteristics as well as the generator speed control mode corresponding to these production periods are shown in Table 7.1. In production periods A and B, the generator is operated in fixed speed mode, which constitutes a worst case scenario from a power quality perspective, while in the production periods D and E, the generator is operated in variable speed mode. In this latter case, storage is available in the form of inertial storage, which leads to a smoother power profile, and thus to a lower flicker level.

7.3 Functional blocks composing a flickermeter

The principle of a flickermeter as defined by the IEC was detailed in Chapter 4. This tool consists of five blocks whose actions on their input signal are recalled below:

- Block 2: squaring multiplier
- Block 3: three combined filters. The first two filters remove the terms whose frequency is less than 0.05 Hz as well as the terms whose frequency is greater than 35 Hz. The third filter applies a gain to the different mono-frequency oscillating terms composing its input signal and which depends on their frequency, as shown in Figure 7.2.
- Block 4: squaring multiplier and first order low-pass filter of gain K'

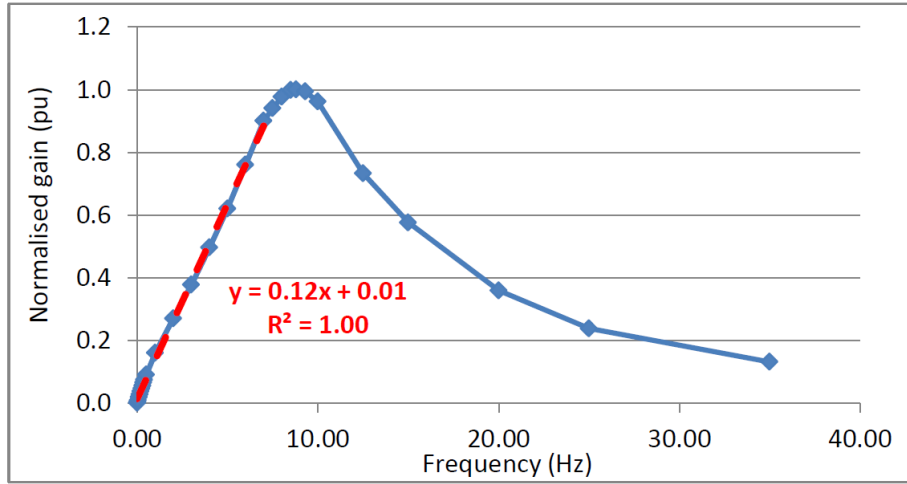


Figure 7.2: Gain applied by the third filter in Block 3 as a function of the frequency of the input fluctuation

- Block 5: a classifier used to generate a cumulative probability function (CPF) of the instantaneous flicker level. The flicker level Pst is then calculated based on a weighted average of defined percentiles of this cumulative probability function.

7.4 Theoretical analysis

7.4.1 Introduction

As will be detailed later in Sections 7.4.4 and 7.4.5, the estimation method is based on the variations of the average voltage V_{avg} and of the maximum voltage difference $\Delta V = V_{max} - V_{min}$ of the voltage profile at the point of common coupling as a function of the impedance angle Ψ_k and of the rated power P_{rated} . The estimation method in relation to the impedance angle Ψ_k is described in the following section.

7.4.2 Estimation of flicker level Pst with respect to different impedance angles Ψ_k

For a given farm power profile, the influence of the impedance angle Ψ_k corresponds to either a decrease or an increase of the amplitude of the voltage fluctuations as well as to a variation of the average voltage V_{avg} . This is illustrated in Figure 7.3 which shows the voltage profile at the point of common coupling for three values of the impedance angle Ψ_k , namely 30° , 50° and 70° . However, the “shape” of the voltage profile remains the same.

It was assumed that the average voltage V_{avg} and the maximum voltage fluctuation ΔV corresponding to any impedance angle Ψ_k may be estimated based on their respective values at a reference impedance angle Ψ_{kref} as:

$$\begin{aligned}
 V_{avg}(P_{rated}, \Psi_k) &= k(P_{rated}, \Psi_k) V_{avg}(P_{rated}, \Psi_{kref}) \\
 \text{and } \Delta V(P_{rated}, \Psi_k) &= k'(P_{rated}, \Psi_k) \Delta V(P_{rated}, \Psi_{kref})
 \end{aligned} \tag{7.5}$$

where k and k' are scale factors which depends on both the rated power P_{rated} and on the impedance angle Ψ_k . For the sake of legibility, this dependence will not be mentioned in the rest of this section and thus the previous equations can be rewritten as:

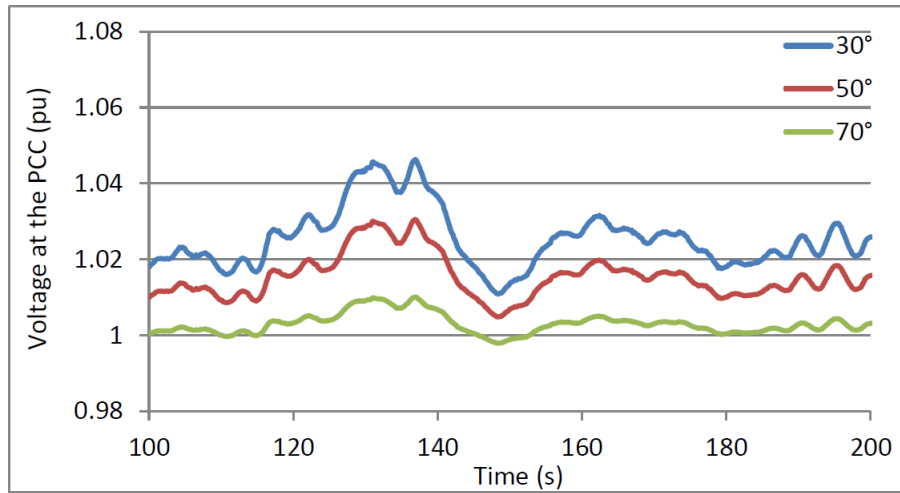


Figure 7.3: Voltage profile at the PCC for a 50 MW farm for different impedance angles Ψ_k

$$\begin{aligned}
 V_{avg}(\Psi_k) &= kV_{avg}(\Psi_{kref}) \\
 \text{and } \Delta V(\Psi_k) &= k'\Delta V(\Psi_{kref})
 \end{aligned} \tag{7.6}$$

The estimation method in relation to the impedance angle Ψ_k proposed in this work presents a limitation. It assumes that the voltage profile corresponding to any impedance angle Ψ_k can be obtained from the product of the characteristics of a reference voltage profile (i.e. average voltage V_{avg} and maximum voltage fluctuation ΔV) times defined scale factors. This implies that the “shape” of the voltage profile is independent of the impedance angle Ψ_k . However, this is only an approximation. On one hand, the voltage fluctuation is proportional to the farm active power P_G when the $P_G R_S \gg Q_G X_S$, which is valid only when the active power P_G is sufficiently low. On the other hand, when the active power P_G is sufficiently high, the reactive power Q_G (which is proportional to the square of P_G) can no longer be neglected. The effect on the voltage of the active power P_G and of the reactive power Q_G being opposed, this means that, for a given voltage profile, the amplitude of the highest voltage peaks are more reduced as a function of the impedance angle Ψ_k than peaks of smaller amplitude. Hence, the voltage profile is more and more smoothened as this variable increases. This is illustrated in Figure 7.4 which shows two voltage profiles corresponding to two different impedance angles equal to 30° and 70° respectively. The ratio of the voltage at 70° to the voltage at 30° at two different instants t is shown in this figure. As expected, these voltage ratios at two different instants, which correspond to two different values of the active power P_G generated by the farm, are not equal. This ratio is lower (equal to 0.21) when the voltage is higher, which corresponds to a higher power level. This confirms that the voltage fluctuations corresponding to a higher power level are more reduced as the impedance angle Ψ_k increases than the voltage fluctuations corresponding to a lower power level. The voltage profile is thus smoother with respect to the case where the impedance angle is equal to 70° than in the case where the impedance angle is equal to 30° .

7.4.3 Estimation of the flicker level P_{st} in relation to the farm rated power P_{rated}

The same method can be used to estimate the flicker level P_{st} in relation to the farm rated power P_{rated} . Hence, (7.5) can be expressed in this case as:

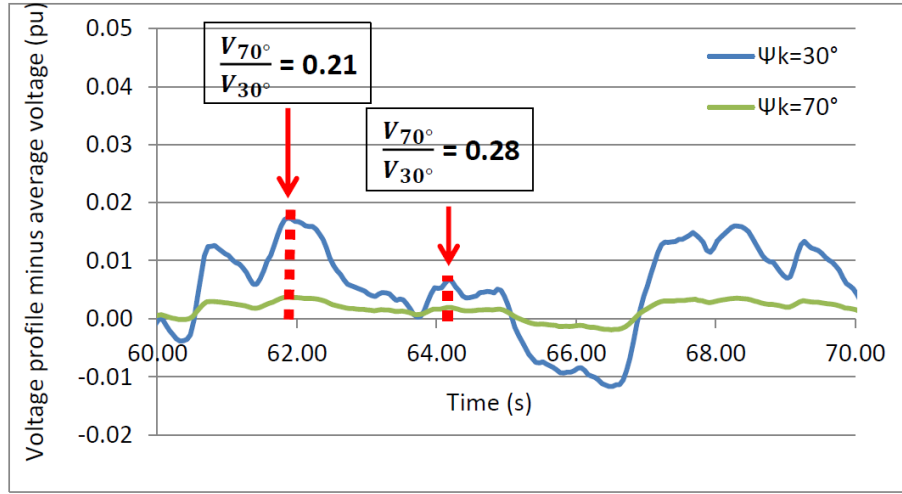


Figure 7.4: Voltage profile for impedance angles equal to 30° and 70°

$$\begin{aligned}
 V_{avg}(P_{rated}, \Psi_k) &= k(P_{rated}, \Psi_k)V_{avg}(P_{ref}, \Psi_k) \\
 \text{and } \Delta V(P_{rated}, \Psi_k) &= k'(P_{rated}, \Psi_k)\Delta V(P_{ref}, \Psi_k)
 \end{aligned} \tag{7.7}$$

However, for the sake of legibility, it will be rewritten as:

$$\begin{aligned}
 V_{avg}(P_{rated}) &= kV_{avg}(P_{ref}) \\
 \text{and } \Delta V(P_{rated}) &= k'\Delta V(P_{ref})
 \end{aligned} \tag{7.8}$$

The influence of an increasing rated power P_{rated} , as represented by scale factors applied to the average voltage V_{avg} and to the maximum voltage fluctuation ΔV , corresponds to a worst case scenario from a flicker generation perspective. This implies that the voltage fluctuations generated by a single wave device (or a single group of wave device) are all in phase with the voltage fluctuations generated by additional wave devices (or group of wave devices) included within the farm. In that case, the power smoothing effect of the aggregation of several wave devices (or group of wave devices) is not represented.

However, in reality, the wave conditions to which wave devices included in a sufficiently large wave farm are subject at an instant t may vary greatly from one device to another. Hence, all the wave devices of a farm do not output power peaks simultaneously. However, it is likely that coincident fluctuations may occur. In the case of wind farms, this level of probability is taken into account in the flicker summation law by multiplying the individual flicker Pst_i times the square root of the number N of wind turbines rather than the number N itself, as shown in (7.4). Based on these observations, it could be expected that using the square root of the scale factor k' corresponding to the maximum voltage fluctuation ΔV would provide a more accurate estimation of the flicker level Pst .

7.4.4 Flicker generated by a sinusoidal voltage profile

An ideal voltage profile $v(t)$ as generated by the injection of a sinusoidal power profile can be expressed as:

$$v(t) = \left(V_{avg} + \frac{\Delta V}{2} \sin(\omega t) \right) \sin(\omega_e t) \tag{7.9}$$

where V_{avg} is the average voltage, ΔV is the maximum voltage fluctuation, thus equal to twice the amplitude of the modulating fluctuation in this case, ω is the radian frequency of the modulating fluctuation, and ω_e is the frequency of the power system. This voltage profile can also be expressed using the scale factors k and k' as:

$$v(t) = \left(kV_{avg}(P_{ref}, \Psi_{k_{ref}}) + k' \frac{\Delta V(P_{ref}, \Psi_{k_{ref}})}{2} \sin(\omega t) \right) \sin(\omega_e t) \quad (7.10)$$

For the sake of legibility, $V_{avg}(P_{ref}, \Psi_{k_{ref}})$ and $\Delta V(P_{ref}, \Psi_{k_{ref}})$ will be referred to as V_{avg} and ΔV in the rest of the demonstration. Hence, the previous equation can be rewritten as:

$$v(t) = \left(kV_{avg} + k' \frac{\Delta V}{2} \sin(\omega t) \right) \sin(\omega_e t) \quad (7.11)$$

Based on this equation, the output $O_2(t)$ of Block 2 of the flickermeter, which consists of a squaring multiplier, can be expressed as:

$$\begin{aligned} O_2(t) &= v^2(t) = \left[kV_{avg} + k' \frac{\Delta V}{2} \sin(\omega t) \right]^2 \sin^2(\omega_e t) \\ &= \left[k^2 V_{avg}^2 + kV_{avg}k' \Delta V \sin(\omega t) + k'^2 \frac{\Delta V^2}{4} \sin^2(\omega t) \right] \sin^2(\omega_e t) \\ &= \left[k^2 V_{avg}^2 + kV_{avg}k' \Delta V \sin(\omega t) \right. \\ &\quad \left. + k'^2 \frac{\Delta V^2}{4} \left(\frac{1 - \cos(2\omega t)}{2} \right) \right] \left[\frac{1 - \cos(2\omega_e t)}{2} \right] \end{aligned} \quad (7.12)$$

The output $O_{3_1}(t)$ of the first two filters of Block 3 which remove the oscillating terms whose frequency is either less than 0.05 Hz or greater than 35 Hz can be expressed as:

$$O_{3_1}(t) = \frac{1}{2} \left(kV_{avg}k' \Delta V \sin(\omega t) - k'^2 \frac{\Delta V^2}{8} \cos(2\omega t) \right) \quad (7.13)$$

The third filter of Block 3, whose Bode diagram is shown in Figure 7.2, applies a gain to each sinusoidal fluctuation depending on its frequency. For the frequency range of interest in the field of wave energy, namely 0.1 Hz to 0.7 Hz as described in Chapter 4, the gain is linear with a gain equal to 0.12 pu/Hz, as illustrated in Figure 7.2. Hence, the gain applied to the term of frequency 2ω is equal to twice the gain K applied to the term of frequency ω . The output $O_{3_2}(t)$ of Block 3 can thus be expressed as:

$$O_{3_2}(t) = \frac{K}{2} \left(kV_{avg}k' \Delta V \sin(\omega t) - k'^2 \frac{\Delta V^2}{4} \cos(2\omega t) \right) \quad (7.14)$$

After Block 4, which consists of a squaring multiplier and of a gain K' , the output $O_4(t)$ entering Block 5 can be written as:

$$\begin{aligned}
O_4(t) &= K' \left[\frac{K}{2} \left(kV_{avg}k'\Delta V \sin(\omega t) - k'^2 \frac{\Delta V^2}{4} \cos(2\omega t) \right) \right]^2 \\
&= \frac{K'K^2}{4} \left(k^2V_{avg}^2k'^2 \Delta V^2 \sin^2(\omega t) - kV_{avg} \sin(\omega t)k'^3 \frac{\Delta V^3}{2} \cos(2\omega t) \right. \\
&\quad \left. + \frac{1}{16}k'^4 \Delta V^4 \cos^2(2\omega t) \right) \\
&= \frac{K'K^2}{4} \left(k^2V_{avg}^2k'^2 \Delta V^2 \sin^2(\omega t) - kV_{avg} \sin(\omega t)k'^3 \frac{\Delta V^3}{2} \cos(2\omega t) \right. \\
&\quad \left. + \frac{1}{32}k'^4 \Delta V^4 (1 + \cos(4\omega t)) \right) \tag{7.15}
\end{aligned}$$

Given that the maximum voltage fluctuation ΔV usually remains at a low level (it was observed not to exceed 0.12 pu in any of the simulations performed in this thesis), the following condition is valid:

$$\Delta V^2 \gg \Delta V^3 \gg \Delta V^4 \tag{7.16}$$

In addition, the average voltage V_{avg} is expected to remain closely around 1 pu, which is effectively observed in the simulations as it ranges between 0.985 pu and 1.096 pu. Based on these observations, the scale factor k is also expected to remain relatively constant and of the order of magnitude of unity. This last observation applies also to k' . Hence, the second and third terms of (7.15) can be considered as negligible and the equation can be rewritten as:

$$O_4(t) = \frac{K'K^2}{4} k^2 V_{avg}^2 k'^2 \Delta V^2 \sin^2(\omega t) \tag{7.17}$$

The classifier in Block 5 creates its classes range based on the maximum instantaneous flicker level $F_{max} = \max(O_4(t))$, which is equal to:

$$F_{max} = \max(O_4(t)) = \frac{K'K^2}{4} k^2 V_{avg}^2 k'^2 \Delta V^2 \tag{7.18}$$

Hence, the maximum flicker level F_{max} is proportional to the square of the term $kk'V_{avg}\Delta V$. The flicker level of each of the $N_{classes}$ classes into which the input signal to Block 5 is divided, as shown in Figure 7.5, can be expressed as:

$$F_i = \frac{F_{max} \times i}{N_{classes}} \tag{7.19}$$

The different levels F_i are thus proportional to the maximum flicker level, itself dependent on the square of the term $kk'V_{avg}\Delta V$. In the cumulative probability function (CPF) generated from the classifier's results, these flicker levels F_i are in abscissa and the percentage of occurrence corresponding to a given flicker level F_i is in ordinate.

Given that varying the amplitude of the voltage profile does not modify its shape, which remains sinusoidal, the cumulative probability function (CPF) generated from the classifier's results is expected to keep the same shape as well, regardless of the amplitude of the input signal. This is confirmed in Figure 7.6 which presents the normalised cumulative

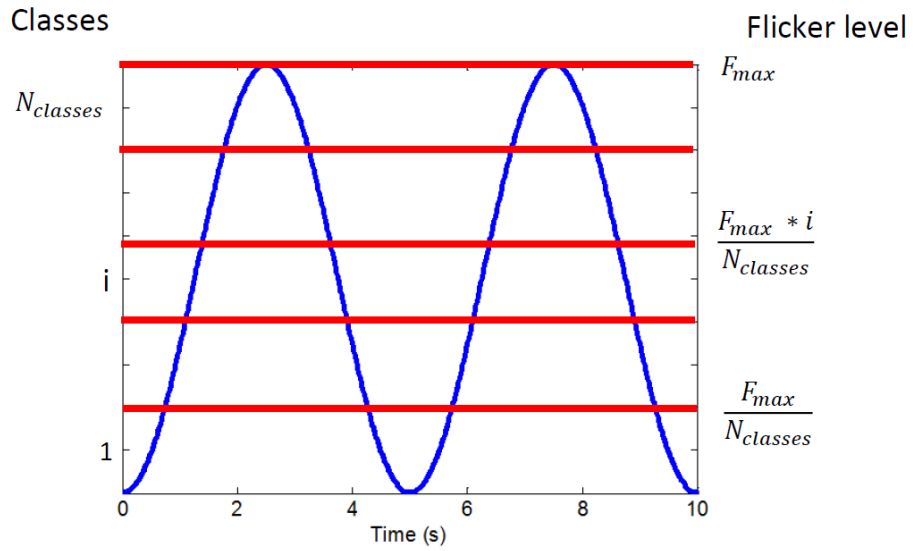


Figure 7.5: Illustration of the classifier

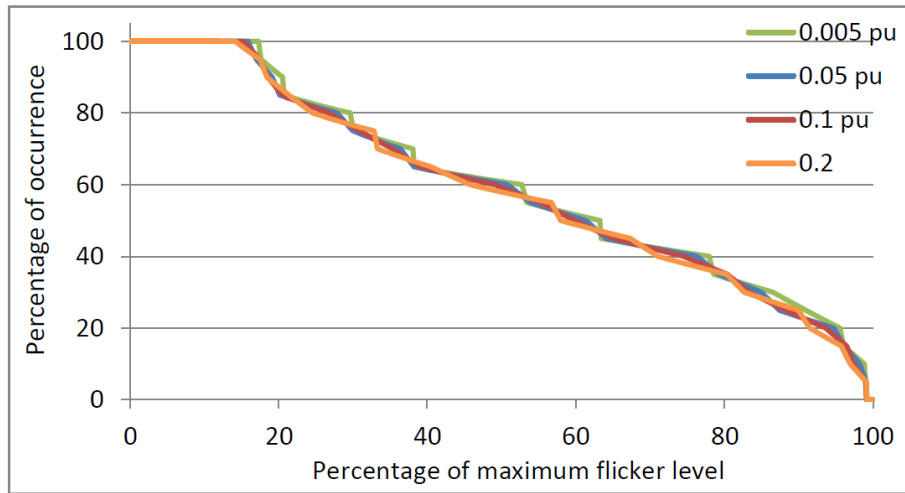


Figure 7.6: Normalised CPF for four different values of the maximum voltage fluctuation ΔV

probability functions corresponding to sinusoidal voltage profiles having different values in terms of the maximum voltage fluctuation ΔV .

Consequently, the abscissa of the CPF's points, called percentiles and referred to as P_i , is proportional to the square of the term $kk'V_{avg}\Delta V$. As defined in the IEC standard 6100-4-15, these percentiles are used in the calculation of the flicker level Pst as:

$$Pst = \sqrt{0.0314P_{0.1} + 0.0525P_{1s} + 0.0657P_{3s} + 0.28P_{10s} + 0.08P_{50s}} \quad (7.20)$$

where

$$\begin{aligned}
P_{50s} &= \frac{P_{30} + P_{50} + P_{80}}{3} \\
P_{10s} &= \frac{P_6 + P_8 + P_{10} + P_{13} + P_{17}}{5} \\
P_{3s} &= \frac{P_{2.2} + P_3 + P_4}{3} \\
P_{1s} &= \frac{P_{0.7} + P_1 + P_{1.5}}{3}
\end{aligned}$$

It was demonstrated earlier that the percentiles P_i are proportional to the square of the term $kk'V_{avg}\Delta V$ so that they can be expressed as:

$$P_i = (kk'V_{avg}\Delta V)^2 p_i = A^2 p_i \quad (7.21)$$

Hence, (7.20) can be rewritten as:

$$\begin{aligned}
Pst &= \sqrt{A^2(0.0314p_{0.1} + 0.0525p_{1s} + 0.0657p_{3s} + 0.28p_{10s} + 0.08p_{50s})} \\
&= A\sqrt{0.0314p_{0.1} + 0.0525p_{1s} + 0.0657p_{3s} + 0.28p_{10s} + 0.08p_{50s}}
\end{aligned} \quad (7.22)$$

so,

$$Pst \propto kk'V_{avg}\Delta V \quad (7.23)$$

In conclusion, the flicker level Pst of voltage profile whose amplitude is modulated by a sinusoidal fluctuation is proportional to the term $kk'V_{avg}\Delta V$. However, considering that the maximum voltage amplitude is expected to present greater variations with respect to the farm rated power and to the impedance angle Ψ_k than the average voltage, the flicker level Pst is expected to be approximately proportional to the term $k'\Delta V$ only. In other words, the ratio $Pst/\Delta V$ depends on the radian frequency ω of the voltage fluctuation only.

7.4.5 Generalisation to a real voltage profile

This statement can be generalised to any voltage profile as generated by a wave farm under real sea conditions, i.e. having a polychromatic spectrum. The fluctuations modulating the voltage profile in this case may be decomposed into a sum of sinusoidal terms of pulsation ω_j and of amplitude ΔV_j dephased by an angle Φ_j as:

$$v(t) = \left(kV_{avg} + k' \sum_{j=1}^n \frac{\Delta V_j}{2} \sin(\omega_j t + \Phi_j) \right) \sin(\omega_e t) \quad (7.24)$$

The output $O_2(t)$ of Block 2, consisting of a squaring multiplier, can be expressed as:

$$\begin{aligned}
O_2(t) = v^2(t) &= \left[kV_{avg} + k' \sum_{j=1}^n \frac{\Delta V_j}{2} \sin(\omega_j t + \Phi_j) \right]^2 \sin^2(\omega_e t) \\
&= \frac{1}{2} \left[k^2 V_{avg}^2 + kV_{avg}k' \sum_{j=1}^n \Delta V_j \sin(\omega_j t + \Phi_j) + \frac{k'^2}{4} \left(\sum_{j=1}^n \Delta V_j^2 \sin^2(\omega_j t + \Phi_j) \right. \right. \\
&\quad \left. \left. + \sum_{j \neq i}^n \Delta V_j \Delta V_i \sin(\omega_j t + \Phi_j) \sin(\omega_i t + \Phi_i) \right) \right] (1 - \cos(2\omega_e t)) \\
&= \frac{1}{2} \left[k^2 V_{avg}^2 + kV_{avg}k' \sum_{j=1}^n \Delta V_j \sin(\omega_j t + \Phi_j) + \frac{k'^2}{8} \left(\sum_{j=1}^n \Delta V_j^2 (1 - \cos(2\omega_j t + 2\Phi_j)) \right. \right. \\
&\quad \left. \left. + \sum_{j \neq i}^n \Delta V_j \Delta V_i (\cos((\omega_j - \omega_i)t + \Phi_j - \Phi_i) - \cos((\omega_j + \omega_i)t + \Phi_j + \Phi_i)) \right) \right] (1 - \cos(2\omega_e t))
\end{aligned} \tag{7.25}$$

The output $O_{3_1}(t)$ within Block 3 after the removal of the oscillating terms whose frequency is either less than 0.05 Hz or greater than 35 Hz can be written as:

$$\begin{aligned}
O_{3_1}(t) &= \frac{1}{2} \left[kV_{avg}k' \sum_{j=1}^n \Delta V_j \sin(\omega_j t + \Phi_j) + \frac{k'^2}{8} \left(- \sum_{j=1}^n \Delta V_j^2 \cos(2\omega_j t + 2\Phi_j) \right. \right. \\
&\quad \left. \left. + \sum_{j \neq i}^n \Delta V_j \Delta V_i (\cos((\omega_j - \omega_i)t + \Phi_j - \Phi_i) - \cos((\omega_j + \omega_i)t + \Phi_j + \Phi_i)) \right) \right]
\end{aligned} \tag{7.26}$$

Considering that the different frequencies $f_j = 2\pi\omega_j$ are expected not to exceed 0.7 Hz, as mentioned earlier, the gain K_j applied to each sinusoidal fluctuation by the third filter of Block 3 can be considered as proportional to its frequency. Hence, the output $O_{3_2}(t)$ of Block 3 can be expressed as:

$$\begin{aligned}
O_{3_2}(t) &= \frac{1}{2} \left[kV_{avg}k' \sum_{j=1}^n K_j \Delta V_j \sin(\omega_j t + \Phi_j) + \frac{k'^2}{8} \left(-2 \sum_{j=1}^n K_j \Delta V_j^2 \cos(2\omega_j t + 2\Phi_j) + \right. \right. \\
&\quad \left. \left. \sum_{j \neq i}^n \Delta V_j \Delta V_i (K_{ji} \cos((\omega_j - \omega_i)t + \Phi_j - \Phi_i) - K'_{ji} \cos((\omega_j + \omega_i)t + \Phi_j + \Phi_i)) \right) \right]
\end{aligned} \tag{7.27}$$

Assuming that the maximum voltage fluctuation ΔV_j is sufficiently small, then:

$$\Delta V_j \gg \Delta V_j^2 \quad \text{and} \quad \Delta V_j \gg \Delta V_j \Delta V_i \tag{7.28}$$

Figure 7.7 which shows the square of the maximum voltage fluctuation ΔV as a function of ΔV . Considering that the maximum voltage fluctuation ΔV observed in the simulations is equal to 0.12 pu, it can be assumed that the terms ΔV_j composing the

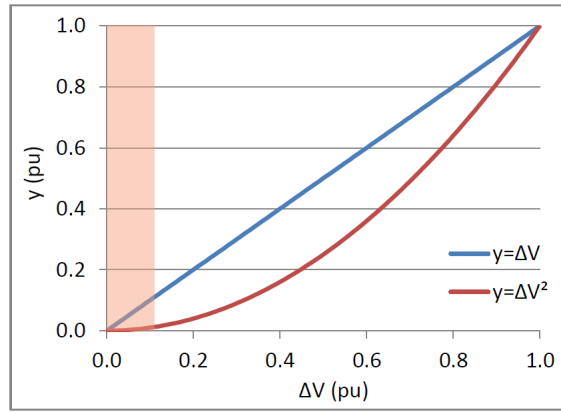


Figure 7.7: Maximum voltage fluctuation ΔV and its square

voltage profile are at most of the same order of magnitude, which is highlighted by the orange-shadowed area. It appears clearly from this figure that, in this case, (7.28) is valid. It is important to bear in mind as well that the simulations performed in the previous chapter, and on which the study presented in this chapter is based, have included very weak networks, that is with a low short-circuit level S_{SC} compared to the maximum power fluctuation generated by the farm and a low impedance angle Ψ_k for which the impact is maximal. In addition, the connection of a medium-size wave farm at nodes having a lower short-circuit level is not expected due to the usually low power transfer capacity at this type of connection points. Hence, it is expected that the maximum value in terms of maximum voltage fluctuation ΔV which has been found in this work and which is equal to 0.12 pu is representative of worst case conditions. Hence, (7.28) can be assumed to be valid for any type of network to which a wave farm can be connected.

Consequently, the second and third terms of (7.27) can be considered as negligible compared to the first one. Hence, this equation can be rewritten as:

$$O_{3_2}(t) \approx \frac{1}{2} \left(kV_{avg}k' \sum_{j=1}^n K_j \Delta V_j \sin(\omega_j t + \Phi_j) \right) \quad (7.29)$$

Based on the previous equation, the output $O_4(t)$ of Block 4 can be expressed as:

$$O_4(t) = \frac{K'k^2V_{avg}^2k'^2}{4} \left(\sum_{j=1}^n K_j \Delta V_j \sin(\omega_j t + \Phi_j) \right)^2 \quad (7.30)$$

where K' is the gain applied by Block 4 after the squaring multiplier. The maximum instantaneous flicker F_{max} , which is used in the classifier of Block 5, is equal to the maximum of output $O_4(t)$, which can be written as:

$$F_{max} = \max(O_4(t)) = \max \left[\frac{K'k^2V_{avg}^2k'^2}{4} \left(\sum_{j=1}^n K_j \Delta V_j \sin(\omega_j t + \Phi_j) \right)^2 \right] \quad (7.31)$$

In similar fashion to the ideal case of a sinusoidal voltage profile, as the flicker level Pst is proportional to the term $\sqrt{F_{max}}$, a relation of proportionality can be established between the flicker level and the maximum voltage fluctuation ΔV_j as:

$$Pst \propto kV_{avg}k' \max \left(\sum_{j=1}^n K_j \Delta V_j \sin(\omega_j t + \Phi_j) \right) \quad (7.32)$$

Considering that the maximum voltage fluctuation is expected to vary in much greater proportions than the average voltage as a function of the farm rated power and of the impedance angle Ψ_k , the scale factor k is expected to remain approximately constant compared to the scale factor k' . Hence, the flicker level Pst is expected to be approximately proportional to the scale factor k' as:

$$Pst \propto k' \max \left(\sum_{j=1}^n K_j \Delta V_j \sin(\omega_j t + \Phi_j) \right) \quad (7.33)$$

As regards the maximum voltage fluctuation ΔV , it can be expressed as:

$$\begin{aligned} \Delta V(P_{rated}, \Psi_k) &= V_{max} - V_{min} \\ &= kV_{avg} + k' \max \left(\sum_{j=1}^n \frac{\Delta V_j}{2} \sin(\omega_j t + \Phi_j) \right) - kV_{avg} - k' \min \left(\sum_{j=1}^n \frac{\Delta V_j}{2} \sin(\omega_j t + \Phi_j) \right) \\ &= k' \max \left(\sum_{j=1}^n \frac{\Delta V_j}{2} \sin(\omega_j t + \Phi_j) \right) - k' \min \left(\sum_{j=1}^n \frac{\Delta V_j}{2} \sin(\omega_j t + \Phi_j) \right) \\ &\approx k' \max \left(\sum_{j=1}^n \frac{\Delta V_j}{2} \sin(\omega_j t + \Phi_j) \right) \end{aligned} \quad (7.34)$$

Hence, the maximum voltage fluctuation ΔV is approximately proportional to the term $k' \max(\sum_{j=1}^n \frac{\Delta V_j}{2} \sin(\omega_j t + \Phi_j))$. Consequently, the ratio of the flicker level Pst to the maximum voltage fluctuation $\Delta V(P_{rated}, \Psi_k)$ can be expressed from (7.33) and (7.34) as:

$$\begin{aligned} \frac{Pst}{\Delta V} &\propto \frac{k' \max \left(\sum_{j=1}^n K_j \Delta V_j \sin(\omega_j t + \Phi_j) \right)}{k' \max \left(\sum_{j=1}^n \frac{\Delta V_j}{2} \sin(\omega_j t + \Phi_j) \right)} \\ &\propto \frac{\max \left(\sum_{j=1}^n K_j \Delta V_j \sin(\omega_j t + \Phi_j) \right)}{\max \left(\sum_{j=1}^n \frac{\Delta V_j}{2} \sin(\omega_j t + \Phi_j) \right)} \end{aligned} \quad (7.35)$$

The term $\max(\sum_{j=1}^n K_j \Delta V_j \sin(\omega_j t + \Phi_j))$ is constant as it corresponds to the reference voltage profile, as well as the term $(\sum_{j=1}^n \frac{\Delta V_j}{2} \sin(\omega_j t + \Phi_j))$. Hence, the ratio of the flicker level Pst to the maximum voltage fluctuation $\Delta V(P_{rated}, \Psi_k)$ is constant.

This means that, for a given farm rated power P_{rated} , the flicker level Pst_1 at any impedance angle Ψ_{k_1} can be calculated based a simple rule of three. The parameters which are necessary for this calculation are a known value of the flicker level Pst_2 at a given impedance Ψ_2 , and the maximum voltage fluctuations ΔV_1 and ΔV_2 corresponding the impedance angles Ψ_{k_1} and Ψ_{k_2} respectively. The rule of three can be expressed as:

$$\begin{aligned} \frac{Pst_1}{\Delta V_1} &= \frac{Pst_2}{\Delta V_2} \\ \text{so } Pst_1 &= \Delta V \frac{Pst_2}{\Delta V_2} \end{aligned} \quad (7.36)$$

In similar fashion, for a given impedance angle Ψ_k , the flicker level Pst_1 generated by a wave farm of given rated power P_{rated_1} can be estimated from the flicker level Pst_2 corresponding to a reference rated power P_{rated_2} , and from the maximum voltage fluctuations ΔV_1 and ΔV_2 corresponding the rated powers P_{rated_1} and P_{rated_2} respectively. In this case, the maximum and minimum active powers $P_{G_{max}}$ and $P_{G_{min}}$ generated by the wave farm of rated power P_{rated_2} are necessary for estimating the flicker level Pst_1 . The implications of these findings will be described in more detail in Section 7.6.

It is interesting to note that the term $max(\sum_{j=1}^n K_j \Delta V_j \sin(\omega_j t + \Phi_j))$, to which the flicker level Pst is proportional as described in (7.33), is characteristic of the frequency spectrum of the voltage profile. However, this spectrum is similar to this of the wave farm power output. Hence, for a wave farm consisting of similar devices which have thus a similar mechanical response to a given sea-state, the frequency content of the spectrum of the wave farm power output is the same as this of the power output of a single wave device. Hence, the frequency content of the voltage profile is the same as that of the power output of a single wave energy device. This is confirmed by the results shown in Figures 7.8a to 7.8c which show the spectra of the voltage profile at the PCC, of the power output of a wave farm and of the power output of an individual wave device. The amplitude of each frequency in these three spectra cannot be compared of course, as the aggregation effect from the farm is not represented in the spectrum of the individual wave device and as there is no relation of proportionality between the active power of the wave farm and the voltage at the PCC. However, it can be observed that the frequency range is indeed the same for the power output profiles and for the voltage profile at the PCC.

7.4.6 Determination of an equivalent sinusoidal voltage profile

It is interesting to observe as well that the linear relationship between the flicker level Pst and the maximum voltage fluctuation ΔV implies that there exists a single sinusoidal fluctuation of period T and of amplitude $\frac{\Delta V}{2}$ whose linear function's leading coefficient coincides with this corresponding to the real voltage profile. The corresponding sinusoidal voltage profile $V(t)$ can be expressed as:

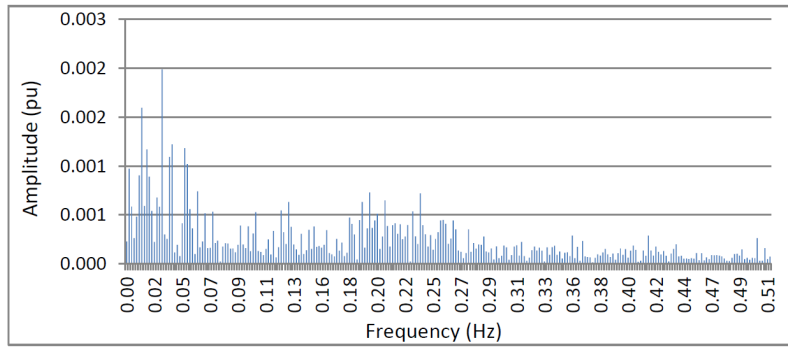
$$V(t) = 1 + \frac{\Delta V}{2} \sin\left(\frac{2\pi t}{T}\right) \quad (7.37)$$

The relation between the flicker level corresponding to a real voltage profile and this corresponding to a sinusoidal voltage profile can be expressed as:

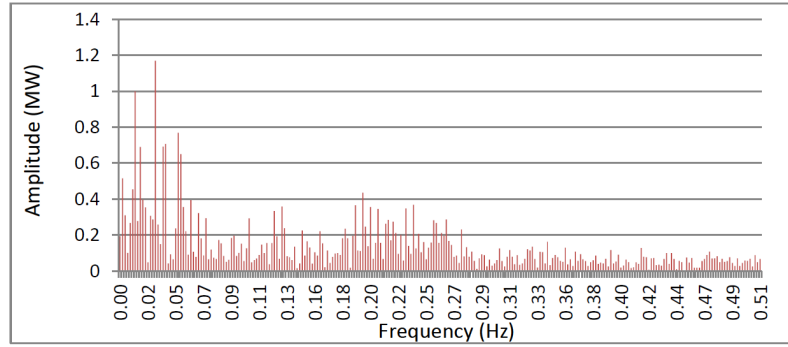
$$\begin{cases} Pst_{real} = a\Delta V & \text{in the case of real voltage profile} \\ Pst_{sinus} = a'\Delta V' & \text{in the case of a sinusoidal voltage fluctuation} \end{cases} \quad (7.38)$$

Hence, if $Pst_{real} = Pst_{sinus}$ and $\Delta V = \Delta V'$, then $a = a'$ and:

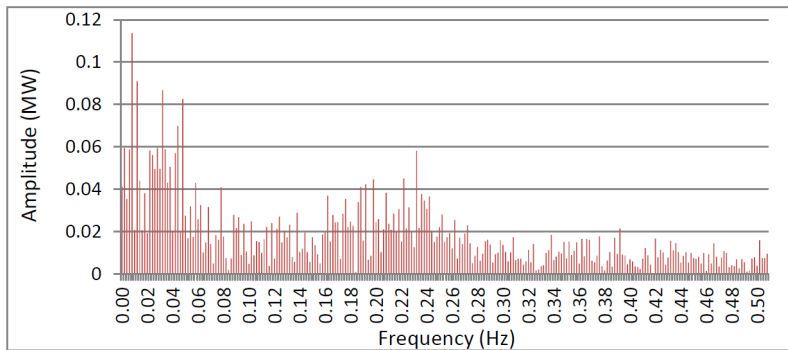
$$Pst_{sinus} = a\Delta V = Pst_{real} \quad \forall \quad \Delta V \quad (7.39)$$



(a) Voltage at the PCC



(b) Power output of the wave farm



(c) Power output of an individual wave device

Figure 7.8: Frequency spectra (the fundamental component has been removed for the sake of legibility)

7.4.7 Determination of the scale factors k and k'

There are several ways to calculate these scale factors, depending on the demanded level of accuracy. Given that a VAR compensator is connected at the point of common coupling (PCC) and assuming that the voltage profiles for each case are not available, the values of the maximum, minimum and average voltage V_{max} , V_{min} and V_{avg} can only be calculated by iteration from the maximum, minimum and average farm power $P_{G_{max}}$, $P_{G_{min}}$ and $P_{G_{avg}}$ by means of the Newton-Raphson algorithm described in Chapter 4. This would require to using a power system simulator, which may be particularly expensive for wave device developers or to develop a load flow programme. Both of these methods require a certain level of expertise in the field of electrical engineering which developers may not all have. However, the results in terms of voltage level which are obtained with and without the VAR compensator show an approximately similar trends, as illustrated in Figure 7.9 which presents the maximum voltage V_{max} as a function of the maximum power $P_{G_{max}}$.

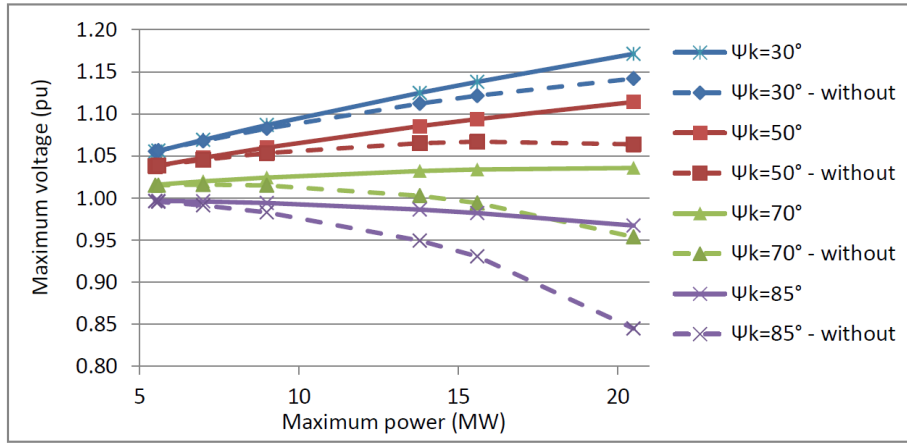


Figure 7.9: Maximum voltage as a function of the maximum power P_G with and without VAR compensator

This means that it may be possible to use analytical formulae in order to obtain rough results at a first stage. Hence, the trend of the voltage at the point of common coupling V_{PCC} as a function of P_G can be estimated approximately as:

$$V = 1 + \frac{(P_{PCC} - P_L)R_S + (Q_{PCC} - Q_L)X_S}{V^2} \quad (7.40)$$

where P_{PCC} and Q_{PCC} are the active and reactive power arriving at the point of common coupling respectively, and P_L and Q_L are the active and reactive power consumption of the load connected at the 38 kV bus representing the consumption of a small town and of its surroundings. Assuming negligible power losses, this equation can be rewritten as:

$$V = 1 + \frac{(P_G - P_L)R_S + (Q_G - Q_L)X_S}{V^2} \quad (7.41)$$

where P_G and Q_G are the active and reactive power generated by the farm and by the farm network respectively. In similar fashion, the trend of the maximum voltage difference ΔV as a function of the maximum power difference $\Delta P = P_{max} - P_{min}$ can be estimated based on the following formula:

$$\Delta V = \frac{P_{G_{max}}R_S + Q_{G_{max}}X_S - (P_{G_{min}}R_S + Q_{G_{min}}X_S)}{V^2} \quad (7.42)$$

In the case where the generator outputting this fluctuating power is operated at unity power factor (which is the case in this study), the reactive power Q_G passing through the PCC in direction of the farm offshore network is absorbed by the combined impedance X_G of the cables and of the overhead line. Hence, it is proportional to the square of the generated active power P_G as:

$$Q_G = -3X_G I_G^2 + Q_{gen} = -3X_G \left(\frac{P_G}{\sqrt{3}V} \right)^2 + Q_{gen} \approx -X_G \left(\frac{P_G}{V} \right)^2 \quad (7.43)$$

where Q_{gen} is the reactive power generated by the cables and is negligible in this case, as shown in Chapter 5. Hence, the reactive power absorption follows the trend of the active power and is maximal when the farm outputs its maximum active power. Consequently, (7.41) and (7.42) can be rewritten as:

$$\begin{aligned}
V &= 1 + \frac{(P_G - P_L)R_S + (Q_G - Q_L)X_S}{V^2} \\
&= 1 + \frac{(P_G - P_L)R_S - (P_G^2 \frac{X_G}{V^2} - Q_L)X_S}{V^2} \\
&= 1 + \frac{(P_G - P_L)R_S V^2 - (P_G^2 X_G - V^2 Q_L)X_S}{V^4} \tag{7.44}
\end{aligned}$$

and

$$\begin{aligned}
\Delta V &= \frac{|(P_{G_{max}} - P_L)R_S + (Q_{G_{max}} - Q_L)X_S - ((P_{G_{min}} - P_L)R_S + (Q_{G_{min}} - Q_L)X_S)|}{V^2} \\
&= \frac{|P_{G_{max}} R_S V^2 - P_{G_{max}}^2 X_G X_S - (P_{G_{min}} R_S V^2 - P_{G_{min}}^2 X_S)|}{V^4} \tag{7.45}
\end{aligned}$$

Considering that the value of the voltage V and of the maximum voltage fluctuation ΔV may be expressed as a function of the active power P_G generated by the farm only, it is possible to estimate the value of these variables with respect to the active power P_G by means of scale factors k and k' .

It must be noted that the average voltage V_{avg} does not necessarily correspond to the average power $P_{G_{avg}}$ and to the corresponding reactive power. However, in all the production periods analysed in the context of this work, the average power P_{avg} was relatively low to generate a negligible reactive power, which leads to a linear relationship between the average voltage V_{avg} and the average power P_{avg} in this case.

7.4.8 Summary

Both the average voltage V_{avg} and the maximum voltage fluctuation ΔV , on which the flicker level Pst is highly dependent, can be estimated approximately with respect to both the farm rated power P_{rated} and the impedance angle Ψ_k at the point of connection as:

$$\begin{aligned}
V_{avg}(P_{rated}, \Psi_k) &= k(P_{rated}, \Psi_k) V_{avg}(P_{ref}, \Psi_{k_{ref}}) \\
\text{and } \Delta V(P_{rated}, \Psi_k) &= k'(P_{rated}, \Psi_k) V_{avg}(P_{ref}, \Psi_{k_{ref}})
\end{aligned}$$

Consequently, this means that it is possible for instance to estimate the flicker level generated by a 50 MW wave farm connected to a node whose impedance angle Ψ_k is equal to 70° based on a limited amount of data concerning a wave farm of much smaller rated power, for example 5 MW, connected at a node whose impedance angle is equal to 50° . The type of data required for the estimation consists of:

- the curve of the maximum, minimum and average active powers $P_{G_{max}}$, $P_{G_{min}}$ and $P_{G_{avg}}$ generated by the wave farm as a function of the rated power P_{rated} ,
- the equivalent resistance R_G and reactance X_G of the farm electrical network,
- and the active and reactive power consumption P_L and Q_L of the load connected to the 38 kV bus.

Considering that the flicker level Pst at a given short-circuit ratio can also be estimated using the flicker coefficient $c(\Psi_k)$ already described in Section 7.1.1, the flicker level which would be generated for a given short-circuit level S_{SC} , a given impedance angle Ψ_k and a given farm rated power P_{rated} can be estimated from the flicker level generated at any other short-circuit level, impedance angle and farm rated power.

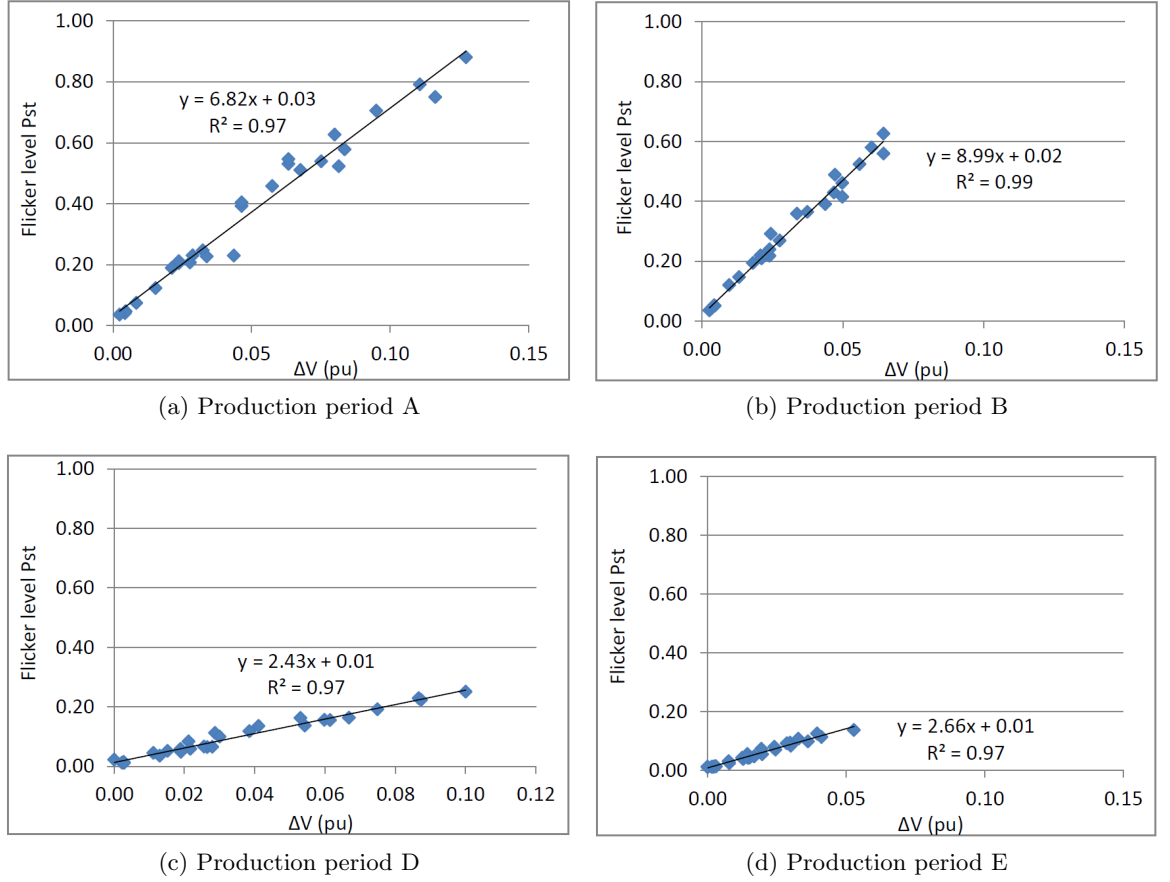


Figure 7.10: Flicker level P_{st} as a function of the maximum voltage fluctuation ΔV

7.5 Results

7.5.1 Relationship between the flicker level P_{st} and the maximum voltage fluctuation $\Delta V(P, \Psi_k)$

It was demonstrated in the previous sections that the relationship between the flicker level P_{st} and the scale factor k' is expected to be linear. Hence, this means that the relation between the flicker level and the maximum voltage fluctuation $\Delta V(P_{rated}, \Psi_k)$, referred to as ΔV in the rest of the chapter, is also linear. This is confirmed by the results shown in Figures 7.10a to 7.10d which present the flicker level P_{st} for each production period as a function of the maximum voltage amplitude ΔV . The results included in each of these graphs were obtained for rated power values of the farm ranging between 5 MW and 50 MW and impedance angles Ψ_k ranging between 30° and 85° .

The leading coefficients of the linear functions are summarised in Table 7.2. These coefficients are greater with respect to the production periods A and B in which the generator is operated in fixed speed mode than for the production periods D and E in which it is operated in variable speed mode. This was expected as inertial storage is not available with the former type of speed control mode, which means that the mechanical power peaks are directly transformed into electrical power peaks.

It is also quite interesting to note that the leading coefficient corresponding to production period A is relatively close to this of production period B, which are the two production periods in which the generator is operated at fixed speed. In similar fashion,

Period label	Leading coefficient
A	6.82
B	8.99
D	2.43
E	2.66

Table 7.2: Leading coefficients of the linear functions $Pst = a\Delta V$ used as an approximation

ΔV (pu)	0.004	0.02	0.04	0.08	0.1	0.12
Period T (s)	11.1	10.5	10.4	10.4	10.4	10.4

(a) Production period A

ΔV (pu)	0.004	0.008	0.02	0.04	0.06
Period T (s)	8.0	7.8	7.8	7.8	7.8

(b) Production period B

ΔV (pu)	0.01	0.03	0.05	0.07	0.09
Period T (s)	32.3	29.9	29.4	29.6	29.5

(c) Production period D

ΔV (pu)	0.01	0.03	0.05	0.07	0.09
Period T (s)	28.6	27.0	26.8	26.8	26.8

(d) Production period E

Table 7.3: Period T of the sinusoidal fluctuation corresponding to given maximum voltage fluctuation ΔV

the leading coefficient corresponding to production period D is approximately equal to this corresponding to production period E. In both of these latter production periods, the generator is operated in variable speed mode. This may mean that the leading coefficient may be extracted from the characteristics of the wave device design and of its operation mode.

Equivalent sinusoidal voltage profile

The period T of the equivalent sinusoidal voltage profile, as described in Section 7.4.6, corresponding to each production period was investigated by determining the expected flicker level Pst for a series of maximum voltage fluctuation ΔV ranging between the minimum and the maximum values observed for each production period. This range was reduced in the case of maximum voltage fluctuations ΔV corresponding to a flicker level Pst less than 0.010, as it is the margin of error of the flickermeter. Tables 7.3a to 7.3d detail the results for each production period while Table 7.4 indicates the average period T as well as the ratio of the energy period T_e of each production period (which is calculated as $T_e = 1.3T_z$ as described in Chapter 4) to this period T .

Interestingly, the ratio of the energy period T_e to the period T corresponding to each of the production periods A and B, during which the generator is operated in fixed speed mode, is close to unity. This confirms that the flicker level Pst of an entire wave farm can be characterised from the mechanical response of its individual devices, as mentioned in Section 7.4.5. On the contrary, the ratio is much smaller for production periods D and E in which the generator is operated in variable speed mode, ranging between 0.3 and 0.4,

Period	Period T (s)	T_e (s)	T_e/T
A	10.4	10.9	1.05
B	7.8	7.3	0.93
D	29.9	8.8	0.3
E	26.8	10.13	0.4

Table 7.4: Period T of the sinusoidal voltage profile corresponding to each production period

which seems also coherent as in this case, the electrical power generation is decoupled to some extent from the fluctuations of the mechanical input power. Hence, the period T cannot be estimated directly from the energy period T_e in this case and information on the voltage profile is thus necessary to estimate its value.

Relation of proportionality between the flicker levels obtained in fixed and variable speed operation

It can be observed that there exists a relation of proportionality between the flicker levels corresponding to the fixed speed and to the variable speed modes. This can be explained from (7.33). This equation defines a relation of proportionality between the flicker level Pst and the gain K_j applied by the Block 3 of the flickermeter and corresponding to a given voltage fluctuation of radian frequency ω . Hence, the flicker level Pst should increase linearly as a function of the radian frequency ω of its equivalent sinusoidal voltage profile. This means that the flicker level Pst_1 corresponding to a sinusoidal voltage profile of radian frequency ω_1 can be calculated with a simple rule of three as:

$$Pst_1 = Pst_2 \frac{\omega_1}{\omega_2} \quad (7.46)$$

where Pst_2 is known and corresponds to a sinusoidal voltage profile of radian frequency ω_2 . Hence, the relation between the two flicker levels Pst_{fix} and Pst_{var} obtained for a given production period during which the generators are operated in fixed and in variable speed mode respectively can be obtained from the rule of three defined in (7.46) using the two radian frequencies ω_{fix} and ω_{var} corresponding to each of these production periods as:

$$Pst_{fix} = Pst_{var} \frac{\omega_{fix}}{\omega_{var}} \quad (7.47)$$

This can be applied to the case of production periods A (fixed speed) and A' (variable speed) which were described in the previous chapter. The period T corresponding to the production period A is equal to 10.4 seconds, as was shown in Table 7.4. As regards the production period A', considering that its flicker level is close to that obtained with the production period D which has similar sea-state characteristics, it can be assumed that the period T corresponding to the production period A' is equal to this of the production period D (29.9 seconds). Hence, the flicker level corresponding to the production period A (fixed speed) should be approximately three times as high as the flicker level obtained with the production period A' (variable speed), as calculated below:

$$\begin{aligned} Pst_{fix} &= Pst_{var} \frac{\omega_{fix}}{\omega_{var}} = Pst_{var} \frac{T_{var}}{T_{fix}} \\ &= Pst_{var} \frac{29.9}{10.4} = 2.9 Pst_{var} \end{aligned} \quad (7.48)$$

Impedance angle Ψ_k ($^\circ$)	30	50	70	85
Pst - A (fixed speed)	0.88	0.58	0.19	0.23
Pst - A' (variable speed)	0.30	0.20	0.06	0.07
Ratio	2.9	2.9	3.1	3.2

Table 7.5: Flicker level obtained with the production period A (fixed speed) and A' (variable speed)

Impedance angle Ψ_k ($^\circ$)	30	50	70	85
Pst_{pwr} (experimental power profile)	0.30	0.20	0.06	0.07
Pst_{volt} (sinusoidal voltage profile)	0.61	0.40	0.06	0.07
Ratio	0.5	0.5	0.6	0.4

Table 7.6: Flicker level as obtained from the filtered experimental power profile (top) and from the filtered equivalent sinusoidal voltage profile (bottom) as a function of the maximum voltage fluctuation ΔV obtained for the fixed speed mode (production period A)

This is confirmed by the results shown in Table 7.5. It is interesting to note that the proportionality coefficient which is equal to 2.9 in the case of the production periods A and A' is exactly equal to the square of the time constant τ_f which represents the inertia of the system and which is equal to 1.7 seconds. If a relation between the flicker level in variable and fixed speed mode based on this time constant τ_f only existed, this would mean that calculating the flicker level corresponding to the variable speed mode with any sea-state would require only data on the flicker level corresponding to the fixed speed mode (which can be easily determined from the energy period T_e) and on the inertia time constant τ_f of the system. However, the absence of complementary data prevented this aspect to be investigated any further.

In addition, it was also found that the flicker level as obtained in variable speed mode can be estimated from the sinusoidal voltage profile corresponding to the fixed speed mode which is filtered by a first order low-pass filter whose time constant is equal to the inertia time constant τ_f of the wave device. The results presented in Table 7.6 show that the relation which exists between the flicker level Pst_{volt} as calculated from the filtered sinusoidal voltage profile and the flicker level Pst_{pwr} which is calculated from the filtered experimental power profile can be defined as:

$$Pst_{pwr} \approx \frac{1}{2} Pst_{volt} \quad (7.49)$$

The existence of this ratio can be explained from the assumptions made with this method. Applying a sinusoidal fluctuation of period T equal to 10.4 seconds to a filter produces a fluctuation of reduced amplitude having the same period, as shown in Figure 7.11 which shows an input voltage fluctuation of amplitude ΔV equal to 0.1 pu. The corresponding output from this filter is also a fluctuation of period T equal to 10.4 seconds, but whose amplitude is smaller. In this case, the amplitude of the input signal is 140% greater than the amplitude of the output signal of the filter. It was observed that the ratio of the amplitude between the input and the output signals depends only on the time constant τ_f of the filter. The trend of this amplitude reduction phenomenon as a function of the time constant τ_f is shown in Figure 7.12.

Hence, as the flicker level Pst is proportional to the amplitude of a sinusoidal voltage fluctuation, this means that the amplitude reduction performed by the filter decreases the

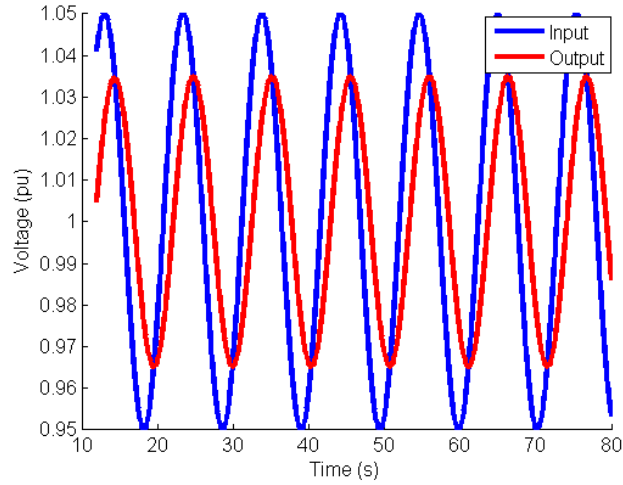


Figure 7.11: Input and output signals of a first order low-pass filter of time constant τ_f

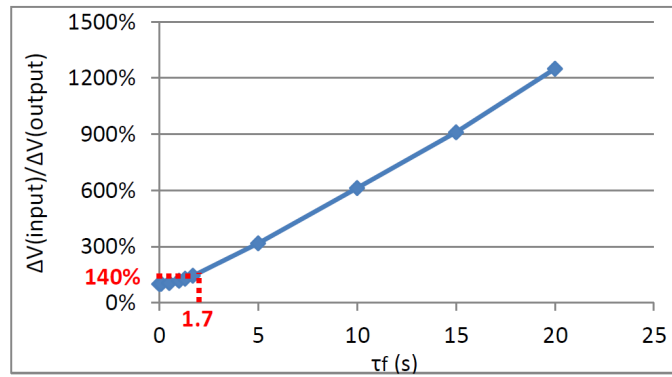


Figure 7.12: Amplitude reduction as a function of the filter time constant $\tau_f=1.7$ seconds

flicker level corresponding to the output by 140% compared to the flicker level obtained with the input power. In addition, the period of the input and output signals is the same. However, the period T corresponding to the variable speed operation is equal to 29.9 seconds. Hence, as the flicker level Pst is also proportional to the frequency of sinusoidal fluctuation, this means that the flicker level as obtained from the filtered sinusoidal voltage profile is increased by $29.9/10.4=290\%$ compared to the flicker level obtained from the filtered power profile. Finally, this means that the flicker level calculated from the power profile Pst_{pwr} should be approximately twice as less as the flicker level Pst_{volt} obtained from the filtered sinusoidal voltage profile which is confirmed by the results shown in Table 7.6. This is summarised mathematically as:

$$Pst_{pwr} = \frac{10.4}{29.9} \times 1.4Pst_{volt} = 0.5Pst_{volt} \quad (7.50)$$

As mentioned earlier, if there existed a simple relation between the periods of the equivalent sinusoidal voltage profiles corresponding to the fixed speed ratio and to the variable speed modes respectively based on the inertia time constant τ_f , this would mean that it would be possible to calculate the flicker level corresponding to different sea-states and to different values of the inertia time constant τ_f based on this parameter and on the energy period of the sea-state under consideration. This would simplify further the estimation of the flicker level generated by a wave farm. This topic will be addressed in future work.

Summary

In conclusion, these results are interesting as they tend to demonstrate that the flicker generated by a wave farm may be estimated with a fairly reasonable level of accuracy by means of an equivalent sinusoidal voltage profile. In addition, a relatively limited amount of data is required concerning the characteristics of the farm's electrical network and of the local network to which it is connected, as well as concerning the design of the wave device. In the case where the energy conversion chain of the wave device includes little to no means of storage, it can be assumed, as a worst case scenario, that the flicker generated by this device is equivalent to the flicker generated by a sinusoidal voltage fluctuation of period T_e . The amplitude of this sinusoidal fluctuation can be calculated from the maximum power fluctuation $\Delta P = P_{max} - P_{min}$.

In the more complex case where some form of storage is used in the energy conversion chain, information regarding the ratio of the energy period T_e to the period T may be required from the developers. Alternatively, this period T may be calculated from a power profile corresponding to the variable speed mode, or from a power profile corresponding to the fixed speed mode which is filtered by a first order low-pass filter of time constant τ_f . This will be addressed in future work. Although this type of data provides enough information for the estimation of the flicker level P_{st} , they have the advantage not to reveal any features of the device design which may be commercially sensitive.

7.5.2 Estimation of the flicker level P_{st} in relation to the farm rated power P_{rated}

This section presents the results regarding the flicker estimation method in relation to the farm rated power P_{rated} . The flicker level generated by a wave farm (whose rated power ranges between 5 MW and 50 MW) was estimated from the flicker level generated by a farm whose rated power is equal to 5 MW. The results were then compared with those obtained by analysing the data generated by the power system simulations.

The flicker level P_{st} was estimated based on the flicker level generated by a farm whose rated power P_{rated} is equal to 5 MW. It was mentioned in Section 7.1.2 that using the square root of the scale factor k' was expected to provide more accurate results than the use of the scale factor itself, considering the fact that voltage fluctuations are expected to be dephased. This was found to be correct, as shown in Figures 7.13a to 7.16d which present the flicker level as obtained from the simulations (labeled "simulation"), the flicker level as obtained from the estimation method with the scale factor ("theoretical") and its square root ("theoretical - sqrt").

The results of an additional study were also presented (labeled as "5 MW scaled up"). These results correspond to the flicker level generated by a fictive voltage profile modeled based on the voltage profile generated by a 5 MW-rated wave farm and which is intended to represent the equivalent voltage profile as generated by a 50 MW-rated wave farm which does not take the power smoothing effect of the aggregation of several devices into account. In other words, the shape of this fictive voltage profile is the same as this obtained with a 5 MW-rated farm but its amplitude is greater and is calculated as:

$$(V(t) - V_{avg})_{scaled\ up} = (V(t) - V_{avg})_{5\ MW} \frac{\Delta V_{50\ MW}}{\Delta V_{5\ MW}} \quad (7.51)$$

where $(V(t) - V_{avg})_{5\ MW}$ is the voltage profile corresponding to a wave farm of 5 MW minus its average voltage, $\Delta V_{50\ MW}$ and $\Delta V_{5\ MW}$ are the maximum voltage fluctuations

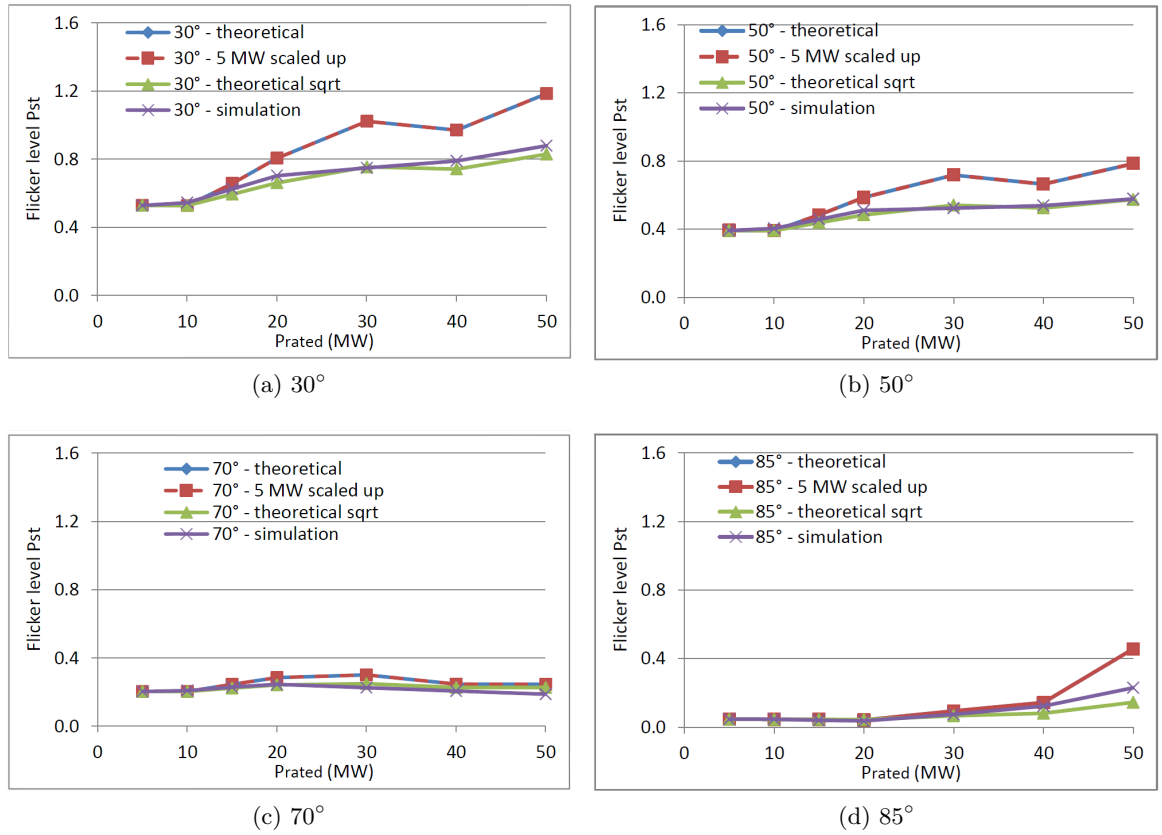


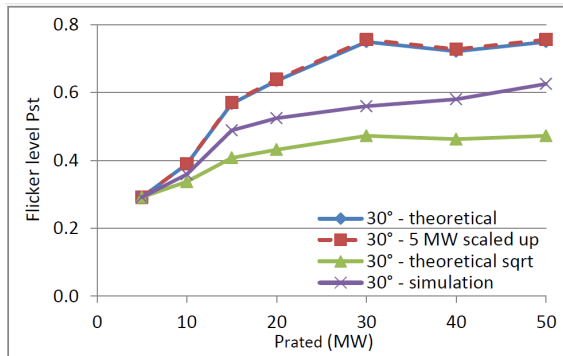
Figure 7.13: Flicker level P_{st} (estimated and simulated) as a function of the rated power P_{rated} , production period A

corresponding to a wave farm of 50 MW and 5 MW respectively. The results shown in Figures 7.13a to 7.16d demonstrate that the results obtained by using the scale factor k' (and not its square root) correspond very well to this case, which is indeed a worst case scenario in terms of flicker. This means that the error between the experimental results and the estimation method are induced by the change of shape of the voltage profile.

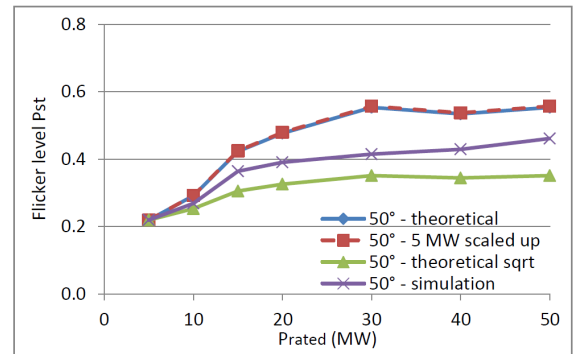
Table 7.7 shows the simulation results (referred to as “Simulation”) corresponding to voltage profile obtained with the experimental power time series for the different production periods considered in this study. They show also the results obtained through the estimation (thus referred to as “Estimation”) of the flicker generated by a 5 MW-rated farm using the square root of the scale factor k' . The error between these two types of results is also presented. The estimation was performed for the following impedance angles Ψ_k : 30° , 50° , 70° and 85° .

Table 7.8 summarises the maximum error obtained for each of the production periods considered in this study. It can be observed that the error remains below 0.1, with the exception of three cases whose values are equal to 0.11, 0.12 and 0.15 respectively. This shows that the estimation method with respect to the farm rated power provides sufficiently accurate results in most cases.

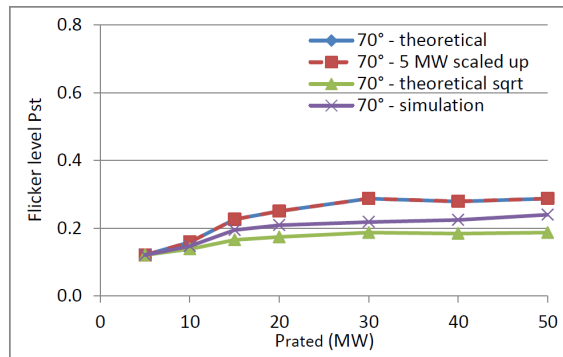
The error usually increases when only the scale factor k' related to the maximum voltage fluctuation ΔV is used in the calculations, with the exception of only two cases. However, this error is negligible. Table 7.9 summarised the difference in terms of error between the results obtained with the approximation minus these obtained with the esti-



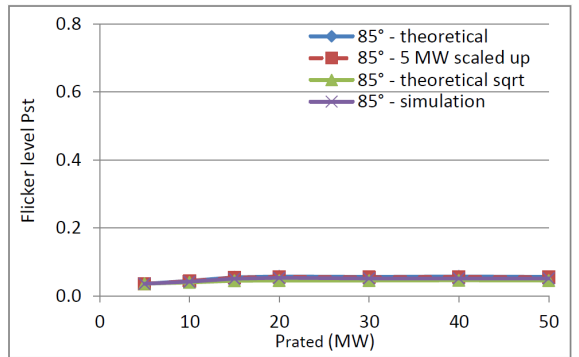
(a) 30°



(b) 50°

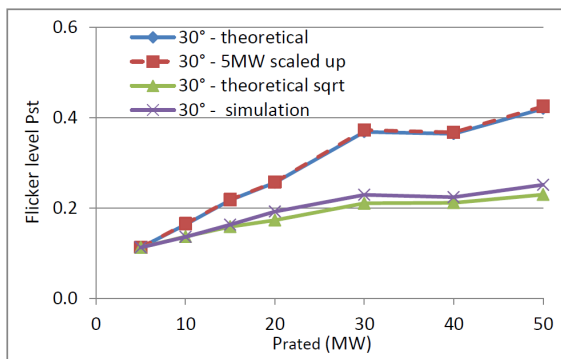


(c) 70°

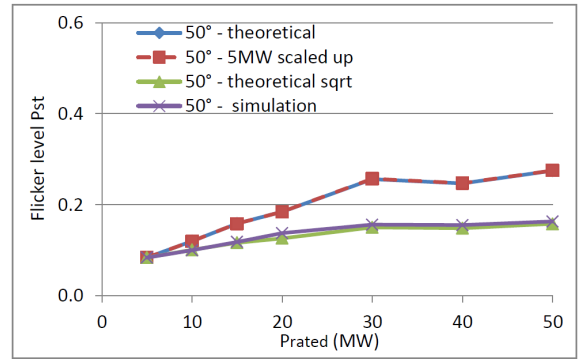


(d) 85°

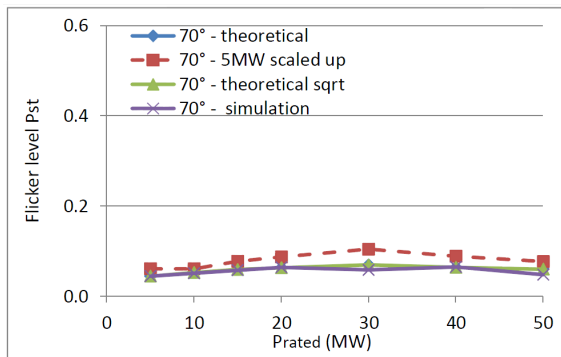
Figure 7.14: Flicker level P_{st} (estimated and simulated) as a function of the rated power P_{rated} , production period B



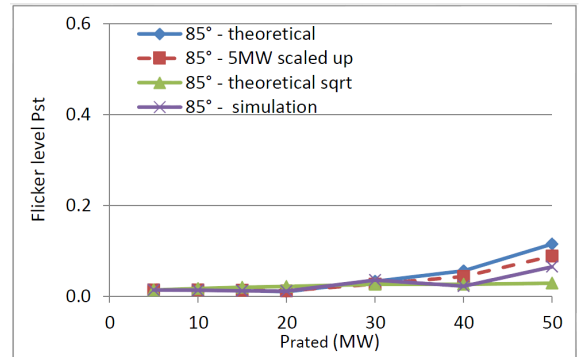
(a) 30°



(b) 50°

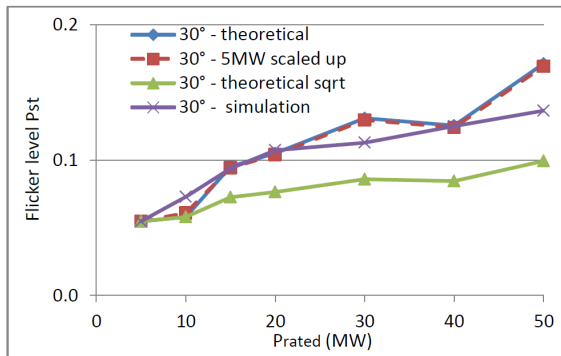


(c) 70°

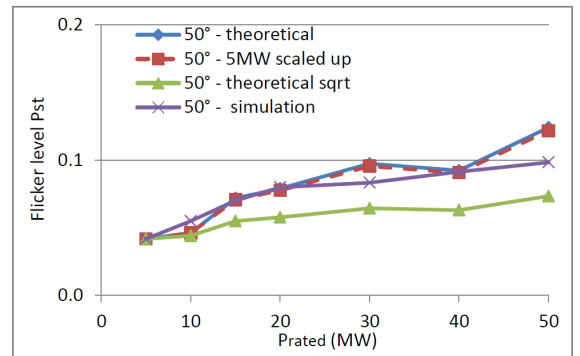


(d) 85°

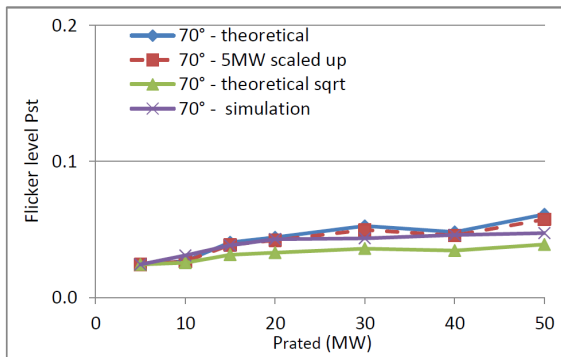
Figure 7.15: Flicker level P_{st} (estimated and simulated) as a function of the rated power P_{rated} , production period D



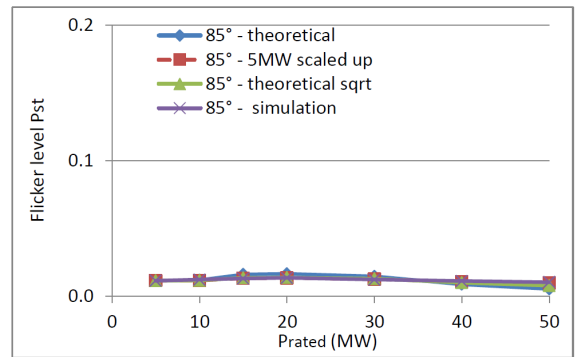
(a) 30°



(b) 50°



(c) 70°



(d) 85°

Figure 7.16: Flicker level P_{st} (estimated and simulated) as a function of the rated power P_{rated} , production period E

Period	Ψ_k		P_{rated}						
			5 MW	10 MW	15 MW	20 MW	30 MW	40 MW	50 MW
A	30°	Simulation	0.53	0.55	0.63	0.71	0.75	0.79	0.88
		Estimation	0.53	0.53	0.66	0.66	0.76	0.74	0.83
		Error	0.00	0.02	0.03	0.04	0.01	0.05	0.05
	50°	Simulation	0.39	0.40	0.46	0.51	0.52	0.54	0.58
		Estimation	0.39	0.39	0.48	0.48	0.54	0.52	0.57
		Error	0.00	0.01	0.03	0.03	0.02	0.01	0.00
	70°	Simulation	0.20	0.21	0.23	0.25	0.23	0.21	0.19
		Estimation	0.20	0.20	0.23	0.24	0.25	0.23	0.23
		Error	0.00	0.01	0.01	0.00	0.02	0.02	0.04
	85°	Simulation	0.05	0.05	0.04	0.04	0.07	0.12	0.23
		Estimation	0.05	0.05	0.05	0.04	0.07	0.08	0.14
		Error	0.00	0.00	0.00	0.01	0.01	0.04	0.08
B	30°	Simulation	0.29	0.36	0.49	0.52	0.56	0.58	0.63
		Estimation	0.29	0.39	0.57	0.43	0.47	0.46	0.47
		Error	0.00	0.03	0.08	0.09	0.09	0.12	0.15
	50°	Simulation	0.22	0.27	0.36	0.39	0.41	0.43	0.46
		Estimation	0.22	0.29	0.42	0.35	0.35	0.34	0.35
		Error	0.00	0.02	0.06	0.04	0.06	0.08	0.11
	70°	Simulation	0.12	0.15	0.19	0.21	0.22	0.22	0.24
		Estimation	0.12	0.14	0.17	0.17	0.19	0.18	0.19
		Error	0.00	0.01	0.03	0.03	0.03	0.04	0.05
	85°	Simulation	0.12	0.15	0.19	0.21	0.22	0.22	0.24
		Estimation	0.12	0.13	0.15	0.15	0.15	0.15	0.15
		Error	0.00	0.01	0.04	0.06	0.07	0.07	0.09
D	30°	Simulation	0.11	0.14	0.16	0.19	0.23	0.22	0.25
		Estimation	0.11	0.14	0.16	0.17	0.21	0.21	0.23
		Error	0.00	0.00	0.00	0.02	0.02	0.01	0.02
	50°	Simulation	0.08	0.10	0.12	0.14	0.16	0.16	0.16
		Estimation	0.08	0.10	0.12	0.13	0.15	0.15	0.16
		Error	0.00	0.00	0.00	0.01	0.01	0.01	0.01
	70°	Simulation	0.05	0.05	0.06	0.07	0.06	0.07	0.05
		Estimation	0.05	0.05	0.06	0.06	0.07	0.07	0.06
		Error	0.00	0.00	0.00	0.00	0.01	0.00	0.01
	85°	Simulation	0.01	0.01	0.01	0.01	0.04	0.02	0.07
		Estimation	0.01	0.01	0.01	0.01	0.05	0.05	0.19
		Error	0.00	0.00	0.00	0.00	0.02	0.02	0.12
E	30°	Simulation	0.05	0.07	0.09	0.11	0.11	0.13	0.14
		Estimation	0.05	0.06	0.10	0.10	0.13	0.13	0.17
		Error	0.00	0.01	0.00	0.00	0.02	0.00	0.03
	50°	Simulation	0.04	0.05	0.07	0.08	0.08	0.09	0.10
		Estimation	0.04	0.05	0.07	0.08	0.10	0.09	0.12
		Error	0.00	0.01	0.00	0.00	0.01	0.00	0.03
	70°	Simulation	0.02	0.03	0.04	0.04	0.04	0.05	0.05
		Estimation	0.02	0.03	0.04	0.04	0.05	0.05	0.06
		Error	0.00	0.00	0.00	0.00	0.01	0.00	0.01
	85°	Simulation	0.01	0.01	0.01	0.01	0.01	0.1	0.1
		Estimation	0.01	0.01	0.01	0.01	0.01	0.1	0.1
		Error	0.00	0.00	0.00	0.00	0.00	0.00	0.00

Table 7.7: Flicker level Pst as obtained through the classical method and through the proposed estimation method for several values of the farm rated power P_{rated}

P_{rated}	Production period			
	A	B	D	E
30°	0.05	0.15	0.02	0.03
50°	0.03	0.11	0.01	0.03
70°	0.04	0.05	0.01	0.01
85°	0.08	0.09	0.12	0.00

Table 7.8: Absolute value of the maximum error with respect to the flicker level Pst between the simulation results and these obtained through the proposed estimation method

P_{rated}	Production period			
	A	B	D	E
30°	0.07	0.01	0.03	-0.01
50°	0.02	0.01	0.01	0.00
70°	-0.01	0.01	0.00	0.00
85°	0.00	0.00	0.00	0.00

Table 7.9: Maximum difference in terms of error between the results obtained through the proposed estimation method and its approximative form based on k' only

mation method which were presented in the first part of this section. This means implicitly that the average voltage V_{avg} can be considered as approximately constant as a function of the rated power P_{rated} .

7.5.3 Estimation of flicker level Pst in relation to different impedance angles Ψ_k

This section presents the results regarding the flicker estimation method in relation to different impedance angles Ψ_k . The flicker level generated by a wave farm whose rated power ranges between 5 MW and 50 MW was estimated from the flicker level obtained with an impedance angle equal to 30°. The results were then compared with those obtained from the power system simulations time series.

Results

Table 7.10 shows the simulation results as well as these obtained through the estimation method. The error between these two types of results is also indicated. The level of error is very low and does not exceed 0.02, as summarised in Table 7.11 which presents the maximum error observed for each production period. This demonstrates that the estimation method proposed in this work provides relatively accurate results.

In similar fashion to the estimation with respect to the rated power, estimating the flicker level Pst by taking into account only the scale factor k' related to the maximum voltage fluctuation ΔV (thus assuming that the average voltage V_{avg} is approximately constant as a function of the impedance angle Ψ_k) leads to a negligible increase of the error. Table 7.12 summarises the difference between the maximum error obtained with the approximative form of the estimation method and these obtained with the non-approximated form of this estimation method. This difference is negligible which means that the flicker level Pst can be safely estimated based on the maximum voltage fluctuation ΔV only.

Period	Ψ_k		P_{rated}						
			5 MW	10 MW	15 MW	20 MW	30 MW	40 MW	50 MW
A	30°	Simulation	0.53	0.55	0.63	0.71	0.75	0.79	0.88
		Estimation	0.53	0.55	0.63	0.71	0.75	0.79	0.88
		Error	0.00	0.00	0.00	0.00	0.00	0.00	0.00
	50°	Simulation	0.39	0.40	0.46	0.51	0.52	0.54	0.58
		Estimation	0.39	0.40	0.46	0.51	0.52	0.54	0.58
		Error	0.00	0.00	0.00	0.00	0.00	0.00	0.00
	70°	Simulation	0.20	0.21	0.23	0.25	0.23	0.21	0.19
		Estimation	0.20	0.21	0.23	0.25	0.22	0.20	0.18
		Error	0.00	0.00	0.00	0.00	0.01	0.01	0.01
	85°	Simulation	0.05	0.05	0.04	0.04	0.07	0.12	0.23
		Estimation	0.04	0.04	0.04	0.03	0.06	0.10	0.29
		Error	0.01	0.01	0.00	0.01	0.02	0.02	0.06
B	30°	Simulation	0.29	0.36	0.49	0.52	0.56	0.58	0.63
		Estimation	0.29	0.36	0.49	0.52	0.56	0.58	0.63
		Error	0.00	0.00	0.00	0.00	0.00	0.00	0.00
	50°	Simulation	0.22	0.27	0.36	0.39	0.41	0.43	0.46
		Estimation	0.22	0.27	0.36	0.39	0.41	0.43	0.46
		Error	0.00	0.00	0.00	0.00	0.00	0.00	0.00
	70°	Simulation	0.12	0.15	0.19	0.21	0.21	0.22	0.24
		Estimation	0.12	0.15	0.19	0.21	0.22	0.22	0.24
		Error	0.00	0.00	0.00	0.00	0.00	0.00	0.00
	85°	Simulation	0.04	0.04	0.05	0.05	0.05	0.05	0.05
		Estimation	0.03	0.04	0.04	0.04	0.04	0.04	0.04
		Error	0.00	0.00	0.01	0.01	0.01	0.01	0.01
D	30°	Simulation	0.11	0.14	0.16	0.19	0.23	0.22	0.25
		Estimation	0.11	0.14	0.16	0.19	0.23	0.22	0.25
		Error	0.00	0.00	0.00	0.00	0.00	0.00	0.00
	50°	Simulation	0.08	0.10	0.12	0.14	0.16	0.15	0.16
		Estimation	0.05	0.05	0.06	0.07	0.06	0.07	0.05
		Error	0.00	0.00	0.00	0.00	0.01	0.01	0.00
	70°	Simulation	0.05	0.05	0.06	0.07	0.06	0.07	0.05
		Estimation	0.05	0.05	0.06	0.07	0.07	0.06	0.05
		Error	0.00	0.00	0.00	0.01	0.02	0.01	0.01
	85°	Simulation	0.01	0.01	0.01	0.01	0.02	0.03	0.06
		Estimation	0.01	0.01	0.01	0.01	0.04	0.02	0.07
		Error	0.00	0.00	0.00	0.01	0.02	0.01	0.01
E	30°	Simulation	0.05	0.07	0.09	0.11	0.11	0.13	0.14
		Estimation	0.05	0.07	0.09	0.11	0.11	0.13	0.14
		Error	0.00	0.00	0.00	0.00	0.00	0.00	0.00
	50°	Simulation	0.04	0.05	0.07	0.08	0.08	0.09	0.10
		Estimation	0.04	0.05	0.07	0.08	0.08	0.09	0.10
		Error	0.00	0.00	0.00	0.00	0.00	0.00	0.00
	70°	Simulation	0.02	0.03	0.04	0.04	0.04	0.04	0.05
		Estimation	0.02	0.03	0.04	0.04	0.04	0.04	0.05
		Error	0.00	0.00	0.00	0.00	0.00	0.00	0.00
	85°	Simulation	0.02	0.03	0.04	0.04	0.04	0.05	0.05
		Estimation	0.02	0.03	0.04	0.04	0.04	0.04	0.05
		Error	0.00	0.00	0.00	0.00	0.00	0.00	0.00

Table 7.10: Flicker level P_{st} as obtained through the classical method and through the proposed estimation method for several values of the impedance angle Ψ_k

P_{rated}	Production period			
	A	B	D	E
5 MW	0.01	0.00	0.00	0.00
10 MW	0.01	0.00	0.00	0.00
15 MW	0.01	0.01	0.00	0.00
20 MW	0.01	0.01	0.01	0.00
30 MW	0.02	0.01	0.02	0.00
40 MW	0.02	0.01	0.01	0.01
50 MW	0.06	0.01	0.01	0.01

Table 7.11: Maximum error with respect to the flicker level Pst between the simulation results and these obtained through the proposed estimation method

P_{rated}	Production period			
	A	B	D	E
5 MW	0.00	0.00	0.02	0.02
10 MW	0.00	0.00	0.03	0.02
15 MW	0.00	0.00	0.02	0.02
20 MW	0.00	0.00	0.02	0.02
30 MW	0.00	0.00	0.01	0.01
40 MW	-0.01	0.00	0.02	0.01
50 MW	0.03	0.00	0.02	0.00

Table 7.12: Maximum difference in terms of error between the results obtained through the proposed estimation method and through its approximative form based on k' only

7.6 Application of the proposed methods for grid connection studies

Grid connection studies are routinely conducted by grid operators as part of grid connection applications. They are intended to determine any potential issues which may arise from the connection of an installation to the network, in order to mitigate them if they prove to be significant. However, the absence of reliable and validated dynamic models of wave devices prevents the comprehensive and accurate assessment of the grid impact induced by wave farms.

The methods proposed in this chapter may greatly facilitate this type of study regarding the flicker which is generated by a wave farm. Firstly, the amount of data which is required from wave device developers is relatively small, as it consists of the maximum, minimum and average active power levels generated by the farm as a function of the number of devices N as well as the inertia time constant τ_f of a wave device in case it is operated in variable speed mode. Grid operators may then use this data in load flow studies to determine the corresponding maximum voltage fluctuation ΔV and average voltage.

The farm maximum, minimum and average active power are highly dependent on the device layout and on the farm orientation compared to the dominant wave direction. Hence, it is proposed that grid operators define a reference device layout and farm orientation which the developers may use to compute these parameters.

It is important to mention that grid operators usually require dynamic models which may be simulated for a simulation time step greater than a pre-defined limit. For instance,

the limit enforced by the Irish grid operators is equal to 5 ms [35]. In addition, wind turbines models for power system studies usually consists of a simplified two-mass model which does not represent the rotor and tower vibration modes nor the vibration of the drive-train, so it is not expected, based on these two observations, that highly detailed models for wave devices will be required either.

7.7 Conclusions

This chapter has presented a method for estimating the flicker level Pst in relation to both the farm rated power and to the impedance angle Ψ_k . This method is complementary to the method described in the IEC standard 61400-21 which defines a flicker coefficient $c(\Psi_k)$ independent of the short-circuit ratio. Based on these three methods, the flicker level as generated by a wave farm at any connection point and for any farm rated power can be estimated based on the data corresponding to one flicker level sample only. This flicker level sample may be obtained from experimental data or simply from data on the considered sea-state and on the inertia time constant τ_{au_f} of the wave device.

The chapter presented the theoretical background underpinning the method. It was demonstrated that the flicker level Pst could be estimated by means of scale factors k and k' related to the average voltage V_{avg} and to the maximum voltage fluctuation ΔV of a voltage profile. More specifically, it was demonstrated that there exists a linear relationship between the flicker level Pst and the product kk' of these scale factors. However, considering that the average voltage V_{avg} remains relatively close to unity whereas important variations are observed for the maximum voltage fluctuation ΔV , this linear relationship was reduced to a proportional relationship between the flicker level Pst and the scale factor k' . These assumptions were verified based on simulations results obtained with PowerFactory. The results obtained through the estimation method proved to be in good agreement with the simulation results.

The estimation method proposed in this work provides a useful and simple tool for the estimation of flicker as well as the dissemination of experimental data. It may help developers to estimate the flicker level Pst generated by a farm composed of their device for any kind of network to which it may be connected. This may greatly facilitate the design process by ensuring that no flicker issue is likely to arise if the devices are connected to any connection points located in the countries or regions targeted by the developer.

In addition, this may also facilitate the grid compliance analyses performed by the grid operators. More specifically, they may for instance base the compliance tests on a number of strictly defined wave device layouts whose characteristics (i.e. geometrical shape, number of devices and inter-device distance) would be communicated to any wave farm owner applying for grid connection. Based on these characteristics, the wave farm owner may compute the maximum, minimum and average active power corresponding to these layouts for different sea-states, as well as the period T of the equivalent sinusoidal voltage profile in case storage means of significant capacity are included in the energy conversion chain. Otherwise, a period equal to the energy period T_e can be retained as a worst case scenario which corresponds to the fixed speed mode. Hence, no commercially sensitive data is to be transmitted to the grid operator, who can however estimate the grid impact of the wave farm both in terms of flicker level and in terms of maximum and minimum voltage. Given that an equivalent sinusoidal voltage fluctuation is sufficient for estimating the flicker level Pst potentially generated by a wave farm during a sea-state of given significant wave height H_s and energy period T_e , a simple dynamic model composed of a constant

(corresponding to the average voltage V_{avg}) and of a sinusoidal signal (corresponding to the voltage fluctuation) may be used. Hence, more detailed models, as currently required for wind turbines, may be necessary only for short-term fault studies and for power system stability studies whose simulation time frame does not usually exceed 30 seconds.

Finally, as no commercially sensitive data are required for estimating the flicker level Pst , the results obtained by different developers may be more easily disseminated. This could greatly increase the knowledge of the wave energy research community with respect to the current wave device designs from a power quality perspective.

Chapter 8

Numerical dynamic modelling of ocean energy devices for power system studies

8.1 Introduction

As mentioned in the state-of-the-art, power system simulators are the tool of choice for assessing the grid impact induced by any system changes. Dynamic models for most of the typical components of a power system are usually provided as built-in models which the user only needs to parameterise.

However, there exists no built-in dynamic model of both wave and tidal current devices (referred to as ocean devices in the rest of this chapter) yet. This absence may represent an obstacle to the large scale grid integration of ocean energy. This in this context that a collaborative research project on this topic was established by the Ocean Energy System-Implementing Agreement in 2009. This intergovernmental organisation promotes the collaboration between countries, and operates under the framework established by the International Energy Agency (IEA).

The objective of this research project was to identify common features among ocean energy devices in order to create the structure of a generic model which may be applicable to most ocean energy devices. Data was also collected in the frame of this project to facilitate the parameterisation of this structure.

The author of this thesis participated in this research project in 2010. The study she conducted consisted of a developer survey focusing on the control strategies used by ocean devices. This work meant to determine whether control strategies should be implemented in a generic model and if so, how they should be modelled. Following this study, she refined the generic model structure initially developed in the frame of this project. A technical report covering the outcomes of this research project was published in 2011 [46].

This chapter details the results of this study which were updated compared to the initial version published in 2011 based on the experience gained, and on the results obtained during this thesis. More specifically, the main modifications to the initial publication concern the generic modelling of wave devices exclusively and are related to the results presented in the previous chapter. These results have a very significant impact with respect to the minimum simulation time frame which is necessary to assess the grid impact of a wave farm. It was demonstrated that the flicker generated by this type of farm may

be estimated with a very high level of accuracy by simulating a sinusoidal voltage fluctuation filtered by a first-order low-pass filter emulating the influence of energy storage means. Hence, it is unnecessary to develop a detailed generic model of wave device for the purpose of flicker analysis.

This finding has major implications regarding the generic modelling of wave devices. It means that the minimum duration of the power system simulations may be reduced in the case of wave farms from 10 minutes (which corresponds to the minimum duration required for the flicker analyses) to 30 seconds which is the typical simulation time frame for stability studies. Consequently, it is unnecessary to model generically with a high level of detail the control strategies whose response time is longer than 30 seconds. This may decrease significantly the level of detail required from a wave device generic model. However, these control strategies must be modelled by means parameters which remain constant over the simulations.

As regards tidal current devices, simulations lasting 10 minutes may still be needed to evaluate the flicker they generate, unless the flicker coefficient $c(\Psi_k)$ developed for wind turbines is used. This flicker coefficient is defined in the IEC standard 61400-21 as:

$$c(\Psi_k) = Pst \frac{S_{SC}}{S_n} \quad (8.1)$$

where S_n is the apparent power of a single turbine. Considering that the input power of the tidal turbines varies slowly as a function of time, the input conditions can be considered as constant over a simulation in the same way as for the simulations based on wind turbines. Hence, their control strategies is not expected to be modelled with a high level of detail. However, in similar fashion to the wave devices, they must be modelled by means of parameters which remain constant over the simulations.

The following section details the generic structure of an ocean device model which was initially developed in the frame of this project.

8.2 Generic structure of ocean energy devices

The results of a developer survey focussing on the control strategies used in ocean devices are presented in this section. This survey meant to complete the results obtained from a first survey undertaken in the frame of the OES-IA collaborative research project in which the author of this thesis did not take part. This first survey was intended to gain more understanding into the type of data developers have the ability to provide in order to parameterise a pre-established generic structure, as well as numerical values for these parameters. The second survey, which was developed, launched and whose results were analysed by the author of this thesis, focuses on refining the knowledge of the different control strategies included in ocean devices as well as on developing their generic representations if necessary.

Thirty-five respondents took part in the second survey whose questionnaire was circulated to the main developers in the industry. Similarly to the first edition, questionnaires were received from various countries and regions including Europe, Canada, the USA, Australia and Russia. It must be noted that the device sample of the second survey had characteristics similar to those of the first survey sample as shown in Figure 8.1, and that the results and conclusions of the previous edition were confirmed by the second.

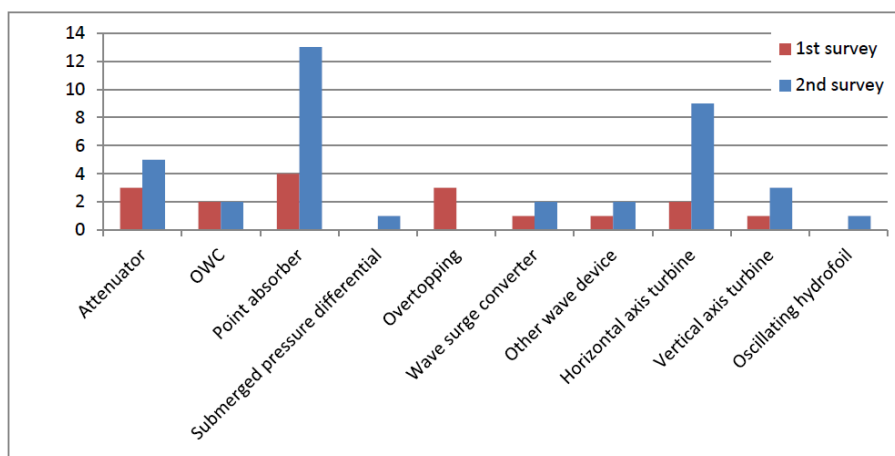


Figure 8.1: Distribution of the devices on which the survey results are based as a function of their types

The results of the survey are based on 22 wave devices and 13 tidal devices. Six functional blocks common to most ocean devices were identified as follows:

- Primary energy capture
Either tidal current or wave energy is captured at this stage and transformed into mechanical, hydraulic or pneumatic energy.
- Prime mover
The prime mover is connected to the generator’s rotor, sometimes through a gearbox. In ocean devices having no storage means and qualified as “direct-drive” devices, the primary power capture and the prime mover functions are performed by the same component, for instance by the rotor in tidal turbines.
- Generator
The generator transforms mechanical energy into electricity.
- Power electronic converters
Power electronic converters, necessary for all grid interface types with the exception of the directly-connected, fixed speed squirrel-cage generator, transforms the electricity produced by the generator into electrical voltage oscillating at the grid frequency. They decouple, either partially or fully, the generator from the network.
- Storage
The storage function is optional and simulates the action of both dedicated storage means (e.g. flywheel) as well as built-in components having a significant storage capability (e.g. hydraulic ram). It may appear in a hydraulic, mechanical or electrical form.
- Control
Control can be applied to all of the functional blocks mentioned above and is thus represented as a transversal functional block. It is necessary to coordinate different systems internal to the device, as well as to optimise the power conversion from the waves. It may also be required to limit power conversion in order to protect the equipment under adverse conditions, such as storm event or fault conditions.

Figure 8.2 shows the functional structure developed at an initial of the research project and refined by the author of this thesis prior to the launching of the second survey. The

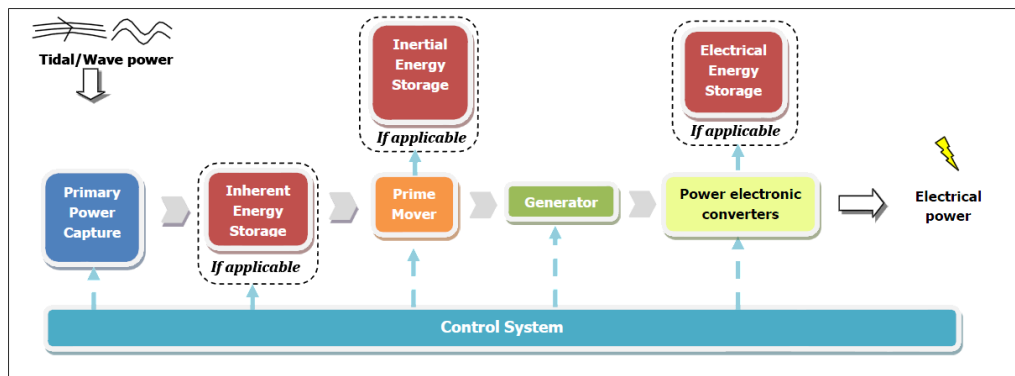


Figure 8.2: Generic model outline

inertial energy storage block is represented in parallel with the prime mover block rather than in series with it, as it was previously presented in the first survey. The modelling in series may have suggested that the energy was stored in a storage component located between the prime mover and the generator, similarly to the inherent energy storage. However, as the energy at this stage is actually stored in the rotation of the prime mover itself, it is preferable to model this block in parallel with the prime mover block. Similarly, the electrical storage block is represented in parallel with the power electronics block. The blocks which may involve some means of control are circled in black. The inertial energy storage at this stage is considered as passive, as opposed to actively controlled, as it may be the case for a majority of devices.

8.3 Survey results

8.3.1 Power optimisation/limitation

A majority of both tidal and wave devices have some means for optimising and/or for limiting power conversion as shown in Figure 8.3. In the case of tidal devices, all of them have optimisation means and 12 out of 13 also have power limitation means. Among the 22 wave energy devices, 19 have optimisation means and 20 have the capability to limit their power outputs.

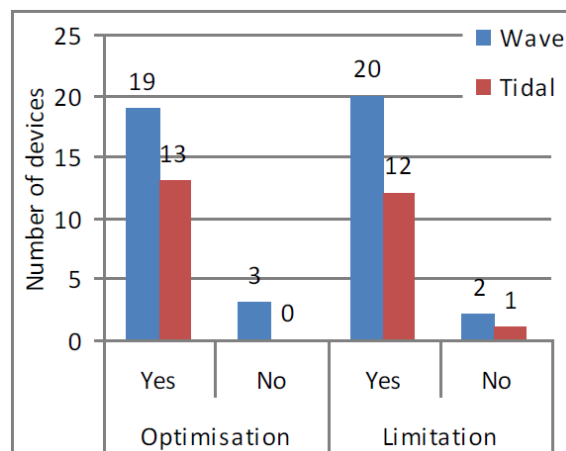


Figure 8.3: Power optimisation/limitation means

In practice, power limitation can be physically implemented in many different ways. However, it may be modelled at a very simple level by integrating an upper power limit

to each block, above which the output power is kept constant to this limit regardless of the input power magnitude. It is also important to model the response time of the power limitation mechanism, e.g. blade pitching, and any constraints that may exist on the peak energy that can be dissipated, e.g. in a dump load. Numerical values for the power limits may be supplied directly by the developers directly, or may need to be calculated from other parameters such as maximum fluid pressures or flows, which may however prove to be more complex to achieve. Alternatively, it may be possible to minimise the efficiency of the primary power capture element, for instance by varying the blade angle in tidal turbines or by de-tuning a wave device as explained in Section 8.3.3.

Considering that power optimisation strategies are very diverse, they may be more complex to implement in a generic model. They are usually applied to the following stages:

- primary power capture: optimising the conversion between wave power and primary mechanical or fluid power by adapting the primary power capture element to changing sea conditions, for instance by tuning the device motion to the dominant wave frequency. This type of optimisation is usually referred to as “tuning”.
- prime mover: optimising the conversion between the primary mechanical/fluid power and the prime mover power, for instance by controlling the input fluid flow to a hydraulic motor or varying the rotational speed of an air turbine.
- prime mover/generator: optimising the conversion between mechanical and electrical power, by controlling the interaction between the magnetic fields of the rotor and of the stator.

Optimising the power conversion may also be applicable at the storage stage by controlling the charge/discharge rates of the storage unit(s) appropriately in order to minimize the charge/discharge losses respectively, for instance to limit friction losses in a fluid accumulator. However, although Figure 8.4 shows that some developers do control these rates, it is still unclear if they do so for power conversion optimisation or for other purposes, e.g. limiting mechanical constraints on the storage means.

Optimisation may be modelled using either time series data sets at different control operating points or curves of optimum efficiencies with respect to sea conditions. Depending on the stage at which optimisation is applied, this data should be representative of either the optimum efficiencies at the primary power capture stage, or of the prime mover/generator speed or torque optimum operating points.

It must be borne in mind that this optimum efficiency data must be representative of the conditions in which the ocean energy device is operating, as imposed by the control strategies. Basing the model on average efficiencies of a part of the device (e.g. primary power capture element) operated in a stand-alone mode, thus excluding the influence of the other parts of the device may not prove to be sufficiently accurate. For instance, in the case of tidal turbines using control strategies similar to those used for wind turbines, several operating points may exist for a single value of tidal flow speed because of the multiplicity of pitch angle/rotor speed configurations. However, control strategies may exclude some of these potential operating points from the range of operation of the device, e.g. prime mover speed restricted to a certain range for given sea conditions, etc. Hence, it is important that the efficiency data provided by the developers corresponds to the optimum efficiency at the operating points chosen with respect to the control strategies.

Optimum efficiency data sets or curves can be selected discretely within the model depending on a range of inputs such as sea conditions (e.g. tidal flow speed, wave frequency/height), or prime mover/generator speed and/or torque. At the primary power capture stage, these efficiency values or curves might be supplied by developers of non-direct-drive systems (i.e. including some sort of hydraulic or pneumatic power) in terms other than power, for instance as pressure or flow, and may need then some conversion work to be implemented in the model. The results of the first survey demonstrated that the average efficiencies of the primary power capture element and of the prime mover are widely available from developers. However, it is still unclear whether this data comes from tests of the primary power capture element or of the prime mover system performed in stand-alone mode, or whether the tests were conducted on the entire ocean device, thus including the impact of control strategies.

If the control parameters vary sufficiently slowly compared to the typical duration of the power system simulations (i.e. not exceeding 30 seconds for wave devices and up to 10 minutes for tidal devices), they can be considered as constant. Hence, the corresponding control strategy does not need to be represented in the generic model with a high level of detail. However, if it appears that the control parameters may vary significantly during the simulations, then it must be modelled with a higher level of detail, but it may be acceptable to utilise average efficiencies at discrete control operating points. Finally, if the control variables vary rapidly, as for instance in very non-linear wave-to-wave control, modelling the influence of the control system on the device power output may become significantly more complex. In this case as well, using data sets indicating the averaged effect of the control variable mean value may remain the best solution, particularly given the confidentiality issues surrounding control strategies.

8.3.2 Actively-controlled parameters

The abbreviations used in the graphs of this section are the following:

FP	Primary fluid pressure
FFR	Primary fluid flow rate
IPS	Minimum input power threshold for energy storage
SCR	Storage charge rate
SDR	Storage discharge rate
Q	Reactive power
SP	Prime mover speed
TQ	Prime mover/generator torque

Figure 8.4 shows the results regarding the actively-controlled parameters in ocean devices. Questions on storage control were based on a simplified storage means model consisting of controllable charge and discharge rates, as well as on an input power threshold above which energy is absorbed and below which energy is released from the storage means.

A large majority of the 13 tidal devices control the prime mover speed as well as the prime mover/generator torque. The absence of storage means for most tidal energy devices explains why control of either the minimum input power threshold for storage (IPS), of the storage charge (SCR) or discharge rates (SDR) is marginal for those devices. Reactive power control (Q) will be discussed later in this section.

Wave devices usually control a larger number of parameters than tidal devices which

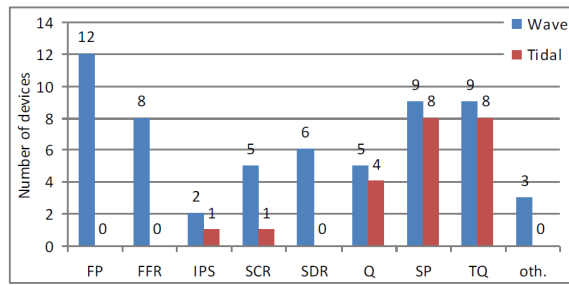


Figure 8.4: Actively-controlled parameters

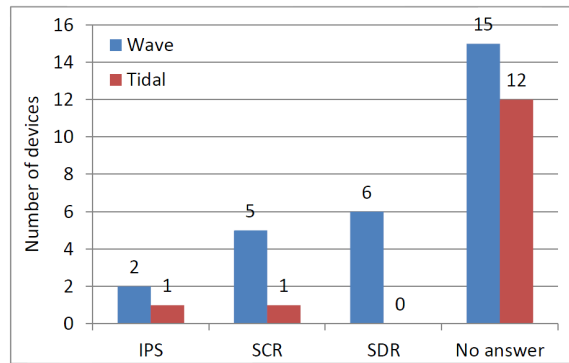


Figure 8.5: Control of IPS, SCR and SDR

is confirmed by this survey. This difference stems from the fact that some form of fluid power is involved in a majority of wave devices, which present thus a more complex design, whereas tidal devices are predominantly direct-drive systems with fewer mechanical parts or energy conversion stages. In addition, energy storage means of significant capacity are likely to be implemented in wave devices rather than in tidal devices which generally have a much smoother power profile.

Storage control

Figure 8.5 shows the results regarding control at the storage stage extracted from Figure 8.4. A large majority of tidal device developers have not answered this question, as their device does not include some means of storage. However, it is interesting to note that this question was not answered either by 15 wave device developers out of the 21 whose device includes storage. It may be assumed from these results that storage is not controlled actively in a majority of devices. However, when it is, the storage charge and discharge rates are both controlled, as may it be expected.

Reactive power control

Figure 8.4 showed that 5 wave devices out of 22 and 4 tidal devices out of 13 control reactive power. However, the use of either fully or partially-rated power electronic converters is likely to be required for a number of reasons, for instance for enabling variable speed operation, improving the device fault ride-through capability, and provide voltage control among others. Hence, the actual proportion of ocean devices controlling reactive power should be greater than the figures given above.

The existing models of reactive power control systems implemented in wind turbines models may be used for ocean devices as well. Should they prove not to be adequate,

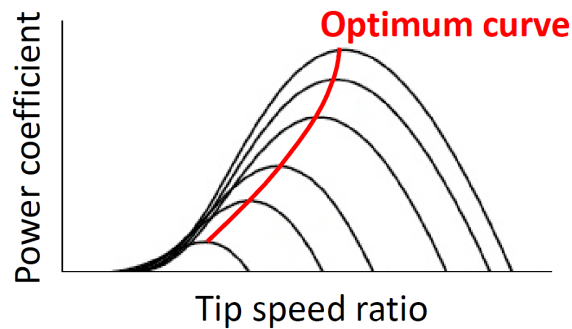


Figure 8.6: Optimum operating curve

they may at least constitute a good starting point for the development of reactive power control models for ocean energy applications.

Prime mover/generator speed and torque

The last controlled variables addressed in Figure 8.4 are the prime mover/generator speed and torque. A large number of wave and tidal devices, more precisely 9 wave devices out of 22 and 8 tidal devices out of 13, control at least one of these variables.

One question posed to the developers regarded their ability to provide some sort of optimum operation curve based on average values of optimum efficiencies representing the response of the prime mover/generator system for a range of input power conditions or any parameter related to this (e.g. current speed, wave height, etc.). This type of curves is already used for solar and wind energy applications. In the case of wind energy, the maximum power point tracking (MPPT) control consists of adapting the rotational speed of a wind turbine as well as its pitch angle to optimise the power extraction from the wind. As shown in Figure 8.6, the power efficiency of the turbine for a given pitch angle is optimum for a given tip speed ratio (black curves). Hence, both the rotational speed and the pitch angle are thus adapted as a function of the wind speed in order to maximise the turbine efficiency. Hence, the complex control strategy of a wind turbine can be represented relatively simply by an optimum operation curve shown in red in Figure 8.6.

A large majority of the 10 tidal devices controlling prime mover/generator speed and/or torque actually uses a maximum power tracking curve (describing either the electrical power or torque as a function of the prime mover speed), as shown in Figure 8.7a. This ability to express the device control strategy in the form of a simple power or torque-speed curve will greatly facilitate its implementation in a generic model.

However, the characterisation of optimum efficiencies with respect to input power/torque or sea conditions is more complex for wave devices, as expected from the varying nature of the input resource. As a result, few wave developers (4) of the 12 whose device controls either prime mover/generator speed or torque can provide some sort of power tracking curve as illustrated in Figure 8.7b. Considering the complexity to represent the efficiency of the generator when it undergoes severe input power variations as in the case of most oscillating wave energy devices, these curves might actually consist of steady-state efficiency curves provided by generator manufacturers. Although representing incompletely the generator's response under very dynamic conditions, they could be used at a first stage in the absence of more precise curves.

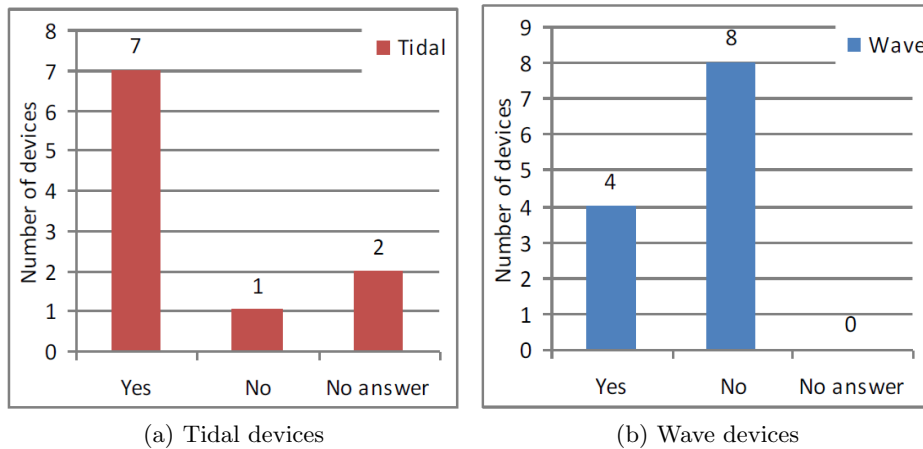


Figure 8.7: Use of some sort of maximum power tracking curve

8.3.3 Tuning

Introduction

Considering the current lack of guidelines regarding the dynamic modelling of ocean devices, it is still unknown whether power system stability studies will be performed for changing sea conditions. To date, grid operators do not require dynamic models for wind turbines to simulate the effect of wind speed variations on their power outputs, as mentioned in the state-of-the-art.

It is important to bear in mind as well that the tidal current speed is unlikely to vary significantly over 10 minutes, which corresponds to the maximum simulation duration usually performed for power system stability studies. Hence, the adaptation of tidal devices to changing sea conditions should not be implemented in a generic model. This section will thus address wave devices exclusively. As regards these devices, simulating constant wave conditions is irrelevant in the case of oscillating wave devices tuning on a wave-to-wave basis. The term “tuning” qualifies usually the control strategies intended to vary the natural frequency of an oscillating wave device as a function of the dominant (or instantaneous) wave frequency in order to achieve resonance. In this thesis, this definition is broadened to define the optimisation of the primary power capture element of any wave device to changing sea conditions (wave frequency/height). De-tuning, meaning reducing the efficiency of the primary power capture element, can also be used by a device to limit the power extraction from the sea in adverse conditions.

Figure 8.8 shows that a large majority of the 22 wave devices are tuneable. In practice, tuning to new prevailing sea conditions may be achieved in many different ways and on various timescales. The means by which a device transforms from one tuned state to another is highly dependent on its own geometric, hydrodynamic and mechanical characteristics, as well as on its control strategies, both of which are very device-specific. Modelling accurately enough the influence of tuning on the power output of a wave device may thus represent one of the main challenges of generic modelling of ocean devices.

It is proposed to model the process of tuning in two phases as illustrated in Figure 8.9. The detection of new sea conditions is assumed to occur at time t_0 . If these detected new sea conditions are maintained for a duration T_d (called “decision time”), the control system of the ocean device, which is still tuned according to the previous sea conditions

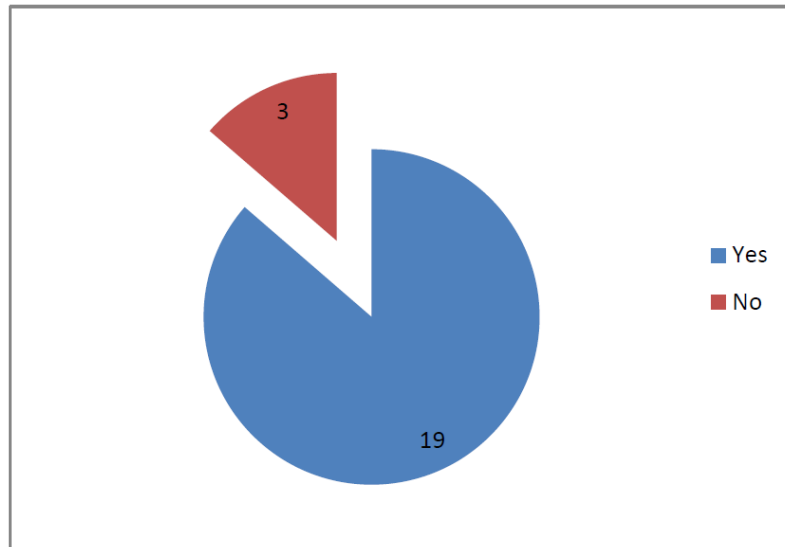


Figure 8.8: Ability to tune to prevailing sea conditions

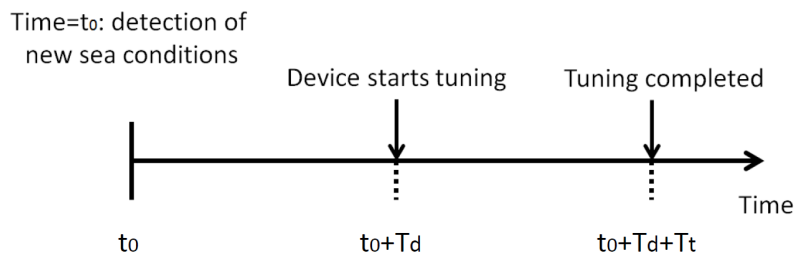


Figure 8.9: Tuning phases

between time t_0 and time T_d , starts adapting its tuning parameters. However, the adaptation to the new sea conditions cannot be considered as instantaneous in most cases and a certain period of time T_t (“tuning time”) is necessary for tuning to be completed. At time $t = t_0 + T_d + T_t$, the device is fully adapted to the new sea conditions.

The following sections detail the answers of the developers regarding the relevance of this representation of tuning compared to the tuning strategy of their device, as well as their ability to provide numerical values for the decision and tuning times T_d and T_t .

Decision time T_d

A majority of wave devices can tune to new wave conditions almost instantaneously as depicted in Figure 8.10 with the label “I”. An equal number claim tuneability after a time delay T_d . A small number of devices tune after a specific number of waves N .

Figure 8.11 shows that tuning delay is linked only to a decision time T_d for a majority of non-instantaneously tuneable devices. Some devices (3) tune according to both time T_d and a number of waves, N . However, only one device tunes according to the number of waves N only. Hence, the predominant reaction is either instantaneous or relying on a parameterisable time delay.

During the decision time T_d , no change is made to the characteristics of the device, such as blade angle or damping level. However, as the sea conditions have changed them-

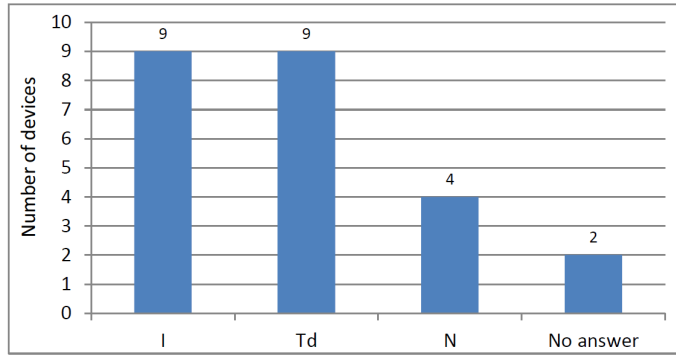


Figure 8.10: Decision parameters

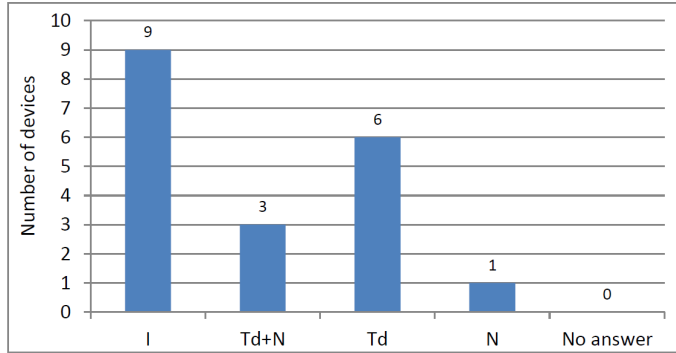


Figure 8.11: Decision parameters (decoupled)

selves, the device is no longer tuned optimally and hence its efficiency decreases. The non-optimal efficiency can be selected from efficiency curves or efficiency maps with respect to the new sea conditions. This highlights that data at both tuned and de-tuned states may be necessary for parameterising a generic model.

Among the 9 wave devices whose tuning strategy is based on a decision time T_d , numerical values can be provided for 8 devices, as shown in Figure 8.12. If time T_d is not constant, an average value may be chosen. As regards the delay time as expressed in number of waves N , 3 wave developers out of 4 can also provide numerical values for this parameter. However, as mentioned earlier, basing the time delay on a decision time T_d seems more suitable than basing it on a number of waves N as this former approach seems predominant.

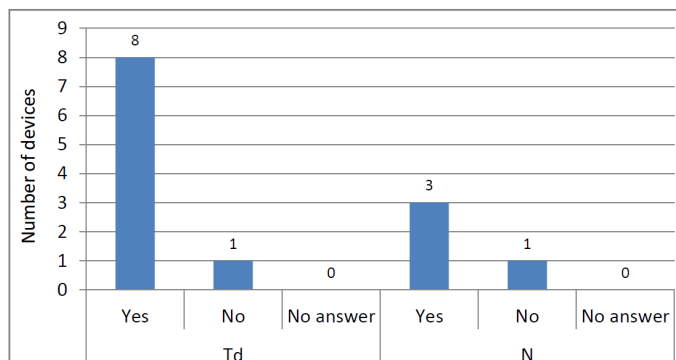


Figure 8.12: Ability to provide numerical values for T_d and N

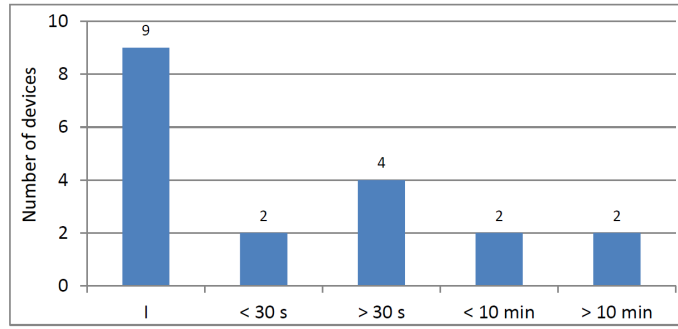


Figure 8.13: Timescale of decision time T_d

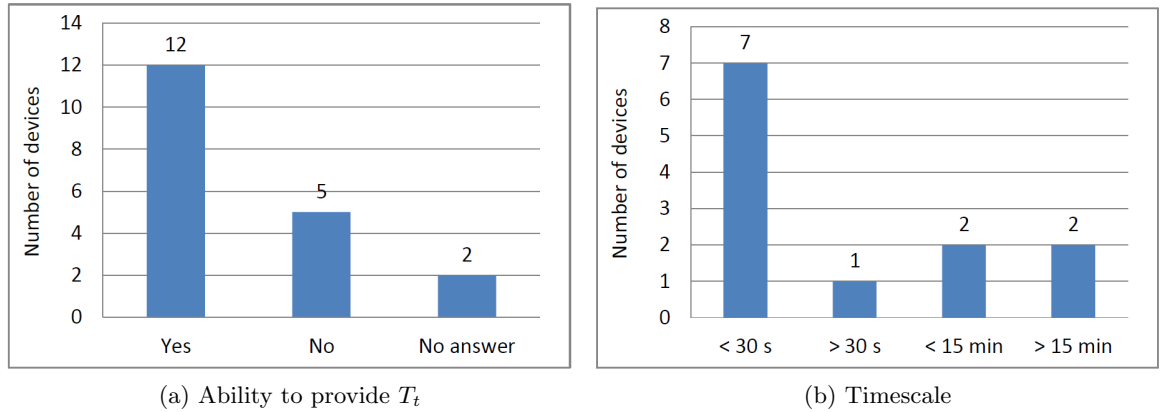


Figure 8.14: Tuning time T_t

The decision time T_d ranges from close to zero (almost instantaneous) to shorter than 30 seconds for more than half of the wave devices, as shown in Figure 8.13. Considering that this time is shorter than the typical simulation time frame for wave energy applications, this phase during which the device is de-tuned compared to the wave conditions should be implemented in a generic model if changing sea-states are taken into account in power system stability studies.

Tuning time T_t

A majority of developers whose device is tuneable, more specifically 12 wave developers out of 19, can provide a numerical value for the tuning time T_t , as illustrated in Figure 8.14a. The tuning time T_t is shorter than 30 seconds for most devices, as shown in Figure 8.14b. This means that the phase during which the device tunes to the new wave conditions should be implemented in a generic model. However, this may constitute a very complex task, as the behaviour of each device may be very specific and as the number of data required for its modelling may be considerable.

Two tuning types must be distinguished: mechanical and electrical tuning. Electrical tuning via generator control will typically be significantly faster in response than via control of mechanical elements. Developing generic control strategies regarding electrical tuning via generator control should require a limited amount of programming work as detailed generator models are already provided within the power system simulator packages. However, this would be different for the devices using mechanical elements to achieve tuning, which may be generically represented by means of modifying the efficiency of the

primary power capture element.

Two options for implementing this time delay in the model may be considered depending on the value of T_t . A first option is proposed for quickly-tuning devices, for instance on a wave-to-wave basis. For these devices, it is recommended that the device efficiency is maintained at the de-tuned efficiency for $t_0 + T_d \leq t \leq t_0 + T_d + T_t$ and then changed to the optimum efficiency with respect to the new sea conditions once the tuning time has elapsed. For devices whose tuning time is longer than few seconds, it may be relevant to include the evolution of the device efficiency over the tuning time. It is proposed that this efficiency is approximated linearly over period T_t with respect to the efficiency of the initial de-tuned state and of the final optimally tuned state.

Summary

In summary, a large number of wave devices start adapting, and achieve tuning to new wave conditions in less than 30 seconds. This means that the behaviour of the wave devices during the time t_0 when new sea conditions are detected and the time $t_0 + T_d + T_t$ when tuning is achieved must be modelled. However, this may constitute a very complex task, as the behaviour of each device may be very specific and as the number of data required for its modelling may be considerable.

Alternatively, it may be observed that the instantaneous tuning, corresponding to the case where both T_d and T_t are approximately equal to zero, represents the worst case scenario from a power quality perspective, as power peaks of maximum amplitude are generated in this case. However, it may give a relevant insight into the level of disturbance which a wave farm may have on the grid. Hence, it may be sufficient at a first stage to model wave devices as tuning instantaneously. This would reduce the amount of data required for the generic model, as only data on the optimum efficiency of the device as a function of the wave conditions would be necessary. As regards tidal devices, considering that the current speed is unlikely to vary significantly over the maximum simulation duration with respect to power system stability studies, tuning should not be modelled in this case.

8.4 Conclusions

This chapter detailed the updated results of a developer survey conducted in the frame of a research project led by the OES-IA. This survey focused on the control strategies used in ocean devices and investigated whether it was necessary to implement them in a generic model. The answer to this question is based on the comparison between the response time of these control strategies and the typical simulation time frame with respect to power system stability studies.

The results presented in Chapter 7 demonstrated that no detailed generic model was necessary to evaluate the flicker level generated by a wave farm, as it could be estimated with a high level of accuracy by means of sinusoidal voltage time series. Hence, the simulation time frame can be reduced to 30 seconds in the case of wave energy applications which corresponds to the typical duration of simulations with respect to power system stability studies. Consequently, this reduces also considerably the modelling work required to enable the accurate simulation of a wave device behaviour. As regards tidal devices, considering that the tidal current speed is unlikely to vary over 10 minutes (which corresponds to the duration required for performing flicker analyses), no highly detailed model

should be required. This hypothesis seems all the more probable that, to date, grid operators do not require dynamic models for wind turbines to simulate the effect of wind speed variations on their power outputs.

Most ocean devices have some sort of power limitation means, which may be modelled at a very simple level by integrating an upper power limit to any functional block of the generic model, above which the output power is kept constant to this limit regardless of the input power magnitude. It is also important to model the response time of the power limitation mechanism. Alternatively, it may be possible to minimise the efficiency of the primary power capture element, for instance by varying the blade angle in tidal turbines or by de-tuning a wave device. In this case, data sets on sub-optimal efficiency of the devices may be necessary.

Most devices include also control strategies for optimising the power conversion. In order to model these control strategies, the concept of an optimum operation curve or data sets was introduced in the survey. It consists of representing the optimal operation of a device in the form of a curve linking the sea conditions to a device variable, such as power, prime mover speed, etc. In this manner, the control strategies used in a device may be summarised in a form easily implementable in a generic model. This type of approach seems suitable for tidal devices, as the operation of most of them can be represented by a maximum power point tracking (MPPT) curve linking the prime mover speed to the sea conditions. However, this is not the case for wave devices, as may be expected from the varying nature of the input resource. It seems possible to use as an alternative data sets or curves on the optimum efficiency of a wave devices as a function of the wave conditions, as most developers have the ability to provide these [46].

As regards oscillating wave devices, the optimisation of the power extraction is usually performed by tuning the devices as a function of the dominant (or instantaneous) wave frequency. A representation of tuning, which was presented in this survey, consists of defining two time delays T_d and T_t which correspond respectively to the time intervals between the detection of new sea conditions and the beginning of tuning, and the beginning of tuning and the moment when tuning is achieved. It was mentioned that modelling this type of control strategy may constitute a very complex task, as the behaviour of each device may be very specific and as the number of data required for its modelling may be considerable. Hence, it is proposed to model all wave devices as instantaneously tuneable. Although this represents a worst case scenario from a power quality perspective, this approach should give a reasonable insight into the level of disturbance which a wave farm may have on the grid.

As regards control strategies in terms of reactive power or applied at the generator stage, the existing models implemented in wind turbine models may be used for ocean devices as well. Should they prove not to be adequate, they may at least constitute a good starting point for the development of reactive power control models for ocean energy applications.

In summary, the data required for implementing the control strategies of ocean devices are the following:

- data sets on the optimal operation of a device, for instance in the form of a maximum power point tracking (MPPT) curve, or in the form of optimum efficiencies as a function of the sea conditions

- power limits and response time corresponding to the power limitation mechanism, if any. In the case where power limitation is implemented by decreasing the efficiency of the primary power capture element, data sets on the sub-optimal efficiency of a device as a function of the sea conditions would be necessary.

Chapter 9

Conclusions

The work presented in this thesis covers four major topics of research related to the grid integration of wave energy. More specifically, the grid impact of a wave farm on the power quality of its local network was investigated. Two estimation methods were developed regarding the flicker level Pst generated by a wave farm in relation to its rated power as well as in relation to the impedance angle Ψ_k of the node in the grid to which it is connected. The electrical design of a typical wave farm design was also studied in terms of minimum rating for three types of costly piece of equipment, namely the VAR compensator, the submarine cables and the overhead line. The power losses dissipated within the farm's electrical network were also evaluated. The feasibility of transforming a test site into a commercial site of greater rated power was investigated from the perspective of power quality, and of cables and overhead line thermal loading. Finally, the generic modelling of ocean devices, referring here to both wave and tidal current devices, was investigated. The following sections summarise the contributions of this thesis to these fields of research.

9.1 Impact of a wave farm on the power quality of its local network

Major challenges regarding the grid impact assessment of a wave farm from a power quality perspective were identified in the state-of-the-art. Prior to this thesis, it was relatively difficult to draw conclusions from the limited number of existing case studies as they present important differences regarding several parameters which are expected to have a significant influence on power quality. In addition, most existing studies are based on numerical models of wave devices which have not been compared against experimental measurements.

The relatively fragmented level of knowledge regarding the grid impact of a wave farm was the reason why two comprehensive case studies, whose results were presented in Chapters 4 and 6, were conducted as part of this thesis. The studies were greatly facilitated by the availability of experimental electrical power time series data generated in the framework of a European FP7 project entitled "CORES". As these time series were generated at a high temporal resolution of 0.1 s, they were scaled and used directly for power system simulations. In order to study the flicker generated by the wave farm, a flickermeter compliant with the IEC standard 61000-4-15 was designed for the purpose of this thesis. In addition, a simplified load flow programme based on the Newton-Raphson algorithm was developed in order to provide a sanity check of the results obtained with the power system simulator PowerFactory. The case studies investigated the influence on power quality of the parameters which are described in the following paragraphs.

9.1.1 Short-circuit ratio and impedance angle Ψ_k

In most of the existing studies, the grid impact assessment is performed for wave farms connected to nodes in the grid having extreme short-circuit ratios (either very low or very high) and different impedance angles Ψ_k . However, the use of different values for both the short-circuit ratio and the impedance angle prevented the direct comparison of the results. In order to fill this gap, the case studies presented in this thesis were performed for typical ranges of the short-circuit ratio and of the impedance angle Ψ_k .

9.1.2 Power quality criteria addressed

Different power quality criteria were addressed in the existing case studies and the grid compliance of the wave farm was assessed based on the requirements defined in different grid codes. In this thesis, this assessment is based on three power quality criteria which are intended to capture the impact on the network of fluctuating power sources such as wave farms. These criteria are the amplitude of the voltage step induced by the sudden disconnection of the wave farm, the maximum and minimum voltages as well as the flicker level *Pst*. The extreme values reached by these variables were compared to the most permissive as well as to the most stringent limits specified by several grid operators in order to perform a grid compliance study which is representative of the requirements enforced by a large number of grid operators around the world. These limits were identified as a result of a detailed review of different grid codes, recommendations and standards.

9.1.3 Farm orientation and device layout

The influence on power quality of the farm orientation compared to the dominant wave direction as well as the device layout within the farm was investigated. Results showed that in farms composed of linear arrays of devices, the farm orientation has a very significant influence on power quality while the influence of the device layout is far more limited.

9.1.4 Sea-state characteristics

Most existing studies being based on a single sea-state, this thesis presented results based on five sea-states. This criteria proved to have a very significant influence on the grid impact of a wave farm.

9.1.5 Additional parameters

The influence on the power quality of two additional parameters which are also expected to have a significant impact on power quality was investigated. They consist of the generator speed control mode and of the power factor applied at the point of common coupling.

The results confirmed that the variable speed mode is an efficient means for reducing the flicker generated by a wave device compared to the fixed speed mode, as is the case for wind turbines. To date, no study had compared quantitatively these two control strategies in the case of wave energy applications. By presenting results regarding the two modes of operation, this thesis contributed in filling this gap. The results showed also that, although the variable speed mode may help in reducing the voltage fluctuations, it may be useless when the average voltage is already over/under, or close to, the allowed voltage limits. In this case, power factor control may be used in a complementary manner. The conclusions are similar concerning the use of collective storage means.

The value of the power factor applied at the point of common coupling constitutes also one of the main differences among the existing studies. Based on this observation, it was decided to perform studies for the typical range of power factor mandated by grid operators. The results demonstrated that this control strategy is efficient for reducing the amplitude of the voltage fluctuations and consequently the flicker level induced by a wave farm. However, the cost of the VAr compensation equipment being dependent on its rating, relying on this control strategy only may decrease the economic viability of a project, especially for wave farms operated at a relatively low voltage as it will be the case at a first stage. Hence, it was shown that it may be relevant to use this control strategy in a complementary manner with storage in the form of generator variable speed control or in the form of dedicated storage means.

9.1.6 Results

The results of the case studies showed that flicker may be a major issue for the test sites connected to a weak grid, especially in the Republic of Ireland where the enforced limits are extremely stringent. It was highlighted that the test site farms are likely to be structured in linear arrays in order to enable the performance monitoring of each device under the best sea conditions. These conditions constitute a worst case scenario compared to the case where devices may be laid out in a more compact shape, such as a square or a rectangle, as it would be the case for a higher-rated, commercial wave farm. In addition, under- and over-voltage was demonstrated not to be an issue for a commercial wave farm rated up to 50 MW. The efficiency of mitigation means in the form of dedicated storage means, generator variable speed control or power factor control was found to be sufficient in most cases. Hence, it can be safely assumed that power quality issues will not constitute a limiting factor to the upgrade of a test site into a commercial site, provided that suitable mitigation strategies are applied.

9.2 Flicker estimation methods

The flicker summation law defined in the IEC standard 61000-3-7 was demonstrated to be inapplicable in the case of wave farms in Chapter 7. Hence, a method intended to estimate flicker for an increasing farm rated power was developed in this thesis. This method consists of representing any voltage profile as the product of a reference voltage profile by two scale factors. The results obtained through this method were compared to those obtained with dynamic simulations performed with PowerFactory and showed good agreement.

This method was also found to be very accurate for estimating the flicker level obtained at different impedance angles Ψ_k . Hence, considering that an additional estimation method in relation to the short-circuit level, which is applicable to wave farms, has already been defined in the IEC standard 61400-21, it is possible to estimate the flicker generated by a wave farm of a given rated power connected at a node of any short-circuit level and any impedance angle Ψ_k .

In addition, it was demonstrated that the estimation of the flicker generated by a wave farm whose generators are operated in fixed speed mode could be performed by means of an equivalent sinusoidal voltage time series whose frequency is equal to the energy period of the sea-state under consideration. In the case where the generators are operated in variable speed mode, the flicker level could be obtained from the power profile corresponding to the fixed speed mode which is filtered by a first order low-pass filter whose time constant τ_f corresponds to the inertia time constant of the system. As the results regarding the flicker level obtained with the variable speed mode and with the collective storage

means proved to be very similar, the determination of the minimum storage level which is required to mitigate any flicker issue may be performed by filtering the power profile corresponding to the fixed speed mode by a variable time constant τ_f and calculating the corresponding flicker level.

The estimation method is intended to facilitate greatly the grid connection studies which are routinely conducted by grid operators as part of any connection application process. This simplified method requires only a limited amount of data regarding the power generated by the farm which the wave device developers have the ability to provide without prejudice to the commercial confidentiality of their device. The grid operator would only need to determine a reference device layout and a reference farm orientation in order for the test site developers to provide data regarding the maximum, minimum and average active power obtained under these conditions for several sea-states. In the case where the generators are operated in variable speed mode, the power profile of the farm corresponding to a given rated power, short-circuit level and impedance angle is necessary. Alternatively, this power profile can be estimated from the power profile corresponding to the fixed speed mode which is filtered by the inertia time constant τ_f of the system.

9.3 Design of the farm's electrical network

The design of a typical wave farm's electrical network was investigated in Chapter 5. The minimum rating required from the VAr compensator was shown to be highly dependent on the length of the overhead line connecting the offshore substation to the point of common coupling. However, the influence of the length of the submarine cables on this rating is more limited, which is explained by the fact that, under the conditions considered in this work, the reactive power generation and absorption at play in the cables are of the same order of magnitude and act as opposite effects. Hence, it is recommended to connect a wave farm to a location where a sufficiently close connection point is available.

The losses dissipated in the farm's electrical network were also investigated. Operating the cables at 10 kV, as it is initially planned for the AMETS test site in Ireland, was shown to lead to excessive losses which may represent up to 9% of the generated electricity and which may render the test site significantly less profitable. Hence, it was recommended to operate these cables at 20 kV, as this reduces the percentage loss to a more acceptable level equal to 2.3% only.

Finally, a study focusing on the minimum rating required from submarine cables was presented. Contrary to the conventional rating estimation methods which are based on a constant current, the method developed in the framework of this thesis is based on the estimation of the thermal loading of the cable and takes into account the current fluctuations induced by the waves. The results obtained through this method showed that the maximum current is no longer a relevant criterion for the estimation of the minimum current rating required from a submarine cable. Conversely, the average current gives a reasonable insight of the minimum current rating as it was shown to range between 22% and 51% of the average current flowing through the cable.

9.4 Generic modelling of ocean devices

The last chapter of this thesis briefly investigated the generic modelling of ocean devices for power system studies. It detailed the updated results of a developer survey, in which thirty-five developers took part, and which was conducted as part of an OES-IA research

project which focused on the control strategies used in these devices. The survey was meant to complete the results of an initial survey focusing on the development of a generic structure common to most ocean devices. However, it was also demonstrated in this thesis that the flicker generated by a wave farm could be estimated by means of an equivalent sinusoidal voltage time series whose frequency is equal to the sea-state energy period. In the case where some means of storage is included in the energy conversion chain (for instance inertial storage when the generator is operated in variable speed mode) or in the farm in the form of collective storage means, the flicker level can be obtained from the power profile corresponding to the fixed speed mode which is filtered by a first order low-pass filter whose time constant corresponds to the inertia time constant of the system. Hence, this means that no detailed generic model is necessary for the flicker analyses in the case of wave farms. Consequently, the expected simulation time frame could be reduced to an order of magnitude of tens of seconds, which reduces also considerably the modelling work associated with the development of a fully dynamic generic model for wave devices, and in particular regarding the implementation of the control strategies used in these types of devices.

The results of this second survey showed that most devices used control strategies for power optimisation and limitation purposes. As regards oscillating wave devices, the optimisation of the power extraction is usually performed by tuning the devices as a function of the dominant (or instantaneous) wave frequency. A generic representation of tuning, which was presented in this survey, consists of defining two time delays T_d and T_t which correspond respectively to the time interval between the detection of new sea conditions and the beginning of tuning, and the time interval between the beginning of tuning and the moment when tuning is achieved. It was mentioned that modelling this type of control strategy may constitute a very complex task, as the behaviour of each device may be very specific and as the amount of data required for its modelling may be considerable. Hence, it is proposed to model all wave devices as instantaneously tuneable at first instance. Although this represents a worst case scenario from a power quality perspective, this approach should give a reasonable insight into the level of disturbance which a wave farm may have on the grid.

As regards tidal devices, it may seem suitable in this case to use an optimum operating curve. This would consist of representing the optimal operation of a device in the form of a curve linking the sea conditions to a device variable, such as power, prime mover speed, etc. In this manner, the control strategies used in a device may be summarised in a form easily implementable in a generic model. This type of approach seems suitable for tidal devices, as the operation of most of them can be represented by a maximum power point tracking (MPPT) curve linking the prime mover speed to the sea conditions.

Reactive power control is expected to be implemented in a large majority of devices as they are likely to require power electronic converters to be able to comply with grid operators' requirements such as fault ride-through, frequency response, voltage control and support during fault conditions. Hence, the existing models implemented in wind turbine models may be used for ocean devices as well. Should they prove not to be adequate, they may at least constitute a good starting point for the development of reactive power control models for ocean energy applications.

Power limitation was identified to be implemented, or planned to be, in most ocean devices. This may be modelled at a very simple level by integrating an upper power limit to any functional block of the generic model, above which the output power is kept con-

stant to this limit regardless of the input power magnitude. In addition, the model should also simulate that an ocean device shuts down above another higher absolute maximum limit, corresponding to storm conditions in the case of wave devices for instance. It is also important to model the response time of the power limitation mechanism. Alternatively, it may be possible to minimise the efficiency of the primary power capture element, for instance by varying the blade angle in tidal turbines or by de-tuning a wave device. In this case, data sets on the sub-optimal efficiency of the devices may be necessary.

In summary, the data required for implementing the control strategies of ocean devices should be provided in the form of data sets on the optimal operation of a device, for instance in the form of a maximum power point tracking (MPPT) curve for tidal devices, or in the form of optimum efficiencies as a function of the wave conditions for wave devices. The power limits and the response time corresponding to the power limitation mechanism, if any, should also be provided. In the case where power limitation is implemented by decreasing the efficiency of the primary power capture element, data sets on the sub-optimal efficiency of a device as a function of the sea conditions would be necessary.

9.5 Future work

In the early future, further studies will be conducted on the proportionality coefficient between the flicker level obtained without means of storage, either in the form of mechanical, hydraulic, electrical or inertial storage (i.e. variable speed mode) and the flicker level obtained when storage is available. It has been highlighted in Chapter 7 that a simple relation involving the inertia time constant τ_f of the wave device may exist between the flicker levels corresponding to these two levels of operation. Future work will investigate this topic.

An experiment will also be set up in order to generate data on the temperature profile of a submarine cable subject to a fluctuating current profile. These experimental results will then be compared to the results obtained with the method described in Chapter 5.

In the longer term, future work is intended to focus on the implementation of a generic model and on the validation of this model based on experimental data. The results of the case studies presented in this thesis will be used as a benchmark.

Appendix A

Estimation of the level of error on the short-circuit level and on the impedance angle

The method described in Chapter 4 which is intended to estimate approximately both the equivalent short-circuit level S_{SC} and the equivalent impedance angle Ψ_k at the high voltage side of the 20/38 kV transformer does not take into account the consumption of the loads between this node and the 110 kV (or 400 kV) connection point, as this data is usually unavailable.

However, this approximation induces only a negligible underestimation of both the short-circuit level S_{SC} and of the impedance angle Ψ_k for both the UK and Irish test sites, as demonstrated in this Appendix.

The network between the bus B_d (i.e. high voltage bus of the 20/38 kV transformer) and the closest 110 kV (or 400 kV) connection point is represented in Figure A.1.

The impedance $\bar{Z}_d = R_d + jX_d$ was assumed to be linearly distributed between the bus B_S and the 110 kV node named $B_{S_{110kV}}$. The individual consumption of the N_f feeders connected to the overhead line(s) is assumed to be mainly resistive and is represented by N_f parallel branches of impedance R_i . Information on this number N_f of feeders is usually unavailable. These resistances are assumed to be all equal and they will thus be referred to as R in the rest of the Appendix. The equivalent impedance of this network, excluding the short-circuit impedance $Z_{SC_{110kV}}$, is designated as $\bar{Z}_{eq} = R_{eq} + jX_{eq}$.

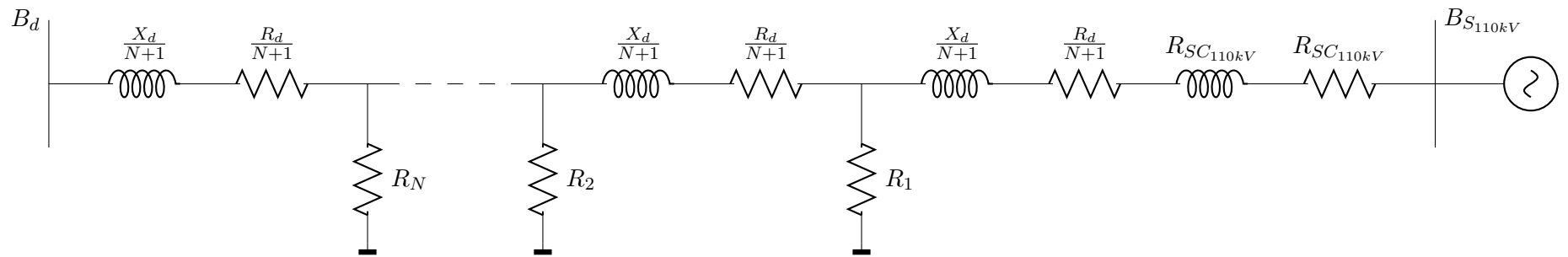


Figure A.1: Diagram of the network between the 110 kV and the 38 kV nodes (Ireland). The resistance $R_{SC_{110kV}}$ and the reactance $X_{SC_{110kV}}$ corresponds to the short-circuit impedance $Z_{SC_{110kV}}$ at the 110 kV node.

The equivalent resistance R_{eq} can be calculated branches to branches from bus $B_{S_{110kV}}$ towards bus B_S as:

$$R_{eq_i} = \left(\frac{1}{R_{eq_{i-1}}} + \frac{1}{R} \right)^{-1} + \frac{R_d}{N+1} \quad (\text{A.1})$$

$$\text{with } R_{eq_1} = \left(\frac{N+1}{R_d} + \frac{1}{R} \right) + \frac{R_d}{N+1} \quad (\text{A.2})$$

The resistance R of each of the N_f branches is calculated from the average power consumption P in the region considered. However, as this data was not available, the average power consumption per capita P_{inh} in regions similar to the west of Ireland and to Cornwall was investigated. It must be borne in mind that the test sites considered in this work are located off relatively rural regions, where the per capita energy consumption is significantly lower than in more industrialised areas.

The average power consumption in a French region with similar characteristics was found to be equal to 191 W/inh [111]. The resistance R can finally be calculated as:

$$R = \frac{V^2}{\frac{P_{inh}N_{inh}}{N_f}} = \frac{V^2N_f}{P_{inh}N_{inh}} \quad (\text{A.3})$$

where N_{inh} is the number of inhabitants in the region considered. In the case of the Belmullet test site, the overhead line connecting the closest 110 kV node located at Bel-lacorick to Belmullet supplies approximately 15,000 inhabitants according to the latest census [71]. In the case of the WaveHub, the line connecting the closest 400 kV connection point, which is located at the small village of Indian Queens, to Hayle was assumed to supply the entire population of Cornwall which is equal to 532,300 inhabitants [112]. As data on the number of feeders N_f connected to each of the overhead lines is usually not available, the error levels on both the short-circuit level S_{SC} and on the impedance angle Ψ_k were calculated based on a number of values for N_f ranging between 1 and 1000, which is assumed to include the actual value of N_f .

The short-circuit level $S_{SC_{eq}}$ which is calculated with the detailed method described in this Appendix can be expressed as a function of the short-circuit level S_{SC} calculated with the approximate method in Chapter 4 as:

$$S_{SC_{eq}} = (1 + \beta_{S_{SC}})S_{SC} \quad (\text{A.4})$$

where $\beta_{S_{SC}}$ is the proportion by which $S_{SC_{eq}}$ is underestimated. Developing this expression gives:

$$\frac{V^2}{Z_{eq}} = (1 + \beta_{S_{SC}}) \frac{V^2}{Z_d} \quad (\text{A.5})$$

which can be reduced to the following expression:

$$\begin{aligned} Z_d &= (1 + \beta_{S_{SC}})Z_{eq} \\ \sqrt{R_d^2 + X_d^2} &= (1 + \beta_{S_{SC}})\sqrt{R_{eq}^2 + X_{eq}^2} \end{aligned} \quad (\text{A.6})$$

As mentioned earlier, the consumption of the feeders is assumed to be purely resistive, hence the equivalent reactance X_{eq} is equal to X_d .

The proportion which the equivalent resistance R_{eq} represents compared to the resistance R_S is represented by a coefficient α defined as:

$$\alpha = \frac{R_{eq}}{R_d} \quad (\text{A.7})$$

The expression described in A.6 can hence be re-written as:

$$\sqrt{R_d^2 + X_d^2} = (1 + \beta_{S_{SC}}) \sqrt{\alpha^2 R_d^2 + X_d^2} \quad (\text{A.8})$$

which is equivalent to

$$R_d^2 + X_d^2 = (1 + \beta_{S_{SC}})^2 (\alpha^2 R_d^2 + X_d^2) \quad (\text{A.9})$$

Hence:

$$\beta_{S_{SC}} = \sqrt{\frac{R_d^2 + X_d^2}{\alpha^2 R_d^2 + X_d^2}} - 1 \quad (\text{A.10})$$

Considering that the impedance angle Ψ_k can be expressed as $\tan(\Psi_k) = \frac{X_d}{R_d}$, this last expression can be re-written as:

$$\begin{aligned} \beta_{S_{SC}} &= \sqrt{\frac{R_d^2 + R_d^2 (\tan \Psi_k)^2}{\alpha^2 R_d^2 + R_d^2 (\tan \Psi_k)^2}} - 1 \\ &= \sqrt{\frac{1 + (\tan \Psi_k)^2}{\alpha^2 + (\tan \Psi_k)^2}} - 1 \end{aligned} \quad (\text{A.11})$$

In similar fashion to the estimation of the error on the short-circuit level, the underestimation β_Ψ on the impedance angle Ψ_{keq} can be expressed as:

$$\begin{aligned} \Psi_{keq} &= (1 + \beta_\Psi) \Psi_k \\ \arctan\left(\frac{X_{eq}}{R_{eq}}\right) &= (1 + \beta_\Psi) \arctan\left(\frac{X_d}{R_d}\right) \\ \arctan\left(\frac{X_d}{\alpha R_d}\right) &= (1 + \beta_\Psi) \arctan\left(\frac{X_d}{R_d}\right) \end{aligned} \quad (\text{A.12})$$

Hence:

$$\beta_\Psi = \frac{\arctan\left(\frac{X_d}{\alpha R_d}\right)}{\arctan\left(\frac{X_d}{R_d}\right)} - 1 \quad (\text{A.13})$$

Both the error $\beta_{S_{SC}}$ on the short-circuit level and the error β_Ψ on the impedance angle depend on this latter parameter as well as on the coefficient α , which depends itself on the value of the individual resistance R . As mentioned earlier, calculations were performed for a number of branches N ranging between 1 and 1000, as well as for the values of the impedance angle Ψ_k corresponding to the WaveHub and to the Belmullet test site which are equal to 78.0° and to 69.2° respectively (including the short-circuit impedance corresponding to the 110 kV (400 kV) node). Coefficient α was found to range between 0.98 and 1 in all the cases considered. This confirms that, as expected, the approximate method described in Chapter 4 leads to a negligible level of error on the short-circuit level as well as on the impedance angle of both the WaveHub and the Belmullet test site. The

Test site	Error on $S_{SC}(\%)$	Error on $\Psi_k(\%)$
WaveHub	0.09	0.3
Belmullet	0.3	0.5

Table A.1: Error on the short-circuit level and on the impedance angle at the WaveHub and Belmullet test sites

results are presented in Table A.1.

In conclusion, the short-circuit level S_{SC} and the impedance angle Ψ_k , as estimated by means of the approximate method described in Chapter 4, can be considered as reliable.

References

- [1] J. Isaacs and R. Seymour. The ocean as a power resource. *International Journal of Environmental Studies*, 4(1-4):201–205, 1973.
- [2] K. Gunn and C. Stock-Williams. Quantifying the global wave power resource. *Renewable Energy*, 44(0):296 – 304, 2012.
- [3] G. Mørk, S. Barstow, A. Kabuth, and T. Pontes. Assessing the global energy potential. In *Proceedings of the OMAE2010 29th International Conference on Ocean, Offshore Mechanics and Arctic Engineering, June 6-11, Shanghai, China, 2010*.
- [4] IEA. Key world energy statistics. Technical report, 2012.
- [5] A. Cornett. A global wave energy resource assessment. In *Proceedings of the 18th Offshore (Ocean) and Polar Engineering Conference (ISOPE), Vancouver, Canada, 2008*.
- [6] T. Thorpe. A brief review of wave energy. Technical report, a report produced for the UK Department of Trade and Industry, 1999.
- [7] Pelamis. P-750 wave energy converter, available at <http://ec.europa.eu/ourcoast/download.cfm?fileID=965>.
- [8] S. Bartow et al. *Ocean Wave Energy, Current Status and Future Perspectives*, chapter The wave energy resource. Elsevier, 2008.
- [9] Illustration of trade winds, http://en.wikipedia.org/wiki/Trade_wind, accessed in March 2013.
- [10] Aqua-RET E-learning Tool, <http://www.aquaret.com/>.
- [11] J. Falnes. *Ocean Waves and Oscillating Systems: Linear Interactions Including Wave-Energy Extraction*. Cambridge University Press, 2002.
- [12] L.H. Holthuijsen. *Waves in Oceanic and Coastal Waters*. Cambridge University Press, 2007.
- [13] B.G. Cahill and A.W. Lewis. Wave energy resource characterization of the Atlantic Marine Energy Test Site. In *Proceedings of the 9th European Wave and Tidal Energy Conference Series, Southampton, UK, 2011*.
- [14] Alain Clément, Pat McCullen, António Falcão, Antonio Fiorentino, Fred Gardner, Karin Hammarlund, George Lemonis, Tony Lewis, Kim Nielsen, Simona Petroncini, M.-Teresa Pontes, Phillippe Schild, Bengt-Olov Sjöström, Hans Christian Sørensen, and Tom Thorpe. Wave energy in Europe: current status and perspectives. *Renewable and Sustainable Energy Reviews*, 6(5):405 – 431, 2002.

- [15] N. Bellamy. The circular Sea Clam wave energy converter. In *Proceedings of the IUTAM symposium on Hydrodynamics of Ocean Wave-Energy Utilization, Lisbon, Portugal*, 1985.
- [16] Website of the WaveBob company, www.wavebob.com.
- [17] Website of the Pelamis Wave Power company, www.pelamiswave.com/.
- [18] Website of the Aquamarine Wave Power company, www.aquamarinepower.com/.
- [19] Website of the Ocean Energy company, www.oceanenergy.ie/.
- [20] Website of the Carnegie Wave Energy company, www.carnegiwave.com/.
- [21] Website of the Wave Dragon company, www.wacompany.net.
- [22] ENTSO-E. Network code on requirements for grid connection applicable to all generators (RfG), 26th June 2012.
- [23] WECC Wind Generator Modeling Group. Wind power plant power flow modeling guide. Technical report, WECC, May 2008.
- [24] A. Hansen and G. Michalke. Fault ride-through capability of DFIG wind turbines. *Renewable Energy*, 32(9):1594 – 1610, 2007.
- [25] T. Ackermann. *Wind Power in Power Systems*. John Wiley & Sons, 2005.
- [26] Website of DIgSILENT, www.digsilent.de/.
- [27] A. Robert and T. Deflandre. Guide for assessing the network harmonic impedance. In *CIREN 97 2-5 June*, number 438. IEE, 1997.
- [28] A. Blavette and J. MacEnri. *Electrical Design for Ocean Wave and Tidal Energy Systems*, chapter Grid integration: Power quality. The Institution of Engineering and Technology (IET), to be published in 2013.
- [29] IEEE. Recommended practice for monitoring electric power quality. *IEEE standard 1159-2009 (Revision of IEEE standard 1159-1995)*, pages 1–81, 2009.
- [30] E. Ossentjuk, C. Elink Sterk, and W. Strom van Leeuwen. Flicker-induced cardiac arrest in a patient with epilepsy. *Electroencephalography and Clinical Neurophysiology*, 20(3):257 – 259, 1966.
- [31] M. Bollen and I. Gu. *Signal Processing of Power Quality Disturbances*. John Wiley & Sons, 2006.
- [32] IEC. Standard 61000-4-15, TC/SC 77A, Electromagnetic compatibility (EMC) - part 4-15: Testing and measurement techniques - flickermeter - functional and design specifications, ed2.0 (2010-08).
- [33] C. Rong, J. Cobben, J. Myrzik, J. Blom, and W. Kling. Flickermeter used for different types of lamps. In *Proceedings of the 9th International Conference on Electrical Power Quality and Utilisation EPQU*, pages 1–6, October 2007.
- [34] B. Heffernan, L. Frater, and N. Watson. LED replacement for fluorescent tube lighting. In *Australasian Universities Power Engineering Conference, AUPEC*, pages 1–6, December 2007.
- [35] ESB. Distribution Code, version 2.0, 2009.

- [36] Eirgrid. Transmission forecast statement 2012-2018. Technical report, 2012.
- [37] National Grid. National Electricity Transmission System (NETS) Seven Year Statement. Technical report, 2011.
- [38] RTE - The French transmission operator, Presentation at the Power System Engineering Research Center (PSERC), Arizona State University, USA, 28th March 2007. Available online at http://www.pserc.wisc.edu/documents/publications/special_interest_publications/grid_reliability/.
- [39] J. Aubry. *Optimisation du dimensionnement d'une chaîne de conversion électrique directe incluant un système de lissage de production par supercondensateurs : application au houlogénérateur SEAREV*. PhD thesis, École normale supérieure de Cachan, France, 2011.
- [40] F. Sharkey, J. MacEnri, Bannon E., M Conlon, and K. Gaughan. Voltage flicker evaluation for wave energy converters - Assessment guidelines. In *Proceedings of the 4th International Conference on Ocean Energy, Dublin, Ireland, 2012*.
- [41] M. Santos, A Blavette, E. Tedeschi, D. O'Sullivan, and F. Salcedo. Case study on the benefits of energy storage for power quality enhancement: point absorber arrays. In *Proceedings of the 4rd International Conference on Ocean Energy, Dublin, Ireland, 2012*.
- [42] A. Nambiar, A. Kiprakis, and A. Wallace. Effects of array configuration, network impacts and mitigation of arrays of wave energy converters connected to weak, rural electricity networks. In *Proceedings of the 3rd International Conference on Ocean Energy, Bilbao, Spain, 2010*.
- [43] T. Brekken, H.T. Özkan-Haller, and A. Simmons. A methodology for large-scale ocean wave power time-series generation. *IEEE Journal of Oceanic Engineering*, 37(2):294–300, April 2012.
- [44] M. Molinas, O. Skjervheim, B. Sørby, P. Andreasen, S. Lundberg, and T. Undeland. Power smoothing by aggregation of wave energy converters for minimizing electrical energy storage requirements. In *Proceedings of the 7th European Wave and Tidal Energy Conference, Porto, Portugal, 2007*.
- [45] R. Alcorn. *Wave Station Modelling Based on the Islay Prototype Plant*. PhD thesis, Queen's University Belfast, UK, 2000.
- [46] D. O'Sullivan, D. Mollaghan, A. Blavette, and R. Alcorn. *Dynamic characteristics of wave and tidal energy converters & A recommended structure for development of a generic model for grid connection*. Technical report, A report prepared by HMRC-UCC for the OES-IA Annex III. [Online], Available: www.iea-oceans.org, 2010.
- [47] S. Lundberg. Electrical limiting factors for wind energy installations. Master's thesis, Chalmers University, Sweden, 2000.
- [48] J. Tande, G. Di Marzio, and K. Uhlen. System requirements for wind power plants. Technical report, SINTEF, 2007.
- [49] A. Nambiar, A. Kiprakis, and A. Wallace. Quantification of voltage fluctuations caused by a wave farm connected to weak, rural electricity networks. In *Proceedings of the 14th International Conference on Harmonics and Quality of Power (ICHQP), Bergamo, Italy, 2010*.

- [50] A. Blavette, D. O’Sullivan, T. Lewis, and M. Egan. Impact of a wave farm on its local grid: Voltage limits, flicker level and power fluctuations. In *Proceedings of the IEEE/MTS OCEANS12 Conference, Yeosu, South Korea*, 2012.
- [51] D. O’Sullivan, F. Salcedo, A. Blavette, M. Santos, and A.W. Lewis. Case studies on the benefits of energy storage for power quality enhancement: oscillating water column arrays. In *Proceedings of the 4th International Conference on Ocean Energy, Dublin, Ireland*, 2012.
- [52] IEC. Standard 61400-21, Wind turbines - part 21: Measurement and assessment of power quality characteristics of grid connected wind turbines, TC/SC 88, 2008.
- [53] R. Green and N. Vasilakos. The economics of offshore wind. *Energy Policy*, 39(2):496–502, February 2011.
- [54] IEC. Standard 60287-1-1, Electric cables - calculation of the current rating - part 1-1: Current rating equations (100 % load factor) and calculation of losses, ed.2.0, 12-2006.
- [55] S. Foss and R. Maraio. Dynamic line rating in the operating environment. *IEEE Transactions on Power Delivery*, 5, April 1990.
- [56] R. Adapa and D. Douglass. Dynamic thermal ratings: monitors and calculation methods. In *Proceedings of the IEEE Power Engineering Society Inaugural Conference and Exposition in Africa*, pages 163–167, 2005.
- [57] J. Hosek. Dynamic thermal rating of power transmission lines and renewable resources. *ES1002 : Workshop March 22nd-23rd*, 2011.
- [58] IEC. Standard 61000-3-7, Electromagnetic compatibility (EMC) - part 3-7: Limits - assessment of emission limits for the connection of fluctuating installations to MV, HV and EHV power systems, 2008-02-22.
- [59] J. Tissandier, A. Babarit, and A. Clément. Study of the smoothing effect on the power production in an array of SEAREV wave energy converters. *Proceedings of the Eighteenth (2008) International Offshore and Polar Engineering Conference, Vancouver, BC, Canada, July 6-11, 2008*, 2008.
- [60] Website of Siemens PTI. Release of PSSE version 32 (including generic wind models), https://www.pti-us.com/pti/software/psse/PSSE_32.cfm, accessed on 11th December 2012., 2009.
- [61] B. Ó Gallachóir and E. McKeogh. Wind energy and security of supply of the wind farm grid connection moratorium in Ireland. In *Report of the 40th International Universities Power Engineering Conference, 7-9 September, Cork, Ireland.*, 2005.
- [62] FERC. Order no. 2003, Appendix C, Standard large generator interconnection procedures (LGIP). Technical report, 2003. Accessible online: <http://www.ferc.gov/legal/maj-ord-reg/land-docs/order2003.asp>.
- [63] Y. Coughlan, P. Smith, A. Mullane, and M. O’Malley. Wind turbine modelling for power system stability analysis: A system operator perspective. *IEEE Transactions on Power Systems*, 22(3):929–936, August 2007.
- [64] E. Muljadi and A. Ellis. Validation of wind power plant dynamic models. In *Proceedings of the 2008 IEEE Power Engineering Society General Meeting Pittsburgh, Pennsylvania, July 20-24*, 2008.

- [65] J. Khan, G. Bhuyan, and A. Moshref. Potential opportunities and differences associated with integration of ocean wave and marine current energy plants in comparison to wind energy. Technical report, prepared by Powertech Labs for the OES-IA Annex III. [Online], Available: www.ica-oceans.org/, 2009.
- [66] J. Khan, A. Moshref, and G. Bhuyan. A generic outline for dynamic modeling of ocean wave and tidal current energy conversion systems. In *Power Energy Society General Meeting, 2009. PES '09. IEEE*, pages 1–6, July 2009.
- [67] D. Mollaghan, S. Armstrong, D. O’Sullivan, A. Blavette, and R. Alcorn. SEAGRID: A new dynamic modelling tool for power system analysis of ocean energy devices. In *Proceedings of the 4th International Conference on Ocean Energy, Dublin, Ireland, 2012*.
- [68] S. Armstrong, D. Mollaghan, A. Blavette, and D. O’Sullivan. An initialisation methodology for ocean energy converter dynamic models in power system simulation tools. In *Proceedings of the 4th International Universities’ Power Engineering Conference, London, UK, 2012*.
- [69] Website of technical committee (TC) 114: Marine energy - wave, tidal and other water current converters, http://www.iec.ch/dyn/www/f?p=103:7:0:::FSP_ORG_ID:1316.
- [70] Website of the Sustainable Energy Authority of Ireland SEAI. <http://www.seai.ie>.
- [71] Irish Central Statistics Office (CSO) . Census 2011-Population classified by area. Technical report, 2011.
- [72] ABB. *Technical data RESIBLOC^{®99Plus}, Efficiency comparison to standard transformers*, 2009.
- [73] SchneiderElectric. *Use and Maintenance of Oil-immersed Distribution Transformers, Elvim range*.
- [74] C. Bayliss and B. Hardy. *Transmission and Distribution Electrical Engineering*. 3rd edition, 2007.
- [75] J. Glover, M. Sarma, and T. Overbye. *Power System Analysis and Design*. Thomson Learning, 5th edition, 2008.
- [76] K. Kiessling, P. Peter Nefzger, J. F. Nolasco, and U. Kaintzyk. *Overhead Power Lines: Planning, Design, Construction*. Springer, 2003.
- [77] Standard EN 50160, Voltage characteristics in public distribution systems.
- [78] Website of the WaveHub. <http://www.wavehub.co.uk/>, accessed on 23/01/2013.
- [79] Website of the EMEC. <http://www.emec.org.uk/>, accessed on 23/01/2013.
- [80] Website of the bimep. <http://eve.es/web/Energias-Renovables/Energia-marina/BIMEP/>, accessed on 23/01/2013.
- [81] Website of the WestWave consortium. www.westwave.ie/.
- [82] F. Thiebaut, D. O’Sullivan, P. Kracht, S. Ceballos, J. López, C. Boake, J. Bard, N. Brinquete, J. Varandas, L.M.C. Gato, R. Alcorn, and A.W. Lewis. Testing of a floating OWC device with movable guide vane impulse turbine power take-off. In *Proceedings of the 9th European Wave and Tidal Energy Conference series, Southampton, UK, 2011*.

- [83] A. Babarit. Impact of long separating distances on the energy production of two interacting wave energy converters. *Ocean Engineering*, 37(8-9):718–729, 2010.
- [84] WavePlam. Wave energy: A guide for investors and policy makers. Technical report, 2009. Project funded under the Intelligent Energy Europe Programme.
- [85] BDEW. Technische Anschlussbedingungen für den Anschluss an das Mittelspannungsnetz (TAB Mittelspannung), 2008.
- [86] National Grid. The Grid Code, issue 4, revision 2, 2010.
- [87] System Utilisation Consultancy Group. Engineering recommendation P-28, Planning limits for voltage fluctuations caused by industrial, commercial and domestic equipment in the United Kingdom, 1989.
- [88] NORDEL. Nordic Grid Code, 2007.
- [89] Rules of detailed connection conditions to the electrical power network in Poland, 25/09/2000 (rozporządzenie ministra gospodarki z dnia 25 wrzesnia 2000, dziennik ustaw nr 85, poz. 957).
- [90] EdF. Contrat d'accès au réseau public de distribution pour une installation de production de puissance > 36 kVA raccordée en basse tension, Conditions générales, 2010.
- [91] Energinet. Technical regulation 3.2.5 for wind power plants with a power output greater than 11 kW.
- [92] DIgSILENT. User's manual, Network representation and calculation methods. Technical report.
- [93] US Navy. Navy issues new shore energy policy to achieve energy security goals. published on 7/10/2012, accessed on 24/10/2012. Website of the US Navy, <http://www.navy.mil/>.
- [94] T. Thiringer, J. MacEnri, and M. Reed. Flicker evaluation of the SeaGen tidal power plant. *Sustainable Energy, IEEE Transactions on*, 2(4):414–422, oct. 2011.
- [95] M. Santos, F. Salcedo, D. Ben Haim, J. Mendia, P. Ricci, J.L. Villate, J. Khan, D. Leon, S. Arabi, A. Moshref, G. Bhuyan, A. Blavette, D. O'Sullivan, and R. Alcorn. Integrating wave and tidal current power: Case studies through modelling and simulation. Technical report, A report prepared jointly by Tecnalia (Spain), Powertech Labs (Canada) and HMRC (Ireland) for the OES-IA. Available: www.iea-oceans.org, 2011.
- [96] Website of SEM-REV, <http://www.semrev.fr/en/>.
- [97] Senergy Econnect and National Grid. Round 3 offshore wind farm connection study. Technical report, 2008. Technical report prepared for the Crown Estate.
- [98] F. Sharkey, E. Bannon, M. Conlon, and K. Gaughan. Dynamic electrical ratings and the economics of capacity factor for wave energy converter arrays. In *Proceedings of the 9th European Wave and Tidal Energy Conference series, Southampton, UK*, 2011.
- [99] IEC. Standard 60287-2-1, Electric cables - calculation of the current rating - part 2: Thermal resistance - section 1: Calculation of thermal resistance, ed1.2 Consol. with am1&2, 05-2006.

- [100] Nexans. Data sheet, technical reference: 2XS(FL)2YRAA RM 12/20 (24)kV, 3 core XLPE-insulated cables with PE sheath and armoring, longitudinally and radially watertight, Accessed on 12th November 2012.
- [101] A. Laughton and D. Warne. *Electrical Engineer's Reference Book*. Elsevier Science, 2002.
- [102] Nexans. Data sheet, *Submarine cable 10kV, 6/10 (12)kV, 3 core Copper XLPE cable, Cu-screen, Al/PE-sheath, Armoring*.
- [103] Nexans. Submarine power cables, May 2008.
- [104] Universal Cable. Catalogue, XLPE insulated power cables.
- [105] MetEireann website. Climate averages and extremes, <http://www.met.ie/climate-ireland/30year-averages.asp>, accessed in March 2013.
- [106] World Bank. Electric power transmission and distribution losses (% of output). Technical report, World Bank, 2012.
- [107] G. Dalton, R. Alcorn, and T. Lewis. Case study feasibility analysis of the Pelamis wave energy convertor in Ireland, Portugal and North america. *Renewable Energy*, 35(2):443 – 455, 2010.
- [108] Scottish Investment Bank. Fund your business, Marine renewable energy.
- [109] Saltire Prize Challenge, <http://www.saltireprize.com/challenge>, accessed in March 2013.
- [110] A. Larsson. *The power quality of wind turbines*. PhD thesis, Chalmers University of Technology, 2000.
- [111] Conseil Général de la Mayenne. Déchets et Energie, <http://www.lamayenne.fr/fr/Au-quotidien/Environnement-et-prevention-des-risques/Dechets-energie-et-agenda-21/L-eolien-en-Mayenne>, accessed on 20/01/2013.
- [112] Website of the Cornwall Council. Population. Technical report, 2011, accessed on 20/01/2013.